Spatially Resolved Spectroscopy for Monitoring the Solvent Content in Pharmaceutical Drying

Department of Chemical and Process Engineering
University of Strathclyde

Mais Al-Attili

This thesis was submitted in fulfilment of the requirements
for the degree of Doctor of Philosophy

2024

Declaration of Authenticity and Author's Rights

This thesis is the result of the author's original research. It has been composed by the author and has not been previously submitted for examination which has led to the award of a degree.

Signed:

Date:

Previously Published Work and Conference Contributions

Published work:

Development of a Spatially Offset Raman Spectroscopy Probe for Monitoring Pharmaceutical Drying. Mais Al-Attili, Carla Ferreira, Chris Price, Karen Faulds, Yi-chieh Chen. Chemical Engineering Research and Design, 2023, volume 192, pages 510-520.

Conference presentations:

- SAR-DRM for the In-line Monitoring of the Solvent Content During Pharmaceutical Drying. Mais Al-Attili, Carla Ferreira, Chris Price, Karen Faulds, Yi-chieh Chen. International Conference on NIR Spectroscopy (ICNIRS21), 18-21 Oct 2021, China-online.
- SORS for Monitoring the Solvent Content During Pharmaceutical Drying. Mais Al-Attili, Carla Ferreira, Chris Price, Karen Faulds, Yi-chieh Chen. Spring SciX, 11-13 Apr 2022, UK.

Conference posters:

- Spatially Resolved Spectroscopy for Monitoring the Solvent Content During Pharmaceutical Drying. Mais Al-Attili, Carla Ferreira, Chris Price, Karen Faulds, Yi-chieh Chen. Advances in Process Analytics and Control Technologies conference (APACT22), 14-16 Sept 2022, UK.
- SORS for Monitoring the Pharmaceutical Isolation Processes. Mais Al-Attili, Carla Ferreira, Chris Price, Karen Faulds, Yi-chieh Chen. 11th pan-European Science Conference on QbD and PAT, 11-13 Oct 2023, UK.

Webinars:

- SAR-DRM for the In-line Monitoring of the Solvent Content During Pharmaceutical Drying. Mais Al-Attili, Carla Ferreira, Chris Price, Karen Faulds, Yi-chieh Chen. Centre for Process Analytics and Control Technology (CPACT), 24 Feb 2022.
- Development of a Spatially Offset Raman Spectroscopy Probe for Monitoring Pharmaceutical Drying. Mais Al-Attili, Carla Ferreira, Chris Price, Karen Faulds, Yi-chieh Chen. Centre for Process Analytics and Control Technology (CPACT), 25 Jan 2024.

Acknowledgements

I am grateful to my supervisors Dr Claudia (Yi-chieh) Chen and Prof Chris Price for accepting me for this PhD and for their continuing support, patience, and valuable advice throughout this project.

I would like to acknowledge the support from the Department of Chemical and Process Engineering, and the Centre for Continuous Manufacturing and Advanced Crystallisation. It was vital for safely and successfully conducting the experimental work, and I have learnt a lot through watching great people do their jobs.

My utmost gratitude to my family for their constant support and guidance.

Abstract

The pharmaceutical drying process is critical to the quality of the active pharmaceutical ingredient or the drug product as it is often the final unit operation. The non-uniformity of drying is particularly challenging as it renders inaccurate the determined solvent content and drying endpoint, which is a critical quality attribute. As process analytical technology further develops, novel techniques are implemented to address process and product challenges. Spatially resolved spectroscopy is a technique in which spectra are collected from spatially resolved distances from the incident light. This technique is used for the characterisation of non-uniform media. In this thesis, the use of spatially resolved spectroscopy for the monitoring of the drying of an active pharmaceutical ingredient is reported.

Pharmaceutical drying of model systems was monitored using spatially resolved spectroscopy. In this work, three bespoke probes were used for the collection of spatially resolved spectra. One probe allows the collection of spatially and angularly resolved diffuse reflectance near-infrared measurements (SAR-DRM), while the other was developed for the collection of spatially offset Raman spectroscopy (SORS) measurements. The third probe combines both techniques and was developed for the collection of both spatially resolved near-infrared spectra and spatially offset Raman spectra and is termed the combined probe. This thesis details the in-line and at-line application for industrial process monitoring using these techniques, which to our knowledge were not applied in this setting.

The drying of two grades of paracetamol, granular and powder, in the solvents n-heptane and methyl tert-butyl ether was monitored using SAR-DRM. The drying of granular and powder paracetamol in the solvents anisole and methyl tert-butyl ether was monitored using SORS. Partial least squares regression (PLSR) analysis was used for the estimation of the solvent content using spectra from the individual signal collection configurations, in addition to a combination of the configurations. Results from both techniques suggest that PLSR models of spectra collected from larger distances lead to more accurate

estimations of the solvent content. This was attributed to the larger volume of the drying powder cake probed by those techniques. Since the drying of paracetamol in methyl tert-butyl ether could be monitored using both techniques, the combined probe was used for monitoring this system, and multi-block PLSR analysis was conducted using both near-infrared and Raman spectra of combinations of the configurations. The multi-block PLSR model performance was similar to that of the individual SORS spectra, which was attributed to the stronger signals and spectral features of the Raman signal compared to the near-infrared measurements. Since the application of SORS for the monitoring of pharmaceutical drying was demonstrated and showed improvement in PLSR model performance and solvent content estimation, SORS was further used for the monitoring of the washing with methyl tert-butyl ether a paracetamol filter cake wet with anisole. The results similarly showed improved estimations of the content of both solvents in the filter cake from spectra from larger offset distances. The outcomes of the studies in this thesis demonstrate the advantage of the application of spatially resolved spectroscopy for monitoring the solvent content in pharmaceutical drying. The use of such novel process analytical technology offers potential for improved process monitoring and accurate prediction of the process end point.

Table of Contents

List of Figures

List of Tables

List of Notations and Units

$\boldsymbol{A}$	Absorbance
$\boldsymbol{b}$	path length of the light or sample thickness
$\boldsymbol{B}$	Regression coefficient
$\boldsymbol{c}$	concentration
Δx	Offset distance
$\boldsymbol{\varepsilon_a}$	Absorption coefficient
$\boldsymbol{\varepsilon_s}$	Scattering coefficient
$\boldsymbol{\varepsilon_{ext}}$	Extinction coefficient
$\boldsymbol{E}$	Error in spectral responses matrix
$\boldsymbol{F}$	Error in the concentrations matrix
$\boldsymbol{I_0}$	Intensity of the incident light
$\boldsymbol{I}$	Intensity of transmitted light
$\boldsymbol{P}$	Loadings of spectral response matrix
$\boldsymbol{Q}$	Loadings of the concentration matrix
$\boldsymbol{R^2}$	Coefficient of determination
$\boldsymbol{SSR}$	Sum of squares of residuals
$\boldsymbol{SST}$	Total sum of squares
$\boldsymbol{T}$	Scores of spectral response matrix
$\boldsymbol{U}$	Scores of the concentrations matrix
$\boldsymbol{X}$	Spectral response matrix
$\boldsymbol{Q}$	Loadings of the concentration matrix
$\boldsymbol{Y}$	Concentration of analyte matrix

°C	Degrees Celsius
cm	Centimetre
cm^{-1}	Wavenumber
µL	Microlitre
mm	Millimetre
mL	Millilitre
mW	MilliWatt
nm	Nanometre
s	Seconds

List of Abbreviations

API	Active pharmaceutical ingredient
Arbitr.Units	Arbitrary units
CPP	Critical process parameter
CQA	Critical quality attributes
2D	2-dimentional
FDA	Food and drug administration
1FPO	1 fibre per offset
GC-MS	Gas chromatography – mass spectrometry
KF	Karl-Fischer titration
LV	Latent variable
LOD	Loss on drying
LOOCV	Leave-one-out cross validation
MTBE	Methyl ter-butyl ether
MLR	Multiple linear regression
MSC	Multiplicative scatter correction
NIR	Near-infrared
NW	Norris-William derivation
PAC	Process analytical chemistry
PAT	Process analytical technology
PC	Principal component
PCA	Principal component analysis
PCR	Principal component regression
PLSR	Partial least squares regression
PSD	Particle size distribution
QbD	Quality by design
QTPP	Quality target product profile

RMSEC	Root mean square error of calibration
RMSECV	Rot mean square of cross-validation
RMSEP	Root mean square error of prediction
RPM	Rotations per minute
SAR-DRM	Spatially and angularly resolved diffuse reflectance measurement
SG	Savitzky-Golay derivation
SNV	Standard normal variate
SR-DRM	Spatially resolved diffuse reflectance measurement
SC	Solvent content
SORS	Spatially offset Raman spectroscopy
TGA	Thermogravimetric analysis
UV-Vis	Ultraviolet-visible

1. Overview

1.1 Introduction

In conventional pharmaceutical drug development and the following drug product manufacturing, the quality of a product is determined through testing the product at the end of the process; thus, achieving quality by testing. Suppose it is established that the quality of the product falls out of the desired specifications. In that case, the process for producing the following batch is adjusted while the previous batch is wasted. A current and more effective method is quality by design (QbD), which aims to enable real-time feedback control over the process to ensure that the desired quality of a product is obtained.

Process analytical technology (PAT) is the tool that transforms and allows for real-time process monitoring. In 2004, the United States Food and Drug Administration (FDA) published a guideline to encourage innovation by introducing process analytical technology (PAT) to the pharmaceutical manufacturing industry. The FDA defines PAT as systems utilised for the timely design, analysis, and monitoring of the critical process parameters (CPPs), which in turn affect critical quality attributes (CQAs) of a drug to guarantee the quality of raw materials and the final product.[1,2] An example of a process where PAT displays a clear advantage is pharmaceutical drying, which involves intrinsically varying rates of heat and mass transfer within a dryer, leading to the nonuniform nature of the drying process. This means that it is vital to obtain representative measurements of the CQAs during drying, the most important of which is the solvent content at the end of the process, termed residual solvent content. The solvent content is conventionally measured by methods that rely on loss on drying (LOD) measurements that capture the difference in the mass of a sample extracted from the process before and after the sample is dried. This implies that the conventional LOD method is invasive and may not represent the bulk of the drying product. This

calls for innovative approaches to replace the conventional methods with real-time and reliable technique.[3]

Near-infrared (NIR) and Raman spectroscopy are complementary spectroscopic methods that measure the transition between vibrational energy levels of a molecule upon absorbing light. Conventionally, light or laser is shone on a sample, and the reflected or transmitted signal is collected from one point. Those techniques can be implemented to capture real-time measurements within process reactors. This quick and non-destructive application makes them desirable for application in process monitoring.[4-12]

More advanced variants of those techniques include spatially and angularly resolved diffuse reflectance NIR measurements (SAR-DRM), also termed multi-point and multi-angle NIR, and spatially offset Raman spectroscopy (SORS). In SAR-DRM, one or multiple illumination points at multiple angles can be applied, and the NIR signals are collected from multiple distances from the incident light. Similarly, in SORS, the laser illuminates a sample, and the signal is collected from multiple spatially offset distances from the illumination point. For a particulate system, the propagation of light is further affected by the light scattering effect where the interaction between light and particulate substance of the system results in the scattering and redistribution of light. Scattered photons migrate laterally within a sample and are then backscattered through the sample surface and are less likely to migrate to the same illumination point. Measuring spectra obtained from various distances from the illumination point offers the potential to characterise the heterogeneous subsurface of a sample due to the larger sampling volumes.[13-16] This presents an opportunity for monitoring pharmaceutical drying as it could show a more accurate representation of the bulk of the powder. Coupled with chemometric techniques such as partial least squares regression (PLSR) for quantitative analysis SAR-DRM and SORS offer real-time monitoring of CQAs, enabling feedback control of CPPs.

In this thesis, studies using SAR-DRM and SORS individually and combined for monitoring pharmaceutical drying are reported. The studies are conducted

to assess the applicability of SRS in industrial settings through evaluating the SRS signal response of an API and solvent mixtures during pharmaceutical drying and the estimation of the solvent content during drying. Moreover, the potential for using SORS for the monitoring of pharmaceutical washing as part of the pharmaceutical isolation unit processes is also explored.

The studies serve to address the following aims:

- Evaluate the SRS signal response of an active pharmaceutical ingredient and solvent mixture during pharmaceutical drying
- Investigate the suitable signal pre-processing and processing methods
- Examine the performance of SRS in PLSR analysis for solvent content estimation individually and as fused multi-block data
- Explore the potential of using SORS for the monitoring of pharmaceutical washing as part of the pharmaceutical isolation unit processes

The objectives of these studies are as follows:

- Evaluate the SAR-DRM and SORS signals in the pharmaceutical drying of two paracetamol grades, granular and powder, wetted by three solvents, anisole, n-heptane, and methyl tert-butyl ether (MTBE)
- Examine the performance of PLSR models with individual SAR-DRM and SORS configurations for estimating the solvent content during drying
- Investigate the PLSR model performance with combined configurations for estimating the solvent content
- Assess the improvement of the PLSR model performance of combined SR-DRM and SORS spectra for estimating the solvent content

Furthermore, a case study was performed to explore the applicability of SORS on washing, the process leading to drying in the isolation unit processes. The objective of the case study is to:

- Apply SORS for the monitoring of pharmaceutical washing

First, an existing SAR-DRM system is implemented for in-line monitoring of laboratory-scale drying of granular and powder paracetamol grades in two solvents, n-heptane and methyl tert-butyl ether (MTBE). The datasets are used to build PLSR calibration sets using each of the configurations individually and in combinations for the estimation of the solvent content. The performance of the spatial and angular configurations in the SAR-DRM system is evaluated to assess the advantage of using SAR-DRM as opposed to conventional diffuse reflectance NIR. Using a recently developed SORS probe, SORS spectra are collected on-line to monitor the drying of granular and powder paracetamol in the solvents anisole and MTBE. For the estimation of the solvent content, PLSR calibration sets are constructed using spectra from each of the spatially offset distances to quantify the solvent content and evaluate the improvement in solvent content estimation compared to the conventional application. Then, a newly developed combined spatially resolved spectroscopy probe, which combines spatially resolved diffuse reflectance NIR and spatially offset Raman spectroscopy, is used for monitoring the content of MTBE in granular and powder paracetamol filter cakes. Multi-block PLSR analysis is explored for constructing calibration sets of the NIR-Raman datasets and the performance of the multi-block calibration sets is compared to that of the individual techniques. Finally, SORS is used for the monitoring of two solvents in a granular paracetamol filter cake wetted with anisole and washed with variable cake volumes of MTBE in order to evaluate the performance of SORS for the estimation of the two solvents in the filter cake, in addition to assessing the efficiency of washing.

1.2 Thesis structure

There are nine chapters in this thesis. Chapter 1, the current chapter, provides an overview of the background and purpose of the work reported in this thesis. Chapter 2 is an introduction to pharmaceutical drying. Chapter 3 presents a literature review and fundamentals of near-infrared and Raman spectroscopy, with a particular focus on spatially and angularly resolved diffuse reflectance near-infrared measurements (SAR-DRM) and spatially offset Raman spectroscopy (SORS). This is followed by a review of the processing and analysis of the data collected using those techniques. Chapter 4 is the experimental section detailing the drying setup, SAR-DRM and SORS instrumental setups, and the collection and analysis procedures and parameters.

Chapter 5, the first results chapter, includes the qualitative and quantitative analysis of the SAR-DRM data collected from the drying experiments. Similarly, Chapter 6 consists of the qualitative and quantitative analysis results of the SORS data collected from the drying experiments. Chapter 7 explores the analysis of combined SAR-DRM and SORS data using multi-block data analysis. Chapter 8 is a freestanding chapter for the case study on SORS application for monitoring the washing process. It includes an introduction to pharmaceutical filtration and washing processes and an experimental section detailing the collection of a SORS dataset following the washing of paracetamol with two solvents and the results of the analysis for the estimation of the content of each of the solvents. Chapter 9 concludes the findings of this thesis, followed by suggestions for future work.

2. Introduction to Pharmaceutical Drying

This chapter introduces the pharmaceutical drying process, including the mechanism, stages, purpose of drying within pharmaceutical manufacturing, and a brief review of the types of dryers used in the pharmaceutical industry. This is followed by a definition of the critical process parameters and the dependant critical quality attributes, as well as an outline of the complexity inherent to the drying process.

2.1 Drying in the manufacturing of pharmaceuticals

Solid pharmaceutical dosage forms are some of the most popular physical forms of drugs. Therefore, it is necessary to develop manufacturing processes to produce those solid pharmaceuticals with desired attributes and reproducible quality.[17] To manufacture a solid dosage form, for example, the first step in the manufacturing process is the synthesis of the chemical entity of the desired pharmaceutical effect, which is the active pharmaceutical ingredient (API). Then, a stable form of this chemical entity is produced and purified through crystallisation,[18] where the product of the crystallisation process is a slurry composed of the API crystals in the crystallisation mother liquor. The solid crystalline API is isolated through the filtration of the slurry to produce a wet cake, followed by the removal of the remaining mother liquor from the crystallised compound in the wet cake by washing with a wash solvent.[19] Then, the wash solvent is removed from the API wet cake through drying. Those previous steps normally constitute the steps for the primary manufacturing of a solid API.[17]

Depending on the desired form of the final pharmaceutical product, a secondary manufacturing stage may also be conducted. The second stage includes a formulation step, which revolves around the formulation of a final pharmaceutical product through the addition of excipients to the API. Those excipients may be mixed with the API and aggregated by applying high stress to a dry-powder mix (dry granulation) or aggregated with the use of a binding solvent (wet granulation). When a wet granulation step is included in the secondary manufacturing stage, a drying step follows to dry the granules prior to further processing.[17,20] Therefore, the drying process can influence the quality of both API and the solid pharmaceutical product as well as impact the processes that follow.

Pharmaceutical drying is a process by which a dry pharmaceutical solid is obtained from an initial solution, suspension, slurry, or wet solid by removing the liquid from the product.[17] It is a thermal process conducted by exposing the moist or wet material to the relatively dry air of a suitable temperature until the

liquid around the solid evaporates. The vapours around the solid are extracted, allowing for further evaporation till the solid is dry. Therefore, drying is a process of transfer of the solvent from within the wet solid to the surface and, subsequently, to the surrounding air and out of the dryer as well as being a process of transfer and distribution of heat within a dryer and the solid particles to evaporate the solvent.[21] Nevertheless, the pharmaceutical solid is not completely dry as some residual solvent will remain within the solid. The remaining solvent content in the dried product is termed the residual solvent or residual moisture. Drying pharmaceutical powders is essential for obtaining products with percentages of residual solvents that would ensure the safety and stability of the product. The amount of residual solvent allowable in the dry consumable product may be determined based on regulatory requirements related to safety or stability considerations.[17,22,23]

2.1.1 Solvent content and the mechanism of drying

The total moisture or solvent content is the overall mass of liquid accompanying the solid and may be expressed as kilograms of liquid per kilogram of completely dry solid or as a percentage of solvent within the wet mass. The total solvent content is divided into free solvent content, also termed the unbound solvent, and equilibrium solvent content, which is termed the bound solvent.[17,21]

The unbound solvent can be relatively easily removed from the wetted powder bed (wet cake). However, following the removal of the unbound solvent, the powder bed is not completely free from the solvent as it is in equilibrium with the solvent present in the surrounding air. Bound solvent is the solvent absorbed within the product or adsorbed on the surface of the product. The bound solvent that is absorbed is enclosed in the solid within capillaries as a result of surface tension, while the adsorbed portion is connected to the surface of the solid and may be joined to form layers on the surface. Both forms of bound solvent are difficult to eliminate by evaporation.[17,21]

The drying process is subject to external and internal conditions. The external conditions include those variables that affect heat transfer to the product including temperature, humidity, direction and rate of flow of air within the dryer, as well as agitation, and the physical form of the solid throughout the process. Those external conditions affect the removal of unbound solvents to a larger extent than the bound solvent. Internal conditions include the temperature and moisture gradients that arise due to the transfer of external heat to the wet particles.[21]

The solvent content of the air within a dryer is affected by the extent of solvent taken up by the air and the temperature changes. During the drying process, the solvent from the drying particles in a wet cake evaporates to the air surrounding it within the dryer. This leads to a decrease in the drying capacity as heat from the drying air is transferred to the wet cake resulting in a decrease in the temperature of the drying air, which is termed evaporative cooling. The decrease in the temperature of the air can also lead to the condensation of solvents.[17]

Once the unbound solvent has completely evaporated, a moisture gradient is created between the interior of the wet cake and its surface. If the process is continued, this gradient could lead to shrinkage upon over-drying and, therefore, cracking due to tension. To counteract the negative effect of the moisture gradient, a balance must be created between the internal moisture relocation due to heat and mass transfer and the relative air humidity within the dryer to achieve the highest rate of moisture relocation while avoiding over-drying.[21,24] Mechanisms of solvent migration within moist particles include capillary flow, diffusion, and internal pressure due to the shrinking of the outer drier parts of the particle.[21,25]

The equilibrium moisture or solvent content of a solid, where water or a solvent is present in the air within a dryer, is dependent on the properties of the solid itself and the relative humidity. Increasing the drying time when the equilibrium solvent content is attained does not lead to any change in the solvent content of the dry product. However, decreasing the relative humidity of the air in the

dryer will lead to a decrease in the solvent content. Nonetheless, if the drying product is stored in conditions where the air is of higher humidity, the solvent will be adsorbed on the product to re-establish equilibrium between the solvent content and surrounding air.[21] Hence, the conditions in which the final drying product will be stored must be taken into consideration when determining the solvent content of the dry product. If high moisture content leads to instability, it is vital for the drying product to be preserved in a sealed container to avoid degradation.[17]

2.1.2 Stages of the drying process

The pharmaceutical drying process may be divided into three stages according to the change in the drying rate and solvent content as shown in Figure 2.1(a). The first stage is the warm-up stage, where the drying is slow before a steady state is reached in the second stage, the constant rate stage. In this stage, the drying is quicker as it is mainly limited by the heat transfer. Finally, in the final stage, the falling rate stage, the rate of solvent removal decreases at the end of the drying process and the drying rate is slowed by the mass transfer. While the drying may be linear during the warm-up and constant rate stages, it deviates from linearity in the falling rate stage due to the nonuniform diffusion during the migration of the solvent within the particles to the surface.[22,24]

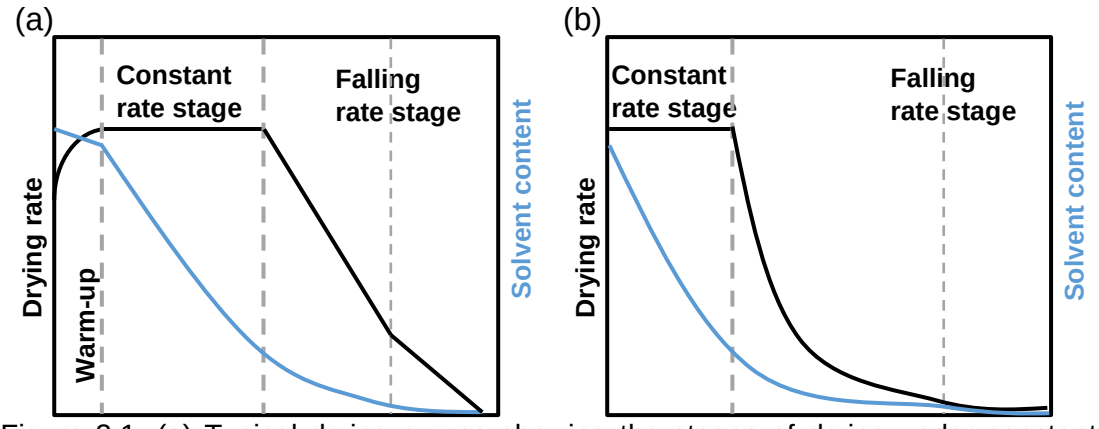

Figure 2.1. (a) Typical drying curves showing the stages of drying under constant conditions. The dashed lines separate the warm-up, constant rate stages, and the two parts of the falling rate stages. Adapted from Murugesan, 2010.[22] (b) Drying stages of a quick drying solvent. Adapted from Hsieh, 2017.[26]

The warm-up stage is the time required for the system to reach the target drying temperature. During this stage, the solvent adsorbed on the surface of the drying product is evaporated and the vapour is eliminated through the vents in the dryer when reduced pressure is employed or using a gas sweep. The temperature of the drying product is decreased in this stage due to evaporative cooling but increases again after the solvent has evaporated and eliminated.[22]

During the constant rate stage, the pressure and rate of heat transfer within the system control the drying rate. The unbound solvent adsorbed on the surface of the drying product continues to vaporise and evaporate, where there is a difference between the set temperature of the dryer and the removed solvent. Enhancing the drying rate can be achieved by increasing the temperature of the dryer or decreasing the pressure. Other factors affecting the speed of drying include the surface area of the drying product, agitation, and the rate of removal of the solvent vapour within the dryer.[27,28] Diffusion of the solvent vapour at the particle-air medium also contributes to the rate of drying during this period.[21] At the end of the constant rate stage, the solvent content reaches the critical moisture or solvent content, where no solvent is present on the surface of the drying product, and the solvent within particles begins to move by capillary forces to the surface.[21,29]

In the falling rate stage, mass transfer expressed by solvent migration from the inside of particles to the surface is the determining factor of the solvent evaporation rate after the solvent on the surface has completely evaporated. This process may cause the drying times to be long.[22] Although the overall drying rate per time is reduced, the drying rate per unit of moist solid surface area is constant during the first part of the falling rate period. In the second part of the falling rate period, the rate-determining step is the solvent migration inside the solid particles across the concentration gradient, which leads to a slower decrease in the drying rate and a steeper curve of the drying rate until the process ends.[21] The rate of drying during this stage is largely dependent on the porosity and internal structure of particles.[27] Conduction of heat also

affects the rate of drying during this period due to the presence of moisture deeper within the particle. Porosity and density of particles govern the extent to which solvent migration and heat transfer affect the rate of drying during this stage.[21] Depending on the suitable residual solvent content, the drying process may not go through all of the aforementioned stages. Where high residual solvent is required, the drying is carried out only through the constant rate period.[21]

Figure 2.1(b) shows the drying curve of a low boiling point (55.2˚C) and fast evaporating solvent, methyl tert-butyl ether (MTBE) as an example, expressed as solvent content versus time. The constant rate stage shows the quick evaporation of the solvent from the surface. The first part of the falling rate stage shows the transition from the solvent evaporating from the surface of particles to the solvent diffusing from within particles in the second part of the falling rate period. In the drying of this solvent, the time needed for the constant rate and the first part of the falling rate stages would exhibit a slight decrease with the increase of temperature, while the time needed for diffusion would show a greater decrease with the increase of temperature.[26] To achieve a shorter constant rate stage, the rate of evaporation may be increased by increasing the temperature or agitation, which in turn enhances the mass transfer within the dryer. On the other hand, the diffusion-controlled rate of drying during the falling rate period may only be improved by raising the temperature.[30]

2.2 Types of dryers used in the pharmaceutical industry

Heat transfer methods of dryers currently used in the pharmaceutical industry are conduction, convection, and radiation dryers.[31] In conductive dryers, heat transfer occurs by conduction, where the solid is in direct contact with a hot surface. Those dryers are also referred to as contact dryers. Examples of those dryers include vacuum ovens, conical dryers, tumble dryers, and filter dryers. In convective dryers, evaporation is induced by supplying a flow of hot air within the dryer. Examples of those dryers include the fluidised bed dryer, spray dryers, and freeze dryers. Radiation dryers generate heat within a drying product using radiation, where microwave dryers are an example.

2.2.1 Conductive dryers

A vacuum oven is an air-tight jacketed chamber that can endure steam pressure and vacuum. A vacuum pump is connected through a liquid receiver and a condenser, which is also called a cold trap. The advantages of the vacuum oven are significantly reducing the likelihood of oxidation, and drying at relatively low temperatures. Therefore, it is suitable for oxygen and heat-sensitive products. Although vacuum ovens are not currently used on a commercial scale, they are used in laboratory development applications.[31]

The conical dryer is conical in shape. This shape imparts a higher surface area to volume ratio, aiding heat transfer to the drying product. Conical dryers contain an impeller, which may also be a heat source, to increase the surface area of the drying product that is in contact with the drying air. The advantages of the conical dryer include good product uniformity and active agitation through the impeller, in addition to the limitation of exposure to the solvent and API. Disadvantages of the conical dryer include high particle attrition, complex scale-up, and difficult sampling.[22]

Tumble dryers are rotating dryers. The drying product tumbles inside the dryer, where the heat from the walls of the dryer accelerates drying while the tumbling motion offers a higher surface area for heat transfer without the shear force

associated with an impeller, such as those in conical dryers.[22] The advantages of the tumble dryer include its suitability for shear-sensitive materials, lower running cost due to the increased heat and mass transfer by the tumbling motion, simple operation, and ease of cleaning. Disadvantages of the tumble dryer include possible prolonged drying time, unsuitability for non-free-flowing materials, and lower efficiency.[22]

Agitated filter dryers are used to filter a slurry, wash the mother liquor from the produced filter cake, and then dry the product. Following the washing of the filter cake, the walls of the dryer provide heat while an impeller is used to increase the contact area of the filter cake, while vacuum pressure is applied to remove the solvent.[22] Advantages of filter dryers include the flexibility in agitation modes due to the adjustable impellers, decreased risk of exposure to the solvent and API, and elimination of product contamination or loss after filtration and washing as there is no transfer between equipment for these steps. Disadvantages of filter dryers include complex scale-up, the possibility of agglomeration, particle attrition due to the impeller, the creation of a heel between the impeller and the filter, and sampling difficulty.[22]

2.2.2 Convective dryers

The fluidised bed dryer includes a perforated base to allow for the drying air to move through the bed composed of the product to be dried. Fast drying is achieved through fluidised bed dryers as the turbulence results in particle mixing and higher mass and heat transfer rates due to the high contact between the air and the solid particles.[31] Advantages of fluidise bed dryers include shorter drying times due to efficient mass and heat transfer rates, which means that they can be used for heat-sensitive products, uniform temperature profile and drying due to turbulence, minimised aggregation, and obtaining high product output from smaller scales due to the shorter drying times. However, this method could result in excessive attrition of the product due to turbulence, and static electric charges may be generated as a result of the friction between the particles and the dry air. The attrition also leads to the

production of fine dust, which also contains static charges, and the mixture with the solvent containing air in the drying could present an increased risk for explosions.[31]

Spray dryers may be used to dry suspensions or products dissolved in a solvent. The liquid is sprayed as the mist of fine particles through a nozzle by dispersing it into a stream of hot gas within a cylindrical dryer, a process termed atomisation. The solvent quickly evaporates, therefore, the heating duration is reduced. Advantages of spray dryers include product uniformity, the possibility of combining the processes of crystallisation and drying, and suitability for heat-sensitive products. Disadvantages of spray dryers include high consumption of sweeping gas and challenging control of the bulk product density.[22]

Freeze drying, sublimation, or lyophilisation is the conversion from the solid phase to the vapour phase directly without converting through the liquid phase. It is suitable for heat-sensitive products.[31] During the process, the solution of the heat-sensitive product is frozen and the pressure is decreased. Following that, the temperature is increased so that the vapour phase is reached while avoiding the transition through the liquid phase.[20] Advantages of freeze drying include producing a porous solid that is light and therefore achieves faster dissolution, it is suitable for heat sensitive products and no hydrolysis or chemical decomposition occurs, oxidation is avoided as the high vacuum conditions during the process prevents contact with air. Porous solids may not always be desirable, and the completely dry product may be hygroscopic. Freeze dryers are expensive, and the procedure is slow.[31]

2.2.3 Radiation dryers

Microwave radiation in the range of 10 mm to 1 m is an efficient heating and drying method and is used in the pharmaceutical industry. Heat generation is uniform throughout the solid, and the vaporised solvent is removed from the dryer as air flows. This technique relies on the fact that water absorbs radiation

more easily than dry solids, and the endpoint is indicated as the residual microwave energy increases when most of the solvent has evaporated.[31] Advantages of microwave drying include quick drying at low temperatures, no attrition or dust formation, and thermally efficient due to microwave energy being almost completely absorbed by the solvent. Disadvantages include the additional safety measures required as microwave radiation can cause organ damage, and the limited batch size of commercial microwave dryers compared to those of other dryers.[31]

2.3 Pharmaceutical drying process considerations

In manufacturing operations, the pharmaceutical drying process is commonly referred to as a black box [3,32] and a bottle-neck.[25,27,33] This is due to the process being dependent on the physicochemical properties of the materials to be dried, properties of the solvent to be removed,[31] type of dryer used, the operational conditions within the dryer,[22] and the scale of the operation.[25,27,34] Furthermore, the physical phenomena of heat and mass transfer concurrently occurring within the drying vessel add complications to the process due to their inhomogeneous and non-linear nature while being the rate-limiting phenomena within the process, which causes problems when scale-up is attempted.[25,35]

Properties of the drying product, such as particle morphology, particle size distribution and solvent content, affect the drying process. Particle morphology and size distribution determine the surface area accessible for heat transfer. The solvent within the drying product affects the drying duration and the properties of the dry product. It may also lead to changes in the particle size distribution of the product through agglomeration or attrition.[22] Drying newly developed APIs is challenging due to the limited information regarding their physicochemical characteristics that are essential for obtaining a product of the required quality.[25]

For the selection of the size and design of dryers, perquisites include knowledge of the drying characteristics, moisture equilibrium, handling limitations, and temperature sensitivity of the solid as well as properties of the dryer, such as the possible temperature range within the dryer.[21] Agitation, intermittent or continuous, may be applied to the process to optimise heat transfer while reducing drying cycle time, but it could affect the particle properties of the product.[28,34] Process scale-up is an issue in terms of maintaining robust production characteristics.[25,36,37] This is due to the heat transfer rate being correlated with the rate of solvent removal, which directly impacts the evaporation process.[26] Larger surface area of the drying product provides a larger area for heat transfer. As a result, applying pressure

(vacuum) during drying, as is done within vacuum filter dryers, makes the process limited by the heat transfer rate rather than the mass transfer rate.[22]

With regard to energy consumption, drying unit operation requires intensive amounts of energy due to the elevated level of heat generally needed.[21] While conductive dryers, where heat is indirectly conducted through a heated surface, are economical as they provide higher thermal efficiency, convective dryers, where heat is provided directly by hot air flowing over the wet product, still form 85% of the dryers used in industrial applications.[21,27] Additional stress is placed on the control of the process parameters when taking productivity and cost reduction into consideration.[33]

The main purpose of considering the previously mentioned factors is to tune the critical process parameters for the achievement of a product that conforms to the critical quality attributes (CQA) for the production of a product with a suitable quality target product profile (QTPP).[23,38]

2.3.1 Critical Quality Attributes and Critical Process Parameters

The International Conference on Harmonisation of Technical Requirements for Registration of Pharmaceuticals for Human Use (ICH), in the pharmaceutical development guideline Q8(R2) published by the European Medicines Agency (EMA), defines a critical quality attribute (CQA) as '*A physical, chemical, biological, or microbiological property or characteristic that should be within an appropriate limit, range, or distribution to ensure the desired product quality. CQAs are generally associated with the drug substance, excipients, intermediates (in-process materials) and drug product…CQAs can additionally include those properties (e.g., particle size distribution, bulk density) that affect drug product CQAs*'. It also defines a critical process parameter (CPP) as '*A process parameter whose variability has an impact on a critical quality attribute and therefore should be monitored or controlled to ensure the process produces the desired quality*'. Both CQAs and CPPs are determined and monitored to achieve a certain quality target product profile (QTPP), which is '*A prospective summary of the quality characteristics of a drug product that ideally will be achieved to ensure the desired quality, taking into account safety and efficacy of the drug product.*'[38]

Based on these definitions, residual moisture or solvent content within the drying product is considered a CQA. The residual solvent levels must be low to maintain the quality of a freely flowing product and prevent degradation or change in the crystal morphology during storage of the primary pharmaceutical product. For the secondary manufacturing of the final dosage form, the residual solvent affects the compressibility, flow properties, and stability.[22,31] In cases other than when residual solvents are to be avoided or limited due to toxicity, minimal amounts of residual solvent (1-2%) are maintained within pharmaceutical products rather than completely dry products as it yields granules that have better compressibility. Also, having completely dry powder will lead to the formation of static charges that prevent the free flow of the dry powder as well as the generation of fines due to attrition when the product is over-dried.[23,31,39] In addition to that, inadequate determination of drying

endpoints indicated by the critical solvent content alters the mass balance required for dosage accuracy, as well as altering the dissolution characteristics.[40] In tablet manufacturing, the moisture content is of crucial importance due to the effect of moisture on powder adhesion to the tablet press during the tabletting step.[32] Stability concerns due to possible phase transition of polymorphs owed to solvent content or thermodynamic and mechanical stresses.[41-44]

Another example of CQA is morphology and particle size distribution (PSD), which are subject to attrition and agglomeration due to a collective effect of CPP, such as agitation, temperature, and pressure, as well as being influenced by other CQA such as the solvent content.[28,34,45,46]

Agitation at a certain level of solvent content leads to the improvement of the drying rate due to the increased surface area in contact with warm air within the dryer. However, at a higher level of the solvent content, termed the sticky point, agitation leads to agglomeration.[25] At lower temperatures, the drying rate is lower, and the process requires a longer cycle time. This leads to obtaining lower PSD in agitated drying due to exposing the particles to attrition for a longer duration. In addition, areas close to the impellers are under high shear and experience attrition and feature particles with smaller PSD due to attrition while those away from the impeller agglomerate. The number and position of impellers are also a source of variability.[28] Due to the change in particle size and shape, the solvent content within the particles also varies. This variation in process parameters leads to inconsistent powder flow behaviour, altered dissolution profile and, therefore, change in bioavailability of the final dosage form.[34]

Considering pressure within the dryer as a CPP, reducing pressure leads to a reduction in heat transfer although it also reduces the boiling point of the solvent. As a result, the drying rate and duration to reach the required solvent content are improved, although the condition may also lead to agglomeration.[34] Solvent vapour residence time and pressure are also crucial in affecting the drying rate and may be controlled by employing a vacuum pump and a nitrogen

sweep to control the pressure within the dryer and the removal of the solvent vapour.[36]

Modifying a process parameter whilst the process is running or between batches within different types of dryers provokes variable effects on the product as well as other concurrent processes. The parameters with the most prominent effect on the outcome of the process include modifying the temperature, humidity and flow of air within the dryer, with the temperature of air having the most significant impact on the drying kinetics and quality attributes.[47]

As mentioned previously, the characterisation of CQA and control of the CPP are vital for optimising both the process and the product. In particular, the solvent content contributes to many of the complications and decision-making points within the drying process. Therefore, by monitoring this CQA, a feedback loop may be created to adjust critical process parameters and avoid possible complications within the process that would affect other CQAs. Monitoring those CQAs and CPPs, as well as creating a feedback loop, may be enabled through applying process analytical technologies. Coupled with multivariate analysis, Quality by Design (QbD) can be achieved. QbD is a concept promoted by the European Medicines Agency and aims to produce medicines with reproducible quality through the use of PAT and analyses for the design of pharmaceutical processes.[48] Process analytical technology and multivariate analysis are introduced in the following chapter.

3. Near-infrared and Raman Spectroscopy, Spectral Pre-processing, and Data Analysis

This chapter includes a review of some of the literature on process analytical technology, including near-infrared and Raman technologies. It is followed by a review of spectral processing and analysis methods for qualitative and quantitative information extraction from the spectral data.

3.1 Process analytical technology

Process analytical chemistry (PAC) refers to the chemical analysis performed on samples from the production stream or the end product to ensure that process parameters are suitable for manufacturing a product of desired quality. Some of those control parameters include moisture, pressure, temperature, and pH. In 2004, the United States Food and Drug Administration (FDA) published a guideline to encourage innovation by introducing process analytical technology (PAT) to the pharmaceutical manufacturing industry. The FDA defines PAT as systems utilised for the timely design, analysis, and monitoring of the manufacturing CPPs and CQAs to guarantee the quality of raw materials and the final product. PAT includes risk and mathematical analysis in addition to the chemical, physical, and microbiological properties monitored as part of PAC. This progress to PAT was driven by the drug quality system of having the quality of products built in by the design of the process, rather than the previous practice of testing the quality into products (QbD).[1,2]

PAT may be applied within manufacturing procedures in various modes including:

1. Off-line measurements: analysing a manually removed sample from the process stream in an external laboratory.
2. At-line measurements: analysing a manually removed sample near the process stream.
3. On-line measurements: analysing a sample automatically extracted from the process stream. The sample may be returned to the same stream after the analysis.
4. In-line measurements: measurement conducted using a probe inserted into a process unit or stream.
5. Non-invasive measurements: in-line measurements collected without contact with a sample.

The purpose of PAT is to obtain real-time data during the processes and enable adjustments to the procedure or process to ensure the quality of the product. This improves process understanding, leading to the manufacturing

of products within the required regulatory specifications and preventing the loss of batches outside the limits of specifications.[49,50] PAT techniques include ultraviolet (UV), near-infrared (NIR), and Raman spectroscopy in addition to other techniques.[2]

3.2 Conventional methods for monitoring the solvent content during pharmaceutical drying

One of the aims of monitoring pharmaceutical drying is to establish the endpoint of drying as the residual solvent content is a critical quality attribute of the product. Conventionally, the process is halted to acquire samples for the determination of the residual solvent content, which is not ideal with regard to the desired consistency in the operation parameters. Loss on drying (LOD) methods, like thermogravimetric analysis (TGA) and Karl Fischer (KF) titration, are the conventional methods employed for solvent content measurement but are obstructive, time-consuming, and may require sample preparation.[27,50]

Loss on drying is the most conventional method for measuring the solvent content within a sample. In this method, a wet sample is weighed after extraction from the process and then put into an oven for drying. After it has dried, the sample is weighed again. The LOD can be expressed as the mass of the solvent within a sample (the difference between the mass of the wet and dry sample) divided by the mass of the wet sample to obtain a percentage of the solvent within the extracted sample. Alternatively, the mass of the lost solvent may be divided by the mass of the dry solid to obtain the mass of the solvent per mass of the solid. In thermogravimetric analysis, the change in the mass of a wet sample is monitored as the temperature is increased. Additional information provided by this technique includes thermal decomposition, phase transition, absorption and desorption.

Some newer techniques for analysing the solvent content include gas chromatography, mass spectroscopy, and nuclear magnetic resonance (NMR). Despite being more enhanced than the conventional methods, those still involve compromising the vacuum condition within the dryer to obtain samples and are not readily applied for in-line measurements. In contrast to the mentioned techniques, in-line PAT methods enable the uninterrupted real-time monitoring of the process, leading to higher production by decreasing drying cycle time, mitigating off-specification batches, and enabling the accurate mechanistic modelling of the process.[27,50]

Near-infrared and Raman spectroscopies are vibrational spectroscopic techniques used to determine the structure of compounds.[51] Both techniques are widely applied as in-line PAT techniques for process monitoring due to the advantages offered. These advantages include fast in-line or on-line measurements for frequent analysis. This ensures operational safety by reducing the risk of exposure to operators and reduces the fluctuation in process conditions.[27]

Although NIR spectroscopy has been proposed to monitor water content off-line since 1968 with results comparable to KF titration,[52] moisture content measurements during granulation and drying processes are still obtained using KF titration and LOD, despite the analysis frequency being limited by the methods.[40] This slow adaptation to PAT may be explained by the complexity of data generated from these techniques and the lack of appropriate knowledge transfer between the API development stages, which may use more sophisticated equipment, and the commercial production stage, which would require equipment that are more automated and simpler to use. Moreover, PAT instruments installation and operation must follow industrial approaches that ensure safety, validity, fitness for purpose, and the evaluation of the long term performance.[50]

In addition to the selection of suitable PAT tools, the location of the tools within the process according to the required measurement, ideal measurement conditions, and performance validation must be taken into consideration in order to effectively monitor the CPP or CQA.[49]

The use of spectroscopic-based PAT often involves using multivariate analysis to derive qualitative and quantitative information from the spectra.[49] With regard to the development of those analyses, validation of the PAT method, and process scale-up, there are barriers surrounding the implementation of those methods, but the benefits brought about by implementing them are driving research to overcome them.[39,53]

3.3 Interactions of light

Light interacts with matter through a phenomenon called electromagnetic radiation. This interaction occurs due to the wave-like and particle-like properties of light. The interaction between light and matter is fundamental to spectroscopy.

When light illuminates a material, the photons may be transmitted, reflected, refracted, absorbed, and scattered. Transmission happens when light passes through a transparent material without being absorbed or scattered, but may be refracted if the direction of light changes as it moves between materials of a different refractive index.[54] Reflection occurs when light bounces off the surface of a material without being absorbed, where the angle of incidence is equal to the angle of reflection. Absorption may occur when light falls on translucent or opaque materials. When light is absorbed, the energy of its photons may be absorbed by the electrons within atoms or molecules of the material causing the electrons to move to higher energy states. Light scattering is a phenomenon in which light may be redirected in multiple directions as it interacts with particles or irregularities in a material. Elastic scattering occurs when the energy of the scattered photon is the same as the incident photon, while inelastic or Raman scattering occurs when the photon scatters at a higher or lower energy compared to the incident photon.[55] In turbid media, constituted of particles suspended in a solution, light scatters through the solid particles multiple times leading to diffuse reflectance and diffuse transmittance. An example of such media is a suspension of crystals an active pharmaceutical ingredient and a solvent, where absorption and scattering would constitute the majority of phenomena taking place.

There are different types of light scattering, depending on the size of the scattering particles. Those include Rayleigh, Mie, and non-selective scattering. Rayleigh scattering occurs when the size of the scattering particles is much smaller than the wavelength of the incident light. Mie scattering occurs when the size of the scattering particles is comparable to the wavelength of light. Non-selective scattering occurs when the size of the scattering particles is

much larger than the wavelength of light. In Non-selective scattering, all wavelengths of light are scattered equally as it is non-wavelength dependant. Non-selective scattering is often observed in pharmaceutical samples, leading to a diffusely scattered signal resulting from multiple scattering incidents.

Absorbance is expressed by the laws of Beer and Lambert. According to Beer's law, absorbance is proportional to the concentration of the absorbing material. According to Lambert's law, when light passes through media, an equal proportion of the light is absorbed by each layer of a medium that the light passes through leading to an exponential decay in the intensity of light. Absorbance may be expressed as the standard logarithm fraction of the incident light detected after penetrating a sample according to Lambert's law.[56] Building on both laws, the concentration of a material that absorbs light may be calculated using Beer-Lambert's law:

$$A = log\left(\frac{I_0}{I}\right) = -log\left(\frac{1}{T}\right) = \sum_{i=1}^{n} \varepsilon_{a,i} b c_i$$

Equation 3.1

where A is the absorbance, I_0 is the intensity of the incident light, I is the intensity of transmitted light, T is the transmittance, ε is the absorption coefficient, b is the pathlength of the light or sample thickness, and c is the concentration of the absorbing chemical. In Equation 3.1, the absorbance is equal to the concentration of the material multiplied by its absorption coefficient at a certain wavelength, which is constant for a material, and the pathlength travelled by the light. This equation relies on the assumption that the light that does not exit a sample is absorbed by the sample, which may be true in non-scattering solutions as particles do not interfere with the travelling light. However, in turbid media, the light goes through multiple scattering incidents causing photons to travel through variable pathlengths.[57]

In the case of turbid media, the scattering coefficient is summed up with the absorption coefficient to compensate for the change in pathlength. Diffuse

transmittance or diffuse reflectance are the measurements that may be obtained from turbid samples, Beer-Lambert's law is adjusted to become:

$$A = log\left(\frac{I_0}{I}\right) = -log\left(\frac{1}{T}\right) = \sum_{i=1}^{n} \varepsilon_{ext,i} b c_i$$

Equation 3.2

where ε_{ext} is the extinction coefficient and is the sum of the absorption coefficient, ε_a, and the scattering coefficient, ε_s. Due to multiple scattering, the pathlength of photons travelling through a turbid sample, which may contain particles of different size and shape, is not constant and compromises the accuracy of results obtained through Equation 3.2.[58]

3.4 Near-infrared spectroscopy

Near-infrared (NIR) spectroscopy refers to the measurement of the extent of absorption of near-infrared light by molecules within a sample. When asymmetric molecules that contain polar functional groups absorb electromagnetic radiation, transitions between molecular vibrational energy levels occur. The resulting NIR spectral features are a result of combination and overtone fundamental vibrations over the wavelength range of 800-2500 nm (4000-12 500 cm^{-1}). Examples of polar functional groups that absorb near-infrared light include O–H, N–H, or C–H bonds. A NIR spectrum appears as broad and overlapped peaks due to their low absorption coefficients.[51] Within the NIR wavelength range, 1200-2500 nm is the wavelength within which characteristic absorption peaks are obtained for pharmaceutical applications. The low absorption coefficient of NIR bands allows for greater optical pathlength although the pathlength and penetration depth within turbid samples could be further affected by the scattering effect. Nevertheless, variation in the physical properties of the samples may lead to higher scattering and therefore complicate the analysis of NIR spectra.[56] NIR spectra are conventionally expressed as absorbance intensity (arbitrary or absorbance units) per wavelength (nm). Conventional NIR measurements are single-point measurements, where the output is an average of the reflectance or transmittance signal collected from the sampling area. The representativeness of the collected NIR signal is dependent on the properties of the sample. In particular, signals collected from heterogeneous samples may be misrepresentative of the bulk of the sample as the signal contains a disproportional contribution from the surface of the probed area and the bulk.[13]

The application of NIR spectroscopy enables quick and non-destructive analysis of the chemical composition samples of a mixture of components, where the spectral measurements require seconds or a few minutes and do not require any sample preparation. NIR spectroscopy may also be used for quick quantitation of materials in gas, solid, or liquid states over a range of temperatures.[51] In addition to the characteristic broad and overlapping peaks

of NIR, spectral data collected using this technique are affected by scatter effects and pathlength variation arising from the sample properties, in addition to the equipment and process noise during signal collection. Due to the level of noise encountered with NIR spectra, smoothing algorithms may be applied prior to further processing of the spectra. In addition to noise, baseline shifts among sample spectra are an often encountered issue. Broad and overlapping NIR peaks and baseline shifts may be resolved through pre-processing.

Signal pre-processing has a significant effect on spectroscopic data, where it is applied to remove the scattering effects arising in the sample spectra and resulting from physical phenomena. The pre-processing techniques that address those scattering effects include derivation, multiplicative scatter correction or standard normal variate, in addition to simple normalisation, which removes baseline shifts and differences in intensity arising from pathlength variation.[56] In addition to pre-processing, the use of chemometrics is common for the extraction of qualitative and quantitative information from NIR spectra.

Some of the fields applying NIR spectroscopy include food and agricultural,[59,60] biomedical,[61,62] and pharmaceutical analysis.[4-7,63-68] Those pharmaceutical applications include end product characterisation[63-65,67,68] and process monitoring.[4-8]

In food and agricultural applications, for example, NIR spectroscopy is used to detect and quantify quality parameters in oils, including moisture, amino acid, protein, and oilseed contents, in addition to the determination of oil types and adulteration in oil products.[59] The maturity, texture, and contamination of fruits are also explored using NIR spectroscopy.[60]

In biomedical analysis, the wavelength range 800-1200 nm is the useful wavelength range for biological samples due to the high optical transparency in this range.[56] The oxygen concentration in tissue may be indicated through NIR spectroscopy, where spectra of oxygenated and deoxygenated proteins, such as haemoglobin and myoglobin, differ. This enables the non-invasive measurement of oxygen saturation levels in tissue using pulse oximeters, in

addition to the study of brain function as the rise in oxygen levels indicates increased blood flow and as a result brain activity.[61]

For end-product characterisation in pharmaceutical applications, the use of NIR spectroscopy is reported for the identification of active pharmaceutical ingredients and excipients,[63,64] and assessing the quality of those solid pharmaceutical products,[67,68] including the homogeneity of tablets.[65] For process monitoring, NIR spectroscopy has been used for monitoring the transformation between polymorphs,[4] density of powder blends,[5,8] API load in low API load powder blends,[6] as well as API content, and average particle size.[7]

3.4.1 Spatially and angularly resolved NIR spectroscopy

Spatially and angularly resolved NIR spectroscopy, also termed multi-point and multi-angle spectroscopy, is applied through shining one or multiple illumination points at multiple angles and the collection of NIR signals from multiple distances from the incident light as shown in Figure 3.1, which shows an illustration of a multi-layered diffusely-scattering sample. In diffusely scattering media, measurements are affected by absorption and scattering of light. Through shining the light from multiple angles, different patterns of light scattering and absorption can be captured as a result of the variable optical paths, which give information related to the physical and chemical characteristics of the samples. Therefore, spectra that contain more representative information about larger volumes of the sample are collected.[13,14] The advantage of collecting a more accurate representation of samples and the opportunity to differentiate the contribution from different optical paths by resolving measurements from different spatial and angular configurations in spatially and angularly resolved spectroscopy makes this technique attractive for application in industrial processes. Nevertheless, variable signal intensities can be obtained from different collection configurations as light diffusion throughout a diffusely scattering sample results in an exponential decrease in signal intensity. A system for the collection of

spatially resolved diffuse reflectance NIR measurements has been commercially developed by Indatech, and a system for the collection of spatially and angularly resolved diffuse reflectance UV-Visible-NIR measurements (SAR-DRM) has been developed by Chen et al.[14]

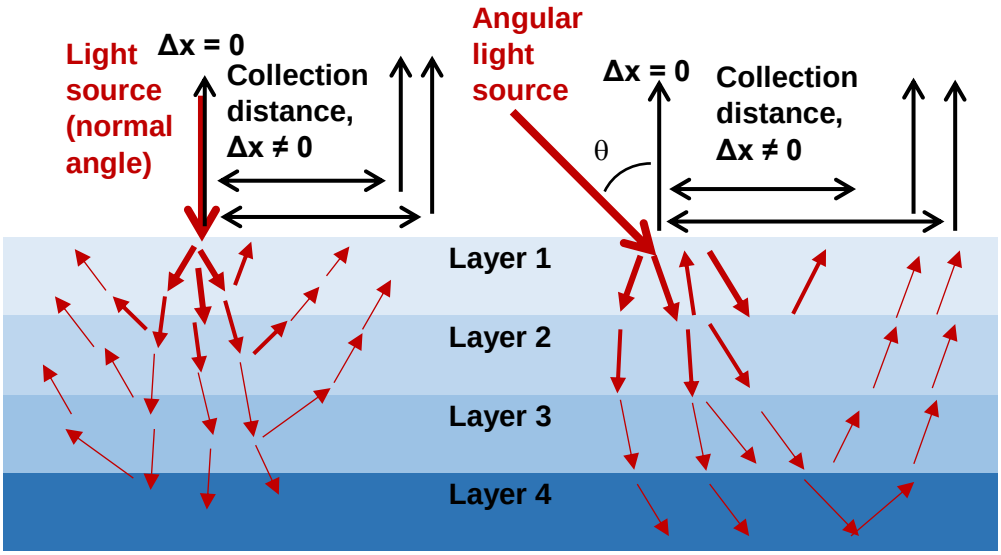

Figure 3.1. Illustration of the concept of spatially and angularly resolved diffuse reflectance spectroscopy. Light is shone at multiple angles to the multi-layered sample and the signal is collected from multiple collection distances, Δx ≠ 0, as opposed to conventional diffuse reflectance NIR measurements, where the light is shone at a normal angle and the signal is collected, Δx = 0.

Spatially resolved diffuse reflectance NIR spectroscopy has been used in the pharmaceutical field for the determination of the quality of tablets through assessing the homogeneity of tablets,[13,68-70] in addition to the use of spatially resolved NIR spectra and known physical properties for the simulation of the behaviour of light in particulate media.[71] Angularly resolved diffuse reflectance NIR spectroscopy has been used for the monitoring of the precipitation of silica and in the identification of phases in microemulsions.[72] Spatially and angularly resolved diffuse reflectance UV-visible measurements have been used for the estimation of concentration and particle size in colloidal suspensions.[14] Despite the similarity in the application of multi-point spatially and angularly resolved spectroscopy, the processing and analysis of the spectroscopic data

collected in those studies varies as a result of the difference in desired output. Therefore, an optimised signal processing approach must be in order to extract useful information from such techniques that generate large amounts of data.

3.5 Raman Spectroscopy

When light interacts with a molecule, the molecule absorbs the energy of the incident photons and is excited to a virtual state and then either returns at the same vibrational level or is shifted up or down one or more vibrational energy levels. Incidents of photons returning to the same vibrational level are regarded as elastic scattering, which is known as Rayleigh scattering as shown in Figure 3.2. The frequency of the scattered photon does not change in Rayleigh scattering as indicated by the upward arrow (laser excitation frequency) matching the length of the downward arrows (frequency of scattered photon). Raman spectroscopy is based on inelastic light scattering, where the energy of the re-emitted photons by the molecule is different to those of the illuminating photons. The phenomenon of inelastic scattering where energy is lower by the energy of one or more vibrational levels is termed Stokes scattering, where the phenomenon is indicated by shorter downward arrows. Anti-Stokes scattering occurs when the re-emitted photon gains the energy of one or more vibrational levels as indicated by the longer downwards arrows. The most likely phenomenon is Rayleigh scattering as the intensity is approximately 10^{-3} compared to the intensity of the incident light, while Raman scattering is approximately 10^{-6} compared to the intensity of the incident light. Stokes scattering is more intense compared to anti-Stokes as indicated by the relative difference in peak heights in Figure 3.2 because the majority of molecules are in the ground state at room temperature. The incidence of Raman scattering is dependent on the potential of a molecule to react to an electric field altering the electron cloud around the molecule, a property termed polarisability. Monochromatic lasers in the UV-Visible regions in addition to NIR region. Laser wavelengths closer to the NIR region, such as 785 nm, are preferred compared to the visible region due to the effect of fluorescence when using wavelength in visible light region. Shorter laser wavelength, such as 532 nm, result in higher Raman signal intensity and are therefore used with inorganic material. Laser wavelength 600-830 nm are used for Raman spectroscopy application in organic chemicals, including pharmaceuticals, as it enables balancing the signal intensity and the effect of fluorescence. [51]

Conventional Raman spectroscopy applications revolve around the illumination of a sample and the collection of the signal typically from 90˚ (right-angle) or 180˚ (backscattering) between the source and the detector configurations.

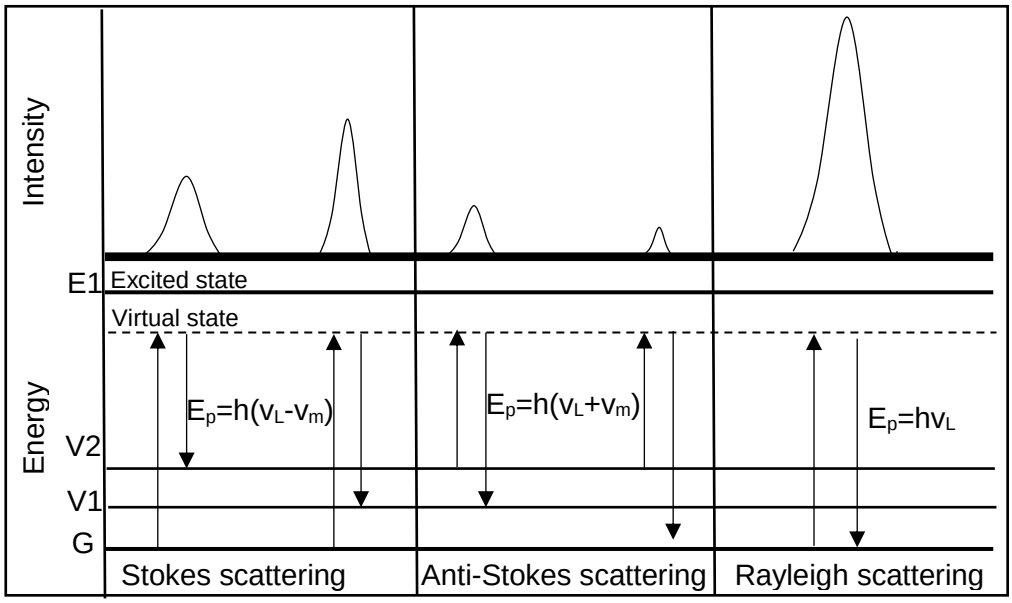

Figure 3.2. Illustration of energy shifts and comparison of the intensity of elastic Rayleigh scattering and the inelastic Stokes and anti-Stokes scattering. Peak heights are relative as the Rayleigh peak intensity is due to the difference in the probability of occurrence of each phenomena. Adapted.[51]

Similar to NIR spectroscopy, Raman spectroscopy allows non-destructive and quick sample analysis and has been used in many fields including forensic, biological, biomedical and pharmaceutical. In forensic analysis, Raman spectroscopy was reported for rapid detection of the presence of solid explosives on clothing.[73] In the biological and biomedical fields, Raman spectroscopy is used for the detection of unique markers such as DNA, proteins, DNA, and cholesterol,[74] in addition to improving the accuracy of cancer tumour identification.[75] In the pharmaceutical field, Raman spectroscopy has been used in the characterisations of pharmaceuticals in addition to quality control and process monitoring. Those include the identifications of polymorphs,[10] monitoring of processes and process

endpoints such as synthesis, crystallisation, powder blending, granulation, and drying.[12,49,50,76]

3.5.1 Spatially offset Raman spectroscopy

Spatially Offset Raman Spectroscopy (SORS) is a subset of Raman spectroscopy; it is applied by collecting measurements from positions laterally offset from the illumination point, as shown in Figure 3.3. It relies on the higher likelihood of photons in the subsurface to migrate horizontally as opposed to migrating back to the illumination point. Therefore, spectra obtained from various distances from the incidence beam offer the advantage of characterising the heterogeneous subsurface of diffusely scattering media.[77] This opposes backscattering Raman, where the scattered light is collected from the same illumination point and mostly contains features of the surface composition of a sample. SORS spectra are typically of lower intensity compared to conventional backscattered Raman spectra due to the diffusion of light through a sample. Nevertheless, this diffusion is the driver for the increased contribution in SORS signals from the sublayers, enabling the probing of larger sample volumes.[78]

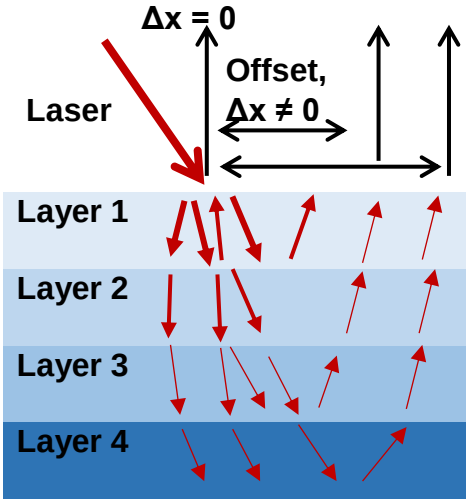

Figure 3.3. Illustration of the concept of spatially offset Raman spectroscopy, where the signal is collected from an offset, Δx ≠ 0, as opposed to conventional Raman spectroscopy measurement, where the backscattering signal is collected, Δx = 0.

SORS has been applied in many fields, such as forensic,[79] biomedical,[80] and pharmaceutical applications.[16] SORS application has been demonstrated for the detection of liquid and solid explosives and precursors within opaque containers.[79,81,82] In the biomedical field, SORS was used for the early diagnosis of breast cancer,[15,83] and for the monitoring of changes in collagen concentration during bone healing,[84] among other applications.[80] In pharmaceutical applications, the technique was investigated for the identification of pharmaceutical tablet and capsule components,[85-87] as well as the quantitative analysis of pharmaceutical formulations.[88] The potential for SORS to achieve spatial and depth-resolved diagnosis from complex tissue structure has led to early efforts to develop SORS probes.[89-91]

3.6 Spectral pre-processing

Pre-processing refers to the treatment of data prior to the extraction of qualitative and quantitative information. It is applied to remove undesired effects in the collected spectral data arising from instrumental noise and signals originating from the collection media. Pre-processing also decreases the variability within spectra due to physical differences in the samples. Therefore, it enhances calibration and classification models and the following data analysis as it may either reduce or sustain the complexity of models. Smoothing, spectral derivatives and scatter correction, which include standard normal variate and multiplicative signal correction, are the most widely used techniques for pre-processing.[92]

Spectral data is associated with variation within sample spectra due to the light scattering and variability in the pathlength of light that affects the sample spectra. This variation is often simplified and regarded as additive and multiplicative effects on the baseline, despite being a result of the collective effect from light-matter interaction. Nonlinearity in instrument response is also a source of variation. Factors that can lead to changing the pathlength include physical properties of the samples, such as particle size distribution, and measurement geometry.[93]

3.6.1 Smoothing and derivation

Spectral data is smoothed to remove peaks that arise as a result of high frequency noise. A simple method to apply smoothing is through the use of a moving average to replace the raw data points, leading to the improvement of the signal-to-noise ratio by removing the random noise that may be captured in the spectra. An odd number or window of points is selected and a measurement over a wavelength is calculated as the average of the measurement point at that wavelength and an equal number of points on either side. Alternatively, a moving window fitted to a curve of a polynomial order may be applied, followed by the derivation of the spectral curve. This method was developed by Savitzky and Golay and is termed the Savitzky-Golay (SG)

method.[94] Another typically used method for spectral derivation is the Norris-William derivation, in which the polynomial order of the curve is set to 0. The advantages of these methods include maintaining the symmetry of peaks and preventing the shift in peak position. 1st-order derivation serves to remove the baseline shifts from spectra, while 2nd-order derivation results in the removal of linear trends (slopes) in the spectra in addition to removing the baseline shifts. Determining the optimal level of smoothing required is critical as exceeding that level will reduce the resolution and intensity of the signal, while sub-optimal smoothing will fail to remove the noise. The number of points to average, polynomial order, and order of derivative must be empirically optimised. Averaging a larger number of points results in a smoother curve but can remove some of the spectral features. Choosing a polynomial of high order leads to a better fit of the spectral curve but would include random noise in the spectrum. Derivation of noisy spectra could emphasise small features arising due to noise.[95]

3.6.2 Baseline correction

Baseline correction is the removal of baseline variation from a spectrum. Some of the methods include de-trending and offset correction. De-trending can be applied through the subtraction of a linear or polynomial fit from the spectrum. De-trending may be applied for the removal of parallel offset and curvilinearity. Offset correction is where the offset value is subtracted from each measurement point on the spectrum individually to remove a parallel baseline shift before further pre-processing.[96]

3.6.3 Normalisation

Normalisation may be done by dividing individual variables by the sum of the absolute value of all variables, the square root of the sum of the squared roots of all variables, or the maximum value among variables for a sample, among

other normalisation methods. Spectral normalisation is applied to individual spectra, where all signal variables or intensities are given the same weight.[97]

3.6.4 Standard normal variate

The standard normal variate (SNV) is a weighted normalisation, where sample spectra are normalised by the standard deviation of all values following subtraction of the mean.[98]

Equation 3.3, can be used to represent the SNV method for calculating the value of corrected spectra:

$$x_{ij(\mathrm{SNV})} = \frac{x_{ij} - \bar{x}_i}{\sqrt{\sum_{j=1}^{p} \frac{x_{ij} - \bar{x}_i{}^2}{J - 1}}}$$

Equation 3.3

Where $x_{ij(\mathrm{SNV})}$ is the transformed spectra x_{ij}, $\bar{x}_i$ is the mean of the spectrum, and J is the number of variables (wavelengths) in the spectrum i.

An advantage of SNV is that each spectrum is treated individually from a dataset. The disadvantage of SNV would be that the multiplicative effects are considered to be identical over the whole range of spectra.[97]

3.6.5 Multiplicative signal correction

Multiplicative signal correction (MSC) is also termed multiplicative scatter correction when applied to process spectral variation due to the light scattering effect. MSC is applied by fitting each spectrum in a dataset to a reference spectrum, resulting in coefficients that are then used to correct the raw spectra.[99]

MSC transformation is expressed by the following equation:

$$x_{\mathrm{ij(MSC)}} = \frac{[x_{ij} - a_i]}{b_i}$$

Equation 3.4

Where x_{ij} and $x_{\mathrm{ij(MSC)}}$ is the original and the MSC transformed spectra, respectively, $\bar{x}_i$ is the reference spectra of i (often taken by the mean spectra of the dataset), and j is the spectral wavelengths. a_i is the specular reflectance effect estimated for the sample (additive offset correction) and b_i is the scatter interference estimated for the sample (multiplicative effect). Least squares regression is used to calculate a_i and b_i for each sample through the following equations:

$$x_{ij} = a_i + b_i \bar{x} + e_{ij}$$

Equation 3.5

$$\bar{x} = \frac{\sum_{i=1}^{N} x_{ij}}{N}$$

Equation 3.6

Equation 3.5 represents the least square regression of the individual spectrum x_{ij} against the average spectrum of the calibration samples $\bar{x}$ over j, where N is the number of data points. Errors/residuals that cannot be modelled are represented by e_{ij}. Following their estimation, a_i and b_i are used for the MSC transformation in Equation 3.4. The value of a_i and b_i is affected by the dataset of spectra and the individual spectra.[100]

3.7 Extracting qualitative information from spectral data

NIR and Raman spectra contain information regarding the chemical and physical qualities of samples. Those qualities are analysed by recognising patterns that relate to certain characteristics within samples and discriminating or classifying them according to those patterns afterwards. Classification techniques are divided into supervised pattern recognition, which is used when there is prior knowledge about the analysed samples, and unsupervised classification, where there is no prior knowledge regarding the samples. In this section, principal component analysis is introduced as an example of unsupervised pattern recognition.[101]

3.7.1 Principal component analysis

While studying different spectra, finding and analysing a number of similar features within the spectra of different samples makes it possible to determine similarities between samples. Thus, samples with similar features are clustered together. Principal component analysis is a method of unsupervised pattern recognition methods used for spectral data analysis.[102]

Principal component analysis (PCA) is the most applied multivariate chemometric technique. PCA addresses the issue of the large volume of data with obscure relations within the data. In order to reduce the volume of data, PCA finds correlations within variables of samples and creates new variables termed principal components (PC). The first principal component contains the largest amount of variation within the data while the remaining principal components contain the largest amount of residual variation. Principal components may be given a physical interpretation in relation to the differences between them. However, PCA is ineffective when there is no correlation between variables.[103]

To employ PCA, the data are arranged in a matrix, where the rows represent samples and columns represent variables as follows:

$$X = CS + E$$

Equation 3.7

Where X is the spectral responses data matrix, C is the different samples, S is the spectra, and E is the error in the spectral responses (X).

PCA transforms the matrix (X) to the following:

$$X = TP + E$$

Equation 3.8

Where T are the scores with the same number of rows as the original matrix, P are the loadings with the same number of columns as the original matrix and the number of columns in the T matrix is equal to the number of rows in P matrix as shown in Figure 3.4. The scores represent the relation between samples while the loadings for each PC represent the relations between individual measurements. The scores and loadings represent the amount of variance characterised by each PC. Errors, E, in PCA are assumed to originate from the measured spectra.[102]

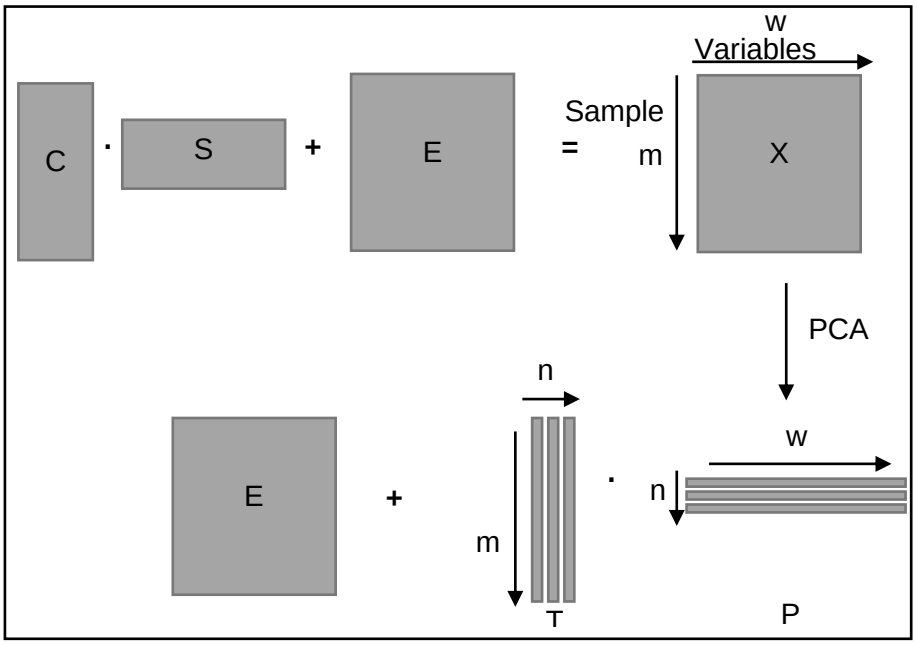

Figure 3.4. PCA transformation of data.

3.8 Extracting quantitative information from spectral data

Quantitative information may be extracted from spectral datasets through the use of chemometric methods. Types of multivariate modelling applied to spectral data for quantitation include multiple linear regression (MLR), principal component regression (PCR), and partial least squares regressions (PLSR).[102,103]

3.8.1 Multiple linear regression

The radiation intensity, expressed as either absorbance or transmittance for example, is related to the concentration of an analyte in a sample through Beer-Lambert's law, where the NIR spectrum is plotted as the intensity versus the wavelength. Beer-Lambert's law is the basis of quantitative analysis of absorption spectroscopy as expressed in Equation 3.1. Univariate regression is based on Beer-Lambert's law. It may be used when all spectral responses are determined by one variable at a certain wavelength.[51]

Beer-Lambert's law is based on the assumption that the incident light is monochromatic from a stable source in a system free of stray light and that no substance in the sample other than the analyte of interest is absorbing the light.[104] However, since non-linearity is encountered due to too high or low concentration of an analyte in samples or the presence of an interfering substance among others, the relationship between absorbance and wavelength will not conform to Beer-lambert's law. Therefore, this non-linearity must be taken into consideration for the calibration process to provide accurate quantitation.[51]

Due to the overlapping of the spectral responses of constituents, and rather than considering the intensities to be dependent variables while concentrations are independent variables, linear regression is used to link the absorbance at every wavelength to the concentrations of analytes within samples. However, this does not account for the interaction between analytes within the samples

or the presence of unknown substances other than the analytes which will affect the absorbance.[103]

When other substances are present in the sample, they are added to the calibration model and a multiple linear regression model is built. The following two-factor, polynomial expression represents the relationship:

$$y = b_0 + b_1 x_1 + b_2 x_2 + \cdots + b_n x_n + e$$

Equation 3.9

Where y is the prediction variables matrix as shown in Figure 3.5, b_0 is the offset value, $b_{1..n}$ are the regression coefficients, x is the spectral responses matrix, and e is the error matrix. [104]

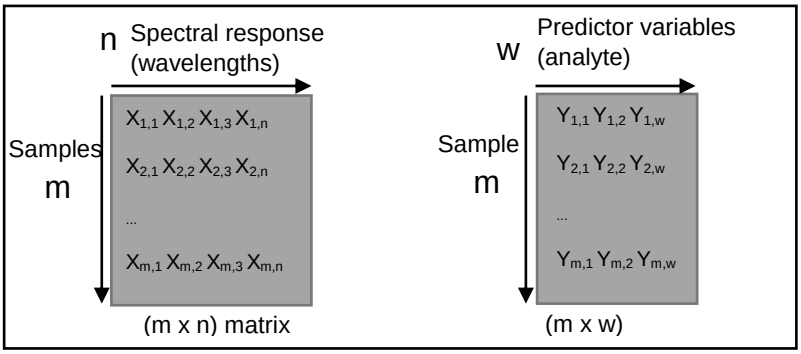

Figure 3.5. Spectral responses and predictor variables matrices dimensions.

Those express the relationship between a number of wavelengths and a characteristic of a sample. To carry out calibration using MLR, the number of samples in the calibration set must be larger than the number of predictors. Every wavelength is correlated to the characteristic of interest where each response spectrum is the sum of analyte spectra multiplied by their concentration. To employ MLR, prior knowledge of the significant constituents within a sample must be available.[102]

3.8.2 Principal component regression

Due to the presence of a high correlation between variables in optical spectra, the prediction obtained through MLR becomes unreliable. Therefore, PCR is employed for spectral analysis where the variation of a large number of wavelengths/wavenumbers can be described with principal components.[103] Also, as an unsupervised modelling method, PCA does not require prior knowledge of the analytes within the sample. Therefore, it must be noted that the principal components obtained may not be correlated to the characteristic of interest. While PCA does not require response variables, the principal components are used as predictors in PCR. [102]

In PCR, PCA is followed by MLR on the predictive variables, which are the scores.[102] PCA is expressed by Equation 3.8. The prediction equation is expressed by:

$$Y = TB + F$$

Equation 3.10

Where Y is the concentration of the analyte matrix (predictors), T is the scores matrix, B is the regression coefficient vector, and F is the error assumed to be in the concentrations matrix, Y.

3.8.3 Partial least square regression

In partial least squares regression (PLSR) analysis, a series of sample response spectra along with concentrations (predictors) can be used to construct a model. The characteristic features extracted are employed using PLSR for the verification of the relationship with the variables within the samples. PLSR models are robust, provided that the unknown samples have features that are related to the data used for modelling. PLSR analysis considers errors in both spectra and concentration values of analytes.[102]

In PLSR, PCA is applied to X as in Equation 3.8 and to Y as follows:

$$Y = UQ + F$$

Equation 3.11

Where Y is the concentrations of the analytes matrix, U and Q are the scores and loadings scalar, respectively, for the concentration, and F is the error assumed to originate from the prepared concentrations. In order to reduce the volume of data, PLSR finds correlations within variables of samples and creates new variables termed latent variables (LVs). The first latent variable contains the largest amount of variation within the data while the remaining latent variables contain the largest amount of residual variation.[102] The higher number of latent variables may be associated with noise and are excluded from models. The selection of the optimal number of latent variables may be selected based on cross-validation, where the prediction residual error sum of squares (PRESS) is calculated and the number of latent variables that gives the lowest total PRESS is selected. Alternatively, the highest number of latent variables may be selected if the ratio of consecutives PRESS is higher than one, which is referred to as Wold's R criterion. Alternatively, information criteria, which are formula calculated to measure a model fit where a lower information criteria is favourable to a higher information criteria. Examples of information criteria include the Akaike information criterion (AIC) and the Bayesian information criterion (BIC). [105]

3.8.4 Model validation

Validation is a requirement in the development of analytical procedures including multivariate analysis as mentioned in the ICH Q14 guideline. This guideline includes a general outline to developing robust analytical procedures, including reference samples and analytical procedure, the selection of samples that include variability encountered in the measured property, and the number of samples used for creating models, among others.[106] Regression models must be validated to determine the error in their predictive ability. Validating a model through calculating the error in the estimations is essential for the selection of the model with a suitable number

of principal components or latent variables. The root mean square error (RMSE) is a measure of the error between the reference value and an estimated value and has the same unit as those values.[102]

A model can be validated with the calibration set used to construct the model through the root mean square error of calibration (RMSEC). However, RMSEC does not reflect the ability of the model to predict new data. Alternatively, cross-validation is used to assess the ability of a model to predict data by leaving out one or a number of samples for building the calibration model, applying the model to predict the samples left out, and repeating the same process until all samples are left out once. Equation 3.12 is used to calculate the root mean square error of cross-validation (RMSECV).

$$RMSECV = \sqrt{\frac{\sum_{i=1}^{I}\left(y_i - y'_i\right)^2}{I-1}}$$

Equation 3.12

Where y_i is the reference value, y'_i is the predicted value, and I is the number of samples in the dataset. When one sample is left out of the calibration set, it is called leave-one-out cross-validation (LOOCV). This method is suitable for small datasets as leaving one sample out from a large dataset would lead to a non-representative and over-optimistic RMSECV. When a larger dataset is collected, it is possible to apply segmented or n-fold cross-validation, where the cross-validation is repeated n-fold by excluding a group of samples from the dataset, which allows for the robust estimation of the RMSECV. Nevertheless, a model must also be tested for its ability to predict new data points.[107]

To overcome the disadvantage of cross-validation, an independent dataset is usually preferred to validate quantitation models. Determining the ideal size of the testing set is crucial. Nonetheless, the testing set must always be representative of the actual data. The test set is then estimated based on the model built on the calibration set, and the root square mean error of prediction (RMSEP) of the test set value is used to summarise the ability of the model built with the calibration set to predict the independent test set.[102]

In addition to the RMSEC, RMSECV, and RMSEP, the coefficient of determination (R^2) may be used to describe the goodness-of-fit of the linear model. It has a value between 0-1, where 0 indicates no correlation, and 1 could either indicate perfect correlation or overfitting. It is calculated by the following equation:

$$R^2 = 1 - \frac{SSR}{SST}$$

Equation 3.13

Where SSR is the sum of squares of residuals and SST is the total sum of squares. A lower value of SSR leads to R^2 values closer to 1 and better correlation between measured reference values and predictions.

4. Experimental Procedure for the Depth of Solvent Detection and Monitoring of Drying

This chapter is arranged into six sections. The first section describes the materials used in the drying and depth experiments, while the second section describes the SAR-DRM, SORS, and combined setups with a brief description of the signal processing applied prior to the analysis. The third section describes the procedure for conducting the depth and drying experiments including the signal collection, followed by a description of the collected datasets in fourth third section. The fifth section details the multivariate regression analysis conducted using the collected datasets.

4.1 Materials

Two commonly used grades of paracetamol, granular and powder (Mallinckrodt Inc., Raleigh, N.C.), were employed in the presented studies. Granular paracetamol had a mean particle size (D50) of 265 µm, while powder paracetamol had a D50 of 43 µm, measured with laser diffraction (Mastersizer 3000 with a dry dispersion unit, Malvern Instruments Ltd, UK). Three wash solvents, in which paracetamol displays minimal solubility, were used with each of the paracetamol grades; those were Anisole (99%, Alfa Aesar, Lancashire, UK), n-heptane (99%, Alfa Aesar, Lancashire, UK), and methyl tertiary-butyl ether (MTBE) (99%, Alfa Aesar, Lancashire, UK). Table 4.1 shows the solubility of paracetamol in those solvents in addition to their boiling points, which are some of the characteristics that were taken into consideration for the selection of the solvents and the following drying process parameters. Anisole typically requires a longer duration of drying at higher temperatures to be removed, while n-heptane and MTBE are volatile solvents that require a shorter duration for drying.[19]

Table 4.1. Solvents used in this study, the solubility of paracetamol in those solvents and their boiling points.[19]

Solvent	Paracetamol solubility at 25°C (g/g)	Boiling point/°C
Anisole	0.0005	154
n-heptane	0.0001	98.4
MTBE	0.0028	55.2

NIR and Raman spectroscopy are complementary branches of vibrational spectroscopy, where NIR provides wide and overlapping overtones and combination bands of polar bonds that display symmetric stretches, Figure 4.1 (a), while Raman spectroscopy provides sharp peaks of polarisable bonds that display asymmetric stretches, Figure 4.1 (b).

The NIR spectra of paracetamol and the solvents in Figure 4.1 (a) show bands at 1100-1200 nm corresponding to the overtones of CH, CH_2 and CH_3, while the bands around 1300-1500 are of overtones of the CO, CONHR, and aromatic OH bonds, in addition to the aromatic CH starting at 1600 nm. Raman

spectra in Figure 4.1 (b) show moderate CH_2 and CH_3 bends and stretches for n-heptane over the wavenumber range in the figure. For paracetamol, MTBE, and anisole, the wavenumber range 800-1300 cm^{-1} includes peaks corresponding to ArOH and COC bonds, 1400-1500 cm^{-1} contains peaks corresponding to the ArOC bond, while peaks over 1500-1700 cm^{-1} result from the aromatic rings.[51]

The selection of the technique for monitoring each of the systems was based on the presence of NIR or Raman peaks of strong intensity taking into consideration the extent of solvent peak overlap with paracetamol as shown in Figure 4.1. From the three paracetamol grade/solvent systems, the drying of n-heptane was monitored using SAR-DRM, anisole was monitored using SORS, while MTBE was monitored using both SAR-DRM and SORS.

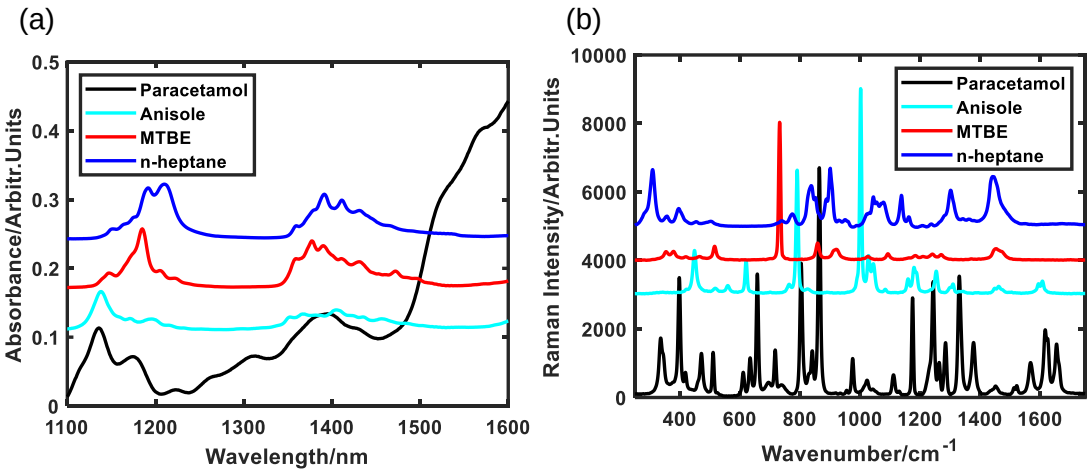

Figure 4.1. (a) NIR and (b) Raman reference spectra of paracetamol, n-heptane, MTBE, and anisole. Spectra are offset on the y-axis.

4.2 SAR-DRM, SORS, and combined setups

This section is further divided into three parts to describe the setup for signal collection for the SAR-DRM, SORS, and combined probes.

4.2.1 SAR-DRM

The setup of the SAR-DRM system shown in Figure 4.2 (a) is composed of a custom-designed SAR-DRM fibre optic probe (FiberTech Optica, Canada),[14] shown in Figure 4.2 (b), tungsten halogen light source of 50W encased in a lighthouse, and a fibre optic multiplexer (FOM-UVIR200- 2x8, Avantes, NL) linked to a UV-Vis spectrometer (USB4000, Ocean Insight, Germany) and a NIR spectrometer (NIRQuest 1.7-512, Ocean Insight, Germany). The spectrometers and multiplexer are controlled by the laptop.

4.2.1.1 Optical setup

At the connection end of the SAR-DRM probe in Figure 4.2 (a), the fibre optic cable is terminated with three ferrules that enclose the illumination fibres. To illuminate a sample at each of the three angles, the respective ferrule can be inserted into a port in the lighthouse, which is also equipped with a shutter to enable blocking the light from exiting from the lighthouse to the ferrule. The incident light from the lighthouse travels to the SAR-DRM probe, which is in contact with the sample. The collection SAR-DRM probe end in contact with samples includes five illumination fibres, shown in Figure 4.2 (c), delivering the incident light from the lighthouse. Among the five fibres, one fibre delivers the incident light at 0° angle, two fibres at 30°, and two fibres at 45° with reference to the axis of the probe. In addition to the five illumination fibres, the probe contains 16 collection fibres at fixed distances from the illumination fibres. The distances of the collection fibres are at 0.3 mm, 0.6 mm, 0.9 mm, and 1.2 mm from each of the aligned five illumination fibres as shown in Figure 4.2 (d). This enables the collection of duplicate measurements for the 30° and 45° illumination angles and four replicates for the 0° angle.

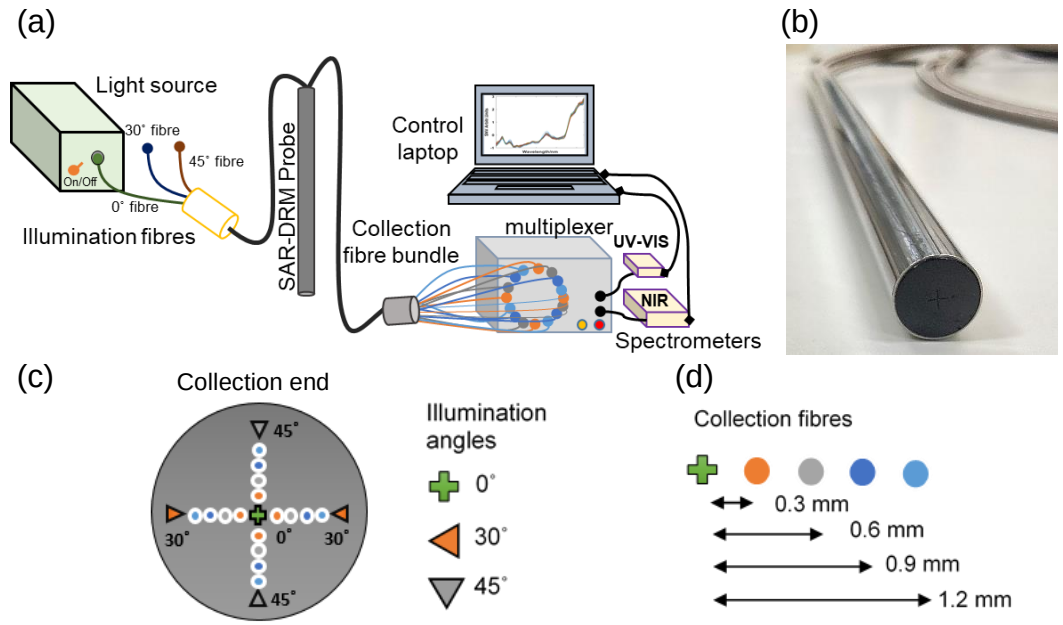

Figure 4.2. (a) SAR-DRM setup including a light source, fibre optic multiplexer, NIR and UV-VIS spectrometers, in addition to the control laptop and the SAR-DRM probe with (b) an illustration of the probe collection end and (c) the collection fibres.

The light reflected from the sample travels through the collecting fibres to the multiplexer, which delivers the NIR and UV signal to each of the spectrometers. Using the NIR spectrometer, spectra over the wavelength range 900-1700 nm are collected on 512 pixels, and through the UV-Vis spectrometer, spectra in the range 350-1000 nm are collected on 3648 pixels. In the studies presented here, the analysis is focused on the NIR spectra obtained. Then, the signals are transferred to be recorded on the control laptop, where a previously developed interface in MATLAB is used to control the settings.

This system enables the collection of 48 spectra that correspond to the combination of 16 collection fibres for each of the 3 illumination angles. For one sample measurement, two spectra can be collected for the same configuration using the 30° and 45° illumination angles, while 4 spectra can be collected using the 00° illumination angle. Since over half of those spectra are repetitions, spectra using two perpendicular branches were collected in the

presented studies adding up to 12 spectra, which correspond to four distances for each of the three angular configurations.

4.2.1.2 SAR-DRM signal collection

For collecting the SAR-DRM signal in both the depth and drying experiments, the 0° incidence angle ferrule was inserted into the light source, and the signal was then collected for each of the four spatially resolved distances consecutively. Next, the 0° illumination light ferrule was replaced by that of the 30° then the 45° incidence angle ferrules to collect the spatially and angularly resolved spectra. The acquisition parameters were an integration time of 1 second with the averaging of 3 spectra. Collection and recording of SAR-DRM spectra is carried out using in-house scripts developed in MATLAB software (Mathworks, USA) with earlier studies.[14,58]

4.2.1.3 SAR-DRM signal processing

To produce a calibrated and processed SAR-DRM signal collected through the SAR-DRM probe or the combined probe, background SAR-DRM spectra were collected using an integrating sphere in addition to dark SAR-DRM signals. The integrating sphere is hollow with diffusely reflecting interior coating of Spectralon®. A beam of light is directed in one direction in the integrating sphere and then reflected around the diffusely reflective spherical surface in a uniform manner representing the absolute reflectance.[108] This measurement is used to normalise the SAR-DRM spectra obtained from samples. To acquire the integrating sphere spectra, the probe tip was fixed at a port of a 3-inch integrating sphere (7N6322A, Newport, US) to an extent where the interior surface is continuous with the probe tip to maintain the spherical dimension within the sphere. SAR-DRM spectra were collected from the integrating sphere with the light source turned on. Spectra corresponding to the dark signal were also collected by collecting a signal from the integrating sphere with the light source turned off. Following the acquisition of the two signals

from the integrating sphere, the sample signal is also collected with the light source turned on for all samples and off for the first sample in an experiment.

The processing of SAR-DRM spectra included three major steps, dark signal subtraction, smoothing, and normalisation. Those three steps aim to remove the noise contribution of the instrument and background from the signal. Details on those steps and how to optimise them were previously investigated.[109]

The steps for SAR-DRM signal processing are performed as follows:

a. Dark signal subtraction: in addition to a signal collected with the light on, a signal with the light off is collected by closing the shutter. The light off signal is then subtracted from the light-on signal. This is done to remove background noise for both the signal collected from the integrating sphere, where the spectra with light on and off are shown in Figure 4.3 (a), and the sample signal in Figure 4.3 (b).
b. Smoothing is performed for both integrating sphere and sample spectra. In the examples shown in Figure 4.3 (c) of the integrating sphere spectra, a built-in function in MATLAB, rloess is used to smooth the spectra; this function employs locally weighted least squares regression and assigns lower weights to outliers. This method was employed due to the higher level of noise in the integrating sphere spectra, which are of lower magnitude than the sample spectra. A fast Fourier transform filter is applied to smooth the paracetamol sample spectra as shown in Figure 4.3 (d).
c. Normalisation is done by dividing the sample spectra by the integrating sphere spectra to obtain the signal shown in Figure 4.3 (e). This step removes the curve in the baseline.
d. To express the sample signal as absorbance, a log transformation of the inverted reflectance[110] is calculated to obtain the signal shown in Figure 4.3 (f).

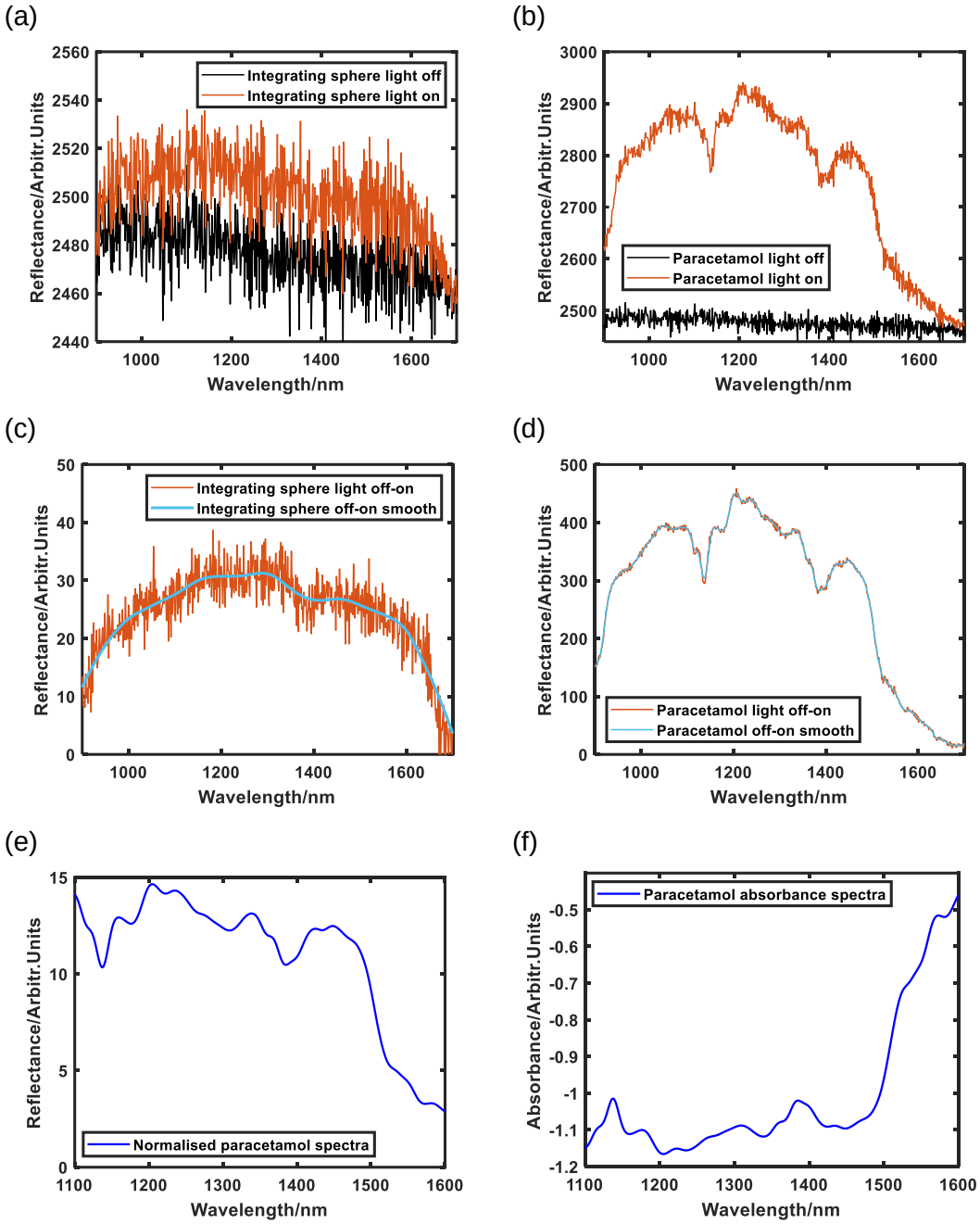

Figure 4.3. SAR-DRM signal processing steps. Dark signal subtraction from (a) integrating sphere and (b) paracetamol sample spectra. Smoothing of (c) integrating sphere and (d) sample spectra. Normalisation of sample spectra in (e) and log transformation to absorbance in (f). Example spectra are collected using 0°/1.2 mm configuration for 1 second with an average of three spectra.

4.2.2 SORS setup

The setup of the SORS collection system shown in Figure 4.4 (a) is composed of a custom-designed SORS fibre optic probe (FiberTech Optica, Canada), a 785 nm laser (I0785MM0350MF, Innovative Photonic Solutions, USA) set to a power of 100 mW measured using a handheld power meter (PM100D/SC130C, Thorlabs GmbH, Germany), and a Raman spectrometer (RXN1, Kaiser Optical Systems Inc., USA) connected to a control laptop.

4.2.2.1 Optical setup

The probe contains one illumination fibre delivering the laser at a 45° illumination angle with reference to the axis of the probe. As illustrated in Figure 4.4 (b) of the collection end, a total of 19 collection fibres to collect the spectra from 0, 1, 2, 3, 4, and 5 mm offset distances from the incident light. The signals are collected using one fibre for the 0 mm offset, one fibre for the 1 mm offset, two fibres for the 2 mm offset, three fibres for the 3 mm offset, five fibres for the 4 mm offset, and seven fibres for the 5 mm offset distance. The design includes more fibres for the collection of signals from the larger offsets functions to increase the signal throughput for each offset configuration. On the opposite end, the collection fibre bundle is connected to the spectrometer via the ferrule illustrated in Figure 4.4 (c), where spacer fibres are included in the array of the collection fibres to separate the collection fibres for each of the offset distance groups to attenuate any signal crosstalk.

The Raman spectrometer consists of a two-dimensional 1024-pixel x 256-pixel detector, where the full spectral range is between 780-1080 nm. The RXN1 spectrometer design includes a grating that splits the signal into two smaller spectral ranges of 780-920 and 920-1080 nm, corresponding to 0-1870 cm^{-1} and 1870-3480 cm^{-1} wavenumbers respectively. The signal is collected through a control software (Andor Solis, Oxford Instruments, UK) from the detector is a two-dimensional (2D) spectral-spatial image with the Raman signals from all 19 collection fibres acquired in a single scan. In the presented

studies, the focus is on the lower wavenumber region as it covers most of the Raman peaks of the materials used as shown in Figure 4.1 (b).

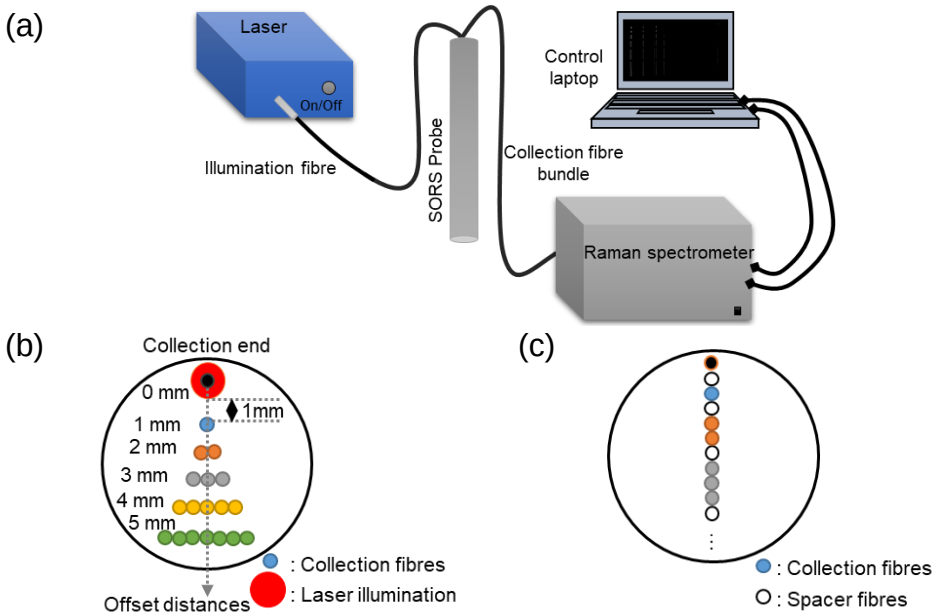

Figure 4.4. (a) SORS setup includes the SORS probe, a laser, a Raman spectrometer, and the control laptop, in addition to illustrations of the (b) collection end of the SORS probe and (c) connection ferrule end.

4.2.2.2 SORS signal collection

For the depth of solvent signal detection, the probe was put in contact with the paracetamol layer and a single scan was collected using an exposure time of 20 seconds with 100 mW laser power.

For the drying experiments, samples extracted from the dryer were introduced to the SORS probe in a glass beaker and the measurement was collected at-line. This was done rather than collecting in-line measurements, by inserting the probe into the dryer, due to the slightly larger diameter of the probe, 31 mm, compared to the diameter of the dryer port, 30 mm.

4.2.2.3 SORS signal processing

SORS signals of all offset distances are obtained as a two-dimensional spectral-spatial image as opposed to sequential acquisition for each of the

offsets.[111] For the optical alignment of the SORS and combined probes and wavelength calibration of the Raman spectrometer, an argon spectral calibration lamp (3060AR, 10 mA, Newport, USA) was used. The SORS probe was inserted through the top port in the integrating sphere so as to form a level surface with the interior of the sphere. The argon lamp was inserted into the integrating sphere from a side port. This was done in order to allow the argon light to equally reach the SORS probe's collection fibres as it is diffusely reflected inside the integrating sphere.

In addition to the sample spectra, a dark SORS signal is collected and is subtracted from the sample spectra to remove background influence. For the sample spectra collected using the SORS probe, spectra corresponding to the 19 collection fibres are acquired in the spectral image and are summed up to produce one spectrum per each of the six offsets.

Following the dark signal subtraction from the sample signal, a spectral image showing the SORS signal as dashed lines, as shown in Figure 4.5, where the dashed lines correspond to Raman peaks. Then, a set of seven linear equations is defined to outline the areas on the spectral image from which the signal per each offset is extracted. In these linear equations, the slope is identical and is multiplied by the number of pixels of the x-axis to draw each of the magenta lines shown in Figure 4.5, where the constant is increased to indicate the area that includes the set of fibres collecting the signal from each of the offsets. For example, the line corresponding to Equation 1 indicates the beginning of the area where the signal from the backscattering fibre is collected. The line corresponding to Equation 2 indicates the beginning of the area where the signal from the 1 mm offset fibre is collected. The area outlined by Equation 1 and Equation 2 is summed to give the signal from the backscattering fibre. This is similarly done for the remaining five offsets.

Spectra collected using the SORS probe were extracted and processed using a script developed in MATLAB. This script follows the same signal processing step for signals obtained from the Raman RXN1 spectrometer including the linear interpolation of the original 1024 signal points to 6518 points. Following

the signal extraction, a 2nd-order polynomial Savitsky-Golay smoothing filter is applied to smooth any remaining noise in the signal.

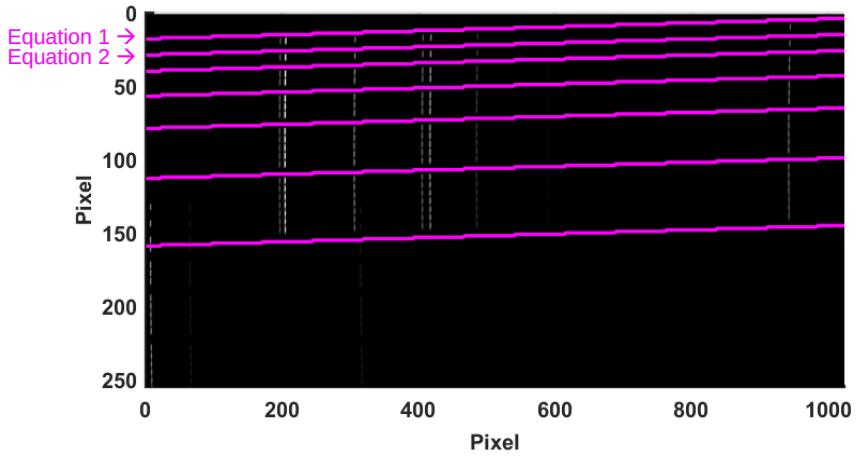

Figure 4.5. SORS spectral image is divided into areas by the magenta lines where the signal intensity is summed up to give the spectra per offset. Grey dashed lines correspond to the SORS signals.

4.2.3 Combined probe setup

The combined setup shown in Figure 4.6 (a) enables the collection of spatially offset diffuse reflectance measurements and spatially offset Raman spectroscopy measurements from a single sampling point. This setup includes the same components used in the SAR-DRM and SORS setups. However, the probe used in this setup is a custom-designed combined probe (FiberTech Optica, Canada) shown in Figure 4.6 (b).

4.2.3.1 Optical setup

To collect SR-DRM spectra, the combined probe signal collection end shown in Figure 4.6 (b) includes a fibre illuminating the sample at 0°, in addition to four fibres for collecting spatially resolved signals at 0.3, 0.6, 0.9, and 1.2 mm, similar to the SAR-DRM probe. To also collect SORS spectra, the probe includes a fibre delivering the illumination to the sample at a 45° angle, in addition to 16 spatially offset signal collection fibres. The fibres collect the

signal at 0, 1.5, 2.5, and 3.5 mm from the illumination point as illustrated in Figure 4.6 (c), where two fibres collect the signal from 0 mm offset, three fibres collect the signal from the 1.5 mm offset, five fibres collect the signal from the 2.5 mm offset, and six fibres collect the signal from the 3.5 mm offset distance. SR-DRM and SORS measurements are collected using the same laptops and software used with the individual probes.

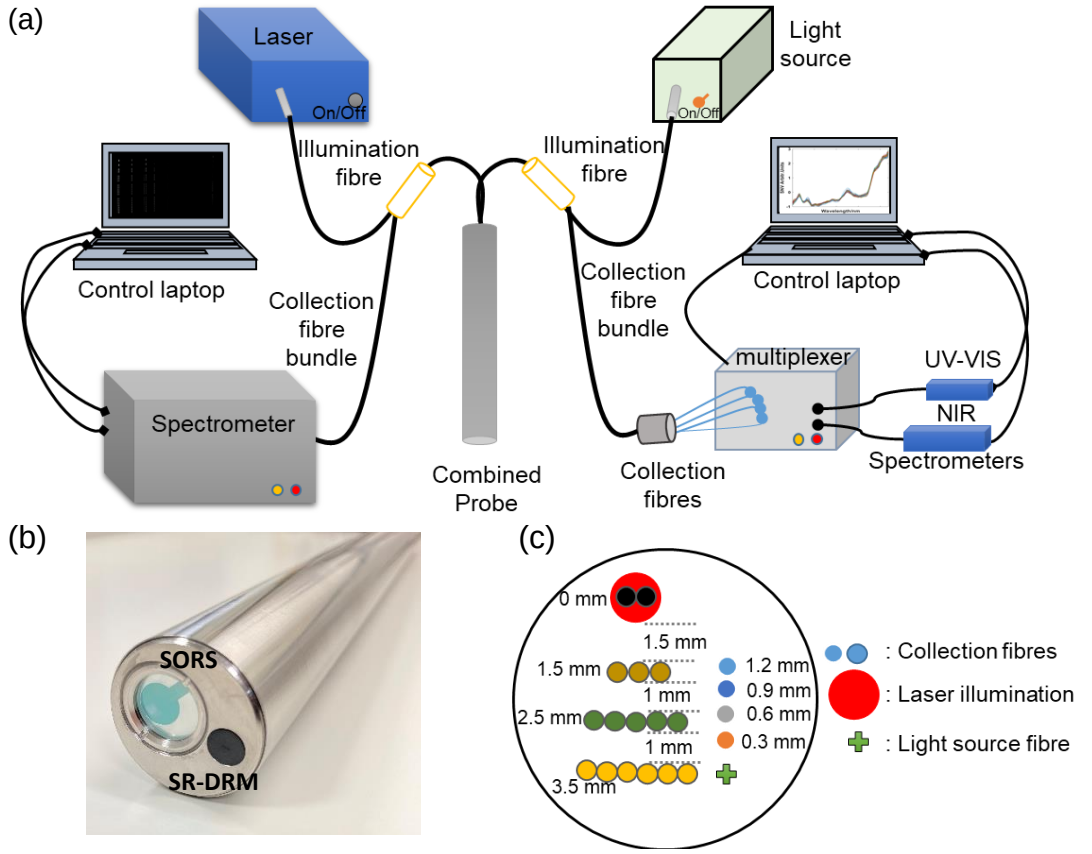

Figure 4.6. Illustration of (a) combined SR-DRM and SORS setup with the combined probe. (b) Combined probe collection end showing the SORS and SR-DRM collection windows. (c) illustration of the combined probe collection end.

4.2.3.2 Signal collection using the combined probe

The combined probe diameter is the same as that of the SORS probe, preventing the collection of in-line measurements. Therefore, at-line measurements were collected using the combined probe in a similar manner to those collected using the SORS probe. The acquisition parameters used

with the combined probe were the same as those used with the individual SAR-DRM and SORS probes. Those were 1-second integration time with the averaging of three spectra for SR-DRM and 20-second exposure time for one scan using SORS.

4.2.3.3 Combined probe signal processing

SR-DRM signals collected using the combined probe are processed in a similar manner to the signal collected using the SAR-DRM probe. For SORS signals collected using the combined probe, the dark signal is subtracted then spectra corresponding to the 16 collection fibres are summed up to produce one spectrum per each of the four offsets. SORS signals collected using the combined probe were not interpolated so as to maintain the original signal dimensions for the following PLSR analysis.

4.3 Experimental procedure

4.3.1 Depth of solvent signal detection

To assess the depth through which the signal of a solvent can be detected, the probes were tested using a setup comprising a layer of dry paracetamol of variable thickness placed over a solvent-filled cuvette, as illustrated in Figure 4.7. The solvent-filled 2 or 10-mm pathlength cuvette (Quartz SUPRASIL® 300, Hellma, Germany) was placed on a diffuse reflectance target (99% reflective Zenith Polymer®, SphereOptics, Germany). A barrier layer of granular paracetamol with variable thicknesses was placed on the cuvette using a stack of 10 custom-made spacer sheets. The spacer sheets used with the SORS probes were of 1.2 mm thickness with anisole as the solvent in a 10 mm cuvette, while those used with the SAR-DRM probe were of 1.6 mm thickness with n-heptane in a 2 mm cuvette. The smaller cuvette thickness was used with the SAR-DRM probe due to the weaker light source intensity. The spacer sheets have a hollow centre of a similar diameter to the probe's diameter. This hollow centre was filled with granular paracetamol. An initial

thickness of 12 mm and 16 mm, corresponding to 10 stacked spacer sheets, of paracetamol for each of the probes was prepared to achieve uniform packing within different barrier thicknesses. Light falls on the surface of the paracetamol in contact with the probe and scatters throughout the sublayers, passing through the quartz cuvette walls to the solvent contained within the cuvette, where the diffuse reflectance target aid in reflecting the signal back to the probe. Then, the thickness was reduced by removing the top spacer sheet with the excess paracetamol to collect the next measurement. This process was repeated till the bottom-most spacer sheet was reached. SAR-DRM or SORS spectra, in the respective experiments, were collected at each thickness. This provides 10 special measurements corresponding to each of the barrier thicknesses.

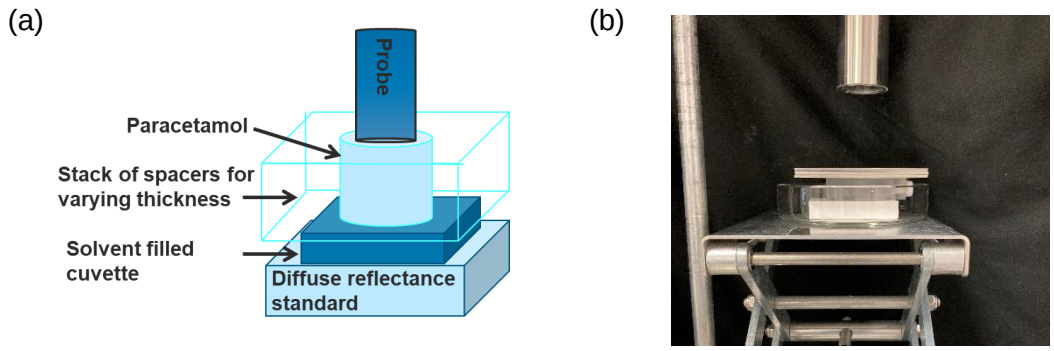

Figure 4.7. (a) Illustration and (b) actual depth of solvent signal detection using diffuse reflectance target underneath a cuvette filled with a solvent and separated by multiple layers of equal thickness of granular paracetamol.

4.3.2 Drying setup and experiments

4.3.2.1 Setup of the dryer

The drying of the paracetamol wet cake was carried out using a 2-litre agitated Nutsche Glass Filter-Dryer (GFD® Lab 050 Series, Powder Systems Limited, UK). The jacket temperature of the dryer was controlled through a heater/chiller (Proline 845, Lauda, Germany). The powder surface temperature was monitored with an infrared sensor (Pyrocouple, PCCFMT-4, Calex Electronics Limited, UK). Additionally, the cake temperature was monitored

using a thermocouple sensor (YC-727, Yu Ching Technology Co. Ltd, Taiwan) placed in the powder bed. Vacuum filtration was performed by means of a diaphragm vacuum pump (MD 12 VARIO, VACUUBRAND GMBH, Germany), and the vacuum pressure within the vessel was monitored using a pressure sensor (PN2694, IFM, Germany). This full setup is shown in Figure 4.8 (a), while the setup with the SAR-DRM probe inserted for in-line measurements is shown in Figure 4.8 (b).

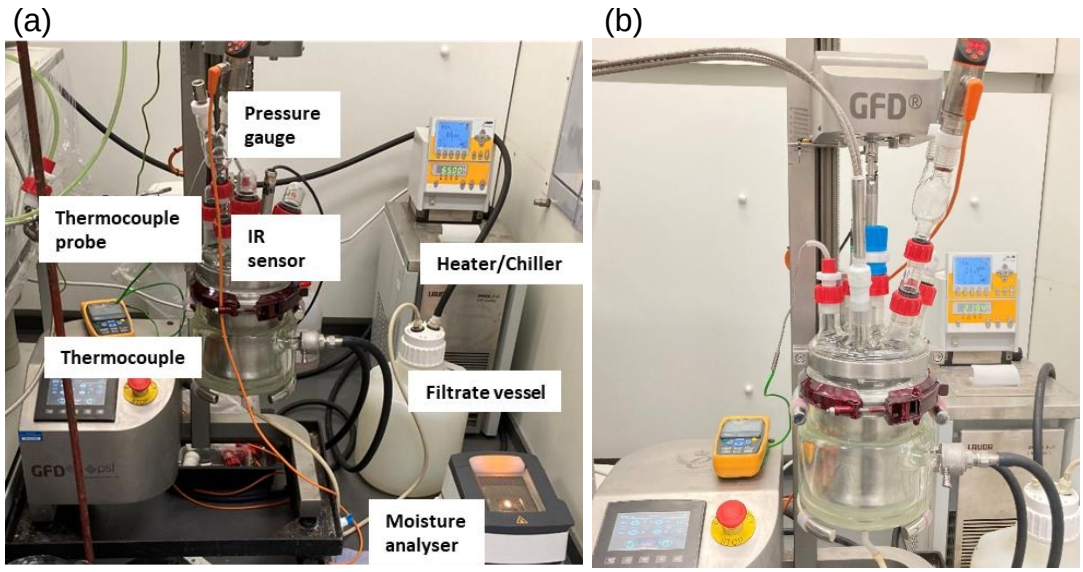

Figure 4.8. (a) Drying setup showing the dryer with accessories, heater/chiller, and moisture analyser. (b) Dryer with SAR-DRM probe inserted. The SAR-DRM probe is typically fixed in place using a retort stand and clamps, those were removed for this photo as they covered the probe.

4.3.2.2 Experimental protocol and conditions of drying

To commence the drying experiments, the heater/chiller was set to the temperatures provided in Table 4.2. This parameter was set with reference to the boiling point of each of the solvents, previously stated in Table 4.1. Another point taken into consideration for the drying temperature selection was controlling the length of the process in order to enable the collection of a suitable number of spectral measurements representing the decrease in solvent content as the drying progresses; this is reflected, for example, in the lower temperature set for MTBE (room temperature) as opposed to that of

anisole. For the n-heptane experiments, a higher temperature was used for the powder paracetamol compared to the granular paracetamol. This was done in order to improve the drying as the vacuum pump was not performing efficiently in these experiments.

Table 4.2. The set temperature for each of the drying systems.

Solvent	**Anisole**	**n-heptane**	**MTBE**
Paracetamol grade	**Set temperature/°C**		
Granular	65	25	25
Powder	65	40	25

After the set jacket temperature was reached, paracetamol was loaded into the dryer followed by the solvent, and the mixtures were agitated at a speed of 5 revolutions per minute (rpm) for the granular grade and 15 rpm for the powder grade, for 10 minutes to ensure that the paracetamol is wetted by the solvent. The agitation parameters were selected to minimise the possible effect on particle size due to breakage or agglomeration. Then, the agitation was paused for de-liquoring with the aid of the vacuum pump. The de-liquoring process was stopped as the solvent reached the surface level of the solid as a fully saturated filter cake, which was the starting point of drying. Clockwise agitation and vacuum were maintained during the drying process and only paused for collecting in-line measurements using the SAR-DRM probe inserted into one of the ports, and for extracting samples from the mixture for SORS measurement collection and reference solvent content measurement. The SAR-DRM probe was inserted into the dryer through one of the lid ports, fitted through with a shaft guide and fixed in place with a retort stand and a clamp. The extracted samples were placed in a beaker for at-line SORS or combined measurements collection. Using the bespoke SORS and combined probes, at-line measurements were collected as opposed to in-line measurements due to constraints of the port size of this laboratory-scale dryer.

4.3.2.2.1 Solvent content reference and particle size measurements

The samples extracted during drying were used for reference solvent content determination using a moisture analysing balance (MA160, Sartorius AG, Germany), a mass Loss on drying method, which provides a reading of the solvent content as a percentage of the mass of the solvent removed from the total mass of the wet sample (%w/w). Then, the particle size distribution of the samples was measured using laser diffraction (Mastersizer 3000 with a dry dispersion unit, Malvern Instruments Ltd, UK) to check if any change occurred to the particle size distribution during the process.

4.3.2.2.2 Collection of pure spectra

Pure NIR spectra of the solvents and paracetamol were collected as a reference through transmittance measurements (Cary 5000 UV-Vis-NIR, Agilent, UK), while the Raman pure spectra were collected using the SORS setup.

4.4 Description of SAR-DRM and SORS datasets from drying

SAR-DRM and SORS spectral datasets corresponding to the systems formed from the combination of the paracetamol grades and solvents are detailed below.

4.4.1 Individual SAR-DRM and SORS probes datasets

The number of samples collected during the drying runs monitored using the SAR-DRM probe from the four systems are summarised in Table 4.3. The number of SAR-DRM spectra collected for each of the samples is 12, corresponding to the four offset distances, 0.3-1.2 mm, from each of the three angular light sources, 0°, 30°, and 45°. For example, the number of reference samples collected from the granular/n-heptane systems is 38, where the SAR-

DRM spectra collected are a total of 456, corresponding to 12 spectra times 38 samples. A SAR-DRM spectrum from one configuration for a sample would be collected as 512 intensity readings over the wavelength range covered by the spectrometer, 900-1700 nm, prior to any spectral truncation of a specific wavelength range.

The datasets collected using the SORS probe to monitor drying are also shown in Table 4.3. For each of the samples, spectra corresponding to the six offsets, 0-5 mm, are collected. As an example, for each of the 78 samples collected from the powder/anisole system, 6 spectra are collected resulting in a total of 612 spectra. A SORS spectrum from one configuration for a sample would be collected as 1024 readings over the wavelength range covered by the spectrometer.

Table 4.3. SAR-DRM and SORS datasets.

		SAR-DRM		
Paracetamol grade	**Granular**		**Powder**	
Solvent	n-heptane	MTBE	n-heptane	MTBE
Number of runs	4	5	4	9
Number of samples	38	51	42	86
Total spectra (12 configurations)	456	612	504	1032
		SORS		
Paracetamol grade	**Granular**		**Powder**	
Solvent	Anisole	MTBE	Anisole	MTBE
Number of runs	7	10	7	9
Number of samples	69	102	78	86
Total spectra (6 configurations)	414	468	612	516

4.4.2 Combined probe dataset

The combined probe collects four SR-DRM configurations corresponding to the offset distances 0.3-1.2 mm, and four SORS configurations, corresponding to 0-3.5 mm. The number of samples collected from the paracetamol/MTBE systems monitored using the combined probe is shown in Table 4.4. Here, the SR-RDM spectra are collected and extracted the same as the original resulting

in 512 intensity readings per spectrum. SORS spectra were collected as 1024 intensity readings per spectrum and extracted as such rather than interpolating them as was done with spectra collected using the SORS probe. This was done considering the use of the combined spectra for the PLSR analysis..

Table 4.4. Combined SR-DRM/SORS datasets collected with the combined probe.

Paracetamol grade	**Granular**	**Powder**
Number of runs	7	6
Number of samples	83	80

4.4.3 Multi-block datasets

A data block is a block of spectra expressed as a matrix and multi-blocks are those data combined to form a larger final block.[112] In addition to PLSR analysis conducted using the spectra obtained from each of the configurations for both of the techniques, spectra from different configurations can be combined to form one final block for PLSR analysis. Those spectra may be from the same technique or multiple complementary techniques, such as NIR and Raman spectroscopy. This aims to provide the PLSR model with information from spectra from multiple configurations and spectroscopic techniques. The two methods tested for the multi-block data analysis were co-addition and augmentation.[14] In co-addition the spectra collected from multiple configurations are summed up to form a block of a size equal to the original spectra. In augmentation, spectra from different configurations for the same sample are concatenated to form a larger block of data in which the number of measurement intensity variables in the final block is the sum of the variables of the individual blocks. A demonstration of spectra combined using both techniques is shown in Figure 4.9.

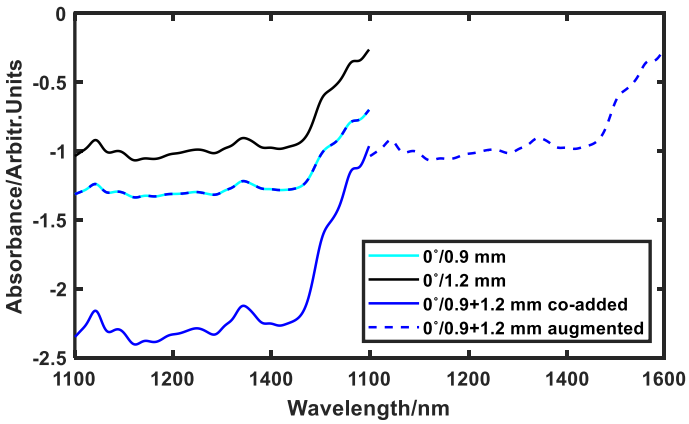

Figure 4.9. Example of the co-adding and augmentation of SAR-DRM spectra of paracetamol collected using 0°/0.9 mm and 0°/1.2 mm configurations.

For combining NIR and Raman spectra collected using the combined probe, augmentation was the method employed in order to preserve and utilise both spectra. However, prior to combining the spectra, two points must be addressed. Those were the contrast in the magnitude of each of the NIR and Raman signals and the difference in the number of variables obtained. The magnitude of the SAR-DRM signals was lower than those of the SORS signals, this is due to the low intensity of the light source. The contrast in magnitude was addressed through SNV pre-processing the spectra from each of the techniques before combining them. The difference in the number of variables obtained from SAR-DRM and SORS measurements is due to the difference in the resolution of each of the NIR and Raman spectrometers, where the signals are collected using 512 pixels with the NIR spectrometer and 1024 pixels for the Raman spectrometer. To address, this mismatch in the number of variables, following the spectral range selection or truncation, the NIR spectra were linearly interpolated to match the size of the Raman signals using the MATLAB built-in function interp1.

In order to match the number of variables provided by the SOR signals before combining SAR-DRM and SORS signals, a number of steps are followed for each type of signal. Figure 4.10 illustrates the overall steps involved in the workflow prior to combining the signal from both techniques. This figure shows the additional interpolation step included for SAR-DRM signals, which follows

the spectral range selection and precedes the pre-processing step. In this step, the number of the variables in the SAR-DRM signal following spectral range selection is increased to match the number of variables obtained following the spectral range selection for SORS spectra. Finally, the spectra from both techniques are independently pre-processed to mitigate the contrast in signal magnitude, and the final block is formed.

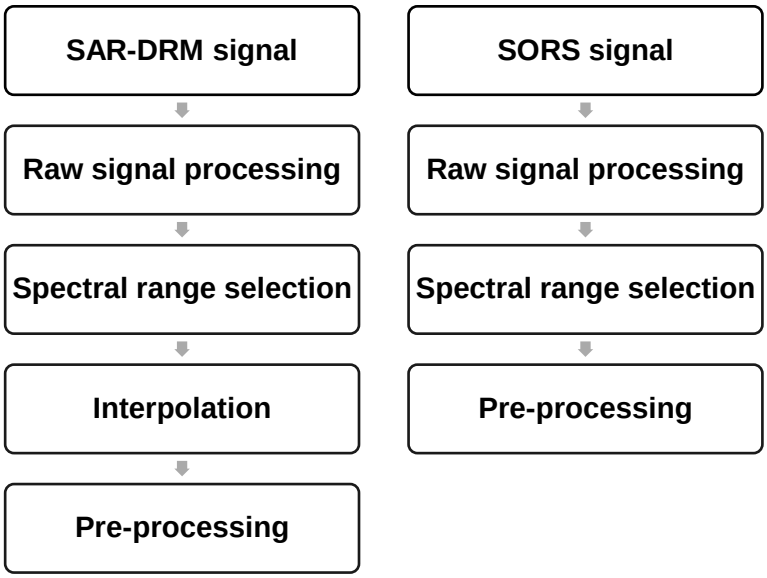

Figure 4.10. SAR-DRM and SORS signal processing steps prior to augmentation.

4.5 Multivariate regression analysis

To evaluate the performance of both techniques in expressing the solvent content, the collected datasets were used in partial least squares regression (PLSR) analysis in MATLAB using a script developed and employed in earlier studies.[14,58] This script enables specifying the spectral range and pre-processing methods of the spectra in the calibration and test datasets independently. Then, cross-validation is performed on the calibration set to test the predictive performance of the PLSR model based on the calibration set spectra. The suitable PLSR model is applied to predict the solvent content in the test set. It is worth mentioning that mean-centring is commonly applied to subtract the average of spectra prior to PLSR analysis, which would result in a PLSR model requiring a lower number of latent variables to describe the models based on the mean-centred spectra. Nevertheless, the approach followed for the presented studies was to minimise data processing and pre-processing to preserve any information derived from the datasets.

The parameters used for PLSR for each of the SAR-DRM and SORS spectra as well as the combined spectra from each of the systems are summarised in Table 4.5. The samples in each dataset were divided into a calibration and test set. Those were divided so as to use a maximum of 75% of the number of sample spectra in the calibration set. Samples in the test set were selected randomly from across the runs to represent the solvent content range of 0-20%. This aims to ensure that the variability from all runs is represented in the test set.

For datasets where less than 50 sample spectra were collected, leave-one-out cross-validation was employed to assess the PLSR model. For datasets of a larger number of samples, k-fold cross-validation was employed. The number of folds was determined based on the number of samples and runs. The k-fold cross-validation method was employed to avoid obtaining misleading results due to the overfitting that could occur when applying leave-one-out cross-validation to a calibration set with a large number of samples.

Table 4.5. SAR-DRM dataset and analysis parameters.

	SAR-DRM			
Solvent	**n-heptane**		**MTBE**	
Paracetamol grade	Granular	Powder	Granular	Powder
Calibration set	26	32	39	63
Test set	12	10	12	23
Cross-validation	Leave-one-out		Leave-one-out	6-fold
Spectral ranges/nm	1100-1600		1100-1600	
Pre-processing	None (raw), SNV			

	SORS			
Solvent	**Anisole**		**MTBE**	
Paracetamol grade	Granular	Powder	Granular	Powder
Calibration set	52	57	62	63
Test set	17	21	40	23
Cross-validation	5-fold		6-fold	
Spectral ranges/cm^{-1}	250-1750, 960-1040, 985-1015, 750-850, 400-500		250-1750, 670-770	
Pre-processing	None (raw), SNV			

	Combined SR-DRM and SORS	
Paracetamol grade	Granular	Powder
Calibration set	63	60
Test set	20	20
Cross-validation	6-fold	
Spectral ranges	1100-1600 nm, 50-1750 cm^{-1}	
Pre-processing	SNV	

5. Spatially and Angularly Resolved Diffuse Reflectance Near-Infrared Measurements for Monitoring Pharmaceutical Drying

5.1 Introduction

In spatially and angularly resolved diffuse reflectance near-infrared measurements (SAR-DRM), light is illuminated at a sample at variable angles and the signal is collected from multiple collection points that are spatially resolved from the incident light. The illumination angles of the probe used in this study are 0°, 30°, and 45°, while the collection distances are 0.3, 0.6, 0.9, and 1.2 mm from the illumination point. This aims to collect the signal from photons that have travelled through different pathlengths through the sample, enabling the collection of complementary information from each of the spatially and angularly resolved configurations.

The first section of this chapter includes the results for the depth of solvent signal detection using SAR-DRM. This experiment was conducted to assess the extent to which the signal of a solvent beyond sublayers of API contributes to the SAR-DRM signal collected at the surface. The second part of this chapter details the results of using SAR-DRM for the in-line monitoring of pharmaceutical drying. This second section is further divided into two parts reporting the qualitative and quantitative analysis of the SAR-DRM response for two paracetamol grades, granular and powder, in two solvents, n-heptane and MTBE. This chapter provides a characterisation of the SAR-DRM signal response in addition to the use of those signals for solvent quantification during drying.

5.2 Depth of solvent signal detection using SAR-DRM

An experiment was conducted to assess the depth through which the signal of n-heptane through layers of dry paracetamol can be detected using SAR-DRM. This was done through collecting SAR-DRM signals from layers of paracetamol of varying thicknesses, where the thickness of a single layer was equal to that of the 1.6 mm spacers used, over a 2 mm cuvette filled with n-heptane, as detailed in section 4.3.1.

Figure 5.1 (a-d) shows the raw SAR-DRM spectra obtained from 0° angular configuration from the four spatial configurations. For the signal from each of the collection distances, differences in the baseline between the samples can be seen and may be explained by the variable scattering patterns of photons travelling through a large number of paracetamol particles in each of the measurements.[14] A small increase in absorbance intensity from the paracetamol layers as the collection distance increases from 0.3 mm in Figure 5.1 (a) to 1.2 mm in Figure 5.1 (d) can be seen. This corresponds to the decrease in reflectance intensity as the collection distance increases, where the incident light diffusely scatters through the sample resulting in the lower intensity of the reflected photons collected by the detector at larger collection distances. This was similarly observed in spectra from the 30° and 45° incident light sources. Nevertheless, the visualisation of raw spectra shown in Figure 5.1 does not show any change in the paracetamol signal intensity that may be related to a change in the signal from n-heptane from the different layer thicknesses. Therefore, those spectra were pre-processed using the SNV pre-processing method for further analysis.

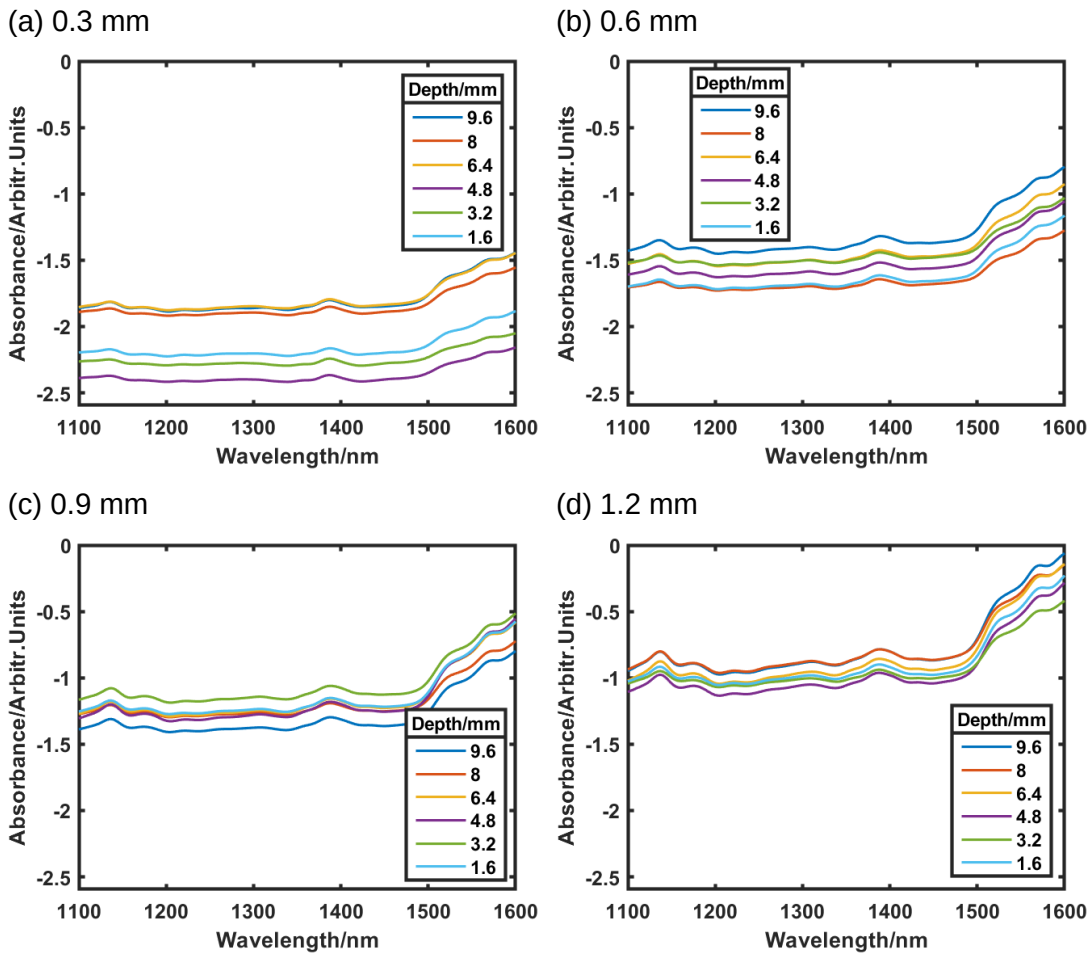

Figure 5.1. Raw spectra of variable layer thicknesses of paracetamol over n-heptane from 00° angle and (a) 0.3 mm, (b) 0.6 mm, (c) 0.9 mm, and(d) 1.2 mm distance from the illumination point.

The raw spectra shown in Figure 5.1 were SNV pre-processed and are shown in Figure 5.2, where the differences in baseline were removed. Nevertheless, no change in intensity was detected at the wavelengths of the n-heptane peaks from those measurements. This may be explained by the low intensity of light that is transmitted through the cuvette to reach the diffuse reflectance target and then travel back to the surface of the powder to be captured by the detector. The illuminating light reaches the surface of the sample, where it is absorbed, diffusely reflected, and transmitted to variable extents. The fraction that is diffusely scattered through the paracetamol reaches the cuvette and is transmitted through the solvent till it reaches the diffuse reflectance standard. Then, the light is diffusely reflected back to be transmitted through the solvent

and scattered through the paracetamol in the same phenomena mentioned earlier before it reaches the collection fibres. Moreover, the SAR-DRM probe collects the signal using one fibre per each of the collection distances although lower light intensity reaches the larger collection distances. Therefore, it is thought that a stronger light source would aid in obtaining the depth of the solvent signal detection using this system.

Although the result of this experiment did not provide more insight regarding the depth of the solvent signal detection obtained through the SAR-DRM setup, possible advantages of using this technique for the in-line monitoring of pharmaceutical drying cannot be ruled out.

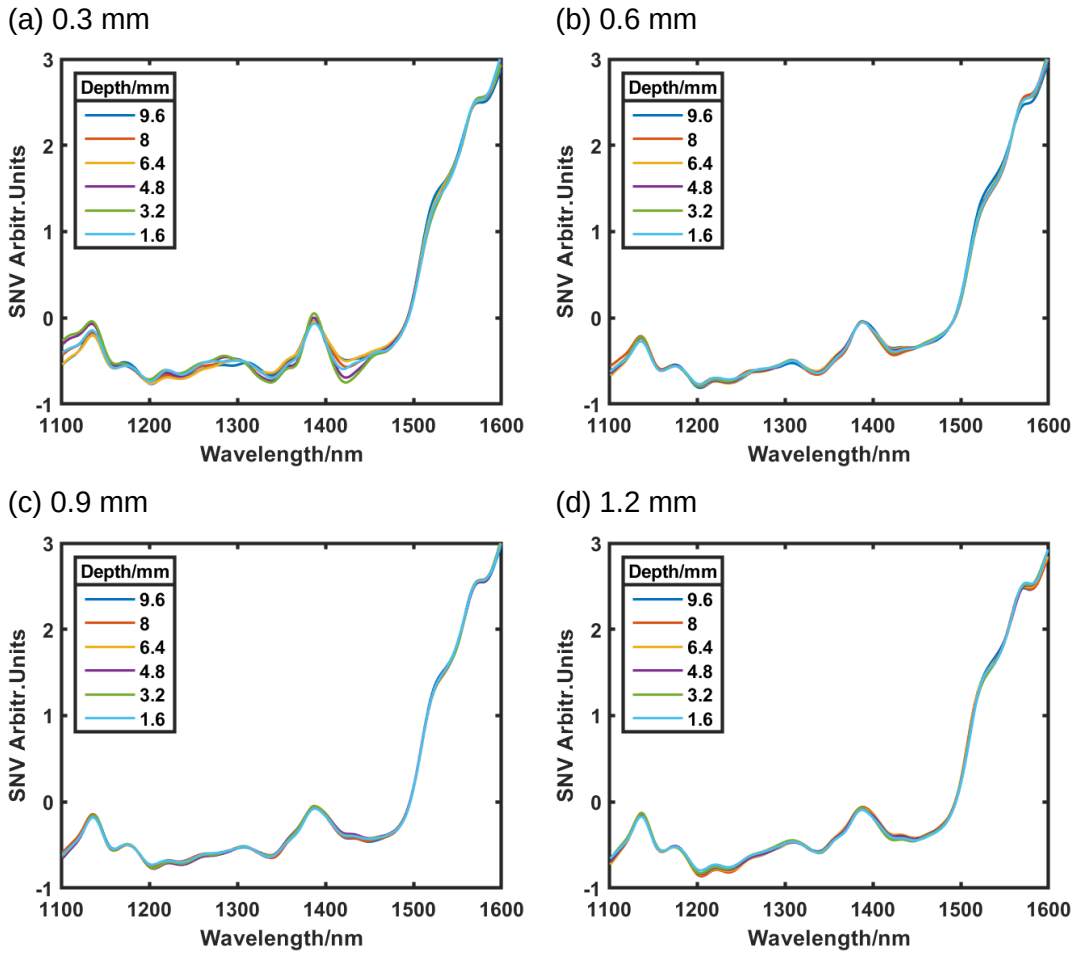

Figure 5.2. SNV pre-processed spectra of variable layer thicknesses of paracetamol over n-heptane from 0° angle and (a) 0.3 mm, (b) 0.6 mm, (c) 0.9 mm, and(d) 1.2 mm distance from the illumination point.

5.3 SAR-DRM for monitoring solvent content during drying.

Washing solvents that have NIR active bands and in which paracetamol displays low solubility were used to conduct a number of washing and drying runs, where mass loss on drying samples and SAR-DRM spectra were collected at different intervals. This was done in order to collect SAR-DRM signals corresponding to a range of solvent content values representative of the drying filter cake. This section reports the results and analysis of those datasets, which are divided per paracetamol grade to report the results found in each of the wash solvents, n-heptane and MTBE.

Figure 5.3 shows the drying profile of both paracetamol grades in each of the solvents. Comparing the drying curves of the granular and powder grades shows that the drying of the powder grades requires longer times and/or higher temperatures of drying compared to those of the granular grades; this can be seen by comparing Figure 5.3 (a-b) and Figure 5.3 (c-d). Moreover, the variability seen among runs of the same system may be attributed to local variation in solvent content within the drying cake as a result of the non-uniformity of drying.[40]

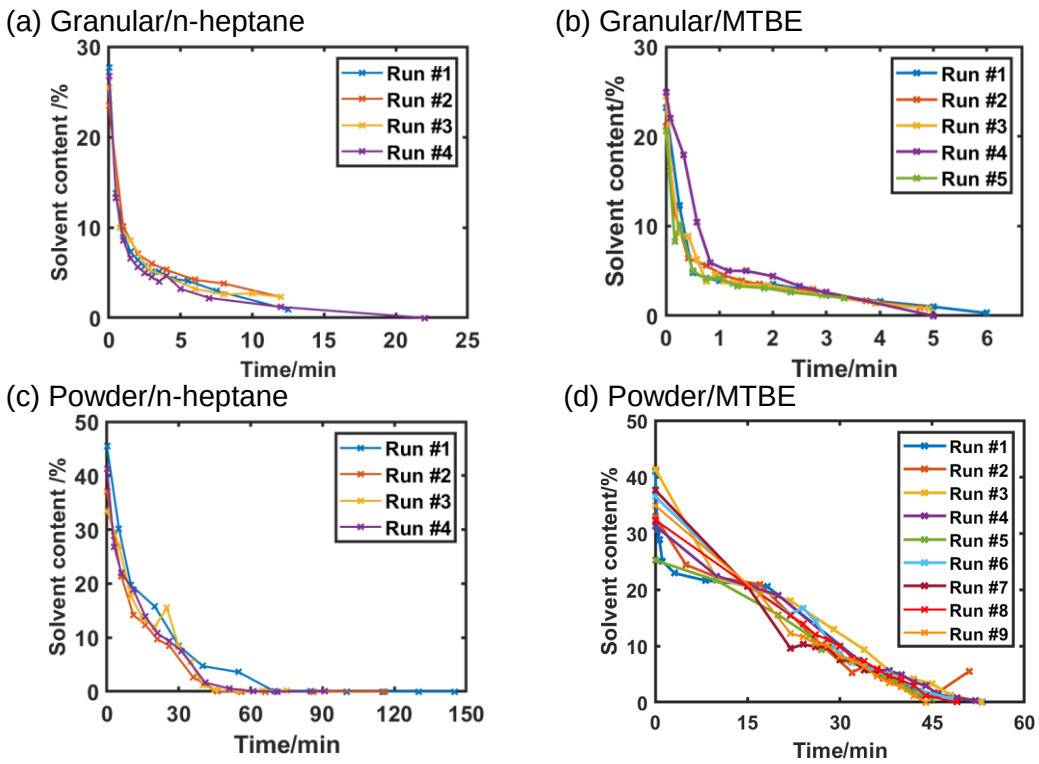

Figure 5.3. Drying profile of multiple batches using granular paracetamol in (a) n-heptane and (b) MTBE and powder paracetamol in (c) n-heptane and (d) MTBE.

5.3.1 Qualitative analysis of SAR-DRM spectra

This section is further divided into two sections reporting the results of the use of SAR-DRM to monitor the drying of granular and powder paracetamol in n-heptane and MTBE. As described in the experimental section 4.1, n-heptane shows a band spanning ~1150-1240 nm, in which a peak at ~1210 nm is least overlapped with the paracetamol peaks; while MTBE shows a sharp peak at 1185 nm that largely overlaps with the paracetamol peak. The variation in the intensity of solvent peaks as a result of the change in solvent content will be evaluated in this section. First, the raw signal quality is assessed from the 12 spatial and angular configurations. Then, the spectra are evaluated following pre-processing.

5.3.1.1 Granular paracetamol systems

To evaluate the quality of SAR-DRM spectra collected during the drying of the granular/solvent systems, the raw spectra representing variable solvent contents from the angular/spatial configurations of closest and farthest distances from the light source were plotted; those are shown in Figure 5.4 for the granular/n-heptane system and in Figure 5.5 for the granular/MTBE system. This figure shows the spectra collected from 0.3 mm from the 0°, 30°, and 45°, in Figure 5.4 and Figure 5.5 (a), (c), and (e), respectively. Spectra from the 1.2 mm distance are shown in Figure 5.4 and Figure 5.5 (b), (d), and (f), respectively. The wavelength ranges around which the peak intensity changes corresponding to the change in solvent content are indicated by the arrows around 1200 nm in the figures for both solvents.

The spectra of a system of two components are expected to show features that are the sum of the spectral features of both components, where the variation in the case of paracetamol with a solvent during drying would be in the solvent peak intensity as the solvent is depleted from the system. However, the spectra collected during drying show additional variation apart from the solvent signal intensity. Among spectra of samples of variable solvent contents from the same configuration, Figure 5.4 (a) for example, a shift in baseline can be seen. This baseline shift may arise as a result of the proportion of light reflected back to the detector and is influenced by light scattering within the sample, which leads to different travelling pathlengths of photons for each of the samples.[107] Those travelling pathlengths are non-reproducible and also differ based on the density or packing of a sample. As the drying process progresses, the solvent content decreases as the wet filter cake is transformed into the dry powder bed, where the solvent suspending the powder is removed and solid particles settle. In addition to the decrease in solvent content, the voids in the cake also decrease. This suggests that this baseline shift may reflect this increase in the packing density of the filter cake. The decrease in the baseline shift as the packing increases is only seen in Figure 5.4 (c), which suggests that this shift may be a result of a combination of factors. Another possible cause of this baseline shift in NIR spectra is a combination of

instrumental noise and a change in temperature.[14,57] Nevertheless, those are overall mitigated through calibration and setting experimental parameters that minimise particle breakage and attrition throughout the drying process. Thus, it is most likely that the baseline shifts seen in this system are a result of the variation in pathlength travelled by photons within the paracetamol cake, where those pathlengths are further impacted by the change in the packing density of the cake.

Comparing the response from spectra from the same angular configuration with different collection distances, Figure 5.4 (a) and (b) from 0°/0.3 mm and 0°/1.2 mm as an example, variation in signal intensity can be seen, where the reflectance intensity from the closer distance is stronger than that of the larger distance. This is a result of the diffusion of light throughout the sample, where photons are absorbed or scattered. Before reaching the detector at the largest spatial distance, more photons would have been absorbed and more scattering incidents would have taken place resulting in reduced intensity of light reflected to be collected from the largest spatial distance.[57] Comparing the response from the three angular configurations for the same spatial configuration, in Figure 5.4 (a), (c), and (e) for the 0.3 mm spatial configuration and Figure 5.4 (b), (d), and (f) for the 1.2 mm spatial configuration, shows the difference in signal magnitude, where the same intensity of light is distributed over a larger area of the sample. Those observations may also be seen in Figure 5.5 of the granular/MTBE system.

The change in signal magnitude and baseline shift prevents the clear visualisation of the change in peak intensity corresponding to the change in solvent content. Therefore, SNV pre-processing was applied to remove those differences as shown in Figure 5.6 and Figure 5.7 of the granular paracetamol in n-heptane and MTBE, respectively, where (a), (c), and (e) show the spectra from 0°, 30°, and 45°, respectively, for the 0.3 mm spatial configuration, and (b), (d), and (f) show spectra from 0°, 30°, and 45°, respectively, for the 1.2 mm spatial configuration. SNV pre-processing was applied as opposed to other common pre-processing methods such as MSC or derivatives. The MSC transformation involves the estimation of a correction coefficient, usually based

on the average of sample spectra in a dataset, which could affect the quality of all sample spectra as a result of one noisy spectrum. The derivative transformation removes the baseline shift and slope in spectra but could result in the enhancement of small peaks arising due to noise. In SNV, a sample spectrum is processed by subtracting the mean of the intensity of this spectrum and then dividing it by the standard deviation of the spectrum. Therefore, SNV was selected for pre-processing those spectra as it involves the pre-processing of each spectrum individually. The baseline shifts seen in Figure 5.4 and Figure 5.5 are removed from the SNV pre-processed spectra where the remaining variation can be attributed to the change in solvent peak intensity as a result of the change in solvent content during drying, in addition to the effects of noise. The changes in peak intensity corresponding to the change in solvent content can mostly be seen around 1210 nm in Figure 5.4 for n-heptane and 1185 nm in Figure 5.5 for MTBE.

Figure 5.6 (a) of 0°/0.3 mm shows variation between sample spectra around the n-heptane peak position. The decrease in solvent peak intensity as the solvent content decreases is not consistently seen in those spectra due to the noise affecting the spectra, particularly at the shorter wavelength range of 1100-1450 nm. NIR peaks at the shorter wavelength range are weaker with reference to those at longer wavelengths as those peaks arise from higher-order overtones and combinations.[57] Nevertheless, Figure 5.6 (b) of 0°/1.2 mm shows the decrease in n-heptane peak intensity around 1200 nm as can be seen from the zoomed-in inset of this peak. This can also be seen from Figure 5.6 (d) and (f) of 30°/1.2 mm and 45°/1.2 mm, respectively, although to a lower extent due to the decreased signal intensity compared to the 0°/1.2 mm configuration. Similar observation can be seen in the granular/MTBE spectra in Figure 5.7; however, pure spectra of paracetamol and MTBE indicate that the MTBE peak overlaps considerably with the paracetamol peak around 1150-1200 nm, resulting in the less clear visualisation of the MTBE peak decrease as drying progresses. Spectra collected from the angular configurations 30°-45° are most affected by this peak overlap in addition to the lower signal intensity from those configurations.

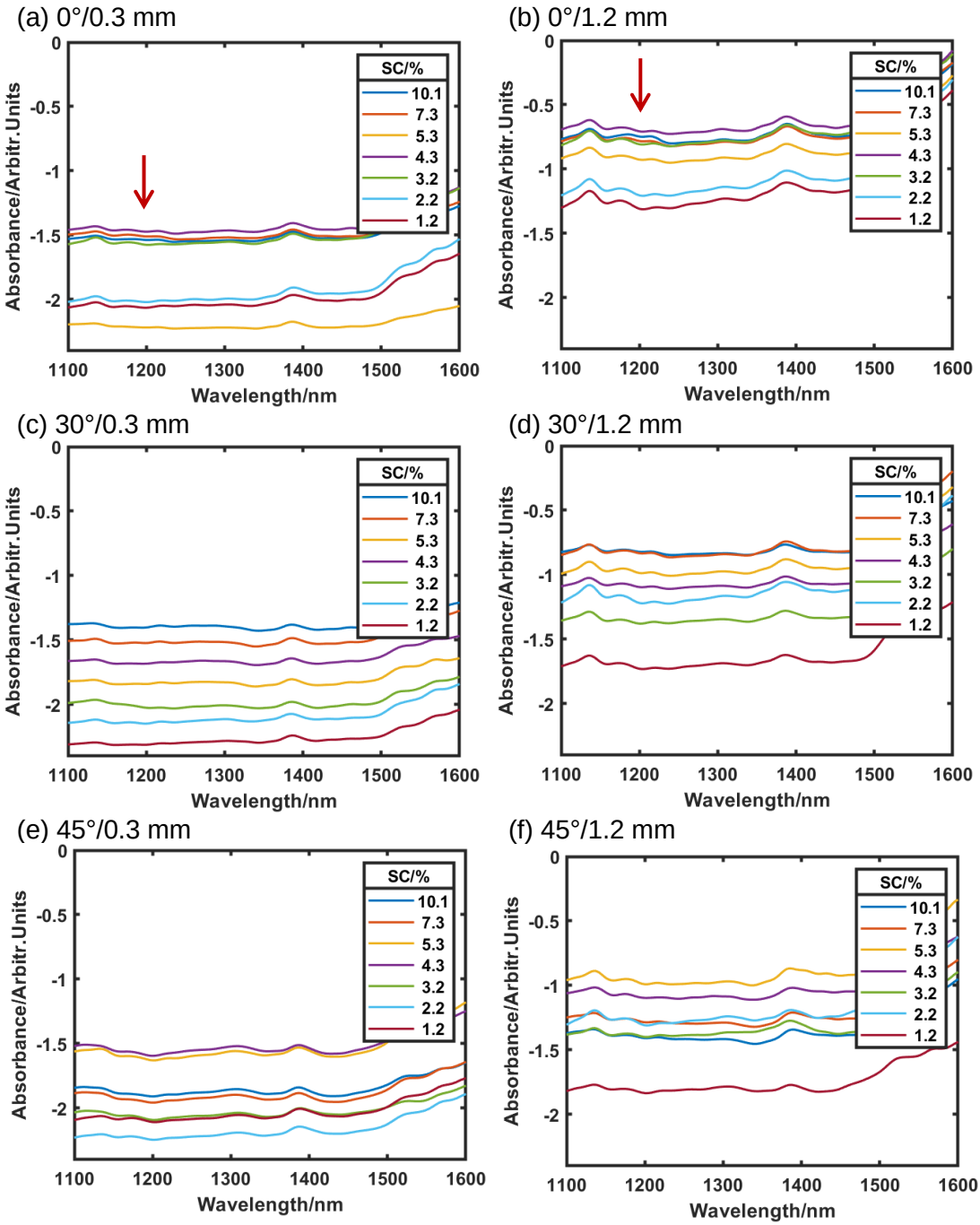

Figure 5.4. SAR-DRM spectra collected using the SAR-DRM probe in the granular/n-heptane drying from (a) 0°/0.3 mm, (b) 0°/1.2 mm, (c) 30°/0.3 mm, (d) 30°/1.2 mm, (e) 45°/0.3 mm, and (e) 45°/1.2 mm configurations. The legend shows the solvent content percentage (SC%) in each sample spectrum. Arrows point to the n-heptane peak position.

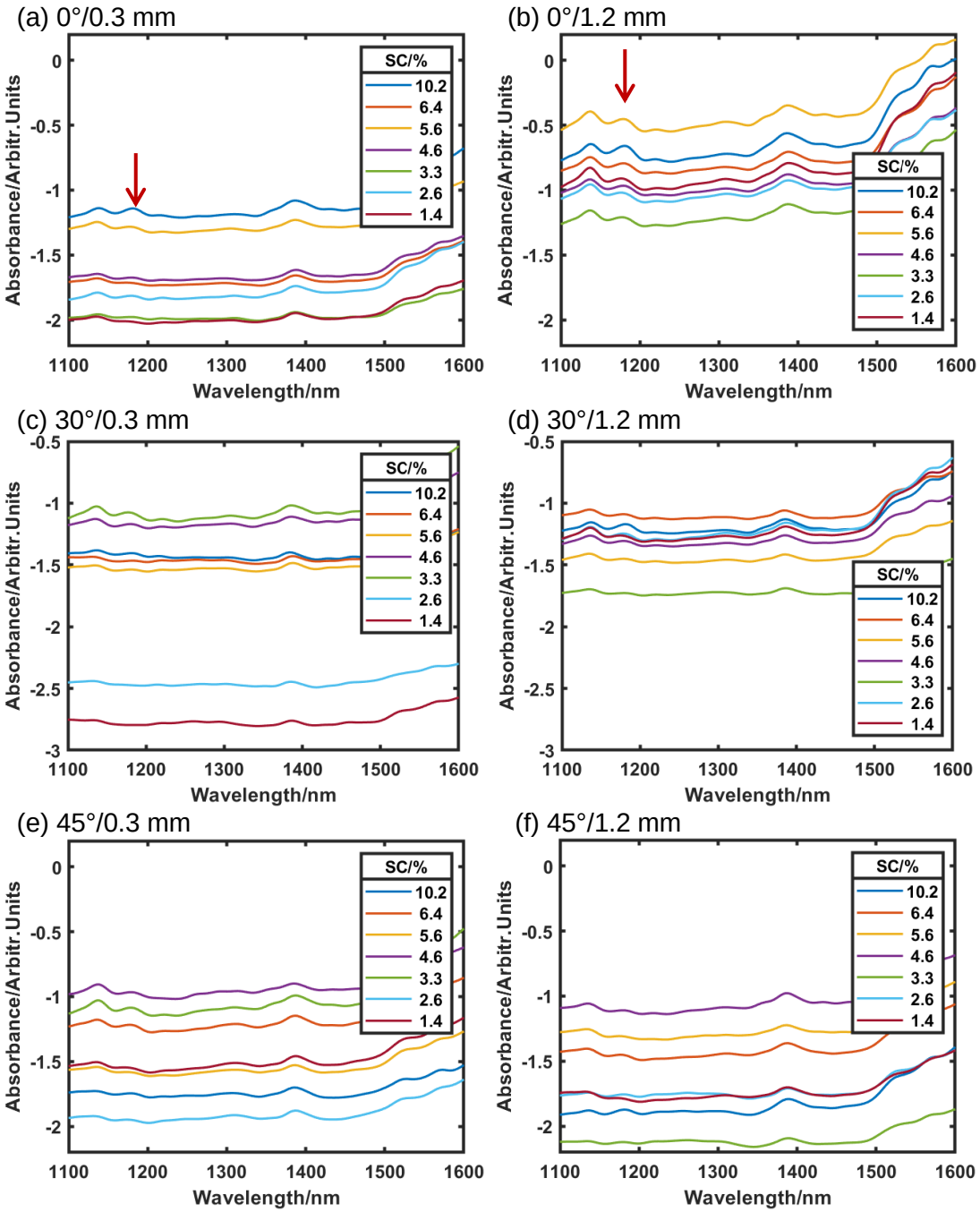

Figure 5.5. SAR-DRM spectra collected using the SAR-DRM probe in the granular/MTBE drying from (a) 0°/0.3 mm, (b) 0°/1.2 mm, (c) 30°/0.3 mm, (d) 30°/1.2 mm, (e) 45°/0.3 mm, and (e) 45°/1.2 mm configurations. The legend shows the solvent content percentage (SC%) in each sample spectrum. Arrows point to the MTBE peak position.

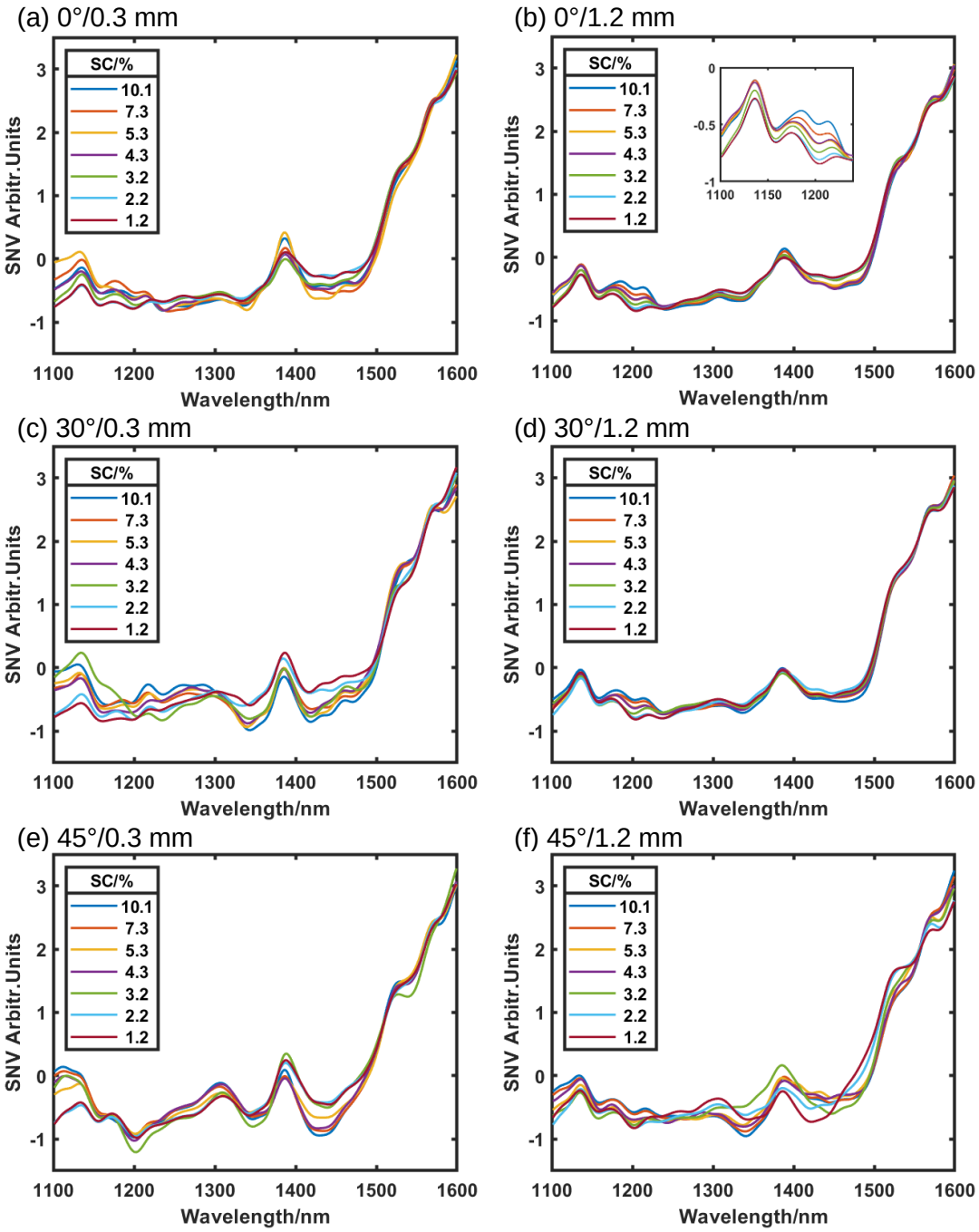

Figure 5.6. SNV pre-processed SAR-DRM spectra collected using the SAR-DRM probe in the granular/n-heptane drying from (a) 0°/0.3 mm, (b) 0°/1.2 mm, (c) 30°/0.3 mm, (d) 30°/1.2 mm, (e) 45°/0.3 mm, and (e) 45°/1.2 mm configurations. The legend shows the solvent content percentage (SC%) in each sample spectrum.

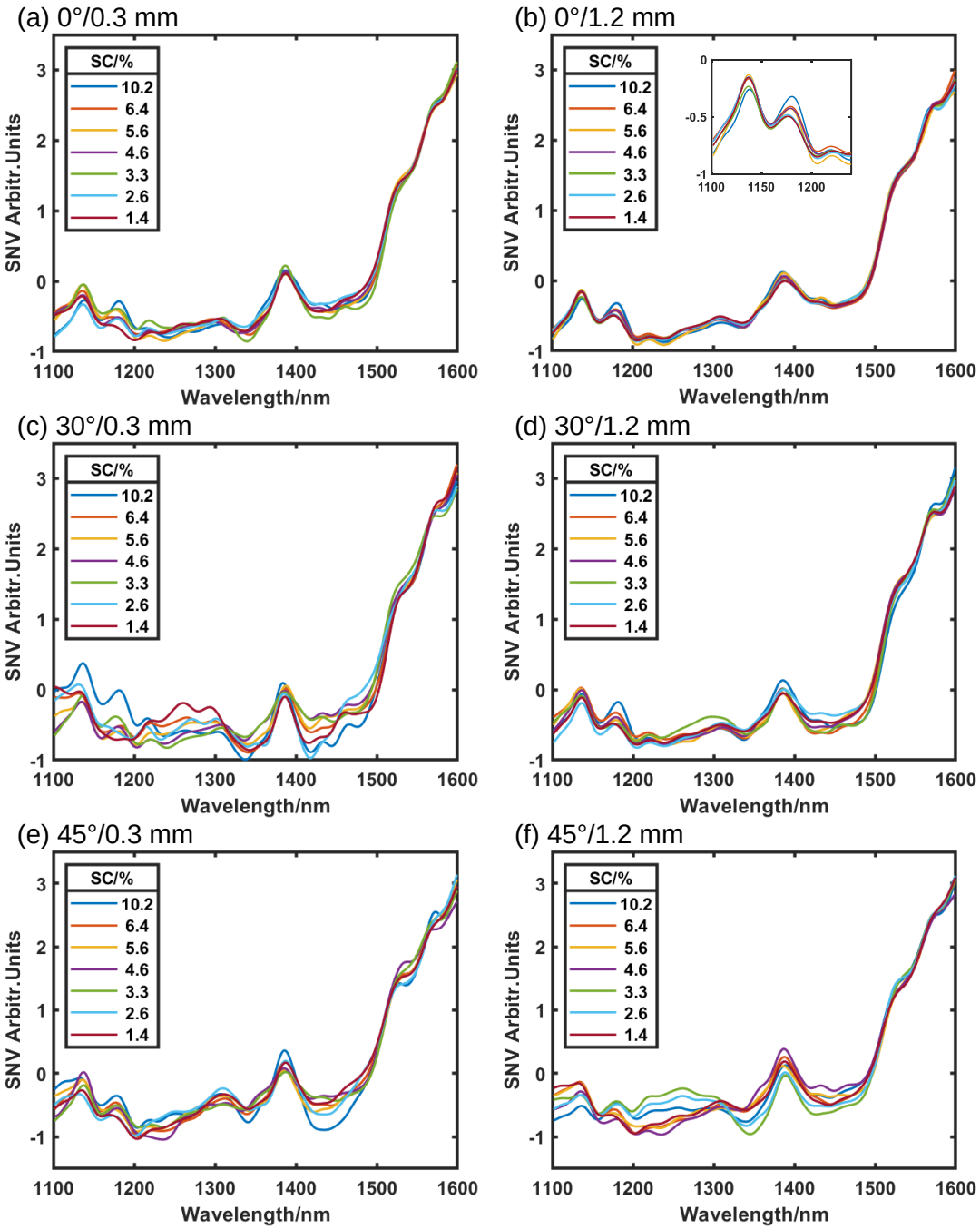

Figure 5.7. SNV pre-processed SAR-DRM spectra collected using the SAR-DRM probe in the granular/MTBE drying from (a) 0°/0.3 mm, (b) 0°/1.2 mm, (c) 30°/0.3 mm, (d) 30°/1.2 mm, (e) 45°/0.3 mm, and (e) 45°/1.2 mm configurations. The legend shows the solvent content percentage (SC%) in each sample spectrum.

5.3.1.2 Powder paracetamol systems

Raw spectra of the powder/solvent systems from the different angular and spatial configurations were also compared and are shown in Figure 5.8 and Figure 5.9 for the n-heptane and MTBE systems, respectively. Those figures show variation in the magnitude and quality of the signal between the closest and farthest distance for each of the angular light sources, similar to what was seen previously in the granular/solvent systems in section 5.3.1.1. Similar to what was seen in the granular systems, the magnitude of the signal is lower from the angular configurations 30°-45° as the light is distributed onto a wider area over the surface of the sample and reaches shallower depths. Using the angular light sources, those fewer photons may be travelling through shorter pathlengths before being reflected through the surface of the powder. Similarly, the signal intensity is lower for larger collection distances compared to the closest distances as a result of the higher incidences of light scattering before reaching the detector.

Comparing the raw signal intensity from both paracetamol grades, SAR-DRM spectra from the powder paracetamol grade show lower signal magnitude as seen in Figure 5.8 and Figure 5.9 compared to Figure 5.4 and Figure 5.5 of the granular grade. Since the particle size of the powder paracetamol grade is smaller (D_{50}= 43 µm) than the granular grade (D_{50}= 265 µm), the surface area of the powder particles is larger and leads to more light scattering and higher absorbance.[113] On the other hand, lower absorbance is seen for the powder paracetamol spectra. Similarly to the granular systems, baseline variation can be seen among the sample spectra of variable solvent content. This may also be linked to the increase in packing density as the solvent is removed from the drying cake in addition to the variation in pathlengths of the light through the powder cake. SNV pre-processing was applied to remove those baseline shifts.

Following SNV pre-processing of spectra from both powder/solvent systems, SAR-DRM spectra collected from the distance farthest from the incident light show better quality as fewer peaks arising due to noise in addition to a more

accurate representation of the solvent content, as seen in Figure 5.10 of the powder /n-heptane system, where the solvent peak intensity decreases as the solvent content decreases. This is less clear in Figure 5.11 of the powder/MTBE system as a result of the overlap of the paracetamol and MTBE peaks around 1150-1200 nm.

Comparison between the spectra collected from the two paracetamol grades shows that the spectra of the granular paracetamol systems are less affected by noise compared to the powder paracetamol systems. With regards to the two solvent systems used with paracetamol in this study, n-heptane has a peak around 1210 nm that has slight overlap with the paracetamol peak as opposed to the MTBE peak around 1185 nm that is more overlapping with the paracetamol peak. This suggests that further qualitative analysis based on the spectra of those systems will be affected by the overlap in those characteristic peaks.

Overall, spectra from 0°/1.2 mm and 30°/1.2 mm configurations mostly show a decrease in solvent peak intensity as the solvent content decreases. The observations from the qualitative analysis of both paracetamol grades suggest that those may be used for further qualitative analysis.

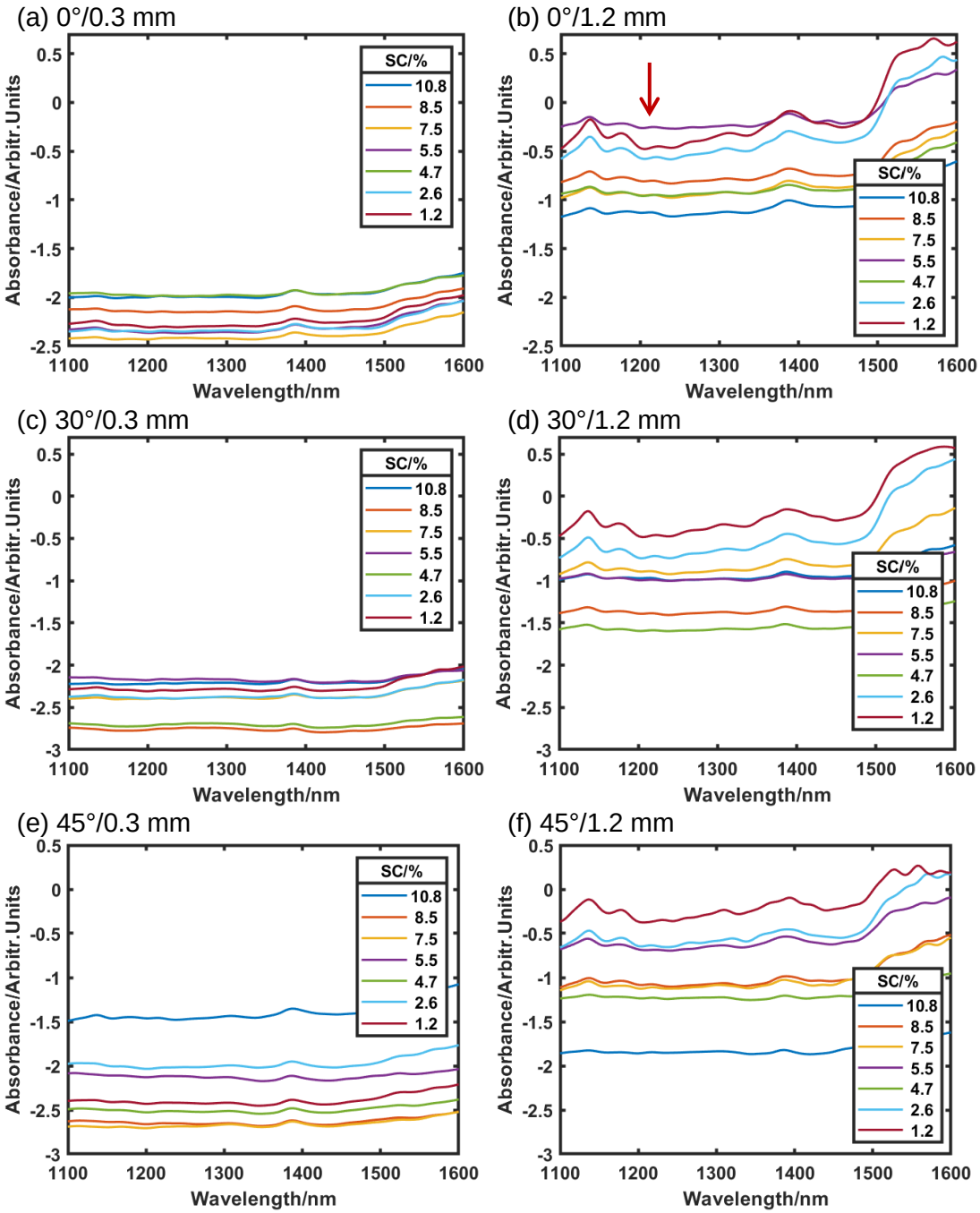

Figure 5.8. SAR-DRM spectra collected using the SAR-DRM probe in the powder/n-heptane drying from (a) 0°/0.3 mm, (b) 0°/1.2 mm, (c) 30°/0.3 mm, (d) 30°/1.2 mm, (e) 45°/0.3 mm, and (e) 45°/1.2 mm configurations. The legend shows the solvent content percentage (SC%) in each sample spectrum. Arrows point to the n-heptane peak position.

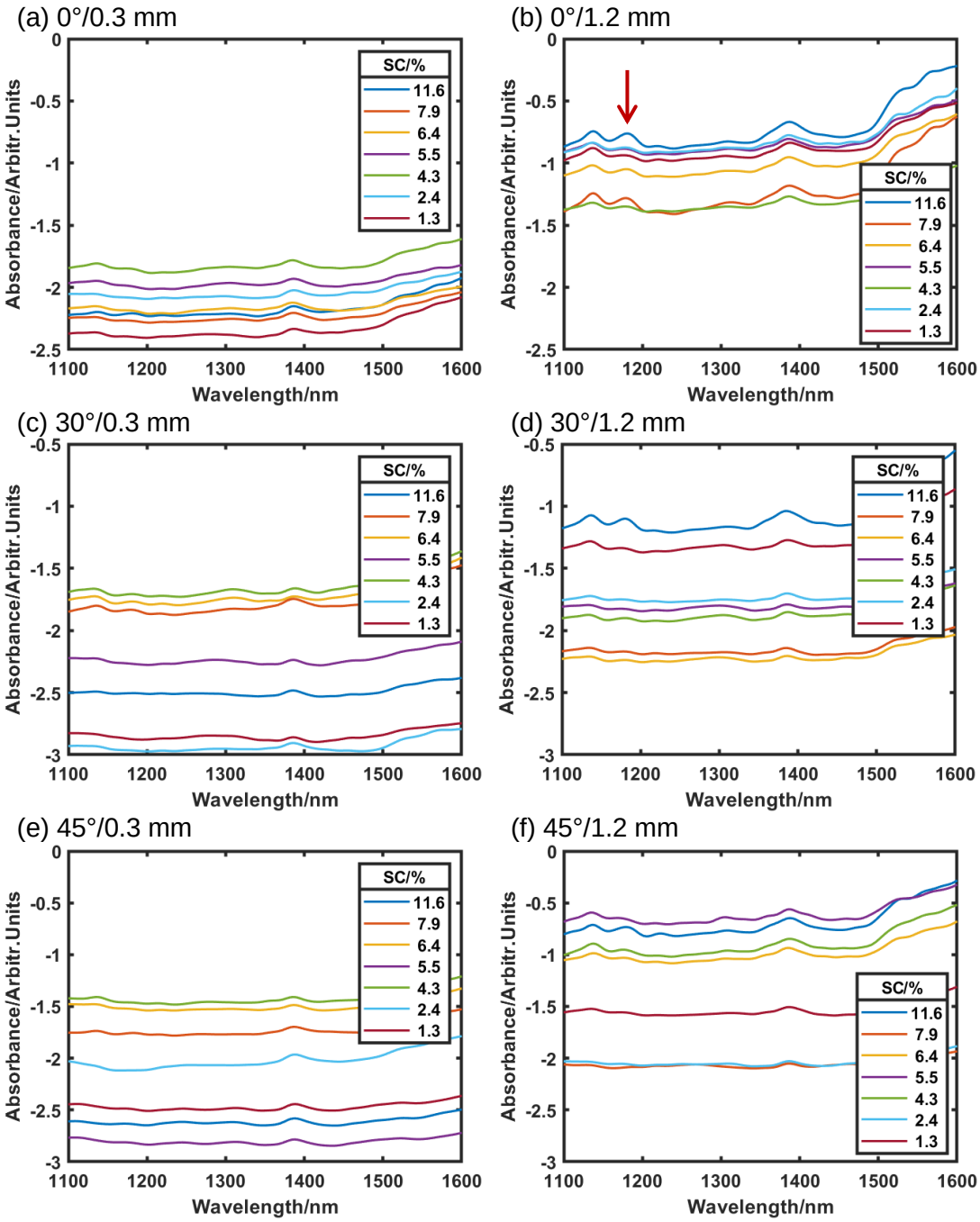

Figure 5.9. SAR-DRM spectra collected using the SAR-DRM probe in the powder/MTBE drying from (a) 0°/0.3 mm, (b) 0°/1.2 mm, (c) 30°/0.3 mm, (d) 30°/1.2 mm, (e) 45°/0.3 mm, and (e) 45°/1.2 mm configurations. The legend shows the solvent content percentage (SC%) in each sample spectrum. Arrows point to the MTBE peak position.

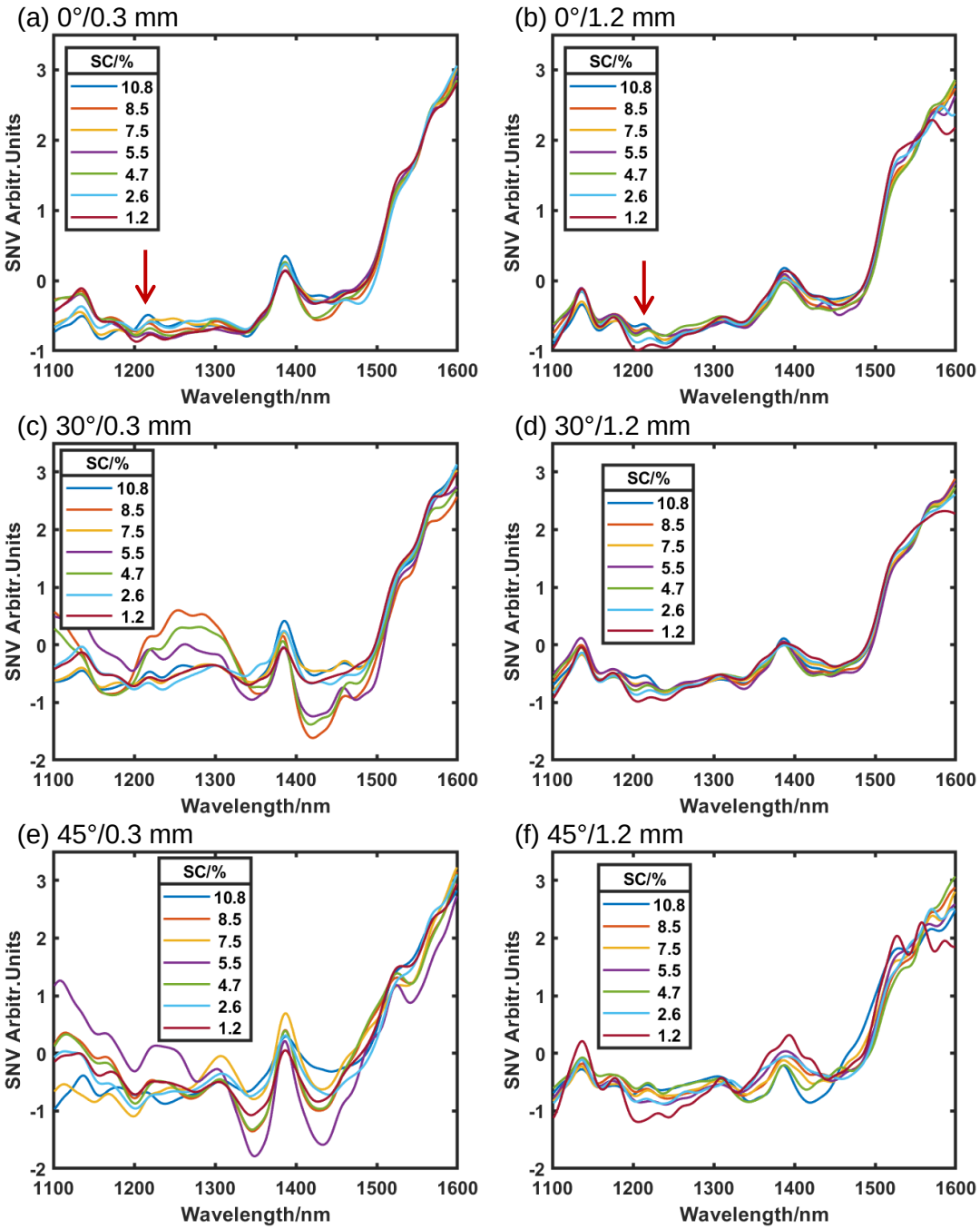

Figure 5.10. SNV pre-processed SAR-DRM spectra collected using the SAR-DRM probe in the powder/n-heptane drying from (a) 0°/0.3 mm, (b) 0°/1.2 mm, (c) 30°/0.3 mm, (d) 30°/1.2 mm, (e) 45°/0.3 mm, and (e) 45°/1.2 mm configurations. The legend shows the solvent content percentage (SC%) in each sample spectrum. Arrows point to the n-heptane peak position.

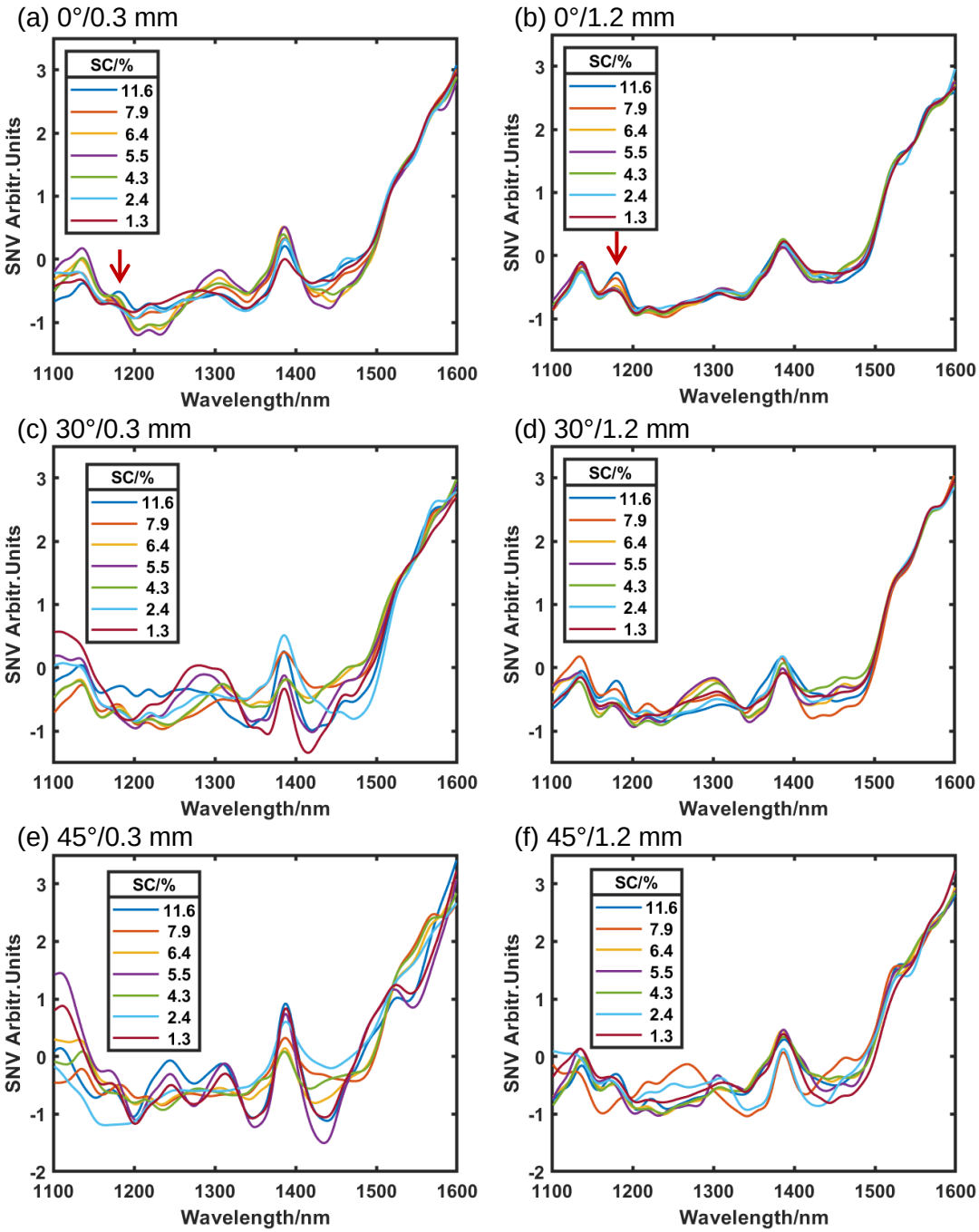

Figure 5.11. SNV pre-processed SAR-DRM spectra collected using the SAR-DRM probe in the powder/MTBE drying from (a) 0°/0.3 mm, (b) 0°/1.2 mm, (c) 30°/0.3 mm, (d) 30°/1.2 mm, (e) 45°/0.3 mm, and (e) 45°/1.2 mm configurations. The legend shows the solvent content percentage (SC%) in each sample spectrum. Arrows point to the MTBE peak position.

5.3.2 Quantitative analysis using SAR-DRM spectra

PLSR analysis was utilised for quantifying the correlation of the solvent content to the SAR-DRM spectra collected during drying. PLSR models were constructed using raw and pre-processed SAR-DRM spectra collected throughout the drying. The number of latent variables sufficient to describe each of the PLSR models constructed using the SAR-DRM configuration was selected after assessing the root mean square error of cross-validation (RMSECV) curves. Then, the calibration model with a suitable number of latent variables was used to estimate the solvent content of the spectra in the test set as described in section 4.5.

First, PLSR models are constructed using spectra from the SAR-DRM configurations individually for each of the granular and powder paracetamol grades in n-heptane and MTBE solvent systems. Then, for each of the systems, SAR-DRM spectra from multiple configurations are combined to assess any improvement in the PLSR model performance of combined configurations.

5.3.2.1 Granular paracetamol systems

SAR-DRM spectra collected during the drying of granular paracetamol in n-heptane and MTBE were used to construct PLSR models, where approximately two-thirds of the sample spectra are used as a calibration set while the remaining are used as a test set as previously explained in section 4.5.

5.3.2.1.1 PLSR of individual SAR-DRM spectra

The RMSECV curves shown in Figure 5.12 were inspected to select the number of latent variables from each of the configurations for each of the systems, where the curves are shown in Figure 5.12 (a-c) of the granular/n-heptane system and in Figure 5.12 (d-f) of the granular/MTBE system for the

three light angles. Those curves show that the RMSECV slightly decrease as the collection distance increases, which can be seen for spectra collected from all three light angles. This reproducibility in the observation suggests that the changes in spectral features related to the change in solvent content are better captured from larger collection distances for both granular/solvent systems. Following SNV pre-processing, RMSECV curves are similar or slightly lower than those of the raw spectra and show a similar decrease in RMSECV as the collection distance increases. Pre-processing aims to enhance spectral features and remove variations in the spectra that are not related to the change in chemical composition.[92]

Despite the improvement in spectral features seen in Figure 5.6 and Figure 5.7 of the granular systems, the minimal differences in the RMSECV curves and number of latent variables following pre-processing suggests that the baseline variation is not a major driver of the variation leading to the level of error in those spectra. Nevertheless, the slight decrease in RMSECV curves in addition to the similarity in the number of latent variables suggests that either that minimal variation irrelevant to the solvent content is contained in these spectra or that SNV pre-processing was not the most ideal pre-processing method.[114] SNV pre-processing might have removed the random variation in those spectra, leaving in some systematic variation. However, since the number of sample spectra collected from multiple drying runs in the calibration set provides a sufficient representation of this systematic variation for PLSR analysis, the capturing of this variation in PLSR models results in the reduction of RMSECV.[95,114] Despite the lower quality of the spectra collected from the 30°-45° light angles seen through the qualitative analysis, RMSECV curves of the PLSR models of those spectra similarly show the decrease in RMSECV as the spatial distance increases.

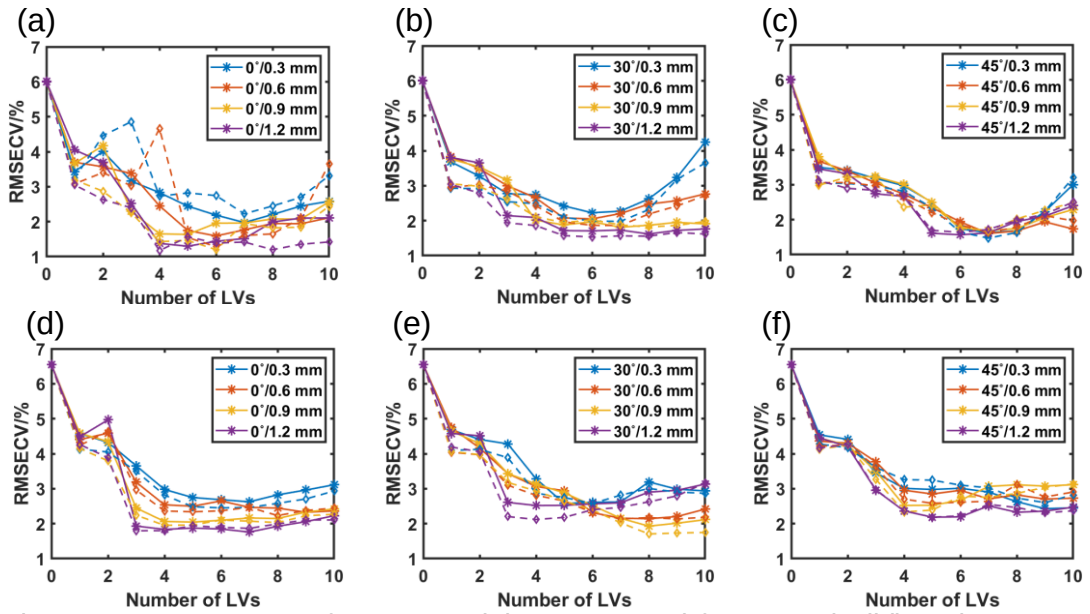

Figure 5.12. RMSECV of PLSR models constructed from raw (solid) and SNV pre-processed spectra (dashed) from (a) 0°, (b) 30°, and (c) 45° for 0.3-1.2 mm collected from granular/n-heptane and (d) 0°, (e) 30°, and (f) 45° for 0.3-1.2 mm collected from granular/MTBE.

Table 5.1 contains a summary of the PLSR models selected based on the RMSECV curves in Figure 5.12. For raw spectra, the minimum expected number of latent variables is two as the system includes two components, the change which would be captured by PLSR models. However, the number of latent variables for PLSR models of both systems ranges between 4-8 LVs, suggesting physical factors driving the variation in model performance in addition to the two chemical system components. Such factors could include the interaction of light with this particulate system, which results in diffuse reflectance to different paths. This increase in the pathlength of photons that are reflected back to the larger distance detectors results in spectra that provide more information about the system. However, those spectra are of variable intensities, are influenced by bulk and particle characteristics, such as packing density and particle size, and are more complex to interpret as a result.

The effect of the factors mentioned previously can be seen in the RMSECV values of PLSR of raw spectra from different configurations. For both of the granular/solvent systems, RMSECV decreases as the collection distance increases for the three incidence light angles. This decrease in RMSECV is

associated with an increase in the coefficient of determination, R^2, suggesting the improvement in the linear correlation of the spectra from larger collection distances. This improvement in RMSECV and R^2 may be attributed to the interaction of light with the sample, where the longer pathlength travelled by the light before reaching the detectors at the larger distances suggests that those photons have scattered through the wet sample carrying stronger signal from the solvent leading to spectra of stronger correlation to the solvent content. Regarding the granular/n-heptane system, there is a 34% decrease in RMSECV of the 0°/1.2 mm spectra compared to the 0°/0.3 mm spectra, 23% decrease in RMSECV of 30°/1.2 mm spectra compared to 30°/0.3 mm spectra, and 4% decrease in RMSECV of the 45°/1.2 mm spectra compared to the 45°/0.3 mm spectra. For the granular/MTBE system, a 30% decrease in RMSECV is seen for the 0°/1.2 mm spectra compared to the 0°/0.3 mm spectra, a 2% decrease in RMSECV of 30°/1.2 mm spectra compared to 30°/0.3 mm spectra, and 27% decrease in RMSECV of the 45°/1.2 mm spectra compared to the 45°/0.3 mm spectra. The decrease in improvement as the incident light angle increases can be related to the quality of the spectra collected, as shown in section 5.3.1.1. The consistency in the decrease in RMSECV of the 0°/1.2 mm spectra compared to 0°/0.3 mm spectra in both systems suggests that this configuration is more suitable for robustly capturing spectra that represent the variation in the solvent content. The slightly lower improvement in the granular/MTBE system compared to the granular n-heptane may be explained by the overlap of the MTBE peak with the paracetamol peak compared to the n-heptane peak as was shown in section 5.3.1.1.

For those raw spectra, RMSEP values generally decrease as the collection distance increases but are slightly higher than those of the RMSECV. Although the calibration set was selected to sufficiently represent the sample spectra, where the RMSEP would be expected to be a value closer to the RMSECV as similar variation is included in both datasets, RMSEP values are larger than those of the RMSEP, suggesting some non-systematic variation in the test set.

Following SNV pre-processing, the RMSECV of PLSR models of the spectra decreases slightly compared to the raw spectra. The RMSECV also decreases as the collection distance increases. This increase is also accompanied by a slight increase in R^2. For the pre-processed granular/n-heptane spectra, there is a 57% decrease in RMSECV of the PLSR model of the 0°/1.2 mm spectra compared to the 0°/0.3 mm spectra, 23% decrease in RMSECV of the PLSR model of 30°/1.2 mm spectra compared to 30°/0.3 mm spectra, and no improvement in RMSECV of the PLSR model of the 45°/1.2 mm spectra compared to the 45°/0.3 mm spectra. For the granular/MTBE system, 27% decrease is seen in RMSECV of the PLSR model of the 0°/1.2 mm spectra compared to the 0°/0.3 mm spectra, 18% decrease in RMSECV of the PLSR model of 30°/1.2 mm spectra compared to 30°/0.3 mm spectra, and 19% decrease in RMSECV of the PLSR model of the 45°/1.2 mm spectra compared to the 45°/0.3 mm spectra. The improvement in for the PLSR model of the 0°/1.2 mm spectra of the granular/n-heptane system compared to the PLSR model of the 0°/1.2 mm spectra of the granular/MTBE system suggests that those differences in the response seen in the qualitative analysis can largely influence the PLSR model performance of the datasets of the different solvents. Moreover, the inconsistency in improvement between the raw and pre-processed 30°/1.2 mm and 45°/1.2 mm spectra suggests that some of the variation due to physical phenomena that were removed by pre-processing is captured to variable extent in each of the configurations and contribute differently to the estimation of the solvent content. The RMSEP of the pre-processed test set spectra increases compared to the raw spectra, this suggests that some of the systematic variation carried in the raw spectra was removed by the pre-processing leading to this increase in error.

Among PLSR models constructed using the spectra from the four distances illuminated from the three light angles, spectra collected from the 0° incidence angle show the lowest RMSECV and RMSEP for raw and pre-processed spectra from both systems. In addition, spectra from the closest collection distance, 0.3 mm, consistently show an error higher than the three other collection distances from the three angles.

Table 5.1. Summary of PLSR model performance of raw and SNV pre-processed spectra of granular paracetamol in n-heptane and MTBE from each of the angular/spatial configurations.

Grade/Solvent	Angle	Distance/mm	Raw				SNV pre-processed			
			LV	RMSE CV/%	RMSE P/%	R^2	LV	RMSE CV/%	RMSE P/%	R^2
Granular/n-heptane	0°	**0.3**	7	1.98	3.18	0.58	4	2.73	3.84	0.20
		0.6	6	1.59	2.40	0.72	6	1.29	2.22	0.82
		0.9	5	1.64	2.31	0.72	4	1.43	2.63	0.77
		1.2	5	1.30	1.76	0.81	4	1.17	2.37	0.85
	30°	**0.3**	6	2.23	2.35	0.47	7	1.98	2.48	0.57
		0.6	6	2.05	2.08	0.57	6	1.87	2.26	0.63
		0.9	5	1.88	2.98	0.61	5	1.94	3.14	0.58
		1.2	5	1.71	2.27	0.69	6	1.53	2.41	0.74
	45°	**0.3**	7	1.63	3.43	0.71	7	1.47	3.10	0.76
		0.6	7	1.61	2.28	0.72	7	1.63	2.56	0.72
		0.9	7	1.69	3.36	0.69	7	1.68	3.12	0.69
		1.2	6	1.57	3.07	0.74	6	1.64	2.75	0.71
Granular/MTBE	0°	**0.3**	7	2.62	1.55	0.59	5	2.48	1.95	0.62
		0.6	4	2.54	1.68	0.61	4	2.36	1.31	0.66
		0.9	4	2.06	1.22	0.74	4	1.95	0.97	0.77
		1.2	4	1.84	1.17	0.80	3	1.80	1.13	0.80
	30°	**0.3**	5	2.58	1.49	0.60	6	2.58	1.17	0.61
		0.6	7	2.16	1.77	0.72	7	2.14	1.68	0.73
		0.9	8	1.93	3.23	0.77	8	1.71	3.13	0.82
		1.2	4	2.52	1.49	0.63	4	2.12	1.25	0.73
	45°	**0.3**	4	3.01	4.04	0.47	9	2.60	4.70	0.64
		0.6	5	2.85	1.76	0.52	5	2.58	1.50	0.60
		0.9	4	2.52	2.28	0.62	4	2.33	2.08	0.67
		1.2	5	2.19	1.67	0.71	5	2.19	1.33	0.71

The regression and residual plots of PLSR models of SNV pre-processed spectra from 0°/0.3 mm in Figure 5.13 (a-b) and from 0°/1.2 mm in Figure 5.13 (c-d). Comparing Figure 5.13 (a) and (c) shows the reliability of 0°/1.2 mm, indicated by the symmetry around the diagonal line, as opposed to 0°/0.3 mm, where the prediction is farther from the actual values. This is also indicated by the residuals plots. It is noted that some of the test set prediction at solvent contents higher than 10% are far from the actual values compared to the lower solvent content spectra. This may be attributed to the fewer sample spectra included in the calibration set for the higher solvent content range resulting in less accurate predictions.

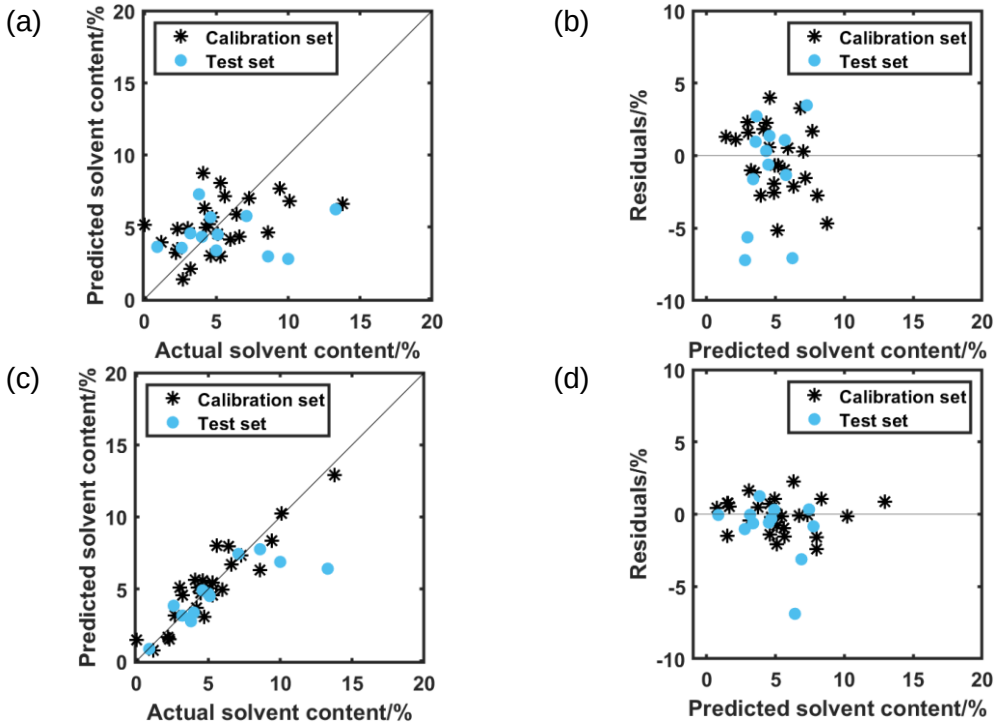

Figure 5.13. (a) Regression and (b) residuals plots of the PLSR model of SNV pre-processed spectra of 0°/0.3 mm from the granular/n-heptane system. (c) Regression and (d) residuals plots of the PLSR model of SNV pre-processed spectra of 0°/1.2 mm from the granular/n-heptane system.

Further investigation into the differences between the PLSR models built with the SNV pre-processed spectra from 0°/0.3 mm and 0°/1.2 mm was needed in order to explain the improvement in the 0°/1.2 mm spectra model performance in estimating the solvent content. Figure 5.14 shows the scores and loadings

of the four latent variables of the PLSR model built with the SNV pre-processed spectra from 0°/0.3 mm. Loadings of the variables can indicate the changes in peak intensities that influence the performance of the PLSR model, while looking at the scores with reference to the solvent content and the loading curve may show grouping between the samples or indicate the relation with loadings.

Figure 5.14 (a) shows the loadings of LV1 in addition to the pure n-heptane and paracetamol spectra as reference. The loadings curve of LV1 is similar to that of paracetamol while peaks around 1200 nm and 1400 nm look sharper as those are the positions of the n-heptane peaks. The scores of LV1 in Figure 5.14 (b) do not show a clear trend related to the change in the solvent content as they are scattered in the figure. Figure 5.14 (c) of LV2 loadings also shows slightly higher loadings around 1200 nm, where the n-heptane peaks are, compared to the rest of the wavelength range while the scores in Figure 5.14 (d) show a horizontal trend, with a slight increase in slope for samples of higher solvent content. Figure 5.14 (e) of LV3 loadings shows higher loadings around 1200 nm and 1400 nm, where the n-heptane peaks are, while the scores in Figure 5.14 (f) show an increase in slope for samples of higher solvent content. Figure 5.14 (g) of LV4 loadings shows high loadings around the n-heptane peak at 1400 nm with a slight trend in Figure 5.14 (h) scores plot similar to that of Figure 5.14 (g).

Figure 5.15 shows the loadings and scores of the PLSR models built with the SNV pre-processed spectra from 0°/1.2 mm. Similarly to Figure 5.14 (a), Figure 5.15 (a) shows that the loadings of LV1 show the pure paracetamol spectral features with some peaks slightly sharper due to the presence of the n-heptane, while Figure 5.15 (b) of LV1 scores not showing clear change related to the change in solvent content. LV2 loadings in Figure 5.15 (c) are higher where the solvent peak is around 1200 nm and 1400 nm, and the scores in Figure 5.15 (d) show a trend of increase as the solvent content increases. Similarly, Figure 5.15 (e) shows higher loadings where the solvent peaks are, with a slight trend in the scores related to the increase in solvent content in Figure 5.15 (f). While the curves in Figure 5.15 show a clear relation to the

solvent, Figure 5.14 shows a weaker relation as fewer loadings can be related to the solvent peaks. This suggests that more information related to the change in solvent content is captured in the PLSR models of the 0°/1.2 mm spectra, which in turn leads to the more accurate estimation of the solvent content obtained from the 0°/1.2 mm spectra compared to the 0°/0.3 mm spectra.

Although PLSR models of 0°/1.2 mm spectra show a more accurate estimation of the solvent content, it could be that spectra collected from each of the distances carry complementary information regarding the probed depth of the wet powder. Moreover, spectra collected from the same distance, but illuminated using a different angle could also reveal different information regarding a sample. To investigate this, SAR-DRM spectra from different configurations are combined in PLSR analysis in the next section.

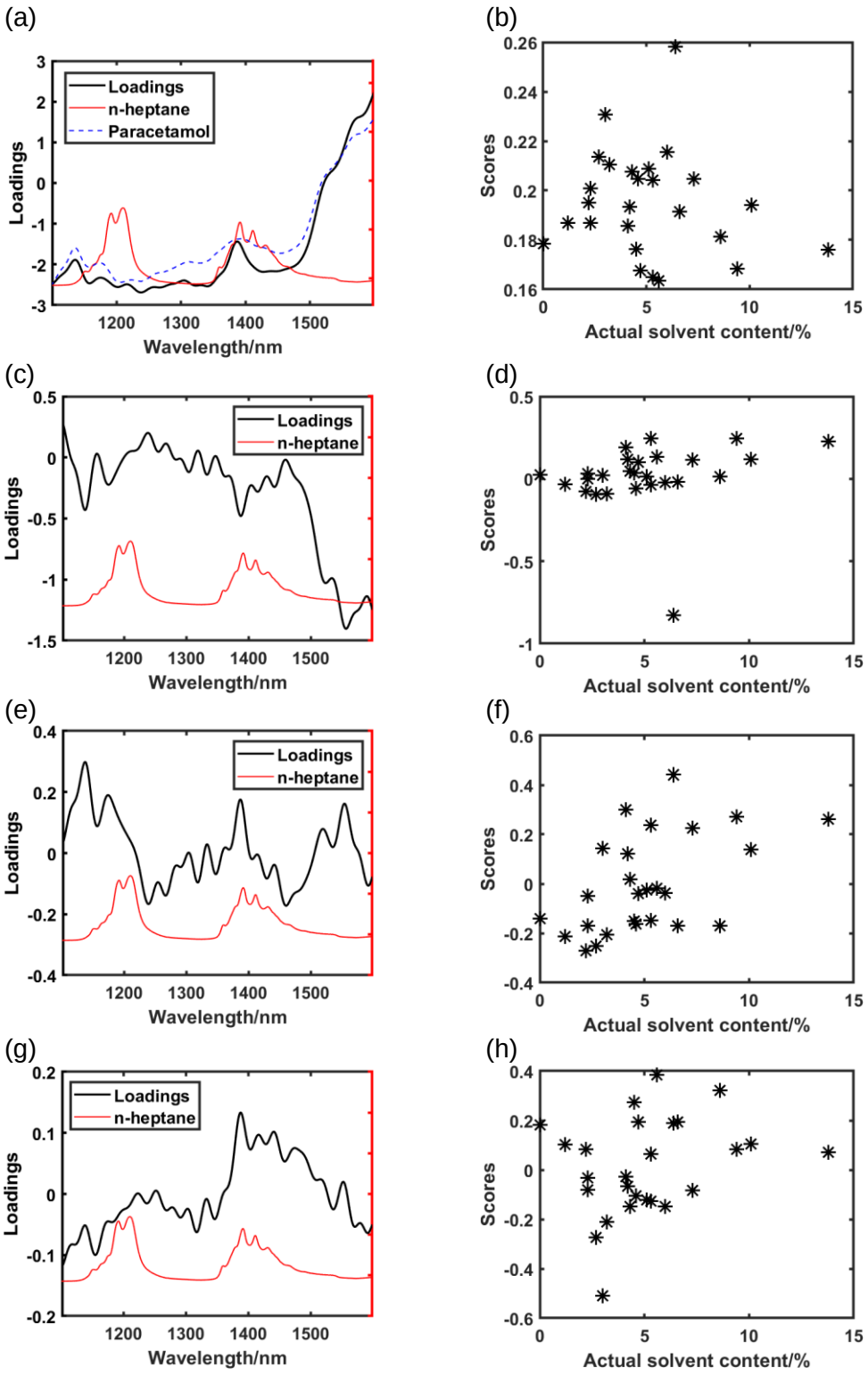

Figure 5.14. (a) loadings and (b) scores plots of LV1, (c) loadings and (d) scores of LV2, (e) loadings and (f) scores of LV3, (g) loadings and (h) scores of LV4 of the PLSR model of SNV pre-processed spectra of 0°/0.3 mm from the granular/n-heptane system. N-heptane pure spectra are also plotted as a reference with the loadings.

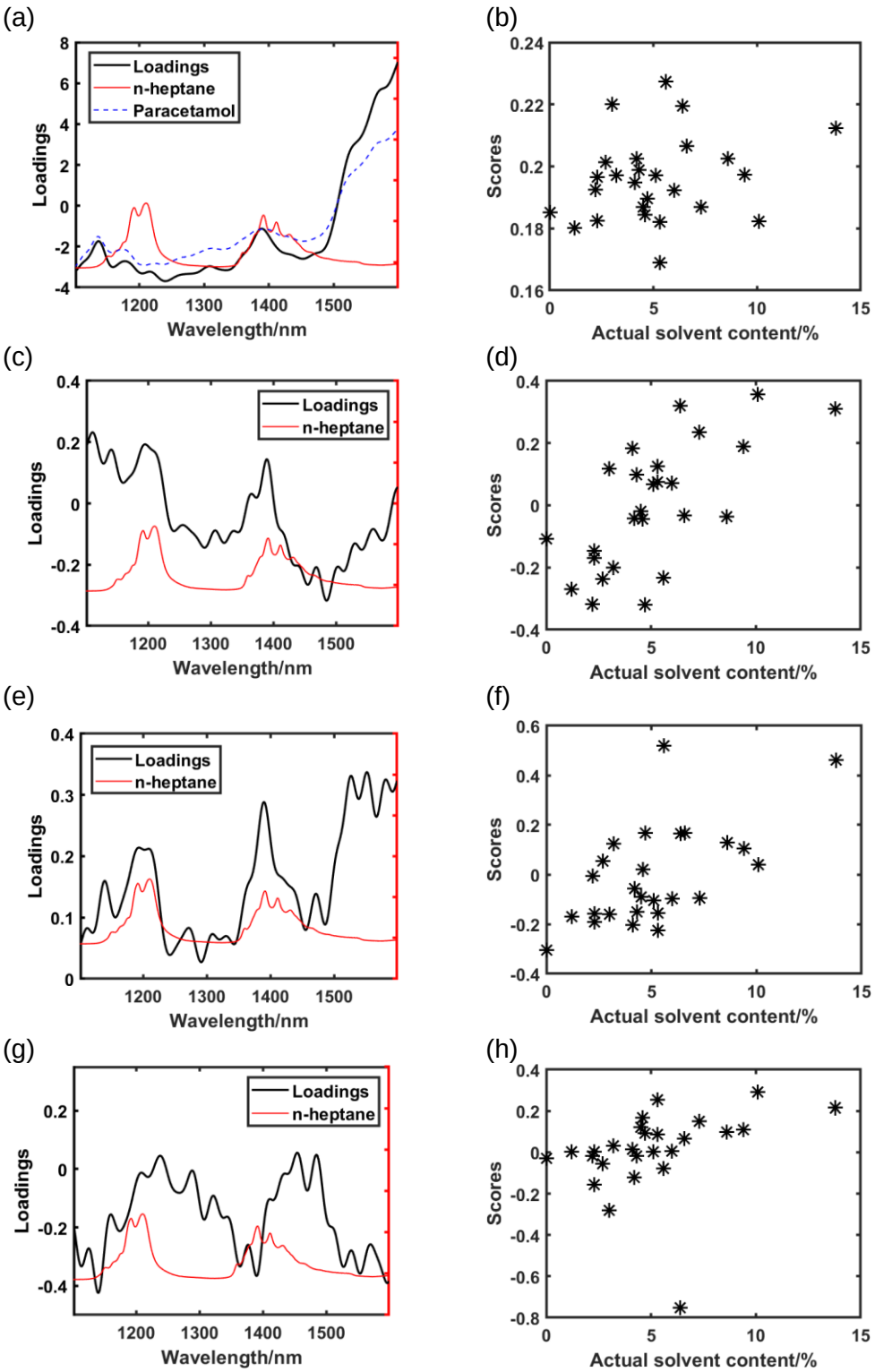

Figure 5.15. (a) loadings and (b) scores plots of LV1, (c) loadings and (d) scores of LV2, (e) loadings and (f) scores of LV3, (g) loadings and (h) scores of LV4 of the PLSR model of SNV pre-processed spectra of 0°/1.2 mm from the granular/n-heptane system. N-heptane pure spectra are also plotted as a reference with the loadings.

5.3.2.1.2 PLSR of combined SAR-DRM spectra

Using individual configuration spectra to build PLSR for the estimation of the solvent content has shown that the performance of those configurations varies, where some configurations of spectra collected from larger distances tend to result in better estimations. To further investigate this, multiple configurations can be combined as this may provide complementary information from the multiple configurations to the PLSR model and improve the estimation. To assess the improvement in model performance from the three angular light sources, SAR-DRM spectra from the three collection distances of 0.6-1.2 mm were combined in order to enrich the PLSR model with features captured from the three angular configurations. Two methods are used for combining the spectra. The first method is augmentation, where blocks of spectra from different configurations are concatenated. The second method is co-addition, where spectra from different configurations are summed up to form one spectrum.

Figure 5.16 shows the RMSECV and RMSEP of the PLSR models resulting from using SAR-DRM spectra individually from each collection distance and for the augmented and co-added spatial spectra from the three light sources. From this figure, PLSR models of spectra from the 0° show lower RMSECV compared to the 30-45° angular configurations, which could be attributed to the stronger signal collected using the 0° light angle compared to the 30-45° angles. Among the three collection distances, 1.2 mm spectra result in lower RMSECV and RMSEP compared to 0.6 mm and 0.9 mm spectra for some of the configurations, but not all of them. However, the qualitative analysis in the previous section 5.3.1 showed that those spectra were most consistent in showing the decrease in solvent peak intensity following the decrease in solvent content. This could be explained by the decrease in signal intensity due to the larger collection distance. Therefore, spectra collected from 0.9 mm and 1.2 mm were thought to be more reliable than spectra from 0.3-0.6 mm. Moreover, the PLSR model of the combined spectra from the three angular configurations shows reduced error for the spectra from the 1.2 mm collection distance, indicating superior PLSR performance to the other distances.

Figure 5.16 shows that when combining the spectra of each of the distances from the three angles, a PLSR model of comparable or lower RMSECV is obtained. Comparing RMSECV of PLSR models of augmented and co-added spectra shows that co-addition led to lower RMSECV, which may be attributed to the improvement in signal-to-noise ratio as the spectra are combined.[14] However, the PLSR model of the augmented spectra from the three angles shows a clear decrease in RMSECV as the collection distance increases, where the RMSECV error value of the PLSR model of the augmented spectra is a value in between that of the individual configurations, but is closer to the lowest value. This observation also suggests that combining those spectra is benefiting the PLSR model since the RMSECV of 1.2 mm augmented and co-added spectra are close values, but the improvement is hindered by the signal quality of the spectra collected from the 30-45° light angles. The RMSEP of the PLSR models of the combined spectra also follows a similar trend to the RMSECV, confirming the trends seen in model performance. The results of the combinations shown in Figure 5.16 suggest that improvement of PLSR models for the estimation of the solvent content can be achieved through combining multiple configurations. Therefore, more combinations of those configurations in PLSR analysis were assessed.

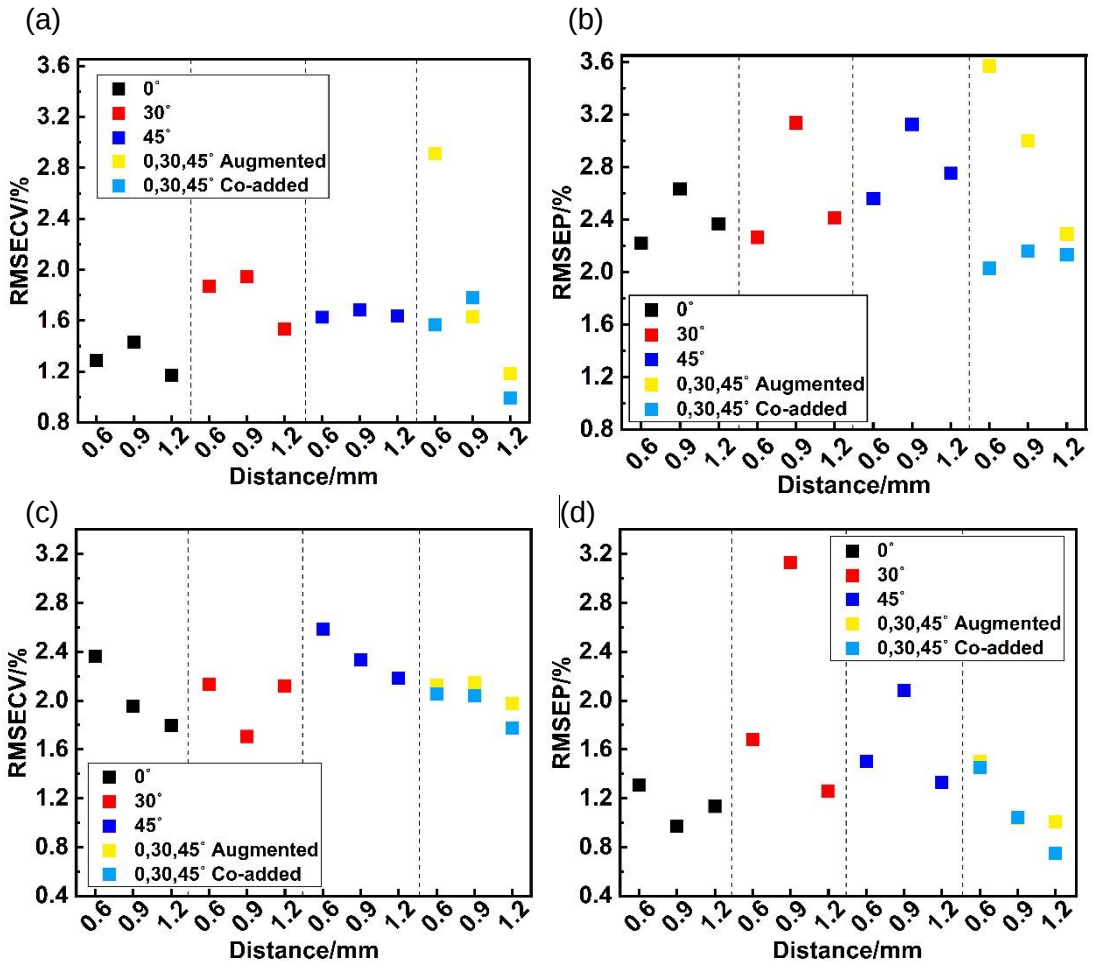

Figure 5.16. (a) RMSECV and (b) RMSEP of PLSR models of SNV pre-processed granular/n-heptane spectra from 0.6-1.2 mm individually and combined from the three light angles and three collection distances. (c) RMSECV and (d) RMSEP of PLSR of the SNV pre-processed granular/MTBE spectra.

The angular/spatial configurations combined and further investigated in PLSR models were spectra with 0°, 30°, and 45° illumination angles and 0.6 mm, 0.9 mm, and 1.2 mm collection, which add up to nine angular/spatial configurations. All possible combinations of those nine configurations result in 502 combinations in PLSR models for each of the two, augmentation and co-addition, combination methods. To compare the PLSR analysis results from those combinations, Figure 5.17 provides a summary of the RMSECV and RMSEP of those PLSR models for the granular/n-heptane system in Figure 5.17 (a) and the granular/MTBE system in Figure 5.17 (b). In this figure, the RMSECV and RMSEP from the PLSR model of the augmented and co-added spectra are provided as box plots, where four boxes are used to summarise

each of the RMSECV and RMSEP of PLSR models of the augmented and co-added spectra. Those box plots show the median, minimum and maximum, the interquartile range, and outliers. To further show the impact of including certain configurations with PLSR models of combined spectra, RMSECV and RMSEP of the models containing those configurations are blotted on top of the boxes.

Comparing the boxes in Figure 5.17 (a) and (b) shows that PLSR models of co-added spectra result in lower RMSECV and RMSEP than those of PLSR models of the augmented spectra. For the granular/n-heptane systems, RMSEP is higher than RMSECV while the opposite is seen for the granular/MTBE system, which may be attributed to the larger number of samples in the granular/MTBE system (39 samples) compared to the granular/n-heptane system (26 samples). This means that the higher number of sample spectra leads to the inclusion of more variation within the calibration set of the granular/MTBE system compared to the granular/n-heptane system leading to the lower RMSEP of the solvent content in the granular/MTBE system. Nevertheless, the calibration sets do sufficiently represent the respective systems and indicate the reliability of those calibration models.

To assess the contribution from specific configurations to the overall level of error, RMSECV and RMSEP of 63 PLSR models that include 0°/1.2 mm spectra are plotted in black, 30°/1.2 mm in red, and 45°/1.2 mm in blue. Among those, RMSECV and RMSEP of PLSR models including 0°/1.2 mm span the lower end of the box plot, which suggests that spectra collected using the 0° result in superior performance and contribute to lowering the RMSECV and RMSEP. Comparing the PLSR of augmented and co-added spectra from those configurations shows that narrower distribution of error among the PLSR models of the co-added spectra compared to the PLSR models of the augmented datasets. This suggests that, by concatenating spectra for augmentation, the resulting PLSR models are more influenced by lower-quality spectra acting as noise compared to co-added spectra, where the overall quality is affected by the contribution of the spectra combined. Since NIR spectra capture the chemical composition and physical features of the samples

that influence the signal as a result of changes in shape, size distribution, and density of the samples,[66] the resulting differences in spectra are less pronounced in co-added spectra due to the averaging of spectral features, whereas those are all included in the augmented spectra. This leads to the higher variability in augmented spectra in addition to the higher complexity of the PLSR models.

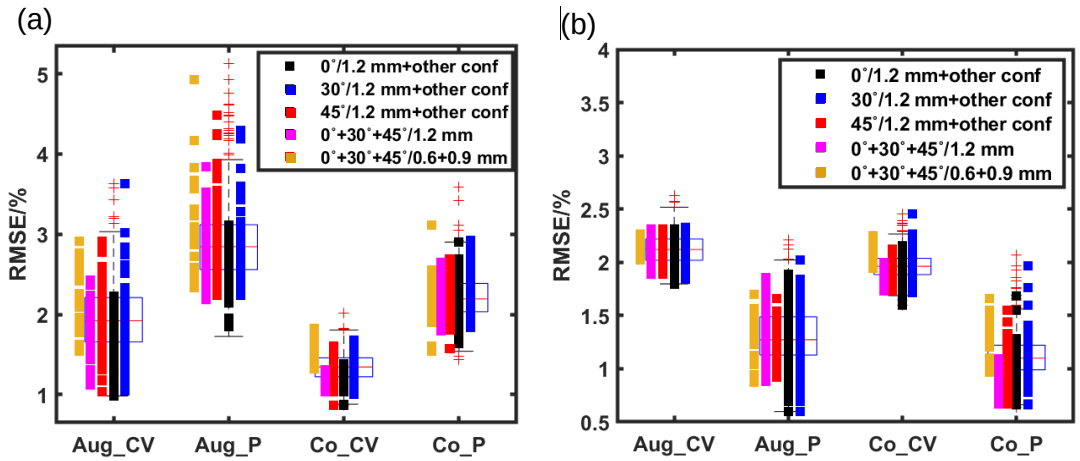

Figure 5.17. RMSECV (CV) and RMSEP (P) of SNV pre-processed spectra combined through augmentation (Aug) and co-addition (Co) from 0-45°/0.6-1.2 mm configurations (conf) from (a) granular/n-heptane and (b) granular/MTBE systems

The main focus in Figure 5.17 was the evaluation of the three incidence angles to the performance of the combined spectra and the next step is assessing the changes in the performance of the PLSR models including the combined spectra from each of the collection distances in addition to the variability between RMSECV and RMSEP. The relation between the RMSECV and RMSEP resulting from the 502 combinations of SAR-DRM spectra is shown in Figure 5.18, in which the RMSECV versus RMSEP are plotted for all combinations of co-added spectra from Figure 5.17. The RMSECV and RMSEP of the PLSR models including spectra from 0° from each of the three collection distances in addition to SAR-DRM spectra from other configurations are highlighted to show the decrease in RMSECV and RMSEP values as the collection distance increases. The difference in the diagonal patterns seen in Figure 5.18 (a) and (b) is attributed to the higher RMSEP compared to

RMSECV for the granular/n-heptane system and lower RMSEP compared to RMSECV for the granular/MTBE system as highlighted earlier. As a close reference to the conventional diffuse reflectance NIR measurements, the RMSECV and RMSEP of 0°/0.3 mm are also shown in this figure and are in contrast to the PLSR models of the other SAR-DRM configurations as they show the highest RMSE. Those observations can similarly be seen for both granular/solvent systems.

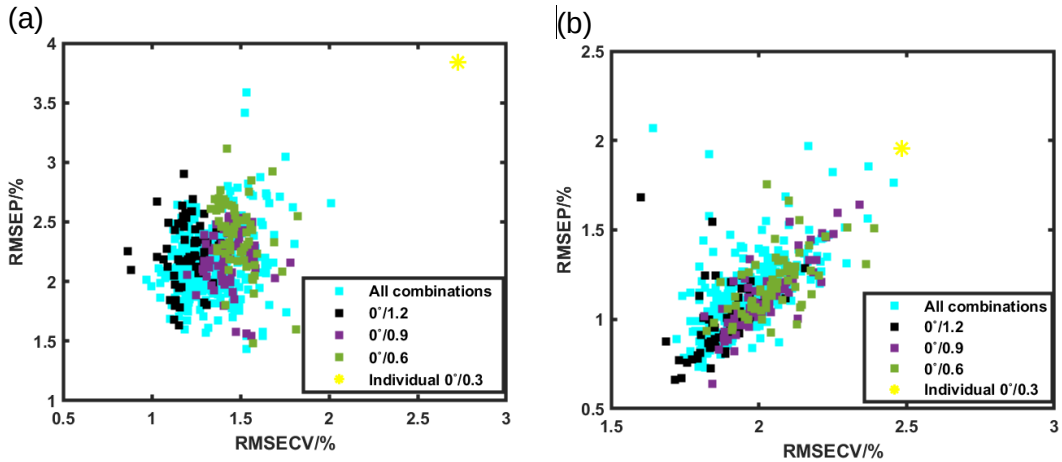

Figure 5.18. RMSECV versus RMSEP of PLSR models of co-added SNV pre-processed SAR-DRM spectra from (a) granular/n-heptane and (b) granular/MTBE systems.

To further compare the results from the PLSR model of the individual SNV pre-processed spectra 0°/0.3 mm to the co-added spectra of 1.2 mm from the three angular configurations, estimations of the solvent content during the runs were plotted. The actual solvent content in one of the runs shown previously in Figure 5.3 obtained from the reference loss on drying method is shown along with those of the estimated content from the PLSR model of SNV pre-processed spectra from 1.2 mm from the three angular configurations and 0°/0.3 mm in Figure 5.19. This figure shows the drying profile obtained from the estimation based on spectra from the 1.2 mm collection distance is close to that obtained from the reference measurement, while estimations base on spectra from 0°/0.3 mm led to higher error. The differences found between the LOD and the estimations based on 1.2 mm from the three angular

configurations could arise from the representativeness of the calibration set spectra, the errors in sampling and measuring the LOD. However, the higher error seen for the estimation from 0°/0.3 mm can be attributed to the representativeness of the samples from those spectra considering the volume of the sample and the depths travelled by the light before being collected at 0.3 mm distance from the incidence point compared to that collected from 1.2 mm distance.

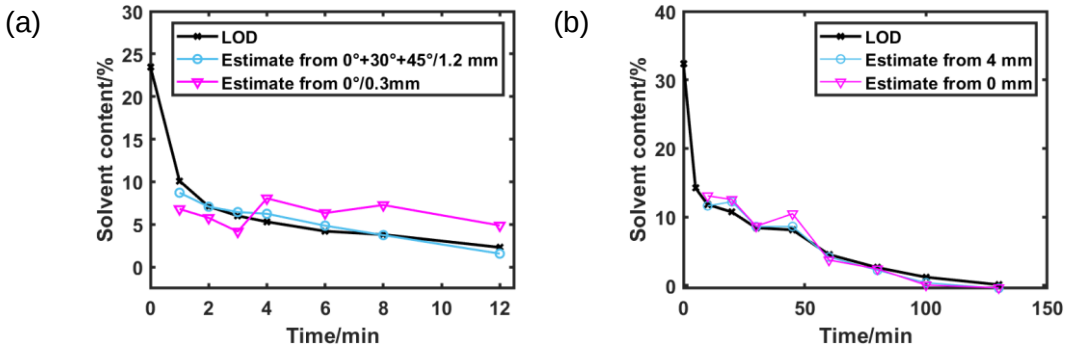

Figure 5.19. Solvent content from LOD and estimates from PLSR models of co-added SNV pre-processed SAR-DRM spectra of 1.2 mm from the three incidence angles and of 0°/0.3 mm from (a) granular/n-heptane and (b) granular/MTBE systems.

5.3.2.2 Powder paracetamol systems

Spectra collected from the two powder/solvent systems from each of the SAR-DRM individual configurations are used to construct PLSR models. Then, SAR-DRM spectra from multiple configurations are combined to assess any improvement in PLSR model performance. The performance of the PLSR models of the powder systems reported here is compared to that of the granular systems reported in the previous section 5.3.2.1.

5.3.2.2.1 PLSR of individual SAR-DRM spectra

PLSR models using spectra from the 12 SAR-DRM configurations were built, where some sample spectra were included in the calibration set and the remaining spectra were used as a test set as previously described in section 4.5.

The RMSECV curves of the PLSR models of the calibration set are shown in Figure 5.20, where the curves of the powder/n-heptane system are shown in Figure 5.20 (a-c) of the powder/n-heptane system and in (d-f) of the powder/MTBE system for the three light angles 0°, 30°, and 45°, respectively. Those RMSECV curves were inspected to select the number of latent variables from each of the configurations for each of the systems, where the curves of raw and pre-processed spectra from the four spatial distances show that the RMSECV is highest for 0.3 mm spectra and decreases as the collection distance increases. This can be seen in spectra collected from all three light angles. Comparing Figure 5.20 (a), (b), and (c) shows that the RMSECV of the 0° illumination angle shows the lowest RMSECV compared to 30-45°, both of which are comparable. This is also seen in Figure 5.20 (d), (e), and (f), where the 0° spectra are of lower RMSECV and RMSEP than those of 30-45°. However, large differences between the RMSECV for each collection distance are seen for spectra with the 30° light source angle. This may be explained by the larger variation in the quality of spectra from each of the collection distances, as seen previously in Figure 5.8 and Figure 5.9 in section 5.3.1.2.

Following SNV pre-processing, RMSECV curves are similar or slightly lower than those of the raw spectra. This suggests that the baseline shifts observed in Figure 5.8 and Figure 5.9 may not have a major contribution to the error in PLSR models of the powder/solvent systems and do provide some variation related to the sample condition as was also seen in the granular/solvent systems.[8,114] Compared to the RMSECV curves of the granular systems in Figure 5.12, the curves of the powder systems in Figure 5.20 show overall higher RMSECV.

RMSECV curves of spectra from the 30°-45° light angles similarly show the decrease in RMSECV as the spatial distance increases. Nevertheless, the decrease is smaller compared to that seen in Figure 5.12 of the granular systems. This may be explained by the lower quality of spectra and larger effect of noise seen from the powder paracetamol grade as seen in Figure 5.8 and Figure 5.9 of the raw spectra and Figure 5.10 and Figure 5.11 of the SNV pre-processed spectra.

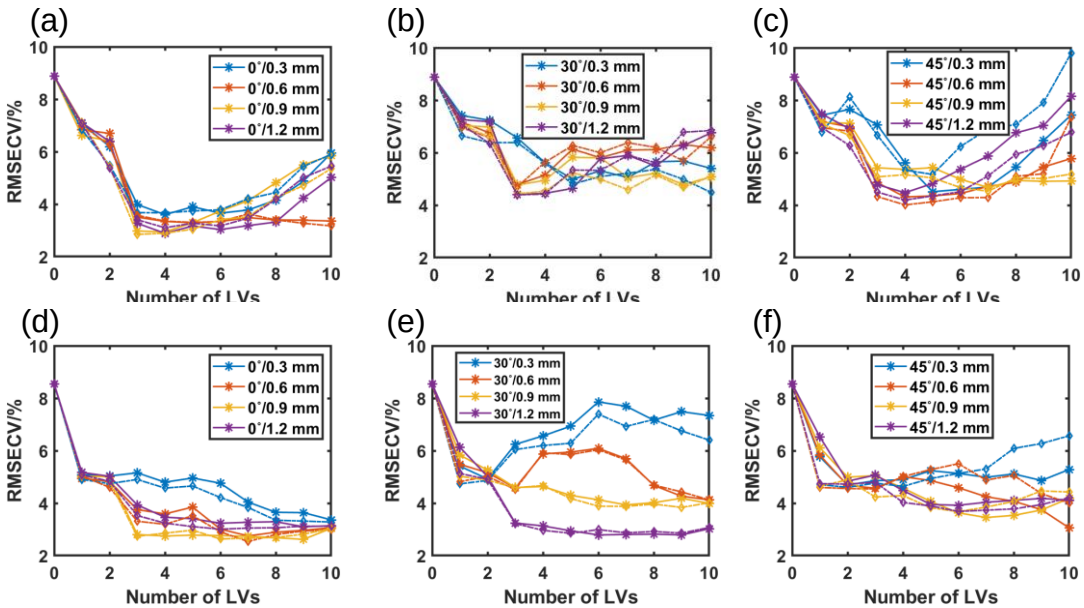

Figure 5.20. RMSECV of PLSR models constructed from raw (solid) and SNV pre-processed spectra (dashed) from (a) 0°, (b) 30°, and (c) 45° for 0.3-1.2 mm collected from powder/n-heptane and (d) 0°, (e) 30°, and (f) 45° for 0.3-1.2 mm collected from powder/MTBE.

The number of latent variables selected based on the RMSECV curves in Figure 5.20 for PLSR models of both systems range between 2-8 LVs. Table 5.2 contains a summary of the PLSR models. The lower number of latent variables, 2 LVs, is seen for the 30°-45°/ 0.3 mm spectra of the powder/MTBE system, which were the spectra of lower quality in Figure 5.9 and Figure 5.11. This suggests that the lower RMSECV of the PLSR models of those spectra may be a result of the exclusion of random variation resulting from noise. The similar number of latent variables in modelling the raw and pre-processed spectra suggests that the factors largely contributing to the PLSR performance remain similar.

Looking at the error values obtained from raw SAR-DRM spectra, the RMSECV decreases as the collection distance increases from the two powder/solvent systems. This decrease in error is associated with an increase in the coefficient of determination, R^2, suggesting an improvement in the model performance since the variation captured in the PLSR model of the signal is more linearly related. For the powder/n-heptane system, there is 20% decrease in the RMSECV of the PLSR model of 0°/1.2 mm spectra compared to the 0°/0.3 mm spectra, 12% decrease in RMSECV of the PLSR model of 30°/1.2 mm spectra compared to 30°/0.3 mm spectra, and 1% decrease in RMSECV of the PLSR model 45°/1.2 mm spectra compared to the 45°/0.3 mm spectra. This larger percentage of decrease in RMSECV for the PLSR model of 0°/1.2 mm spectra compared to the 30°/1.2 mm spectra and 45°/1.2 mm spectra was also observed in the granular/n-heptane system. For the granular/MTBE system, an 11% decrease is seen for the RMSECV of the PLSR model of the 0°/1.2 mm spectra compared to the 0°/0.3 mm spectra, 43% decrease in RMSECV of the PLSR model of 30°/1.2 mm spectra compared to 30°/0.3 mm spectra, and 16% decrease in RMSECV of the PLSR model of the 45°/1.2 mm spectra compared to the 45°/0.3 mm spectra. Although the larger percentage of decrease in the RMSECV of the PLSR model of 30°/1.2 mm spectra compared to 30°/0.3 mm spectra might suggest an improved performance for the PLSR of the 30°/1.2 mm configuration, the apparent higher percentage of decrease is due to the poor performance of the

PLSE model of the 30°/0.3 mm configuration. A similar percentage of improvement for the 0°/1.2 mm spectra compared to the 0°/0.3 mm spectra and the 45°/1.2 mm spectra compared to the 45°/0.3 mm spectra was also seen in the granular/MTBE system. This suggests that the overlap in the peak of paracetamol and MTBE similarly affects the PLSR performance of the powder/MTBE system. The RMSEP of the PLSR models of the raw spectra follows the same trend as the RMSECV, indicating the reliability of the calibration models. Comparing RMSECV and RMSEP of SAR-DRM spectra collected from the same distance from each of the illumination angles, those errors are lower for the 0° angle spectra as opposed to 30-45° spectra.

For the SNV pre-processed spectra, as the collection distance increases RMSECV of the PLSR models decreases while R^2 values increase. For the pre-processed granular/n-heptane spectra, there is a 16% decrease in RMSECV of the PLSR model of the 0°/1.2 mm spectra compared to the 0°/0.3 mm spectra, 9% decrease in RMSECV of the PLSR model of 30°/1.2 mm spectra compared to 30°/0.3 mm spectra, and 13% in RMSECV of the PLSR model of the 45°/1.2 mm spectra compared to the 45°/0.3 mm spectra. For the granular/MTBE system, 10% decrease is seen in RMSECV of the PLSR model of the 0°/1.2 mm spectra compared to the 0°/0.3 mm spectra, 41% decrease in RMSECV of the PLSR model of 30°/1.2 mm spectra compared to 30°/0.3 mm spectra, and 20% decrease in RMSECV of the PLSR model of the 45°/1.2 mm spectra compared to the 45°/0.3 mm spectra. Compared to the granular/solvent, those values are smaller, suggesting that the higher level of noise seen in the powder systems affects the improvement in the PLSR performance.

Comparison between the PLSR results of the raw and SNV pre-processed SAR-DRM spectra shows that the error values of pre-processed spectra are either similar or decrease slightly. The increase in error following SNV pre-processing is seen for the closest collection distance, 0.3 mm, suggesting that due to the lower signal quality obtained from this detector, the physical effects removed by pre-processing contribute to the PLSR model performance. The RMSEP of the PLSR of the SNV pre-processed spectra follows a similar trend

to the RMSECV indicating a robust performance of the PLSR of those calibration sets.

Overall, the PLSR results shown in Table 5.2 look to be most influenced by the signal, as seen in the 1.2 mm spectra performing more reliably, along with signal intensity, as is seen when comparing the signal collected through the 0° light illumination angle compared to the 30-45° angles, in addition to some effect of physical phenomena as seen from the slight performance variation following pre-processing. Since qualitative analysis seen from section 5.3.1.2 showed that spectra from 1.2 mm follow the decrease in intensity as the solvent content decreases, the similarity in performance from 0.3 and 1.2 mm PLSR models seen in the powder/n-heptane system is attributed to the random noise, despite the similarity in the number of LVs.

Table 5.2. Summary of PLSR model performance of raw and SNV pre-processed spectra of powder paracetamol in n-heptane and MTBE from each of the angular/spatial configurations.

Grade/Solvent	Angle	Distance/mm	Raw				SNV pre-processed			
			LV	RMSE CV/%	RMSE P/%	R^2	LV	RMSE CV/%	RMSE P/%	R^2
Powder/n-heptane	0°	**0.3**	4	3.60	2.82	0.71	3	3.68	3.40	0.69
		0.6	4	3.34	3.33	0.75	4	3.35	3.20	0.75
		0.9	3	2.98	3.05	0.80	3	2.85	2.54	0.82
		1.2	4	2.89	2.35	0.81	4	3.10	2.20	0.78
	30°	**0.3**	5	4.99	2.53	0.47	5	4.81	2.13	0.50
		0.6	3	4.79	4.46	0.48	3	4.70	4.01	0.50
		0.9	3	4.77	3.84	0.50	3	4.44	3.71	0.56
		1.2	3	4.40	3.97	0.57	3	4.39	3.94	0.57
	45°	**0.3**	5	4.51	4.25	0.55	5	5.17	4.40	0.47
		0.6	4	4.31	2.93	0.58	4	4.01	2.99	0.64
		0.9	7	4.68	7.45	0.54	7	4.53	7.31	0.57
		1.2	4	4.47	3.60	0.56	4	4.19	4.19	0.60
Powder/MTBE	0°	**0.3**	8	3.65	2.92	0.47	8	3.35	2.86	0.52
		0.6	7	2.75	2.31	0.68	7	2.54	2.41	0.72
		0.9	4	2.75	2.70	0.68	6	2.63	2.22	0.72
		1.2	6	3.24	3.11	0.58	6	3.01	2.64	0.63
	30°	**0.3**	2	4.92	5.16	0.00	2	4.87	5.28	0.02
		0.6	3	4.59	4.50	0.15	3	4.52	4.31	0.16
		0.9	7	3.94	3.80	0.42	6	3.88	3.39	0.45
		1.2	6	2.79	3.92	0.67	5	2.85	3.35	0.66
	45°	**0.3**	2	4.69	5.90	0.04	2	4.61	5.98	0.08
		0.6	3	4.57	5.30	0.13	3	4.54	5.25	0.14
		0.9	7	3.45	3.93	0.53	6	3.68	3.73	0.47
		1.2	5	3.95	3.01	0.38	6	3.69	3.03	0.45

To further assess the difference in PLSR performance of spectra from 0°/0.3 mm and 0°/1.2 mm, the regression and residuals plots of PLSR models of SNV pre-processed powder/MTBE spectra, as an example, from 0°/0.3 mm in Figure 5.18 (a-b) and from 0°/1.2 mm in Figure 5.18 (c-d). The regression and residuals plots in Figure 5.18 (a-b), respectively show that, although the predicted solvent is closer to the actual values in the lower solvent content range of 0-5%, higher error in the predicted solvent content is seen for the higher solvent content 15-20% spectra. Figure 5.18 (c-d) shows that the error in prediction is relatively consistent across the solvent content range. The differences in Figure 5.18 (a-b) and (c-d) show that, despite the close values between PLSR of pre-processed 0°/0.3 mm (RMSECV of 3.68% and R^2 of 0.69) and 0°/1.2 mm spectra (RMSECV of 3.10% and R^2 of 0.78), the predictions of the PLSR model of the 0°/1.2 mm spectra are more consistent, suggesting a more robust PLSR model.

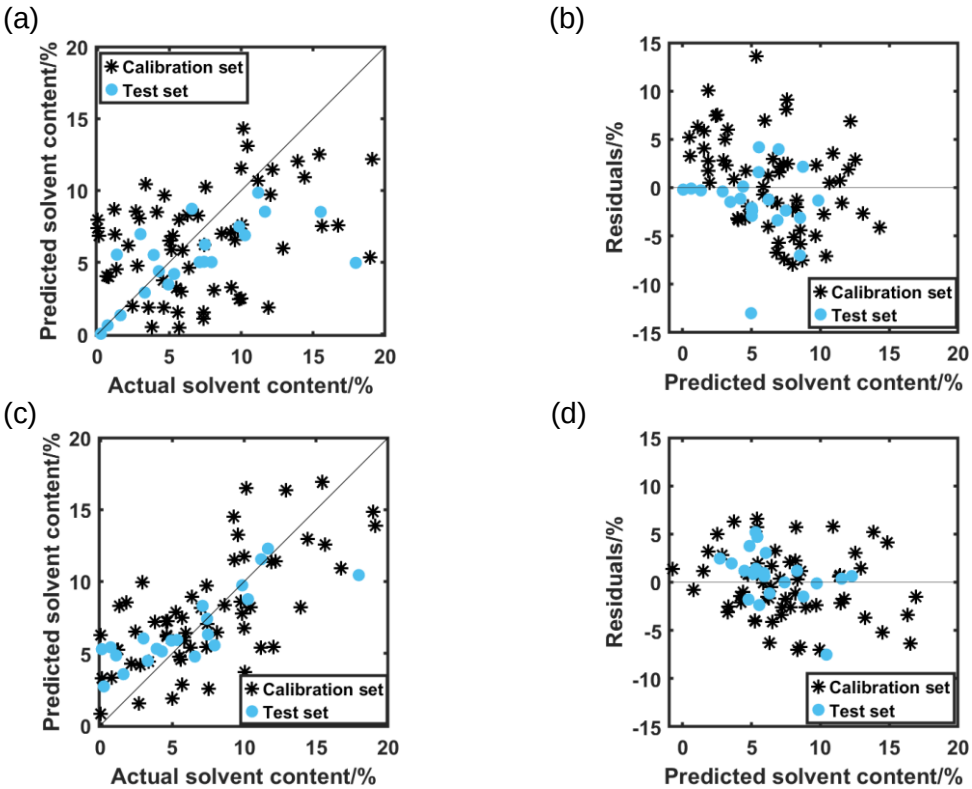

Figure 5.21. (a) Regression and (b) residuals plots of the PLSR model of SNV pre-processed spectra of 0°/0.3 mm from the powder/MTBE system. (c) Regression and (d) residuals plots of the PLSR model of SNV pre-processed spectra of 0°/1.2 mm from the powder/MTBE system.

5.3.2.2.2 PLSR of combined SAR-DRM spectra

Results from the analysis of the PLSR performance in the previous section generally indicate the improvement of the performance of the SAR-DRM spectra as the collection distance increases. However, some of the spectra do not show the same decrease in error as the collection distance increases. Therefore, spectra from the three incident lights of the same collection distance were combined through augmentation and co-addition and analysed. This would allow for a more thorough investigation of including specific or multiple configurations on the PLSR performance.

Figure 5.22 shows a comparison of the RMSECV and RMSEP of the PLSR models of SNV pre-processed spectra from the individual configuration as well as the combined configurations from the three light sources. This figure allows for the visualisation of the variation of the PLSR model error among those configurations. For the PLSR model results of the powder/n-heptane in Figure 5.22 (a-b), RMSECV slightly improves or is at a similar level as the collection distance increases for spectra of 0.6-1.2 mm. The RMSEP slightly decreases as the offset distance increases from 0.9 to 1.2 mm for 0° and 45° spectra suggesting a more robust performance of PLSR models of those configurations. As for the combined spectra, RMSECV and RMSEP look to be a value close to the average of the RMSECV and RMSEP of the spatial configuration from the three incidence angles, where co-added spectra show lower error than the augmented spectra. For the powder/MTBE spectra in Figure 5.22 (c-d), RMSECV decreases as the collection distance increases for the 30° incidence angle spectra, while for RMSEP this is seen with 30-45° spectra. The combined spatial configurations from the three angles also show RMSECV lower than the individual 30-45°, but higher than that of 0° for the augmented and co-added configurations, where those co-added spectra show lower error compared to augmented spectra. RMSEP of combined spectra decreases as the collection distance increases and is also a value lower than that of 30-45° and higher than 0°, with co-added spectra being only slightly lower than augmented spectra. The lower error values for the co-added

spectra in both systems are explained by the improvement in signal-to-noise ratio as a result of the summation of the spectra.

The RMSECV and RMSEP of the PLSR of individual SAR-DRM spectra as well as the combined spectra, shown in Figure 5.22, do not clearly reflect the improvement in peak resolution seen from the spectra collected from larger distances as was seen in the qualitative analysis of the spectra in Figure 5.10 and Figure 5.11. Therefore, further multi-block analysis could show a clearer indication of the improvement in the performance from the spectra from larger collection distance configurations.

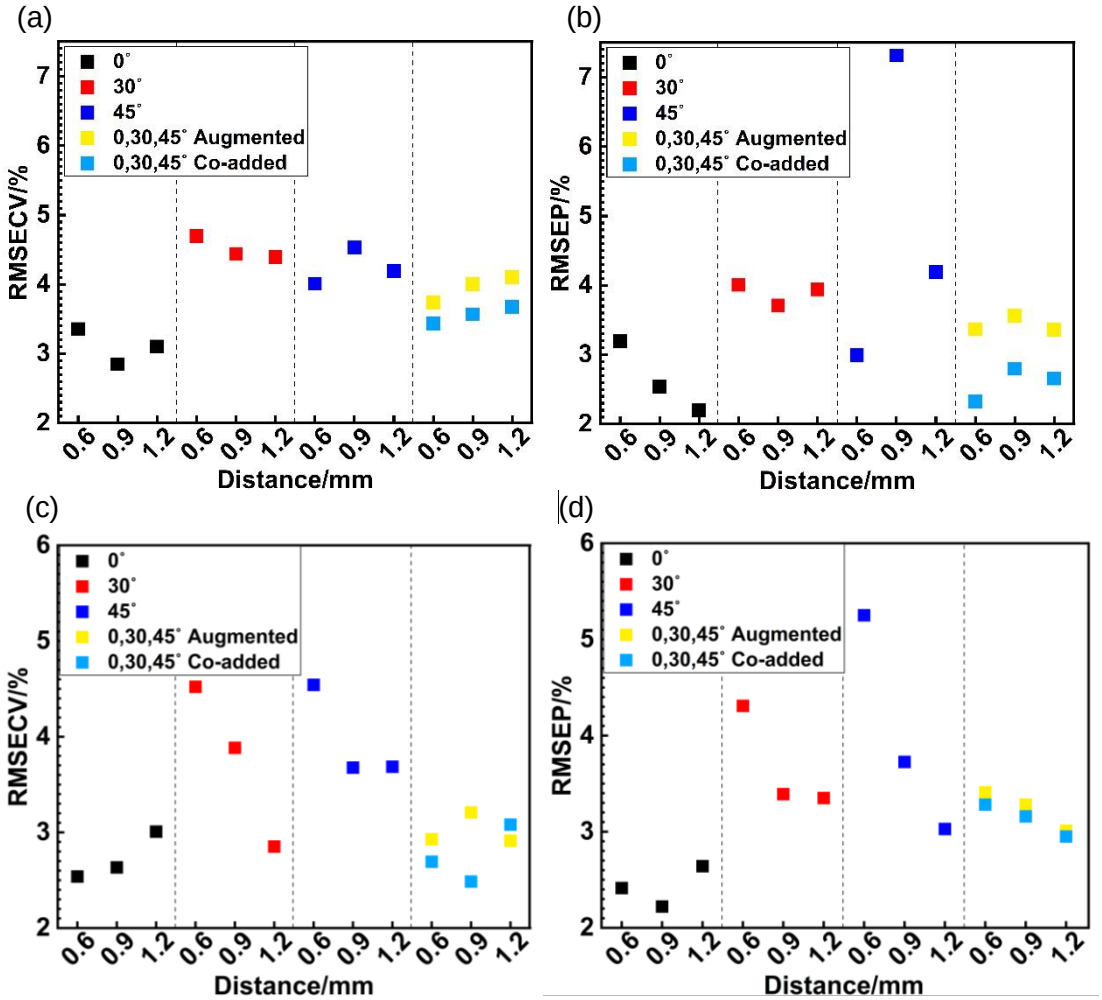

Figure 5.22. (a) RMSECV and (b) RMSEP of PLSR models of the SNV pre-processed powder/n-heptane spectra from 0.6-1.2 mm individually and combined from the three light angles and three collection distances. (c) RMSECV and (d) RMSEP of PLSR of SNV pre-processed powder/MTBE spectra.

In order to assess the performance of the different SAR-DRM spectra, the nine configurations from Figure 5.22 spectra were combined in multi-block PLSR models considering all possible combinations of those configurations. The RMSECV and RMSEP of the PLSR models of those combined configurations add up to 502 combinations and are shown as box plots in Figure 5.23 (a) for the powder/n-heptane system and Figure 5.23 (b) for the powder/MTBE system. The first observation from Figure 5.23 is the higher level of error seen for the augmented spectra compared to the co-added spectra, similar to what was seen in the granular/solvent systems in Figure 5.17.

In order to assess the contribution of spectra from each of the angular light sources to the PLSR model error, PLSR models of combinations including 1.2 mm collection distance from one of the incidence angles in addition to any other configuration from the other two incidence angles are highlighted in Figure 5.23. Those correspond to 63 combinations for each incidence angle and are highlighted in black for 0°, blue for 30°, and red for 45°. Among PLSR models of augmented combinations of spectra from those three angles only, the RMSECV and RMSEP of PLR models containing 0°/1.2 mm configuration are less spread and are at the lower end of the box, while the RMSECV and RMSEP of combinations of 30°/1.2 mm and 45°/1.2 mm with other configurations show wider distribution around the mean of the error compared to combinations of configurations with 0°/1.2 mm. Considering the co-added combination on the right side of the graphs in Figure 5.23, RMSECV and RMSEP of the three sets of combinations show less spread and a lower mean of error compared to the augmented configurations. This variation in the spread of error may be attributed to the mechanism of each of the combination techniques, where each of the combined spectra equally contributes to the performance of the final block in PLSR analysis in augmentation while the final spectrum in co-addition is an average of the combined configurations.

To further compare spectra containing other spatial/angular configurations with the three sets mentioned earlier, 65 combinations including 1.2 mm from the three incidence angles are also shown in Figure 5.23 as magenta markers. For both augmented and co-added combinations, the spread of the RMSECV and

RMSEP of those combinations is narrower compared to the three sets highlighted earlier but is not lower than any of the three sets. However, the lack of improvement in this set of combinations from the three incidence angles is attributed to the contribution of the spectra from 30-45°, as was seen in Figure 5.11 and Figure 5.22.

To contrast the result seen from the four previous sets of combinations focused on the 1.2 mm collection distance, 27 combinations that include 0.6-0.9 mm spectra from the three incidence angles are also highlighted in yellow in Figure 5.23, where those show wider spread and higher error for augmented spectra compared to the co-added spectra for the same reasons as those of the other three sets of combinations. Nevertheless, this set of combinations of spectra from 0.6-0.9 mm from the three incidence angles shows a lower level of RMSECV and RMSEP compared to the other sets of co-added combinations in Figure 5.23 (a), but not in Figure 5.23 (b). This may be a result of the improvement in the quality of spectra in both systems. Figure 5.23 (b) shows that the overall level of error from the powder/MTBE system is lower than that of the powder/n-heptane, which is a result of the larger number of sample spectra representing the system included in the calibration set of the powder/MTBE system as mentioned in section 4.4.1. The observations from the powder/n-heptane system are similarly seen for the powder/MTBE system. However, the improvement in the powder/n-heptane in Figure 5.23 (a) compared to Figure 5.23 (b) may be attributed to the presence of a non-overlapping peak in n-heptane, whereas the MTBE peak is largely overlapped with that of paracetamol around 1150-1200 nm.

Figure 5.23 (a) of the powder/n-heptane system shows that the level of RMSEP is lower than that of the RMSECV, while Figure 5.23 (b) of the powder/MTBE system shows that the RMSEP is lower than the RMSECV. This is opposite to what was seen for the granular systems in Figure 5.17 and is explained by the spread of the sample spectra collected over the solvent content range as was shown in the drying profile in Figure 5.3. Although a larger number of sample spectra were included in the calibration set of the powder/MTBE system compared to the powder n-heptane system, the MTBE

calibration set contains more sample spectra over the solvent content range of 0-15% as opposed to the powder/n-heptane samples which are more equally distributed. This was also shown in regression and residuals plots example in Figure 5.21.

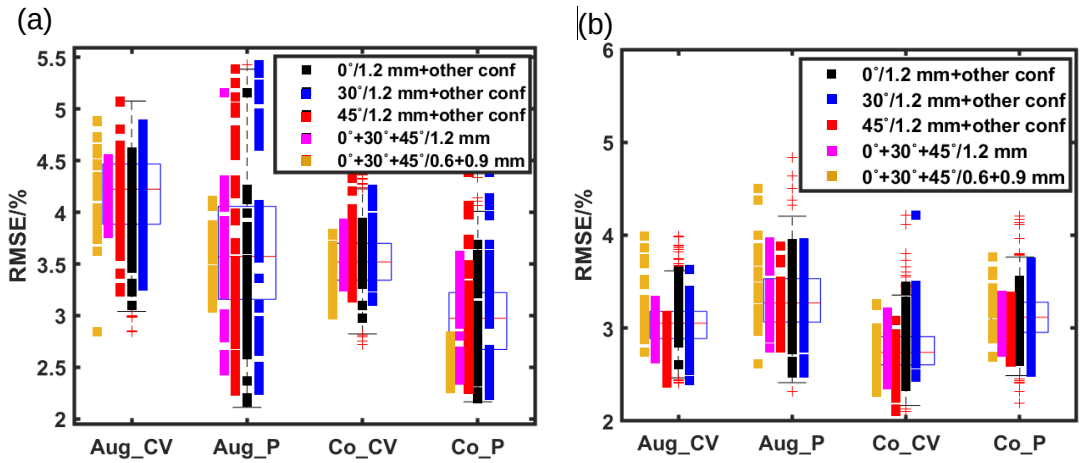

Figure 5.23. RMSECV (CV) and RMSEP (P) of SNV pre-processed spectra combined through augmentation (Aug) and co-addition (Co) from 0-45°/0.6-1.2 mm configurations (conf) from (a).powder/n-heptane and (b) powder/MTBE systems

The previous figure focusses on the analysis of the contribution of each of the incidence angles to the performance of each of the combined sets. In order to further assess the contribution from each of the collection angles, combinations of spectra including spectra from each of the collection distances from 0° incidence angles, in addition to combinations of any other configurations. The consistency in the RMSECV and RMSEP resulting from the 502 combination of SAR-DRM spectra may also be seen in Figure 5.24, in which the RMSECV and RMSEP are plotted for all combinations of co-added spectra from Figure 5.23. In contrast to the RMSECV and RMSEP of the PLSR models including spectra from 0° from each of the three collection distances in addition to SAR-DRM spectra from other configurations seen in the granular/solvent systems in Figure 5.18, RMSECV and RMSEP of the powder/solvent systems in Figure 5.24 do not decrease as the collection distance increases. This suggests that, with reference to the particle size of the material, PLSR models including different spatial/angular configurations

may result in more accurate estimations of the solvent content. This may also be related to the variation in the quality of spectra and performance of the individual models seen previously in Figure 5.10, Figure 5.11, and Table 5.2.

The overlap seen in the RMSECV and RMSEP from each of the combinations in Figure 5.24 may be a result of the balancing out of the contribution of the spectra of good quality from 0° incidence angle with spectra from variable quality from the other configurations. As a reference to the conventional diffuse reflectance NIR measurements, the RMSECV and RMSEP of 0°/0.3 mm are also shown and marked by a yellow asterisk in this figure and shows that RMSECV and RMSEP similar to the other combined configurations, but is not superior to the individual nor the combined spectra.

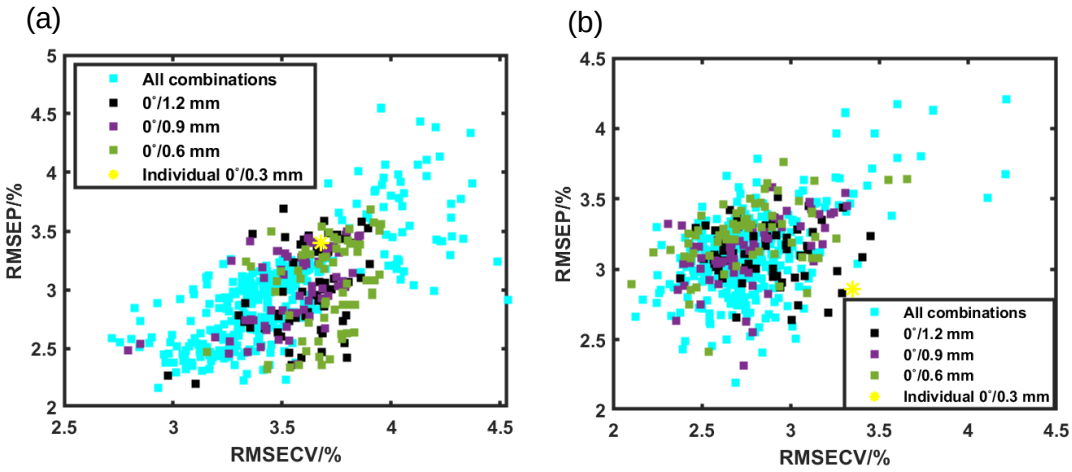

Figure 5.24. RMSECV versus RMSEP of the PLSR model of the co-added SNV pre-processed SAR-DRM spectra from (a) powder/n-heptane and (b) powder/MTBE systems.

5.4 Conclusions

An experiment was conducted to determine the depth through which the signal from a solvent, n-heptane, may be detected beneath layers of dry granular paracetamol, using SAR-DRM spectra collected with the bespoke SAR-DRM probe. The resulting SAR-DRM spectra from the twelve configurations did not show the characteristic peak of the solvent. This may be overcome by using a stronger light source to improve the signal intensity.

SAR-DRM spectra were collected during the drying of two paracetamol grades, granular and powder, in two solvents, n-heptane and MTBE. The spectra from the four systems were analysed qualitatively and quantitatively. Qualitative analysis of raw spectra showed that the visual detection of the variation in the solvent characteristic peak was hindered due to the baseline shifts among spectra collected at different time points. This baseline shift was attributed to the change in packing density and was removed by applying SNV pre-processing. Qualitative analysis of SNV pre-processed spectra showed that the detection of the decrease in the solvent peak as the solvent content decreases may be seen most clearly from the farthest collection distance 1.2 mm from the three illumination angles, which was attributed to the larger distance travelled by light through the wet paracetamol cake before being collected at the farther collection distance; thus including more contribution of the signal from the solvent. Spectra of configurations illuminated through the 0° incidence angle have shown superior quality compared to those illuminated through the 30° and 45°, which was explained by the stronger signal from those spectra.

Quantitative analysis of the individual raw SAR-DRM spectra collected during the drying of the two paracetamol grades showed improved PLSR performance as the collection distance increases to 1.2 mm. This was seen through the slight decrease in the RMSECV and increase in the coefficient of determination, R^2, along with the decrease in the RMSEP. Among the three illumination angles, spectra illuminated through the 0° incidence angle showed improved performance compared to the 30° and 45° incidence angles,

agreeing with the qualitative analysis. Following pre-processing, slight improvement was seen in the PLSR performance, suggesting that the physical effects removed through pre-processing contribute to the PLSR performance.

Since PLSR analysis of SAR-DRM spectra showed a slight improvement in performance, all combinations of 0.6-1.2 mm spectra from the three angular configurations were augmented and co-added to obtain a collective trend of the PLSR performance of these configurations. This was beneficial for determining better-performing spatial and angular configurations. Results of the combined configurations of paracetamol/solvent systems showed that combinations including 1.2 mm spectra result in lower RMSECV and RMSEP followed by 0.9 mm then 0.6 mm spectra, affirming the qualitative results where the quality of spectra improved as the collection distance increased. SAR-DRM spectra illuminated through the 0° angle light source had more contribution to lowering the RMSECV compared to 30° and 45° illumination angles, which was further confirmed through the RMSEP.

Overall, observation from the results obtained from the analysis of SAR-DRM spectra collected during the drying of the granular and powder paracetamol in n-heptane and MTBE show potential for the application of this technique for in-line monitoring or pharmaceutical drying. Considering the signal collected from the 0°/0.3 mm as a representation of the signal collected from a conventional NIR system, the results presented in this chapter show superior performance by the spatially resolved configurations. However, the issue of low signal intensity may be addressed through the use of an illumination source of stronger intensity. Although further development is required before acceptable ranges of error for the estimations are obtained for the reliable determination of the end point, this technique offers an in-line alternative for monitoring the drying process.

6. Spatially Offset Raman Spectroscopy for Monitoring Pharmaceutical Drying

6.1 Introduction

In spatially offset Raman spectroscopy (SORS), Raman signals are collected from distances laterally offset from the illumination point as opposed to conventional Raman spectroscopy, where the backscattering signal is collected. SORS measurements depict spectral features of the sublayers in addition to the surface of the measured area. This offers an advantage when the measured system is non-homogeneous as it enables probing a larger volume of the sample beneath the surface. Pharmaceutical drying is an example of a non-homogenous system that has previously been monitored using conventional Raman spectroscopy. This study details the application of SORS for the monitoring of pharmaceutical drying of paracetamol.

The first part of this chapter includes an experiment conducted in order to assess the depth through which the sublayer signal from a solvent can be detected beyond a barrier of dry paracetamol. In the second part, SORS was employed for the monitoring of pharmaceutical drying of two grades, granular and powder, of paracetamol in two solvents, anisole and MTBE. The SORS spectral response in each of the drying systems is analysed to assess the advantage of applying SORS for the monitoring of drying. Partial least squares regression analysis is applied for the estimation of the solvent content based on SORS spectra. The effect of pre-processing, spectral range selection, and combining configurations in PLSR are also explored.

6.2 Depth of solvent signal detection using SORS

SORS was applied to assess the depth through which the signal from a solvent can be detected underneath dry API as described in section 4.3.1. In this experiment, signals from ten thicknesses of paracetamol over an anisole-filled cuvette were collected. SORS and backscattering spectra were assessed to detect the anisole peak through each of the paracetamol thicknesses. Figure 6.1 shows raw SORS spectra of the various depths of paracetamol over the anisole cuvette obtained from the 2 mm collection offset as an example, where paracetamol peaks can be seen. The inset in Figure 6.1 shows a zoom-in over the wavenumber range in which the change in peak intensity due to the signal from anisole around 1000 cm^{-1} might be seen. Nevertheless, baseline shifts prevent the clear visualisation of the change in solvent peak intensity. Those baseline shifts arise from the different travelling paths of photons in the raw spectra. Therefore, baseline subtraction was applied to the spectra.

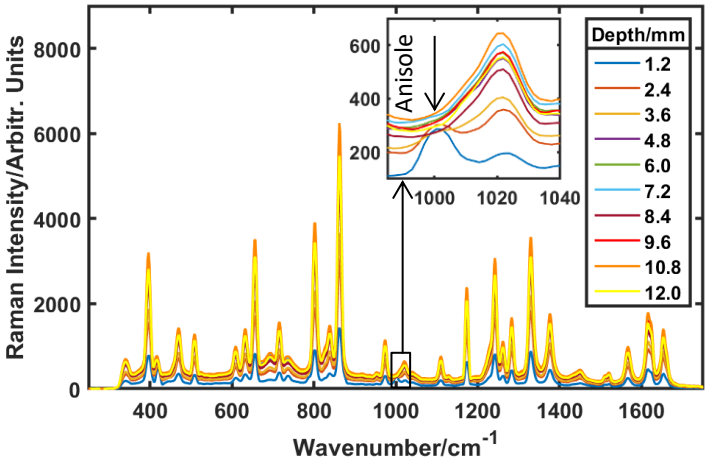

Figure 6.1. SORS spectra from 2 mm collection offset of 10 layer thicknesses of paracetamol over an anisole-filled cuvette. The inset shows a zoom-in on the wavenumber range including the anisole peak.

Figure 6.2 shows a zoom-in on the spectra over the spectral range 960-1060 cm^{-1} collected from the six offset distances for the 10 thicknesses following baseline correction. The anisole peak around 1002 cm^{-1} can visually be seen from a thickness of 1.2 mm for the 0 mm offset spectra, 1.2-2.4 mm for the 1-

3 mm offset spectra and 1.2-3.6 mm for the 4-5 mm offset spectra. This figure shows an increase in anisole peak intensity as the thickness of the paracetamol layer decreases. The decrease in anisole peak intensity is not equal from all offsets.

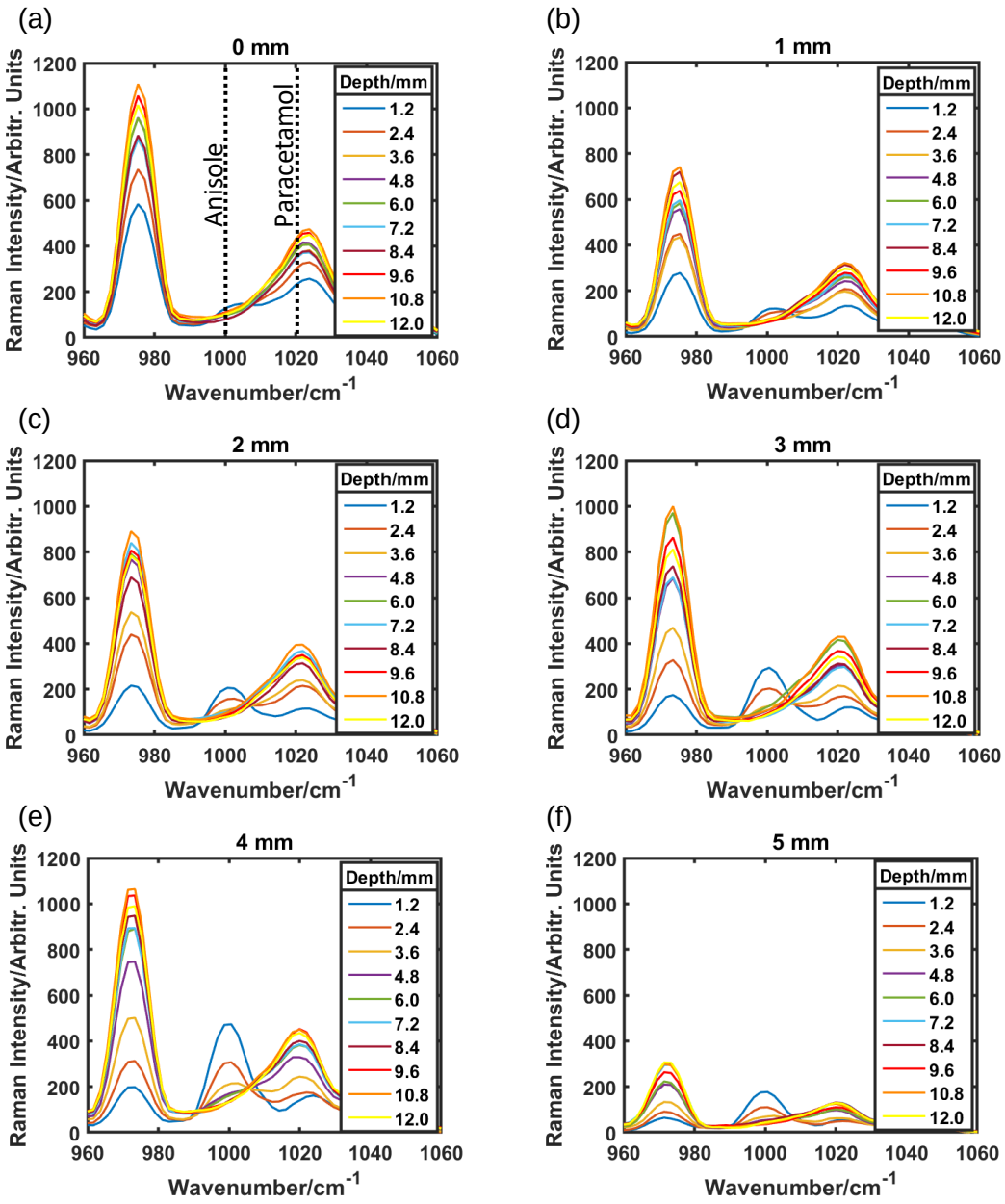

Figure 6.2. (a-f) correspond to 0-5 mm offset distances of SORS spectra of an anisole-filled cuvette underneath ten layers of paracetamol.

In order to assess the response from each of the offsets at the variable thicknesses, the anisole peak intensity at 1002 cm^{-1} seen in Figure 6.3 was divided by the neighbouring paracetamol peak intensity at 1020 cm^{-1} in spectra from the six detector offsets to assess the change in anisole peak intensity with reference to the paracetamol peak. Then the ratio for each offset was plotted at each of the thicknesses and is shown in Figure 6.3. In this figure, the ratios are larger at smaller depths and decrease gradually to reach a plateau, suggesting that the solvent signal is no longer detected at larger thicknesses. This allows the estimation of the limit of depth of the solvent signal detection. Observations from Figure 6.2 and Figure 6.3 indicate that a stronger solvent signal can be detected from larger offsets. This in turn indicated that there is a stronger contribution from the solvent in the signals collected from larger offsets. The curve in Figure 6.3 is flat beyond a depth of 1.2 mm for the backscattering spectra. This is increased to 3.6 mm for the 1 and 2 mm offsets, a depth of 4.8 mm for the 3 mm offset, and exceeds 6 mm for the 4 and 5 mm offsets. The difference in depths reached from each offset is attributed to the propensity of photons for lateral migration within the sample and then return back to the surface where the signal is collected.[77] The larger depth reached by the larger offset distances observed in Figure 6.3 illustrates the advantage of using SORS for characterising the subsurface of non-homogeneous systems.

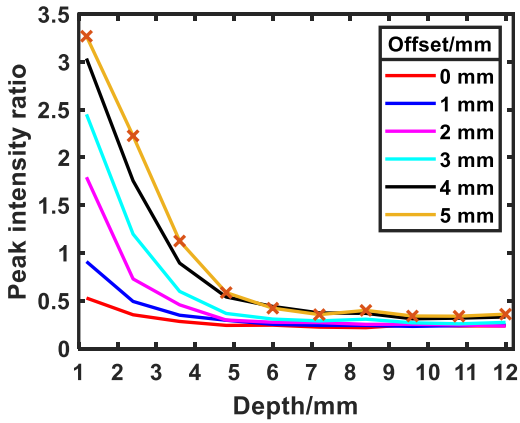

Figure 6.3. The ratio of anisole peak at 1002 cm^{-1} to paracetamol peak at 1020 cm^{-1}. Crosses are added to highlight the actual depth where the measurements were taken.

6.3 SORS for monitoring the solvent content during drying

This section reports the results obtained using SORS for at-line monitoring of pharmaceutical drying. The SORS response is investigated for two particle size grades and two solvents as described in section 4.3.2. The two main sections of qualitative and quantitative analysis are further divided into two sections per the two grades used in these experiments, granular and powder. Two particle size grades and two solvents were tested in order to assess the SORS response in a range of possible API grade/solvent systems.

The drying curves for the conducted runs are shown in Figure 6.4 for the four systems. Several drying runs of each of the systems were conducted in order to collect a dataset of spectra sufficiently representing the range of solvent content following de-liquoring. The drying curves of granular and powder paracetamol in anisole in Figure 6.4 (a) and (c) and in MTBE in Figure 6.4 (b) and (d) show that the drying of anisole starts with a higher solvent content in the drying cake and requires longer duration than that of MTBE. This is explained by the difference in boiling points of each of the solvent. Whereas anisole is a viscous solvent, MTBE is volatile and readily removable. Variations between the runs can also be seen in Figure 6.4. A smaller level of variation may be attributed to the inherent non-uniformity in the drying paracetamol. Some inconsistencies in the performance of the vacuum pumps have also led to the larger variation in the curves of the drying of paracetamol in anisole.

A comparison between the drying curves shows that the drying of the powder grade requires a longer duration. The powder grade is characterised by a smaller particle size, where those particles can retain more of the solvent compared to the larger size and smaller surface area of the granular grade. This is also indicated by the solvent content at the beginning of drying, which is between 35-45% for the powder grade and 25-35% for the granular grade. Moreover, those particles could coalesce to form lumps of larger size that trap the solvent inside, thus requiring extended durations for drying.[19] The qualitative analysis in the next section aims to assess the SORS response in those API grade/solvent combinations.

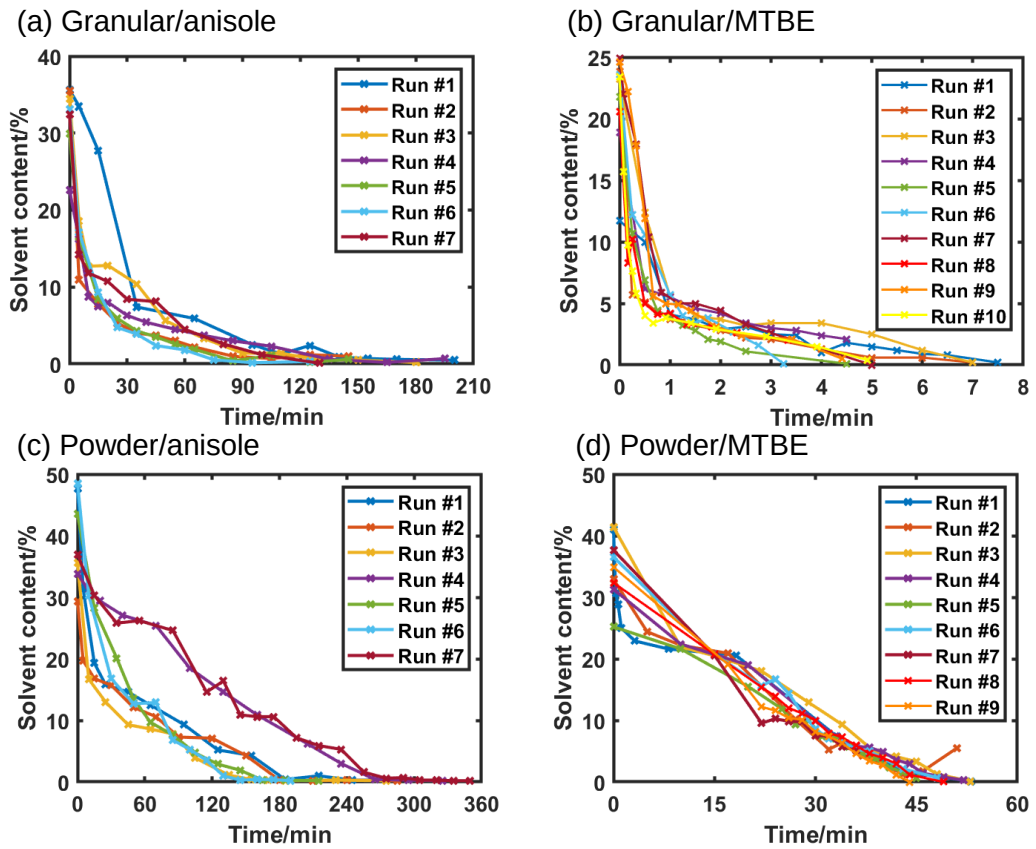

Figure 6.4. Drying profile of multiple batches using granular paracetamol in (a) anisole and (b) MTBE, and powder paracetamol in (c) anisole and (d) MTBE. the point at which a sample is extracted and spectra are measured is indicated with a cross symbol.

6.3.1 Qualitative analysis of SORS spectra

This section is further divided into two sections reporting the results of the use of SORS to monitor the drying of granular and powder paracetamol in anisole and MTBE.

6.3.1.1 Granular paracetamol systems

Figure 6.5 and Figure 6.6 shows the raw spectra collected using the SORS probe over the wavenumber range 250-1750 cm^{-1} from each of the offsets during one of the drying of granular paracetamol in anisole and MTBE, respectively. While the overall decrease in signal intensity in the raw spectra was mitigated in the design of the SORS probe through employing multiple

collection fibres for the offset spectra, spectra collected from the largest offset of 5 mm (Figure 6.5 (e) and Figure 6.6 (e)), are of lower intensity compared to the smaller offset distances. This decrease in intensity is observed in SORS spectra as the collection offset distance increases as the light diffuses through the sample, where a lower intensity is measured at larger offset distances.[77,78]

Variation in the baseline can be seen in the raw spectra, in addition to the variation in the intensity of solvent peaks; mainly at the anisole peak of strongest intensity at 1002 cm^{-1} in Figure 6.5 and MTBE peak around 730 cm^{-1} in Figure 6.6; insets are provided to show a zoom-in on this change in intensity. Those baseline shifts are a result of the different paths of the photons that exit the excitation and travel through the sample before reaching the detector. Those paths are influenced by factors such as sample positioning and compactness.[115,116] To eliminate the effect of those baseline shifts due to variations in the physical state of the sample and allow for clearer visualisation of the decrease in solvent peak intensity following the decrease in solvent content as the drying progresses, standard normal variate (SNV) pre-processing was applied. This pre-processing method was selected considering its advantages of processing each sample spectrum independently without the need for a reference spectrum, such as what would be required in multiplicative signal correction formulae, and not requiring user-defined parameters as would be used for baseline correction. [92]

Raw SORS spectra shown in Figure 6.5 and Figure 6.6 following SNV pre-processing are shown in Figure 6.7 and Figure 6.8, where the baseline shifts seen in the raw spectra were removed. As a result, the decrease in solvent peak intensity can be seen from all offsets as the zoomed-in insets on the solvent peaks show. For the pre-processed granular/MTBE spectra, the decrease in MTBE peak intensity also followed the decrease in solvent content as the drying progressed.

The solvent peak intensity decrease seen in Figure 6.7 and Figure 6.8 may be similarly perceptible from all offset spectra, but results from the depth of solvent signal detection in the previous section 6.2 suggest otherwise. To enable the

comparison of the spectral response from the six offsets over the solvent content range, the Raman peak intensity of anisole at 1002 cm^{-1} was divided by that of the neighbouring paracetamol peak intensity at 1020 cm^{-1} shown in Figure 6.9 (a) while the Raman peak intensity of the MTBE peak at 730 cm^{-1} was divided by the paracetamol peak intensity at 715 cm^{-1} and is shown in Figure 6.9 (b). A larger peak intensity ratio would indicate a stronger signal from the solvent. In Figure 6.9 (a), the peak intensity ratio for the solvent content range 5-20% is highest for the backscattering spectra, 0 mm offset, and lowest for the 5 mm offset distance. Over this solvent content range, the ratio decreases as the offset increases. On the contrary, over the solvent content range of 0-5%, the highest peak intensity ratio is obtained from the 5 mm offset spectra while the lowest ratio is from the backscattering spectra. For the granular/MTBE system in Figure 6.9 (b), the ratio obtained from spectra collected is larger for larger offsets and is the largest for the 5 mm offset and lowest for the backscattering spectra.

Despite the lower intensity obtained from the largest offset, seen in Figure 6.5 and Figure 6.6, spectra from this offset seem to contain more contribution from the solvent in the signal. This suggests more sensitivity to the change in solvent content as the offset distance increases and agrees with the observations seen in the previous section 6.2 reporting the results for the depth of solvent signal detection. Spectra from each of the offset distances represent sample layers of variable depths as a result of the travelling of photons from deeper layers back to the surface of the sample.

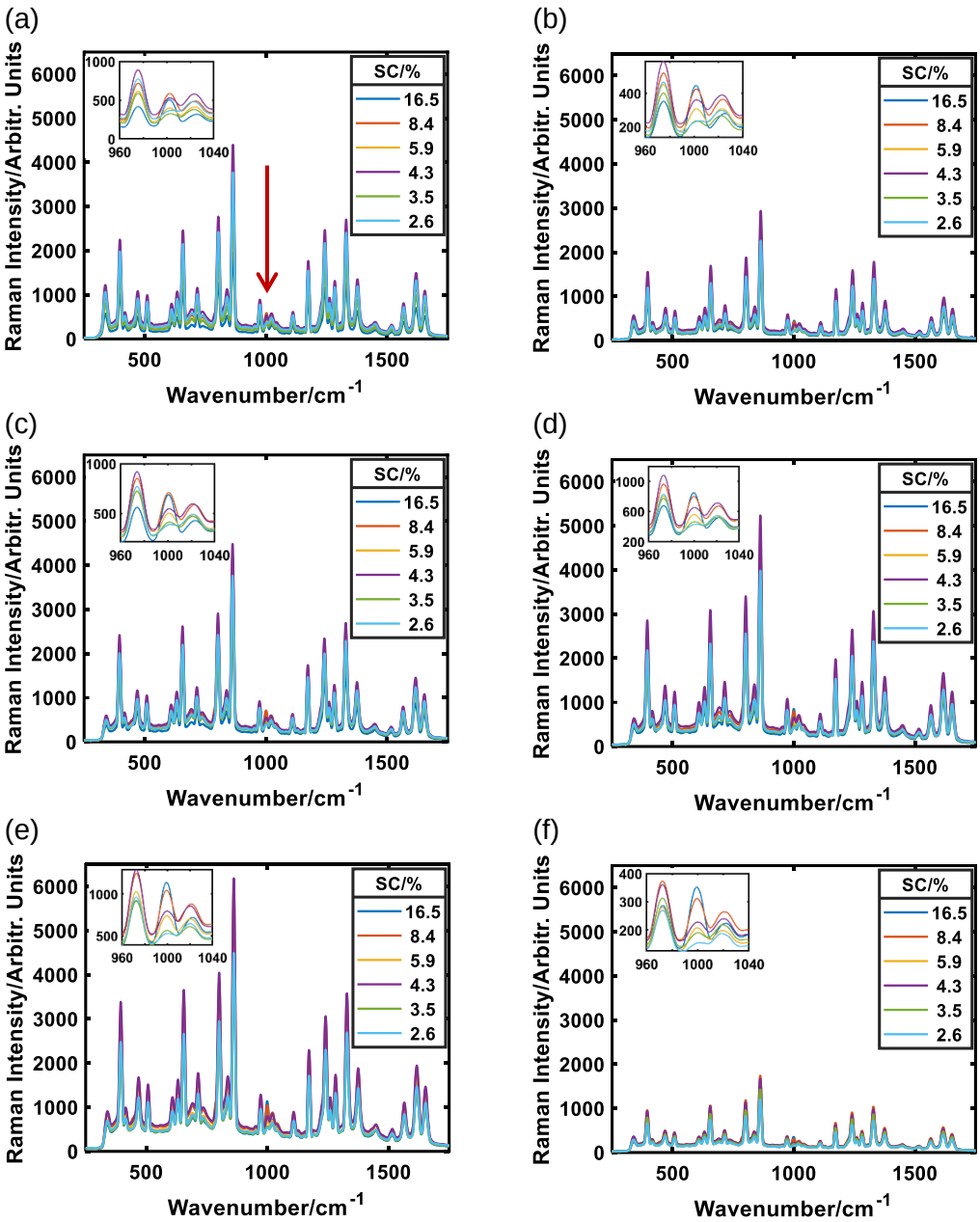

Figure 6.5. SORS spectra collected using the SORS probe during the drying of granular paracetamol in anisole from (a) 0 mm, (b) 1 mm, (c) 2 mm, (d) 3 mm, (e) 4 mm, and (e) 5 mm offset distances. Insets show a zoomed-in view of the main anisole peak. The legend shows the solvent content percentage (SC%) in each sample spectrum. The arrow in (a) points at the anisole peak of highest intensity.

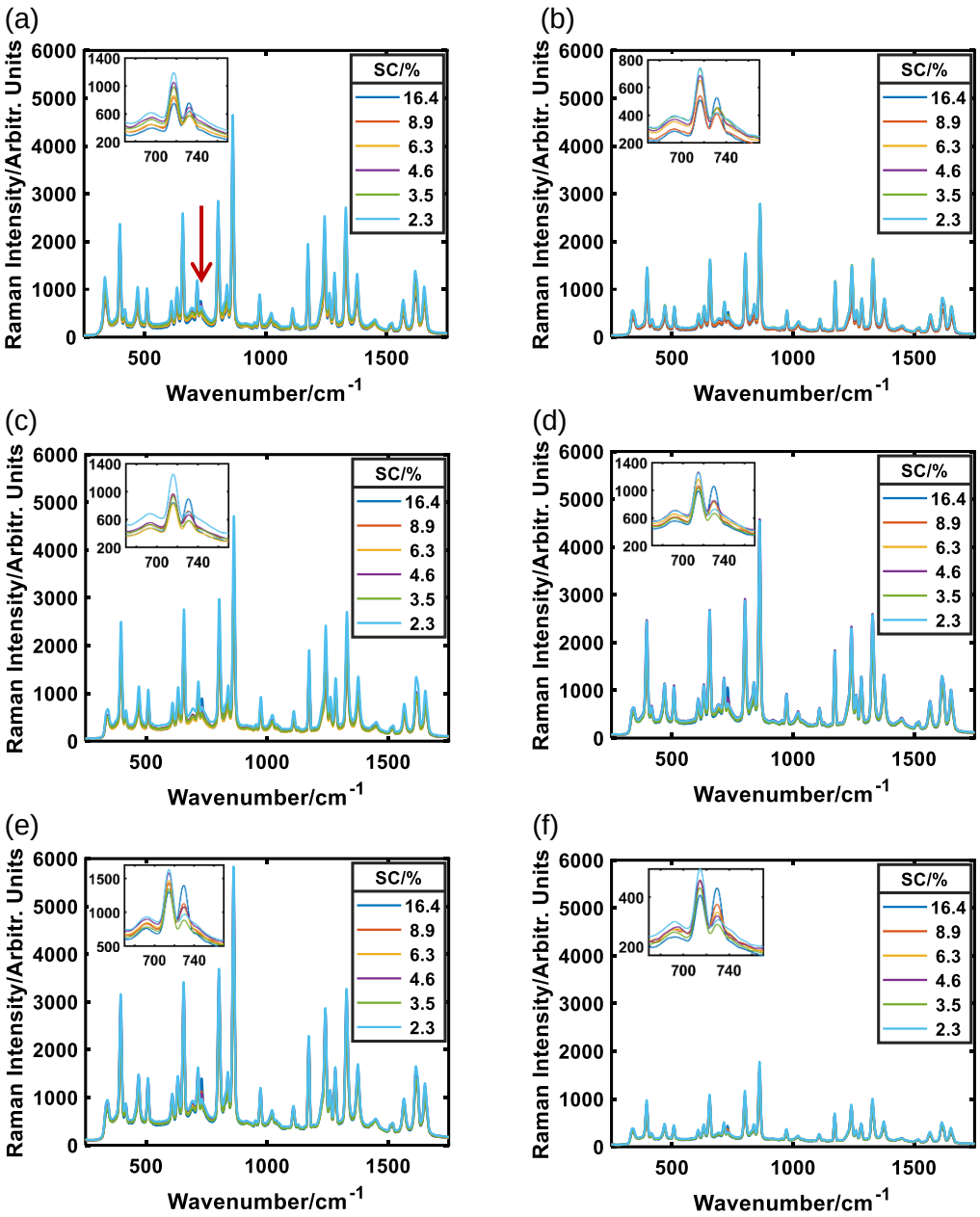

Figure 6.6. SORS spectra collected using the SORS probe during the drying of granular paracetamol in MTBE from (a) 0 mm, (b) 1 mm, (c) 2 mm, (d) 3 mm, (e) 4 mm, and (e) 5 mm offset distances. Insets show a zoomed-in view of the main MTBE peak. The arrow in (a) points at the MTBE peak of highest intensity.

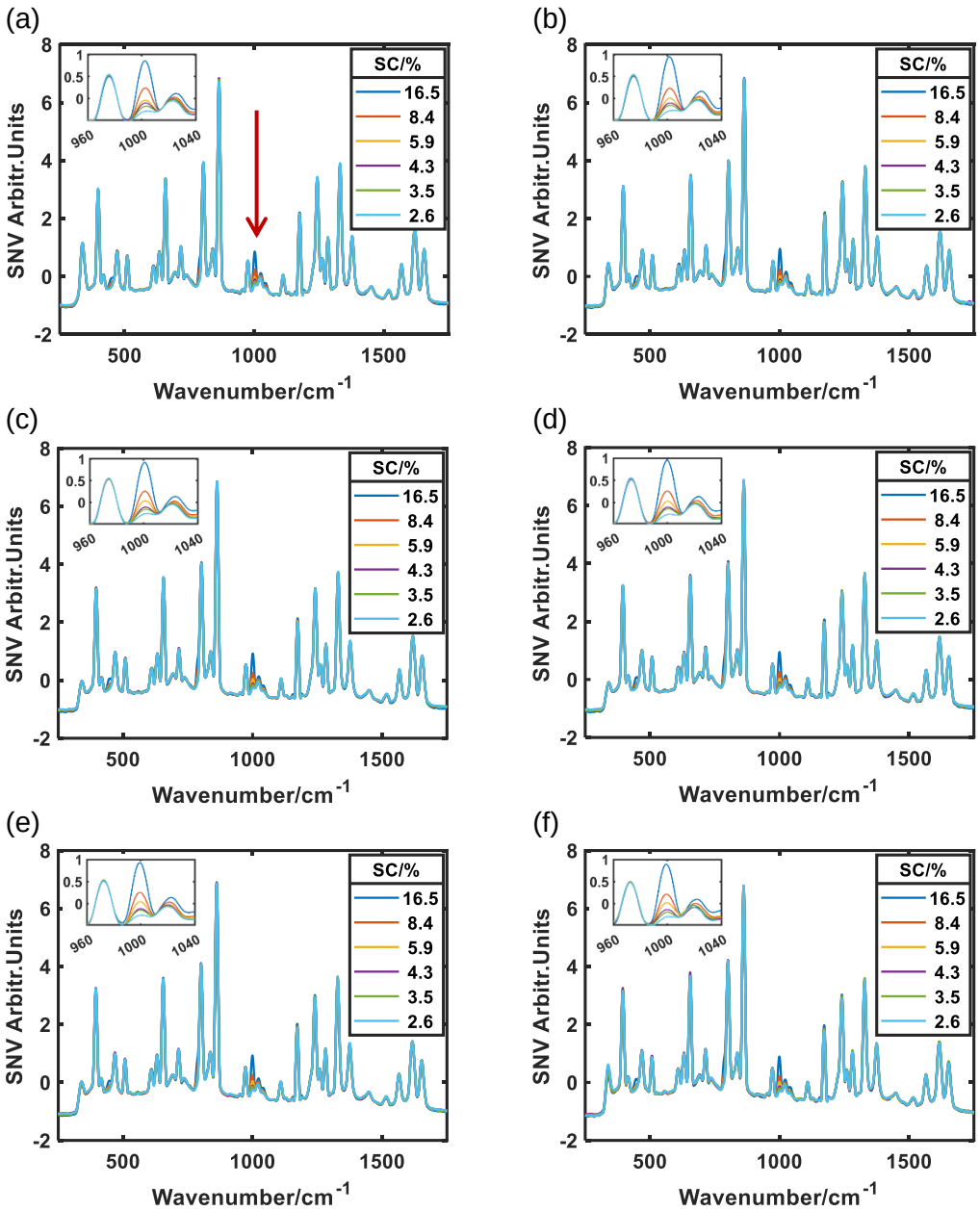

Figure 6.7. SNV pre-processed SORS spectra (raw in Figure 6.5) collected during the drying of granular paracetamol in anisole from (a) 0 mm, (b) 1 mm, (c) 2 mm, (d) 3 mm, (e) 4 mm, and (e) 5 mm offset distances. Insets show a zoomed-in view of the main anisole peak. The arrow in (a) points at the anisole peak of highest intensity.

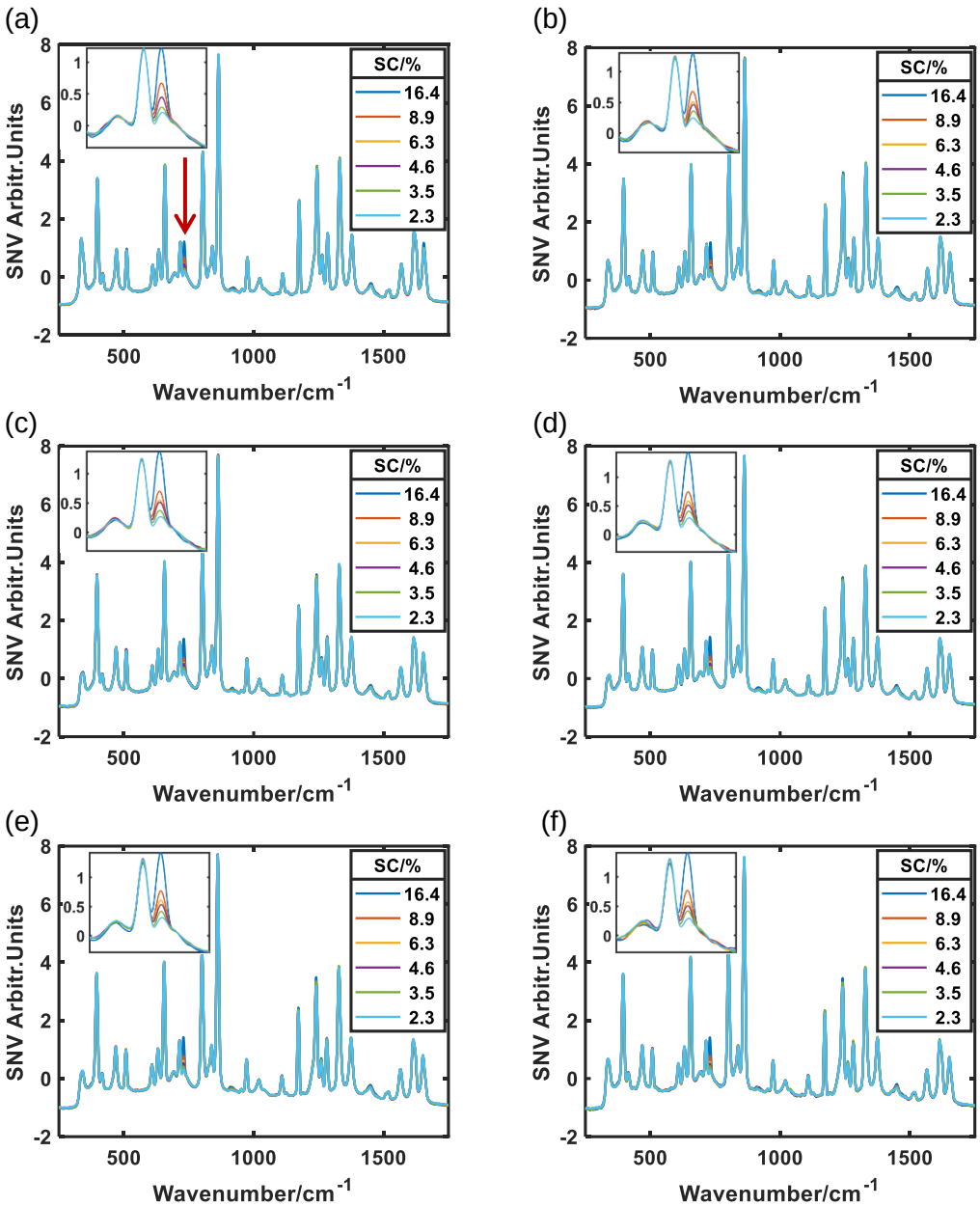

Figure 6.8. SNV pre-processed SORS spectra (raw in Figure 6.6) collected during the drying of granular paracetamol in MTBE from (a) 0 mm, (b) 1 mm, (c) 2 mm, (d) 3 mm, (e) 4 mm, and (e) 5 mm offset distances. Insets show a zoomed-in view of the main MTBE peak. The arrow in (a) points at the MTBE peak of highest intensity.

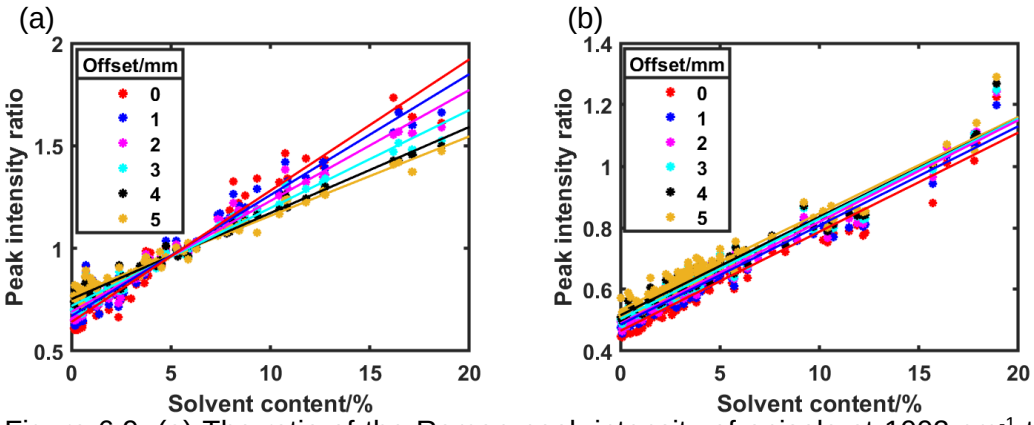

Figure 6.9. (a) The ratio of the Raman peak intensity of anisole at 1002 cm^{-1} to the Raman peak intensity of paracetamol at 1020 cm^{-1} in spectra obtained during the drying of granular paracetamol in anisole. (b) The ratio of the Raman peak intensity of MTBE at 730 cm^{-1} to the Raman peak intensity of paracetamol at 715 cm^{-1} in spectra obtained during the drying of granular paracetamol in MTBE.

6.3.1.2 Powder paracetamol systems

Figure 6.10 and Figure 6.11 show an example of SORS spectra collected from one of the drying runs of powder paracetamol in anisole and MTBE, respectively. Similar to the observations from the granular/solvent systems, baseline shifts and solvent peak intensity variations can be seen in this figure. Here, the baseline shifts are larger than those seen in the granular systems. It was noted that lower signal intensity was obtained from the powder paracetamol systems compared to the larger granular paracetamol systems. Due to differing observations and conclusions regarding the effect of particle size on Raman intensity across reported literature, there is no consensus on the explanation of the relation between particle size and Raman intensity response, i.e. whether Raman intensity increases as the particle size increases.[10,116-119] Those studies reported in literature link the particle size to Raman intensity, where powder particles are separated into size ranges through sieving in most cases. The particle diameter is then related to the change in Raman intensity. The use of particle size based on the diameter assumed from sieving does not take into account the morphology of a particle. A particle diameter may be representative of a spherical particle but would not

be representative of a long needle-shaped particle. Similarly, particles separated to size ranges through sieving might also be needle-shaped and could therefore fall through or get retained on a mesh based on the orientation of the particle. Nevertheless, it could be explained that the Raman intensity increases as the particle size increases as a result of the reduced diffuse reflectance in larger particles compared to smaller particles, which means that a smaller volume of a sample (of small particle size) would be captured in the Raman signal.[118]

The powder paracetamol systems were more affected by the decrease in signal intensity in SORS spectra from the larger offset distances, most notably those collected from the 5 mm offset compared to the 0 mm offset. Spectra collected from the 1 mm offset also have lower intensity compared to that seen from the granular paracetamol system in Figure 6.5 and Figure 6.6. This can similarly be attributed to the diffusion of light between the particles upon contact with this particulate sample.[118] The variation in peak intensity can be visually seen in the insets in Figure 6.10 and Figure 6.11 of the anisole and MTBE, respectively. To remove the baseline shifts resulting from the physical differences between the samples, SNV pre-processing was applied to spectra from both systems. This pre-processing also helps to better illustrate the decrease in solvent peak intensity as the drying progresses as shown in Figure 6.12 and Figure 6.13, where a clear decrease in solvent peak intensity can be seen through the zoomed-in inset of both solvent peaks.

To enable the comparison of the spectral response from the six offsets over the solvent content range, the same steps followed for the granular systems were carried out for the powder systems. The Raman peak intensity of anisole at 1002 cm^{-1} was divided by that of the neighbouring paracetamol peak intensity at 1020 cm^{-1} indicated with an arrow in Figure 6.14 (a) while the Raman peak intensity of the MTBE peak at 730 cm^{-1} was divided by the paracetamol peak intensity at 715 cm^{-1} and is indicated with an arrow in Figure 6.14 (b). Despite the difference in Raman intensity seen from the two paracetamol grades, larger peak ratios were seen from the larger offsets over the solvent content range of 0-5% in the powder/anisole system and over 0-

15% in the powder/MTBE system, indicating stronger solvent contribution in the signal.

The sensitivity in SORS signal response to the change in solvent content in both paracetamol grades and solvents suggests that those spectra may also prove to be advantageous when used to estimate the solvent content during drying. The results of the quantitative analysis are reported in the following section.

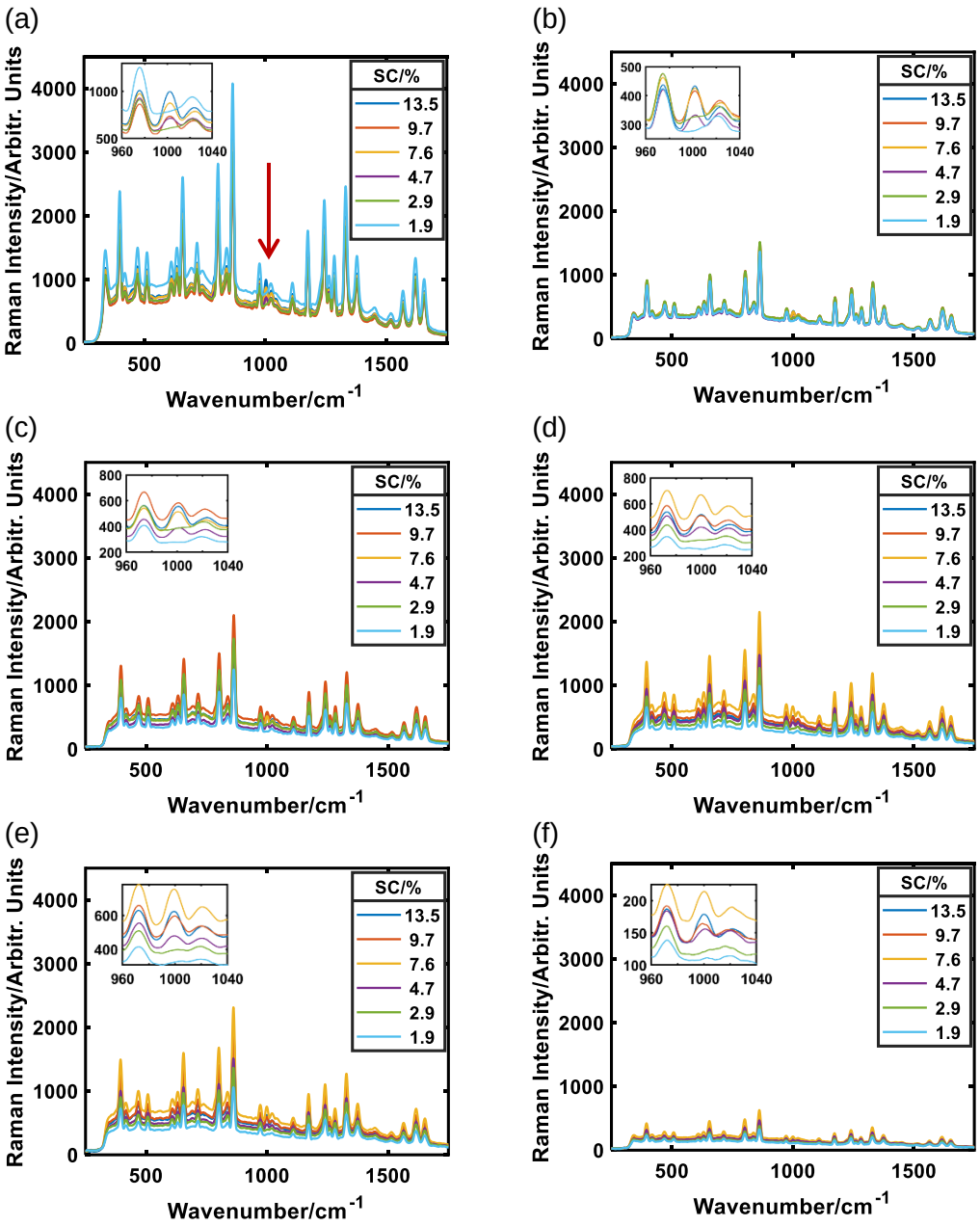

Figure 6.10. SORS spectra collected using the SORS probe during the drying of powder paracetamol in anisole from (a) 0 mm, (b) 1 mm, (c) 2 mm, (d) 3 mm, (e) 4 mm, and (e) 5 mm offset distances. Insets show a zoomed-in view of the main anisole peak. The arrow in (a) points at the anisole peak of highest intensity.

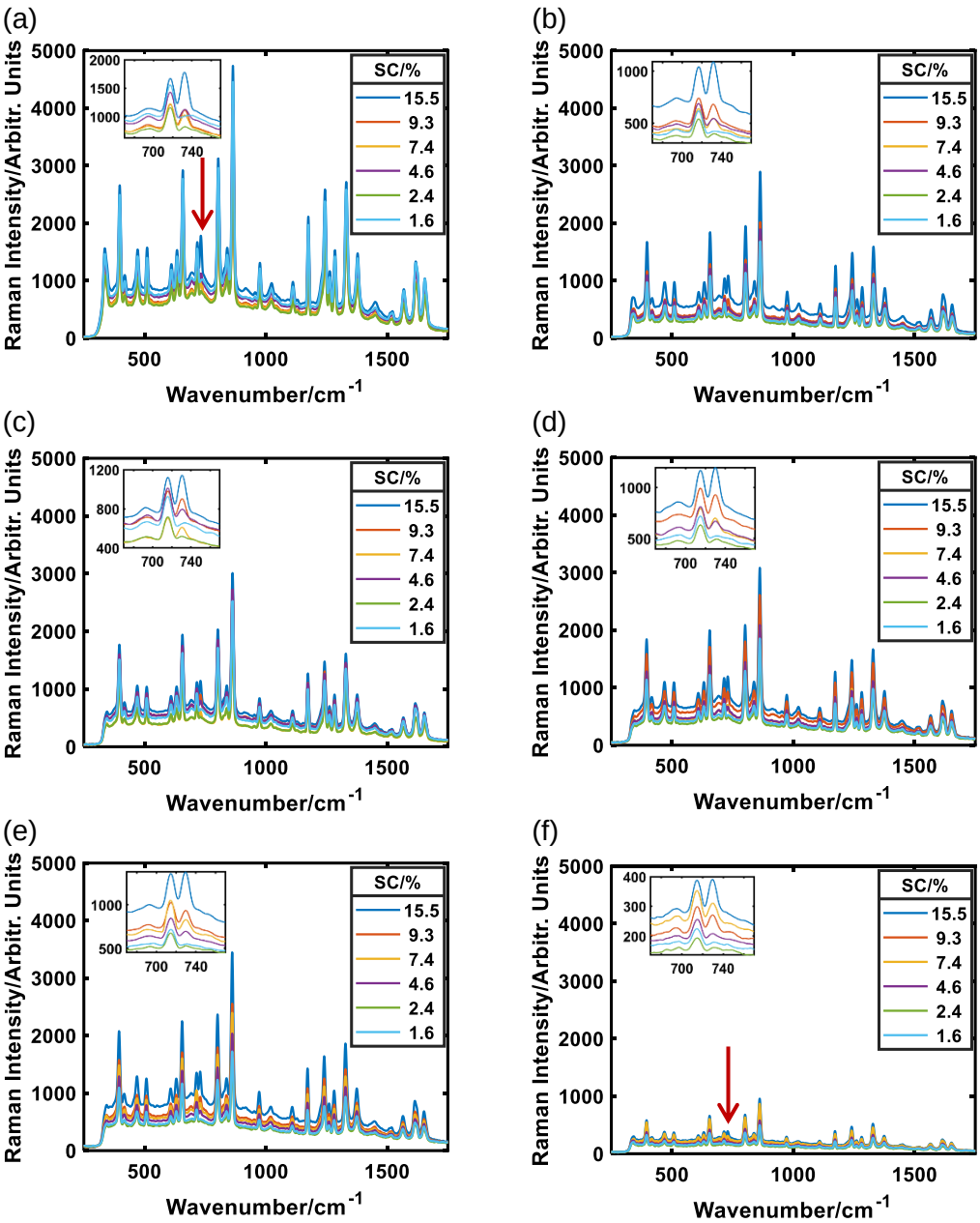

Figure 6.11. SORS spectra collected using the SORS probe during the drying of powder paracetamol in MTBE from (a) 0 mm, (b) 1 mm, (c) 2 mm, (d) 3 mm, (e) 4 mm, and (e) 5 mm offset distances. Insets show a zoomed-in view of the main MTBE peak. Arrow in (a) and (e) points at the MTBE peak of highest intensity.

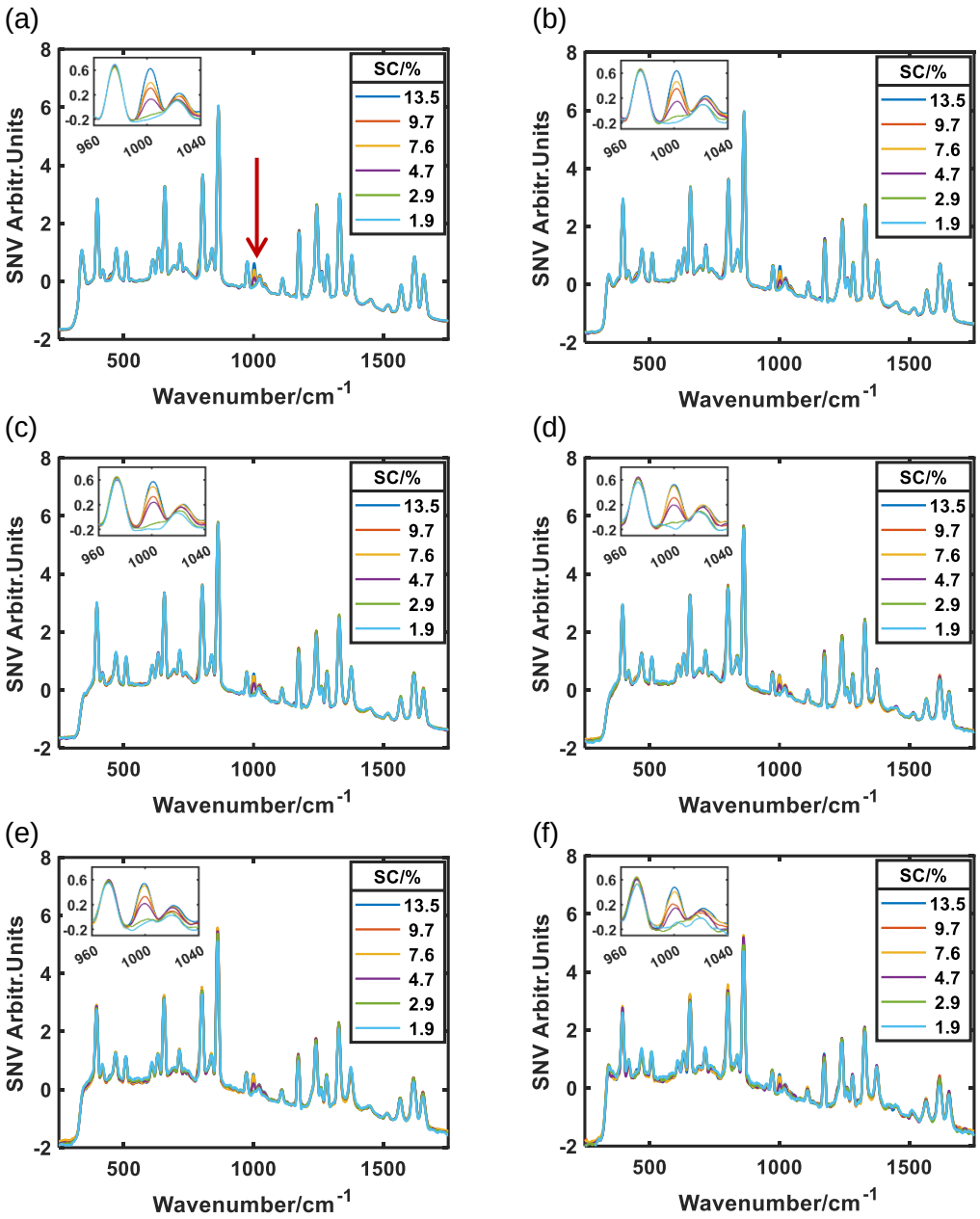

Figure 6.12. SNV pre-processed SORS spectra (raw in Figure 6.5) collected during the drying of powder paracetamol in anisole from (a) 0 mm, (b) 1 mm, (c) 2 mm, (d) 3 mm, (e) 4 mm, and (e) 5 mm offset distances. Insets show a zoomed-in view of the main anisole peak. The arrow in (a) points at the anisole peak of highest intensity.

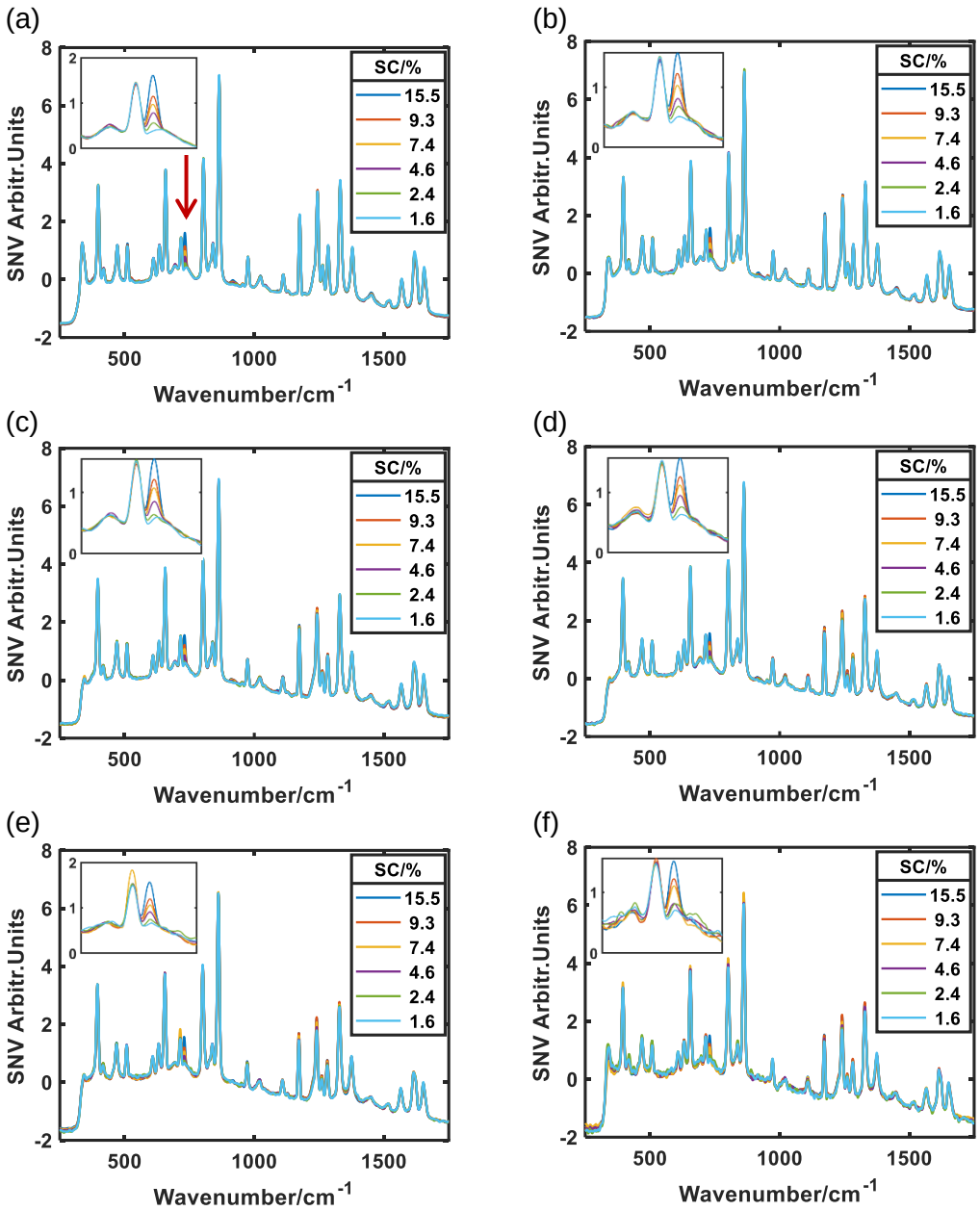

Figure 6.13. SNV pre-processed SORS spectra (raw in Figure 6.6) collected during the drying of granular paracetamol in MTBE from (a) 0 mm, (b) 1 mm, (c) 2 mm, (d) 3 mm, (e) 4 mm, and (e) 5 mm offset distances. Insets show a zoomed-in view of the main MTBE peak. The arrow in (a) points at the MTBE peak of highest intensity.

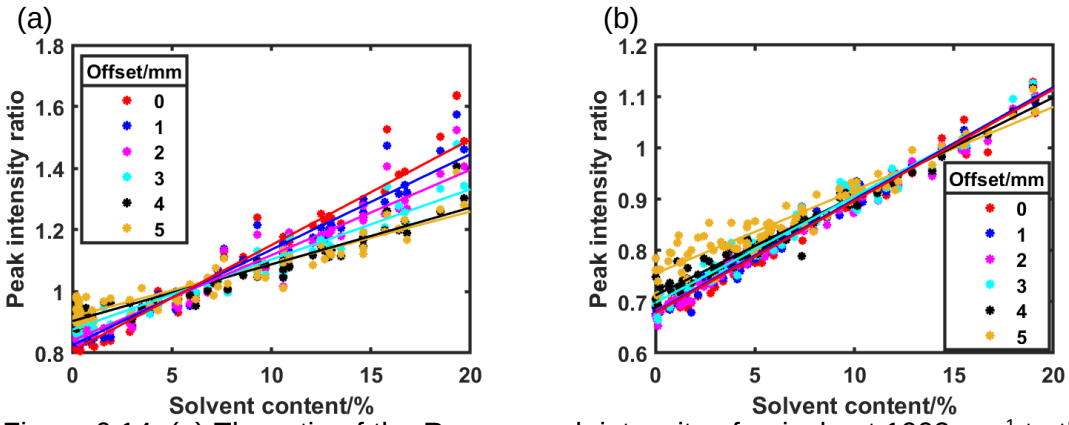

Figure 6.14. (a) The ratio of the Raman peak intensity of anisole at 1002 cm^{-1} to the Raman peak intensity of paracetamol at 1020 cm^{-1} in spectra obtained during the drying of powder paracetamol in anisole. (b) The ratio of the Raman peak intensity of MTBE at 730 cm^{-1} to the Raman peak intensity of paracetamol at 715 cm^{-1} in spectra obtained during the drying of powder paracetamol in MTBE.

6.3.2 Quantitative analysis of SORS spectra

Partial least squares regression (PLSR) analysis was utilised for the quantitative analysis for the estimation of the solvent content throughout drying using SORS spectra collected during the process. PLSR analysis was applied using spectra collected from all runs for each of the offset distances, where those are compared to the 0 mm offset/backscattering spectra over the full wavenumber range 250-1750 cm^{-1} as a benchmark. This analysis was conducted to investigate the model performance of the different offset distance spectra, spectral range, and the effect of pre-processing SORS spectra. SORS spectra from multiple configurations are also combined in PLSR analysis to investigate the possibility of enriching the models to obtain more accurate solvent content estimations.

6.3.2.1 Granular paracetamol systems

PLSR models were constructed using the raw and pre-processed SORS spectra collected from the drying of granular paracetamol. The number of latent variables (LVs) sufficient to describe each of the PLSR models constructed using the SORS spectra was selected after assessing the root mean square error of cross-validation (RMSECV) shown in Figure 5.12 (a) for the granular/anisole system and Figure 5.12 (b) for the granular/MTBE system for raw and pre-processed spectra. The latent variable at which the curve displays a plateau or the lowest RMSECV is selected to represent the variance within the model. For spectra collected from this two-component system, a minimum of two latent variables is expected to represent the two components.

Figure 6.15 (a) shows a sharp decrease in the RMSECV after the first two LVs for PLSR models of the raw spectra of 0-2 mm offset distances suggesting that the majority of variation is captured by those two LVs, while the decrease is less sharp for RMSECV curves of PLSR models of 3-5 mm offset distance spectra. Moreover, the RMSECV curves gradually decrease overall as the offset increases from 0 to 5 mm. Following SNV pre-processing, the level of RMSECV is lower than that of the raw spectra, in addition to less fluctuation in the curves after the plateau. There are less differences between the RMSECV curves of the pre-processed SORS spectra compared to the raw spectra. This suggests that the differences eliminated through SNV pre-processing were due to physical differences in the filter cake and that spectra from each of the SORS offsets could contain different amounts of variation in relation to the solvent content. For RMSECV of the granular/MTBE system in Figure 6.15 (b), the decrease is gradual from the first to the fourth LV in PLSR of raw spectra. For pre-processed granular-MTBE spectra, the curves are the decrease is sharp from the first to the second LV and where the RMSECV curves show subtle differences indicating that the majority of the variation is captured in the first two LVs. Since PLSR relies on maximising the covariance between the spectra and the reference values, the solvent content, comparison of Figure 6.15 (a) and (b) suggests a higher level of variation in the raw SORS spectra in the granular/anisole system compared to the granular/MTBE.

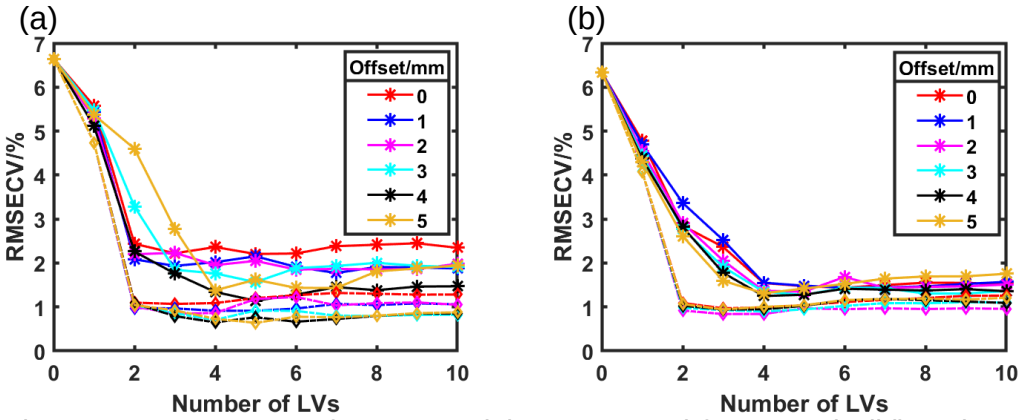

Figure 6.15. RMSECV of PLSR models constructed from raw (solid) and SNV pre-processed spectra (dashed) from 0-5 mm collected from granular paracetamol in (a) anisole and (b) MTBE.

Table 6.1 shows a summary of PLSR models selected based on the RMSECV curves in Figure 6.15. For PLSR models of the raw granular/anisole spectra, the RMSECV decreases as the offset distance increases to 4 mm, where it is reduced by half compared to the PLSR model of the 0 mm spectra and increases slightly for the PLSR model of the 5 mm spectra compared to the PLSR model of the 4 mm spectra. The values of the coefficient of determination, R^2, increase as the offset distance increases to 4 mm and suggest that PLSR models of the raw spectra of 4 mm offset distance show the most correlation to the solvent content. A similar trend to the RMSECV is seen for the RMSEP values, which are slightly higher than the RMSECV apart from the 0 mm spectra, indicating the representativeness of the calibration set spectra of the system and the robust performance of the PLSR calibration models. The larger RMSEP values may be attributed to some physical variation in the test set samples that were not captured in the calibration set. Following the SNV pre-processing, the RMSECV decreases as the offset distance increases and is 50% lower in the PLSR model of the 4 mm spectra. Similarly, the RMSEP also decreases as the offset distance increases. Here, the PLSR model of the 5 mm spectra shows similar performance to that of the 4 mm spectra. This also suggests that the pre-processing step was more critical to the spectra of lower signal intensity, as was seen in Figure 6.5 (f).

Here, the RMSEP is at a level similar to or lower than that of the RMSECV, confirming that the variation not included in the raw test set was not related to the solvent content but to physical differences between the samples. This is further supported by the lower number of LVs describing this model and the rise in R^2 values following pre-processing as the non-linear changes in spectra are removed before applying.

For the granular/MTBE PLSR results in Table 6.1, the RMSECV also decreases as the offset distance increases up to 4 mm, while the R^2 values increase. The RMSEP also decreases as the offset distance increases and is at a similar level to the RMSECV. This shows that the PLSR calibration models were reliable in predicting the solvent content in the test set. For the PLSR models of the granular/MTBE SNV pre-processed spectra, the RMSECV and RMSEP are lower compared to the raw spectra. However, the performance of PLSR for all offset spectra from each of the offsets is similar. The decrease from variable levels of the RMSECV and RMSEP in the raw granular/MTBE spectra to similar levels in the pre-processed spectra suggests that spectra from larger offsets carried less non-solvent related variation compared to the smaller offset spectra as the PLSR models of those spectra had lower error compared to the larger offset spectra.

Table 6.1. Summary of PLSR model performance of raw and SNV pre-processed spectra of granular paracetamol in anisole and MTBE from each of the offsets.

Grade/Solvent	Pre-processing	Raw				SNV Pre-processed			
	Offset distance/ mm	LV	RMSE CV/%	RMSE P/%	R^2	LV	RMSE CV/%	RMSE P/%	R^2
Granular/Anisole	0	3	2.22	1.47	0.78	3	1.07	0.76	0.95
	1	3	1.93	2.32	0.83	2	0.98	0.93	0.96
	2	4	1.95	2.54	0.83	3	0.85	0.76	0.97
	3	5	1.57	2.02	0.89	4	0.71	0.63	0.98
	4	5	1.14	1.28	0.94	4	0.65	0.58	0.98
	5	4	1.38	2.23	0.91	5	0.64	0.55	0.98
Granular/MTBE	0	4	1.54	1.67	0.85	3	0.97	1.18	0.94
	1	4	1.55	1.44	0.85	3	0.84	0.90	0.96
	2	4	1.37	1.22	0.89	2	0.92	0.88	0.95
	3	4	1.35	1.25	0.89	2	0.98	0.93	0.94
	4	4	1.25	1.08	0.90	3	0.94	0.88	0.95
	5	4	1.31	1.34	0.89	3	0.94	0.96	0.95

Looking further into the performance of the PLSR models of those offset spectra from the granular/anisole system, the regression and residuals plots are shown in Figure 6.16 (a-b) of the PLSR models corresponding to the 0 mm offset spectra and Figure 6.16 (c-d) of the 4 mm offset spectra. Comparison between Figure 6.16 (a) and (c) shows that the predicted solvent content values over the entire solvent content range are closer to the reference line; this is also seen when comparing Figure 6.16 (b) and (d). This shows that, in addition to more accurate predictions obtained from the 4 mm spectra, the error is consistently lower over the entire solvent content range.

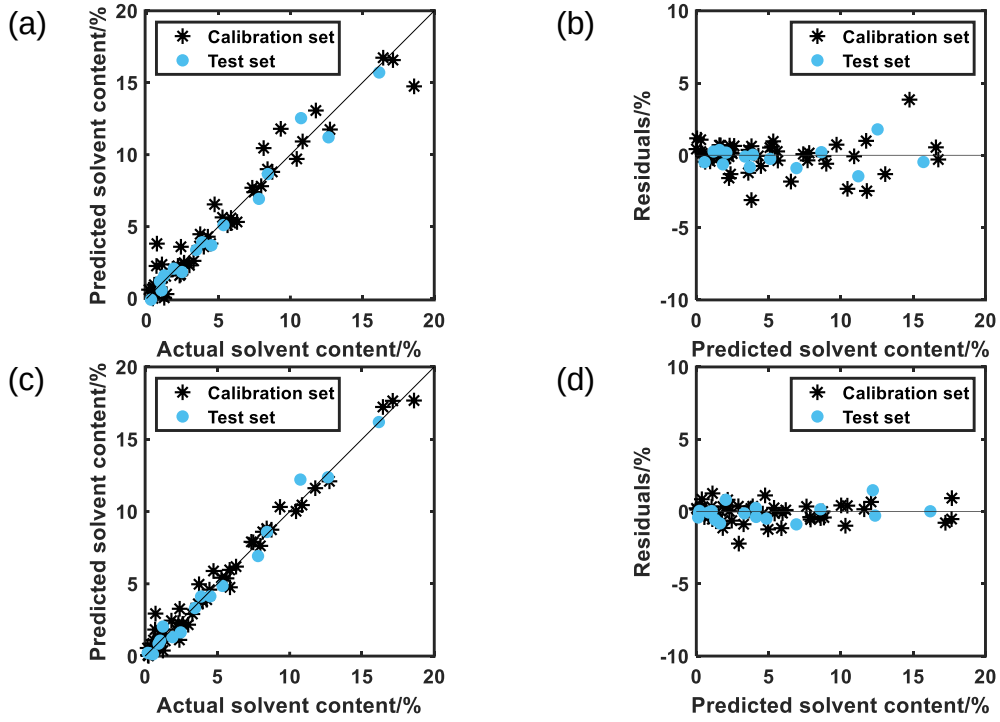

Figure 6.16. Regression and residuals plots of PLSR models constructed from (a-b) 0 mm, (c-d) 4 mm SNV pre-processed granular/anisole spectra over 250-1750 cm^{-1}.

The scores and loadings of the PLSR models for each of the SORS offset distances were also assessed to investigate the PLSR model performance of the larger offset distance spectra, where figures 0 mm and 4 mm offset distance spectra will be shown for comparison. The loadings curves were compared to the two pure component spectra as shown in Figure 6.17 of the loadings of the three LVs from the SNV pre-processed 0 mm spectra of the granular/anisole system. In Figure 6.17, the loadings curve of LV1 shows peaks corresponding to the paracetamol spectrum and a small peak corresponding to the strong anisole peak at 1002 cm^{-1}. The loading curve of LV2 shows all peaks corresponding to those of anisole. LV3 shows some peaks corresponding to anisole around 790 and 1002 cm^{-1}, and to paracetamol at the spectral range over 1100 cm^{-1}. Those loadings curves suggest that LVs 2-3 contain most of the variance related to the solvent content. Also, the scores were plotted against the reference solvent content values to investigate the relation to them as shown in Figure 6.17. The trend in the scores of LV2 shows

a relation to the solvent content. Similarly, for PLSR models of the SNV pre-processed 4 mm spectra in Figure 6.18, the loadings curve of LV1 includes peaks corresponding to those seen in the paracetamol spectra and a small peak corresponding to the strong anisole peak. The loadings curve of LV2 all peaks corresponding to those in the anisole spectra. Scores of LV2 of the 4 mm spectra also show a relation to the solvent content. LV3 loadings contain peaks of both paracetamol and anisole, while the scores suggest some relation to the solvent content. The loadings curve and scores of LV4 show no clear correlation to either component but could capture some systematic variation. The systematic improvement in PLSR model performance seen in Table 6.1 and Figure 6.16 as the offset distance increases can be attributed to the increase in the volume of the sample probed by the larger offsets as was demonstrated in section 6.2.

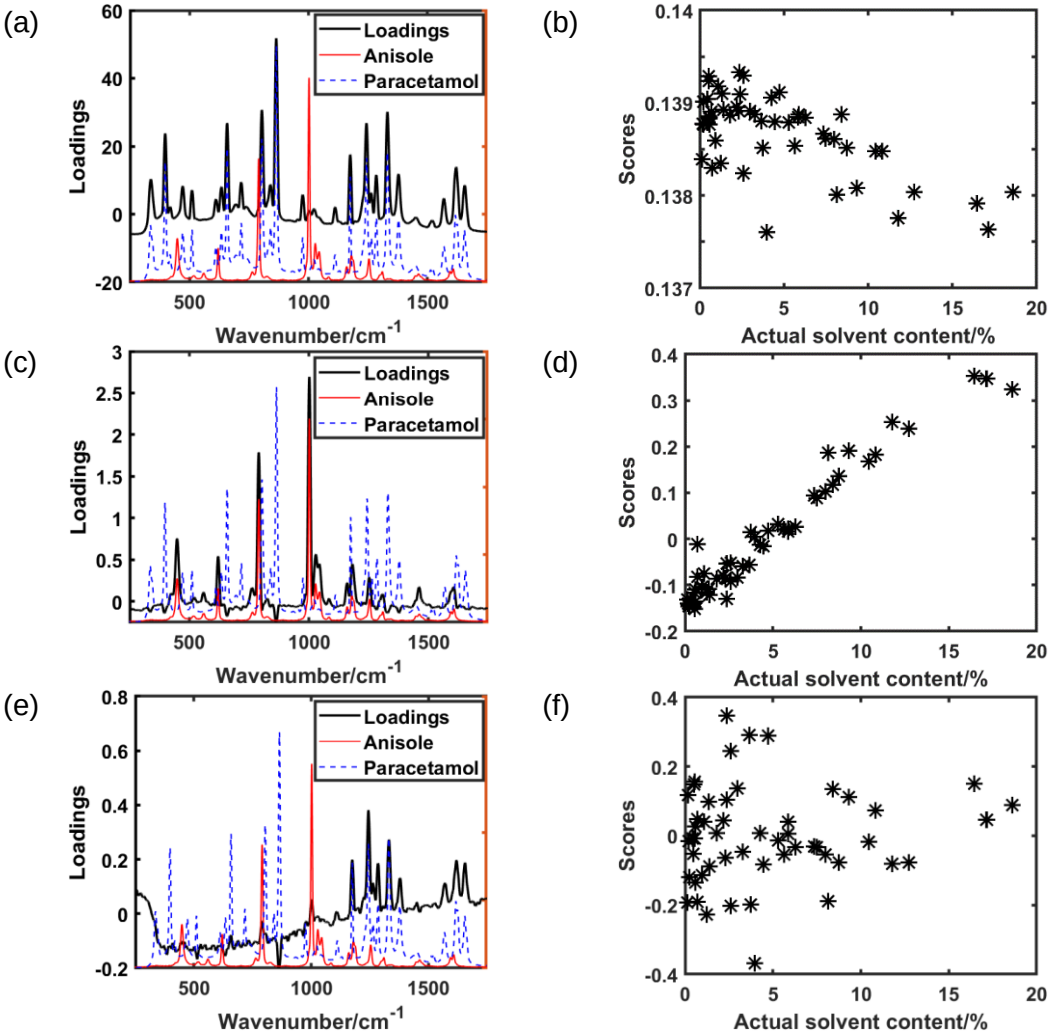

Figure 6.17. (a) loadings and (b) scores plots of LV1, (c) loadings and (d) scores of LV2, (e) loadings and (f) scores of LV3 of the PLSR model of the 0 mm offset SNV pre-processed spectra from the granular/anisole system. Curves of the paracetamol and anisole are also plotted with the loadings for reference.

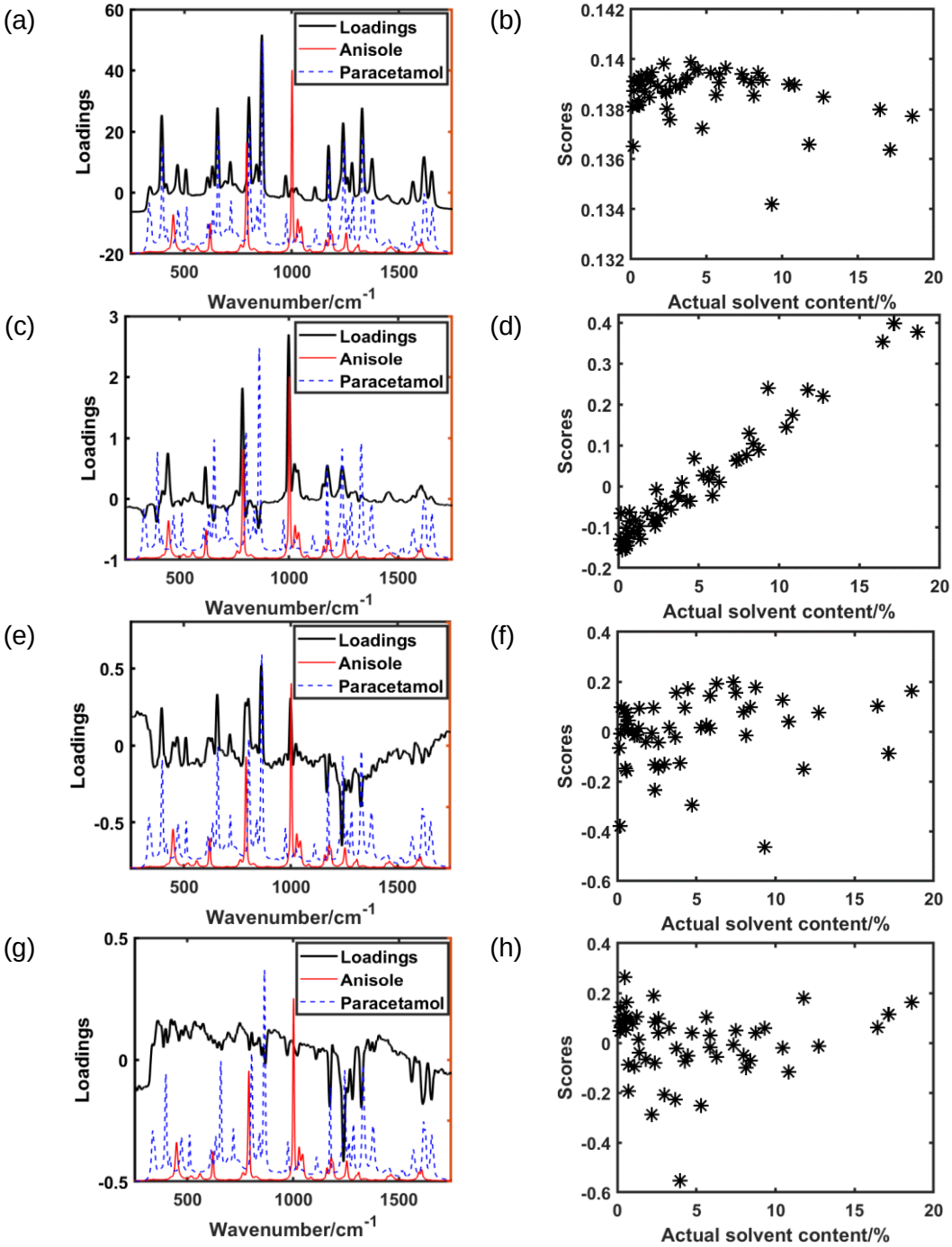

Figure 6.18. (a) loadings and (b) scores plots of LV1, (c) loadings and (d) scores of LV2, (e) loadings and (f) scores of LV3, (g) loadings and (h) scores of LV4 of the PLSR model of the 4 mm offset SNV pre-processed spectra from the granular/anisole system. Curves of the paracetamol and anisole are also plotted with the loadings for reference.

To further investigate the improvement in the PLSR performance of SORS spectra of the granular/anisole system as the offset increases, the percentage of variance captured by the PLSR model of 0 mm and 4 mm spectra is shown in Table 6.2. The variance captured by PLSR of the granular/anisole spectra of 0 mm adds up to 98.07%, of which 47.63% show relation to the solvent content as seen from the scores and loadings of LV2-3 in Figure 6.17. For the granular/anisole 4 mm spectra, the sum of variance captured is 99.36%, of which 48.87% is related to the solvent content as seen from the loading curves in Figure 6.18.

Table 6.2. Percentages of variance captured in PLSR models SORS spectra from 0 and 4 mm of granular paracetamol in anisole system.

Offset distance/mm	**0**	**4**
LV	Variance in LV/%	
1	50.44	50.40
2	47.17	47.33
3	0.46	1.54
4	-	0.08
Sum of variance related to the solvent	47.63	48.87
Sum of variance	98.07	99.36

In the granular/MTBE system, the performance of PLSR models of the SNV pre-processed spectra was found to be similar as the RMSECV was between 0.84% and 0.97%, the R2 between 0.94 and 0.96, and the RMSEP between 0.88% and 1.18%. To investigate the performance of the PLSR models, models of the 0 mm, 1 mm, and 4 mm offset SNV pre-processed spectra will be compared, where the PLSR model of the 0 mm SNV pre-processed offset spectra is a benchmark, and the PLSR model of the 1 mm offset SNV pre-processed spectra shows the lowest RMSECV of 0.84%. The PLSR model of the 4 mm offset raw spectra had the lowest RMSECV and RMSEP, but the PLSR model of the SNV pre-processed spectra of the same offset shows improved performance that is similar to the other offsets. Therefore, the PLSR model of the 4 mm SNV pre-processed spectra will also be investigated.

The regression and residuals plots for the 0 mm spectra from the granular/MTBE system are shown in Figure 6.19 (a-b), while those of the 1 mm and 4 mm spectra are in Figure 6.19 (c-d) and Figure 6.19 (e-f), respectively. The distribution of the points around the fitted line is largely similar since the RMSECV of the 1 mm and 4 mm spectra are 0.84% and 0.94 respectively while the RMSEP are 0.88% and 0.90% compared to those of the 0 mm offset, which shows similar RMSECV of 0.97% and RMSEP of 1.18%. Despite the similarity seen in those regression and residuals plots, systematic improvement can be seen as the markers are seen closer to the reference line. Comparing the regression plots of PLSR models of 1 mm and 4 mm offset spectra, the estimated solvent content is closer to the actual solvent content in the solvent content range of 0-5% for the PLSR model of the 1 mm offset spectra, and the estimated solvent content is closer to the actual solvent content in the range of 5-20% for the PLSR model of the 4 mm offset spectra. This shows that the minor difference between the PLSR performance of spectra from the offsets may be due to the differences in performance of predicting the solvent content over different solvent content ranges. This in turn could be related to the depth of the sample reached from each of the offsets.

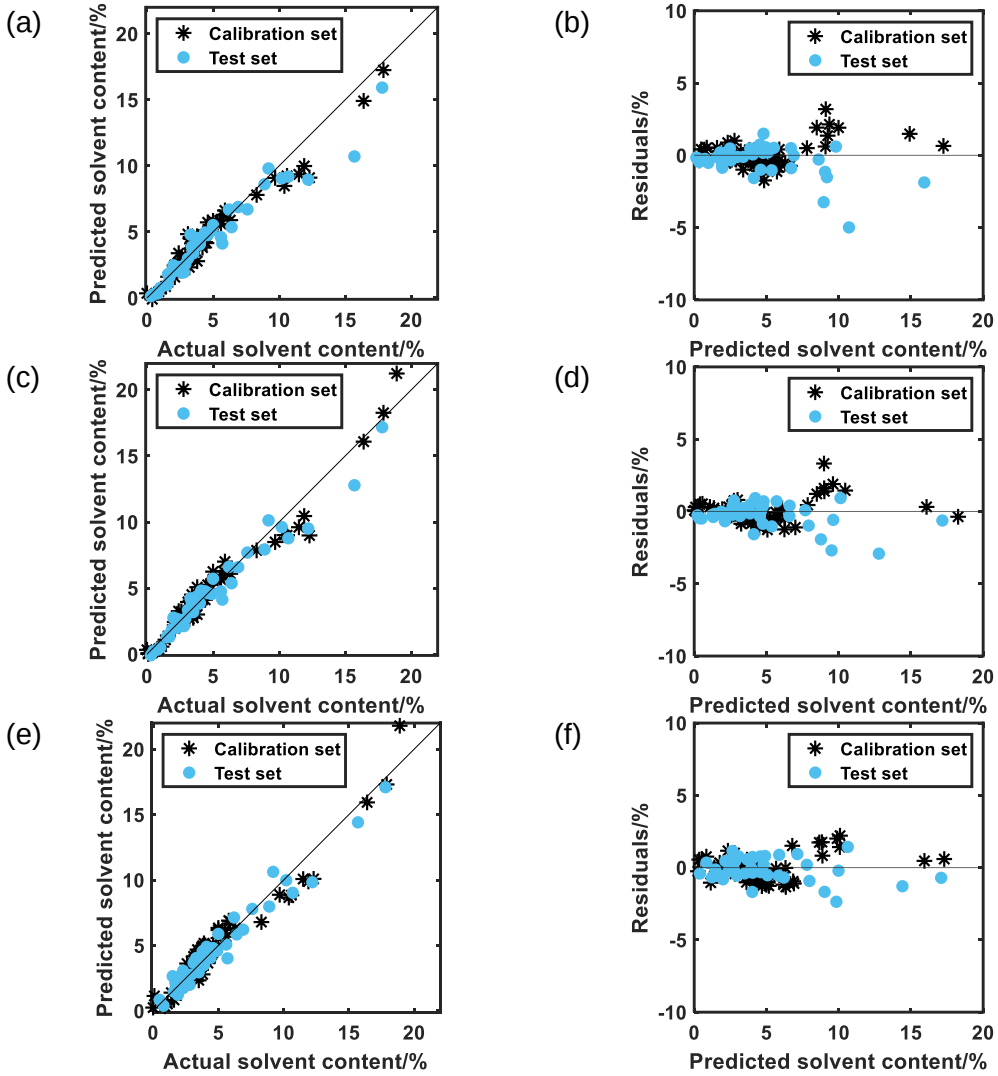

Figure 6.19. Regression and residuals plot of PLSR models constructed from (a-b) 0 mm, (c-d) 1 mm, and (e-f) 4 mm SNV pre-processed granular/MTBE spectra over 250-1750 cm^{-1}.

For the granular/MTBE system, the scores and loadings in Figure 6.20, Figure 6.21, and Figure 6.22 of the three LVs of the PLSR model of 0, 1, and 4 mm offset SNV pre-processed spectra, respectively, show the correlation of LV1 with paracetamol and LV2 with MTBE, while LV3 can be correlated to both system components as indicated by the loadings curve. The similarity between the figures reflects the close values of RMSECV and RMSEP seen in Table 6.1. Only small differences are seen in the scores of the LVs between the figures corresponding to each of the SORS offsets.

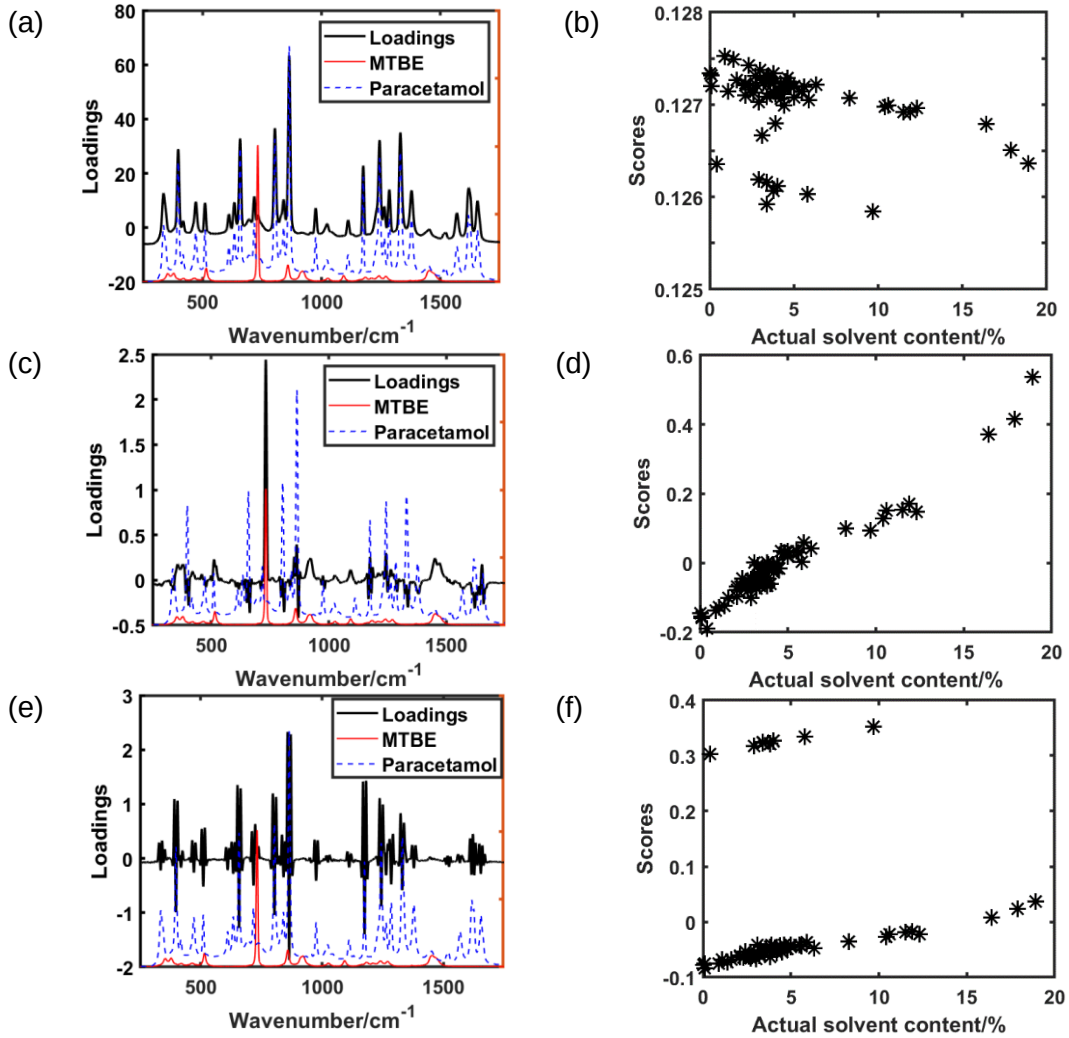

Figure 6.20. (a) loadings and (b) scores plots of LV1, (c) loadings and (d) scores of LV2, (e) loadings and (f) scores of LV3 of the PLSR model of the 0 mm offset SNV pre-processed spectra from the granular/MTBE system. Curves of the paracetamol and MTBE are also plotted with the loadings for reference.

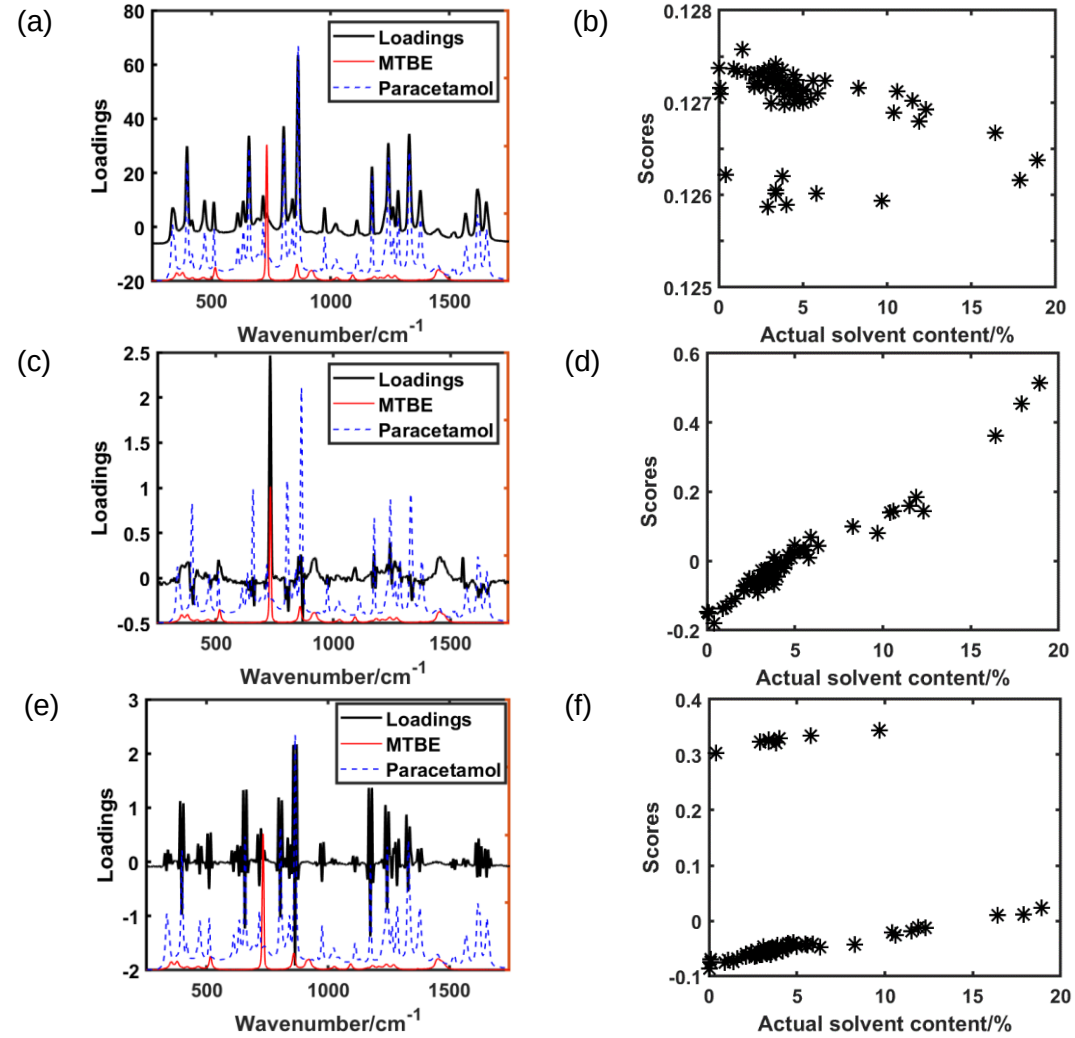

Figure 6.21. (a) loadings and (b) scores plots of LV1, (c) loadings and (d) scores of LV2, (e) loadings and (f) scores of LV3 of the PLSR model of the 1 mm offset SNV pre-processed spectra from the granular/MTBE system. Curves of the paracetamol and MTBE are also plotted with the loadings for reference.

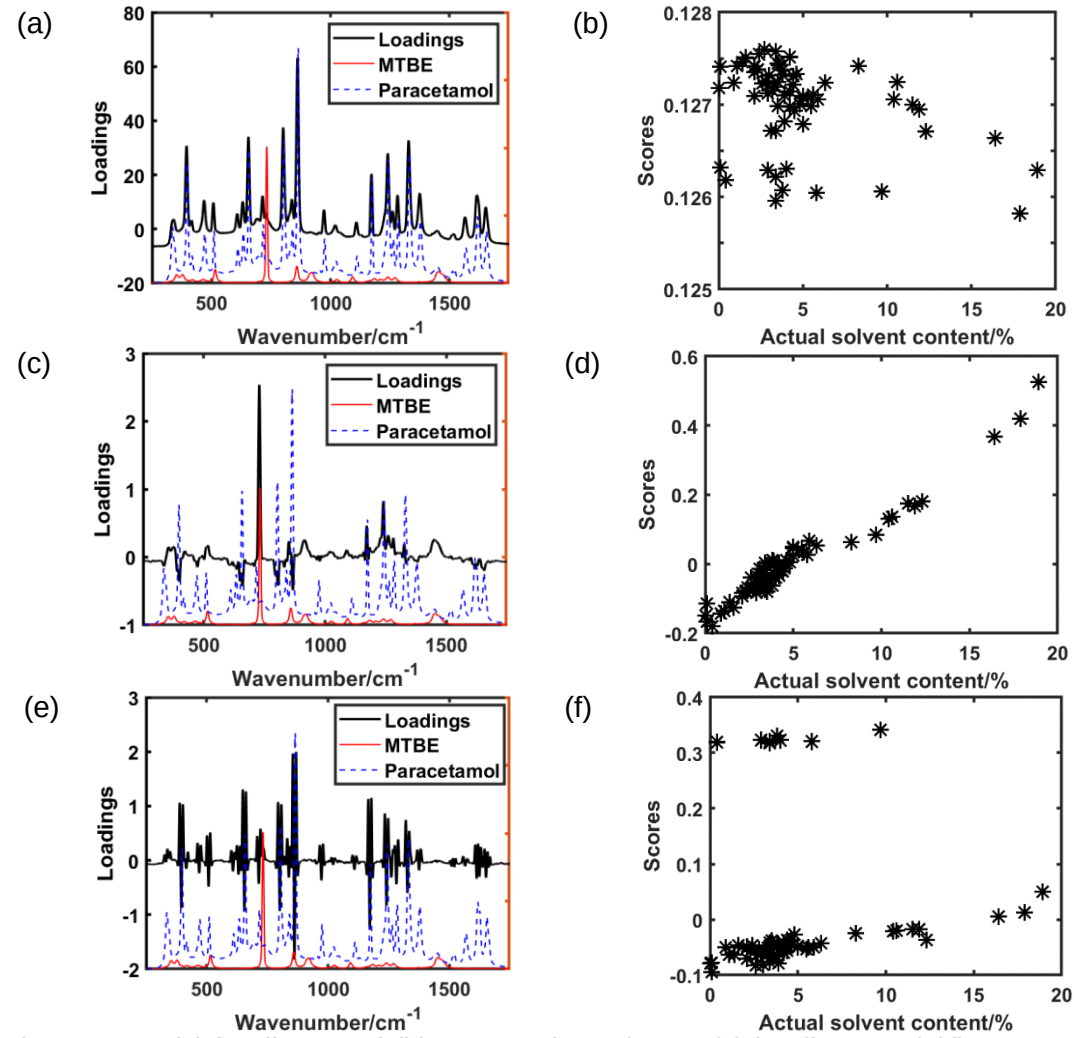

Figure 6.22. (a) loadings and (b) scores plots of LV1, (c) loadings and (d) scores of LV2, (e) loadings and (f) scores of LV3 of the PLSR model of the 4 mm offset SNV pre-processed spectra from the granular/MTBE system. Curves of the paracetamol and MTBE are also plotted with the loadings for reference.

Table 6.3 shows the percentage of variance captured by PLSR models of 0, 1 and 4 mm for further assessment of the improvement in PLSR performance of SORS spectra of the granular/MTBE system as the offset increases. PLSR model of SORS spectra of 1 mm from the granular/MTBE system shows the largest total sum of variance (98.51%), and variance related to the solvent content from LV2-3 (38.90%) compared to both 0 and 4 mm spectra. The higher percentage of variance related to the solvent content captured in the PLSR model of spectra from the 4 mm offset compared to the 0 mm spectra can explain the lower error seen with the 1 mm and 4 mm spectra.

Table 6.3. Percentages of variance captured in PLSR models SORS spectra from 0 and 4 mm of granular/anisole and 0, 1, and 4 mm of the granular/MTBE system.

Offset distance/mm	**0**	**1**	**4**
LV	Variance in LV/%		
1	59.69	59.61	59.61
2	38.19	38.56	38.25
3	0.42	0.34	0.35
Sum of variance related to the solvent	38.19	38.90	38.60
Sum of variance	98.23	98.51	98.20

Observations from the PLSR model performance of raw spectra of granular paracetamol in both anisole and MTBE in Table 6.1 show that lower RMSECV is seen as the offset distance increases. This decrease in RMSECV as the offset distance increases is maintained for the PLSR models of SNV pre-processed spectra of granular paracetamol in anisole, while the SNV pre-processed spectra of granular paracetamol in MTBE from all offsets perform similarly. Nevertheless, the PLSR models of SNV pre-processed 1 mm and 4 mm spectra from the granular/MTBE system were found to capture a larger percentage of variance related to the solvent content. The differences between SORS response in the two systems may be related to the signal obtained from each of the solvents, where the anisole spectrum includes a strong intensity peak with minimal overlap with paracetamol peaks, while the MTBE spectrum includes a peak that overlaps with paracetamol peaks.

Further evaluation of the estimation is done through the comparison of the drying profiles obtained from the reference LOD measurement of one of the runs, previously shown in Figure 6.4, and from the estimations of the PLSR models of SORS spectra of granular paracetamol in anisole and MTBE as shown in Figure 6.23. The drying profiles obtained through estimations from both solvent systems are similar to those obtained through the reference LOD method. It can be noted in Figure 6.23 (a) that the estimations from the PLSR model of the 0 mm offset spectra are consistently higher or lower than the reference LOD measurements, whereas the estimations from the 4 mm offset distance are closer to the reference value. Although the estimations in Figure 6.23 (b) follow a similar trend to that of the reference measurement, it can be noted that the each of the curves from each of PLSR models estimations is closer to other estimates compared to LOD curve. This may be contributed to errors arising from the reference LOD method or the SORS measurements as discussed in section 5.3.2.1.2.

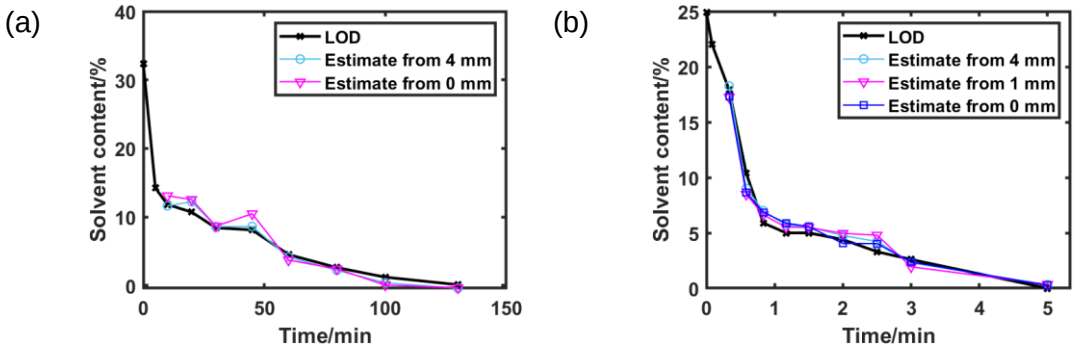

Figure 6.23. Solvent content from LOD and estimates from PLSR models of SNV pre-processed SORS spectra of 0, 1, and 4 mm collection offsets from the (a) granular/anisole and (b) granular/MTBE systems.

6.3.2.2 Powder paracetamol systems

PLSR models were constructed based on raw and SNV pre-processed spectra collected during the drying of powder paracetamol. The number of latent variables was selected after assessing the RMSECV curves shown in Figure 6.24 (a) for the powder/anisole system and Figure 6.24 (b) for the power/MTBE system. The RMSECV curves of raw powder/anisole spectra in Figure 6.24 (a) show a sharp decrease in RMSECV for 0-3 mm offsets compared to 4-5 mm, which decreases gradually suggesting that the variance in the 0-3 mm models is captured in fewer LVs. Following pre-processing, the overall level of RMSECV is lower, where the RMSECV curve of spectra from 5 mm offsets is the lowest among the other SORS spectra. The larger differences between the RMSECV curves of PLSR models of the raw spectra in Figure 6.24 (a) compared to the curves of the SNV pre-processed spectra can be related to the physical differences captured in the sample spectra and eliminated through pre-processing. The RMSECV curves of raw spectra from the powder/MTBE system in Figure 6.24 (b) show a narrow variation between the RMSECV curves of the PLSR model so of the offset spectra, which is further narrowed following SNV pre-processing.

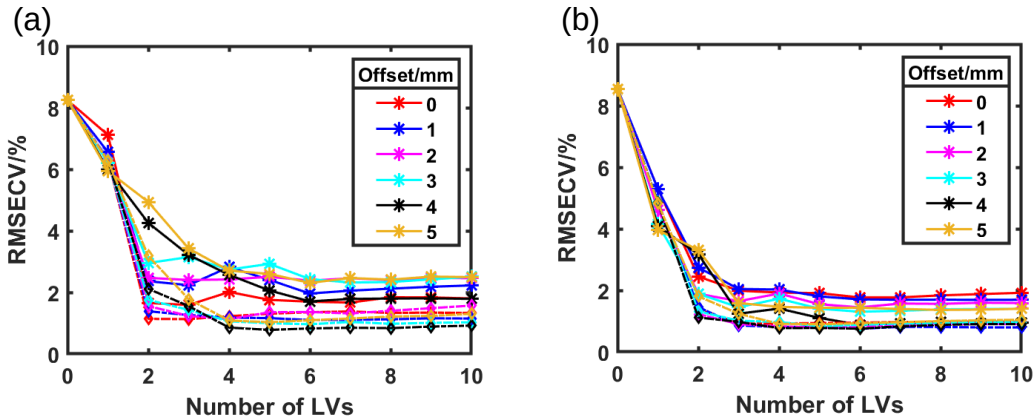

Figure 6.24. RMSECV of PLSR models constructed from raw (solid) and SNV pre-processed spectra (dashed) from 0-5 mm collected from powder paracetamol in (a) anisole and (b) MTBE.

Following the determination of the optimal number of LVs, characterised by the lowest RMSECV, after which the curves plateau, those calibration models were then used to predict the solvent content values of the test set for spectra of each of the offsets. A summary of the performance of the PLSR models is presented in Table 6.4. For the raw powder/anisole spectra, the RMSECV values are the lowest for PLSR models of 0 and 4 mm offset distances, with close R^2 values. This suggests a similar performance from PLSR models of those offset spectra. The PLSR models of the raw spectra from the offset distances 1-2 mm and 5 mm perform similarly and show higher RMSECV and lower R^2 compared to PLSR models of the 0 mm and 4 mm offset spectra, while the PLSR model of the 3 mm offset spectra shows the highest RMSECV. For all PLSR models of raw powder/anisole spectra, the RMSEP is higher compared to the RMSECV indicating additional variation in the test set that was not captured in the calibration sets. The PLSR models of the SNV pre-processed spectra show a decrease in the RMSECV compared to the raw spectra, which is attributed to the removal of physical effects from those spectra. A similar performance is seen between the PLSR models of the SNV pre-processed offset spectra, with a small decrease in the RMSECV as the offset distance increases to 4 mm then slightly increases for the 5 mm offset spectra. The R^2 values suggest a similarly linear response from all SNV pre-processed offset spectra. The RMSEP of the models of the pre-processed spectra is comparably higher than the RMSECV. This indicates that the scattering effect removed by SNV pre-processing was the cause of the higher RMSEP values seen in the models of the raw spectra.

For the PLSR models of the raw powder/MTBE spectra, the RMSECV decreases as the offset distance increases to 4 mm and increases for the 5 mm offset distance. The R^2 values increase as the offset distance increases indicating a slight increase in the variation explained by the PLSR models of the larger offset spectra. The RMSEP values of the PLSR models of the raw powder/MTBE spectra are comparable to the RMSECV, indicating that the calibration set sufficiently represents the dataset. The PLSR models of the SNV pre-processed powder/MTBE spectra show similar values of RMSECV,

with the lowest RMSECV being that of the PLSR model of the 4 mm offset spectra, which has the highest R^2 along with the PLSR model of the 1 mm offset spectra. The RMSEP values of the PLSR models of the SNV pre-processed spectra are also comparable and are the lowest for the PLSR models of the 4 mm offset spectra. The slight increase in RMSECV and RMSEP of the PLSR model of the 5 mm offset spectra can be attributed to the lower signal intensity seen for this offset.

Table 6.4. Summary of PLSR model performance of raw and SNV pre-processed spectra of powder paracetamol in anisole and MTBE from each of the offsets.

Grade/Solvent	Pre-processing	Raw				SNV Pre-processed			
	Offset distance/ mm	LV	RMSE CV/%	RMSE P/%	R^2	LV	RMSE CV/%	RMSE P/%	R^2
Powder/Anisole	0	3	1.59	3.23	0.93	2	1.14	1.34	0.97
	1	3	2.23	3.67	0.87	4	1.18	1.53	0.96
	2	3	2.40	3.99	0.85	4	1.13	1.60	0.97
	3	2	2.96	6.02	0.77	5	1.00	1.79	0.97
	4	6	1.71	4.50	0.92	5	0.78	1.93	0.98
	5	6	2.31	3.32	0.87	4	1.09	1.79	0.97
Powder/MTBE	0	4	1.93	1.46	0.84	3	0.92	0.55	0.96
	1	3	2.05	1.53	0.83	3	0.86	0.61	0.97
	2	3	1.65	1.10	0.88	3	0.90	0.77	0.96
	3	3	1.45	1.07	0.91	3	1.01	0.73	0.95
	4	3	1.24	1.32	0.93	4	0.77	0.48	0.97
	5	3	1.59	1.18	0.89	4	0.91	0.60	0.96

To investigate the differences between the PLSR model of the offset showing improved performance compared to the 0 mm offsets as a benchmark, the regression and residuals plots of the PLSR models of spectra from 0 and 4 mm offsets of the powder/anisole system are shown in Figure 6.25 (a-b) and (c-d), respectively. Comparing Figure 6.25 (a) and (c) show a similar distribution of the calibration set points around the reference line in PLSR models of both 0 and 4 mm offset spectra over the entire solvent content range.

However, the test set points are more uniformly distributed in Figure 6.25 (a). This is similarly seen in Figure 6.25 (b) and (d).

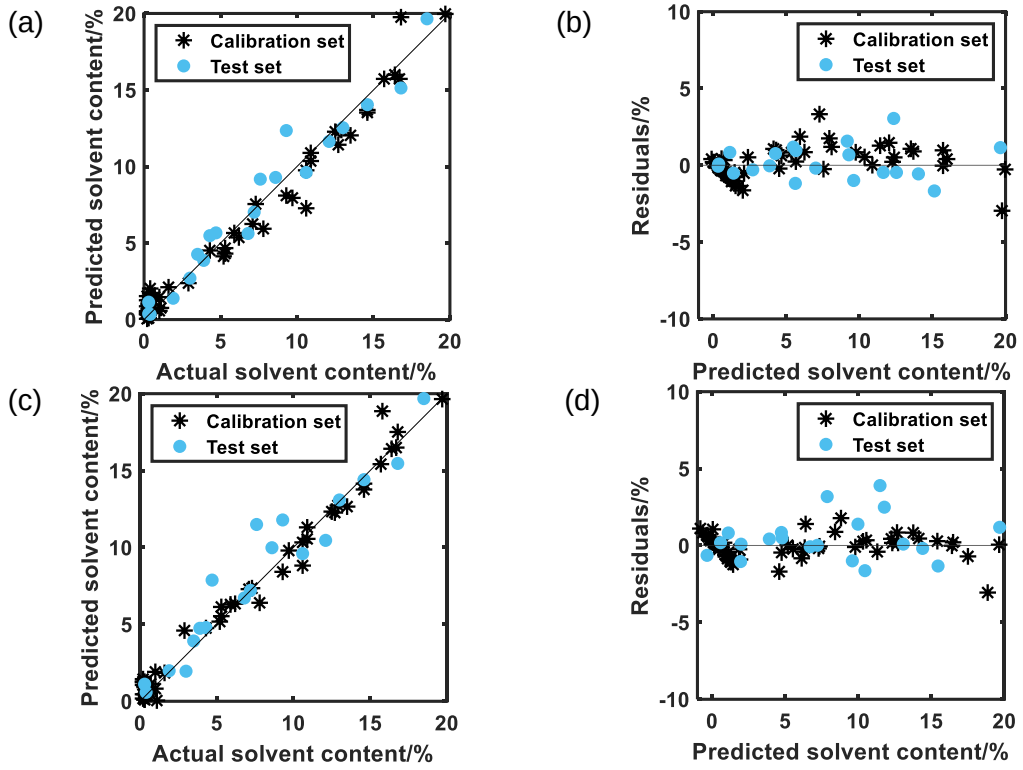

Figure 6.25. Regression and residuals plot of PLSR models constructed from (a-b) 0 mm, (c-d) 4 mm SNV pre-processed powder/anisole spectra over 250-1750 cm^{-1}.

To further investigate the PLSR model performance, the loadings and scores of the PLSR model corresponding to SNV pre-processed SORS spectra from 0 mm and 4 mm offsets of the powder/anisole and powder/MTBE systems were also assessed. The loadings and scores of the two latent variables capturing the variance of the 0 mm offset spectra from the powder/anisole system are shown in Figure 6.26. The loadings curves suggest that LV1 is correlated with paracetamol while the scores do not show a clear trend related to the increase in solvent content. The loading of LV2 is similar to the anisole spectrum suggesting that this LV captured variance related to the solvent content, while the scores show a clear trend of increase as the solvent content increases. For the powder/anisole PLSR model of SORS spectra from 4 mm,

5 LVs capture the variance from the system. The first two LVs can be correlated to paracetamol and anisole, respectively, as was seen from the 0 mm offset PLSR. However, for this offset, 3 more latent variables were needed to capture the variance. Loadings of LVs 2-4 show a correlation to anisole and the scores of LV3 increase as the solvent content increases in those figures. Loadings and scores of LV5 do not show a clear correlation to either component. Compared to the PLSR model of 0 mm offset spectra, the PLSR model of the 4 mm offset spectra includes three additional latent variables, two of which include variance related to the solvent content as suggested by the loadings and scores.

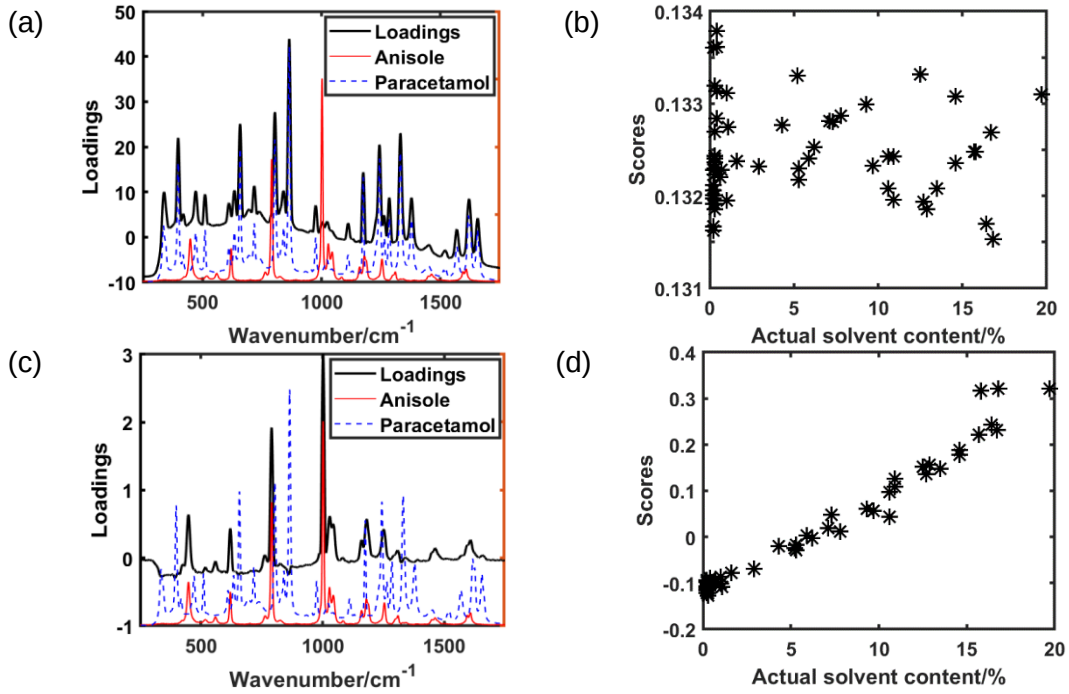

Figure 6.26. (a) loadings and (b) scores plots of LV1, (c) loadings and (d) scores of LV2 of the PLSR model of the 0 mm offset SNV pre-processed spectra from the powder/anisole system. Curves of the paracetamol and anisole are also plotted with the loadings for reference.

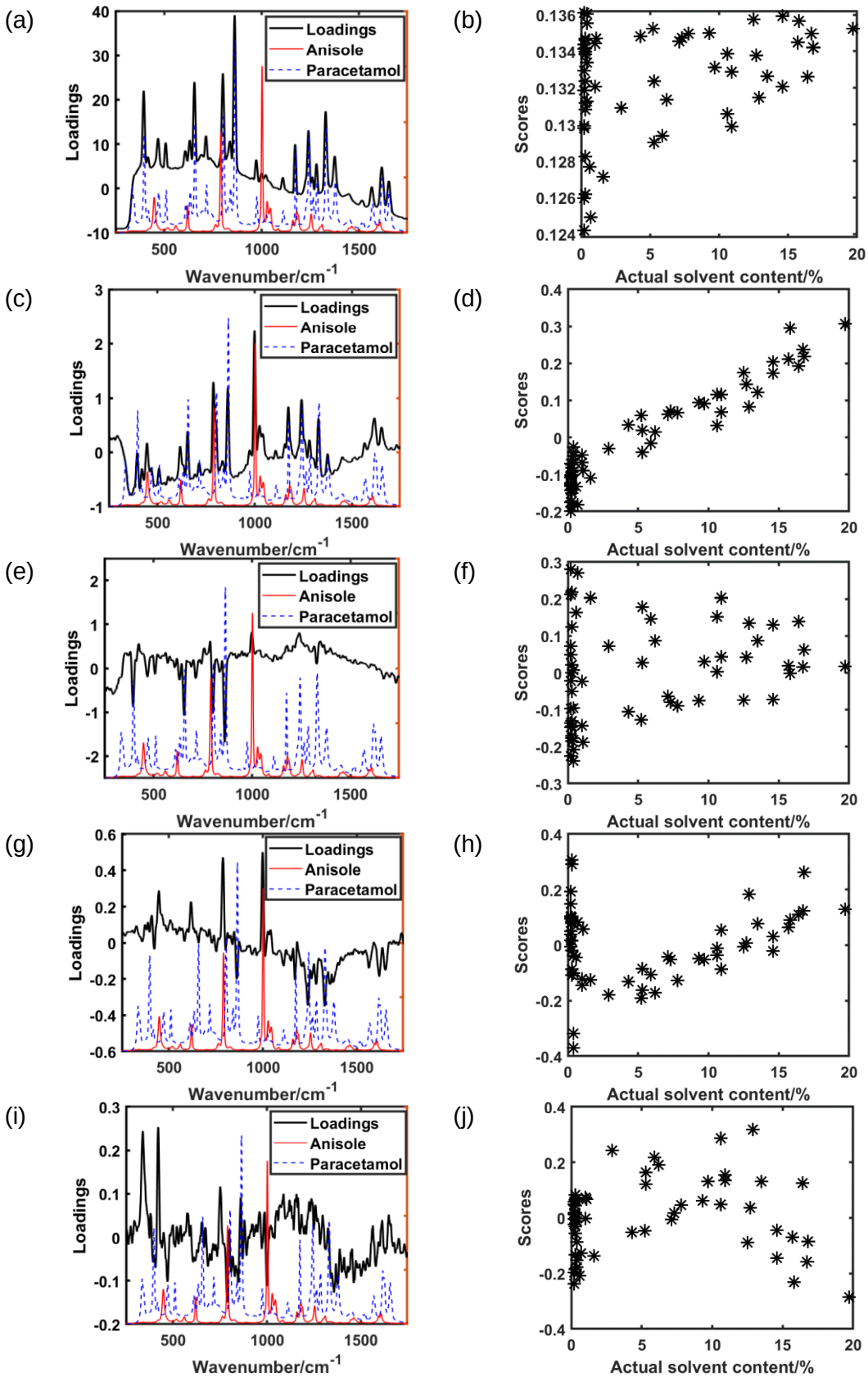

Figure 6.27. (a) loadings and (b) scores plots of LV1, (c) loadings and (d) scores of LV2 of the PLSR model of the 4 mm offset SNV pre-processed spectra from the powder/anisole system.

A comparison of the variance captured by the 0 mm and 4 mm offsets of the SNV pre-processed SORS spectra is shown in Table 6.5. The percentage related to the solvent content is higher for the 4 mm spectra compared to the 0 mm spectra from the powder/anisole system; Nevertheless, the total sum of the percentage of variance captured in the models of spectra from the larger offsets is higher compared to that of the 0 mm offset spectra in both systems. Therefore, the improvement in the PLSR performance of SORS spectra from the 4 mm offset may be attributed to the larger percentage of variance captured in those models compared to the conventional 0 mm spectra.

Table 6.5. Percentages of variance captured in PLSR models SORS spectra from 0 and 4 mm of powder/anisole system.

Offset distance/mm	**0**	**4**
LV	Variance in LV/%	
1	45.32	46.03
2	53.05	48.24
3	-	3.30
4	-	1.68
5	-	0.21
Sum of variance related to the solvent	53.05	53.21
Sum of variance	98.36	99.45

The regression and residuals plots of PLSR models of spectra from 0 and 4 mm offsets of the powder/MTBE system are shown in Figure 6.28 (a-b) and (c-d), respectively. The improvement seen in Figure 6.28 (c-d) of the 4 mm spectra is the lower error over the solvent content range as compared to Figure 6.28 (a-b) of the 0 mm spectra PLSR model which displays a higher error over the solvent content range 10-20%. This may be attributed to the lower number of sample spectra representing the solvent content range. The observation from the PLSR model of the 4 mm spectra suggests that those could estimate the solvent content more accurately over the solvent content range.

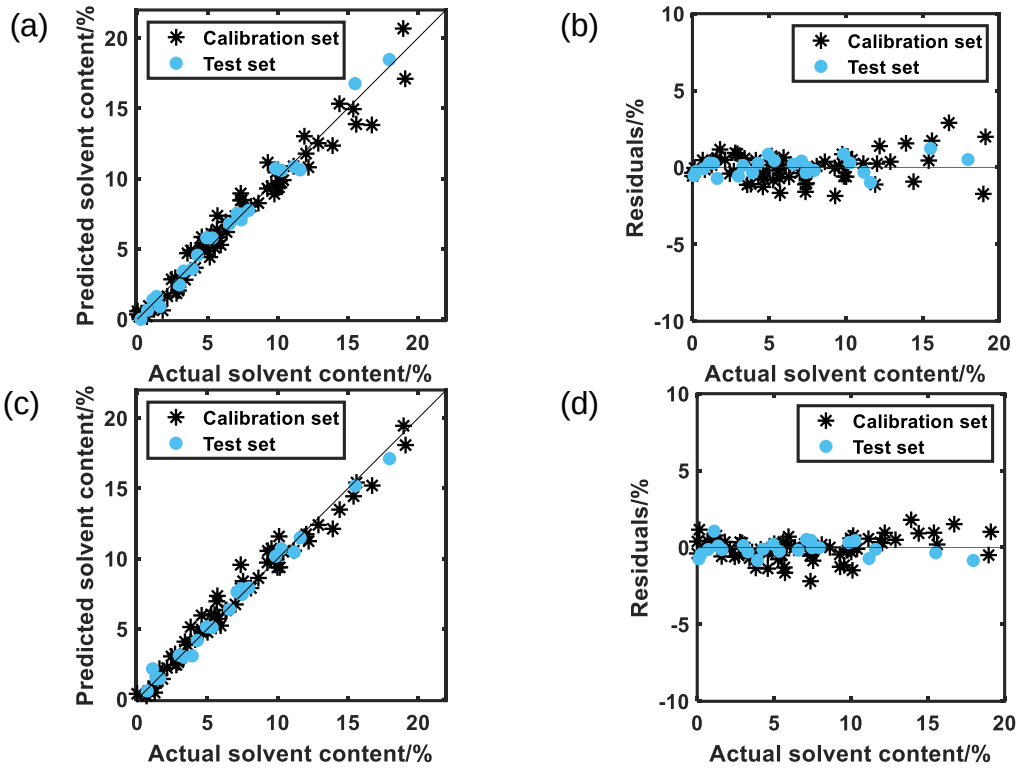

Figure 6.28. Regression and residuals plot of PLSR models constructed from (a-b) 0 mm, (c-d) 4 mm SNV pre-processed powder/MTBE spectra over 250-1750 cm^{-1}.

The loadings and scores of the three LVs capturing the variance of the 0 mm offset spectra of the powder/MTBE system are shown in Figure 6.29. The loadings curve of LV1 shows a correlation to paracetamol while the scores look to decrease as the solvent content decreases. The loadings of LV2 show peaks corresponding to MTBE and the scores increase as the solvent content increases. Loadings of LV3 show peaks corresponding to both MTBE, at 730 cm^{-1}, and paracetamol over the full wavenumber range. The loadings and scores of the four LVs of PLSR of the 4 mm spectra from the powder/MTBE system are shown in Figure 6.30. LV1-2 show a similar trend to the 0 mm spectra. Loadings of LV3 show peaks from both paracetamol, at the wavelength range 250-1000 cm^{-1}, and MTBE at 730 cm^{-1} suggesting a contribution from both components. Compared to the PLSR model of 0 mm offset spectra, the PLSR model of the 4 mm offset spectra includes an additional latent variable capturing solvent-related information.

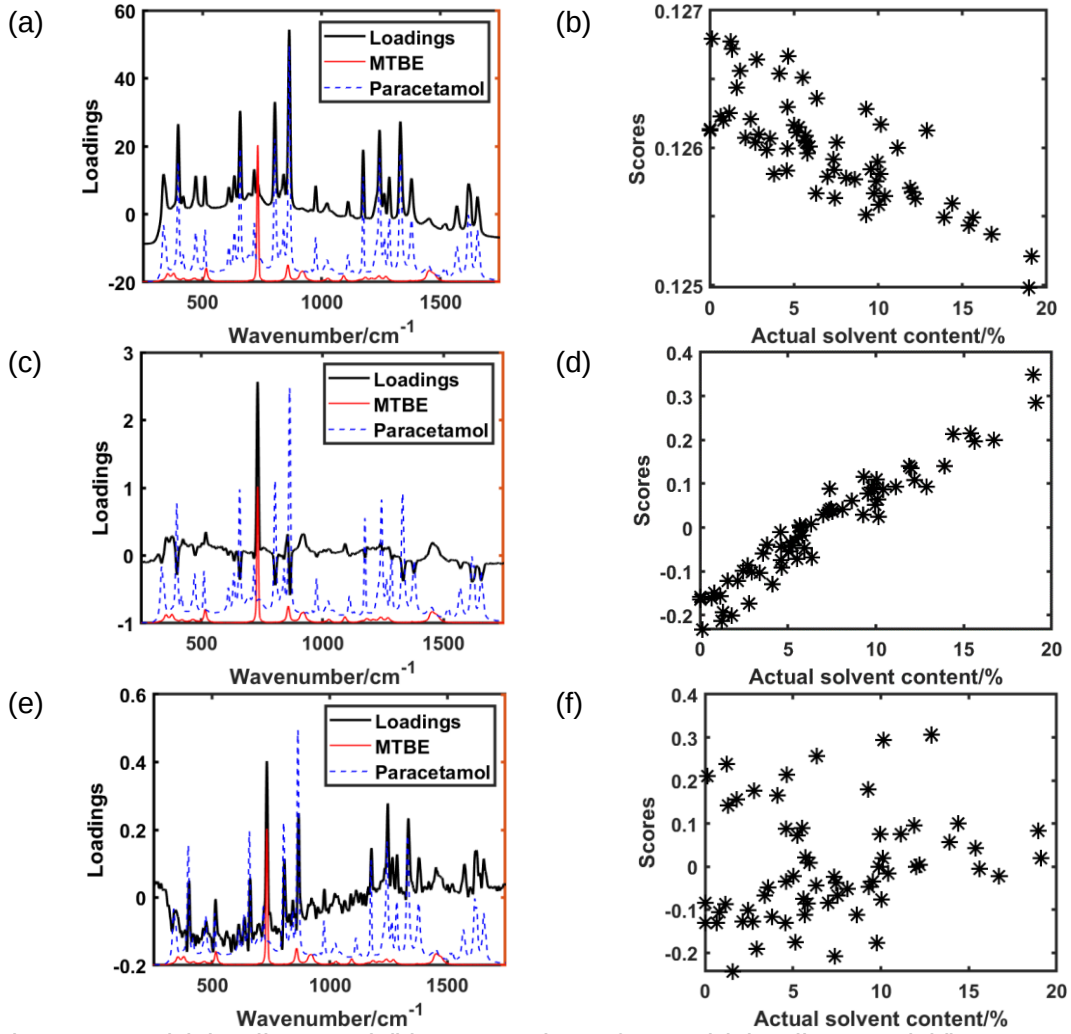

Figure 6.29. (a) loadings and (b) scores plots of LV1, (c) loadings and (d) scores of LV2 of the PLSR model of the 0 mm offset SNV pre-processed spectra from the powder/MTBE system. Curves of the paracetamol and MTBE are also plotted with the loadings as a reference.

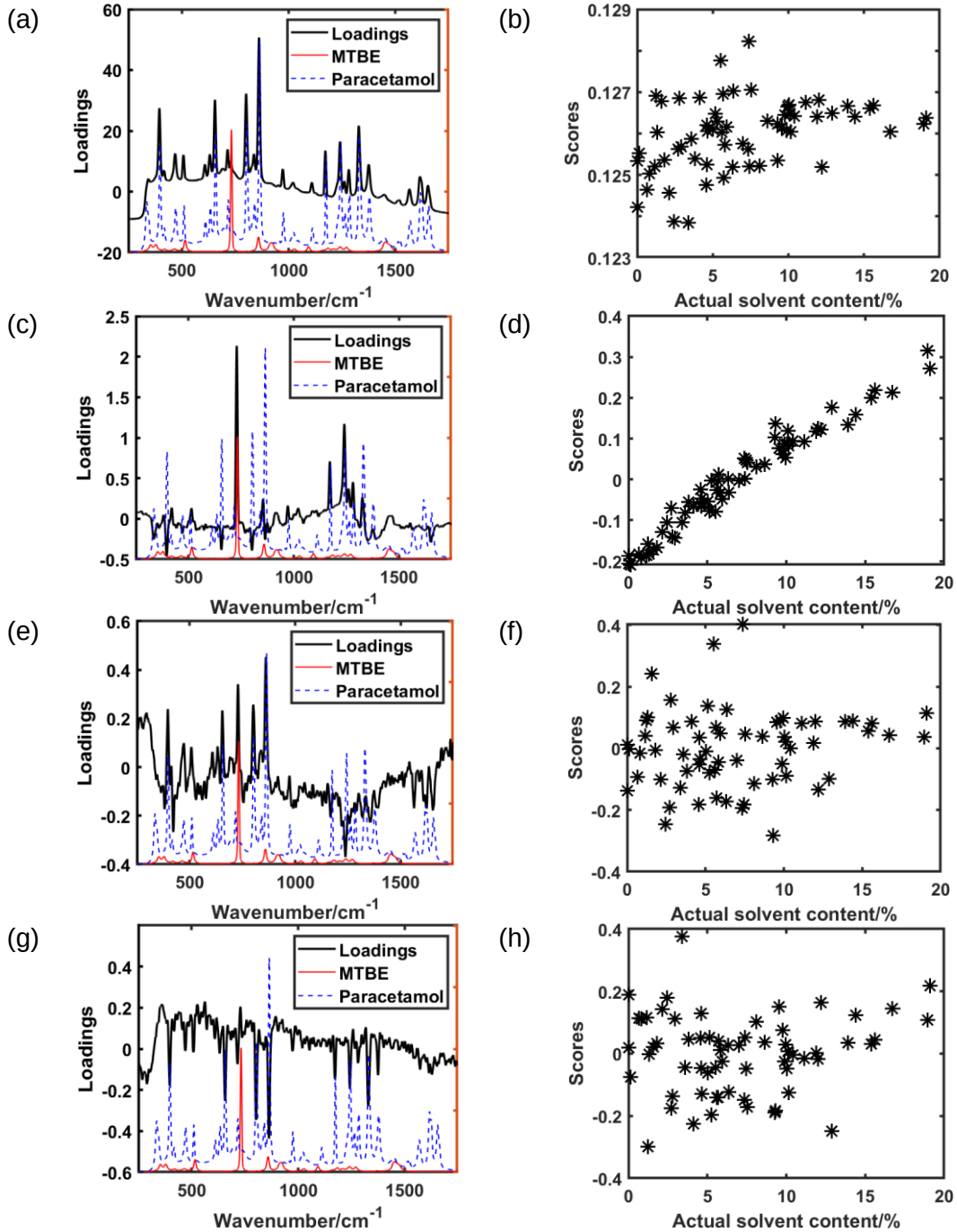

Figure 6.30. (a) loadings and (b) scores plots of LV1, (c) loadings and (d) scores of LV2 of the PLSR model of the 4 mm offset SNV pre-processed spectra from the powder/MTBE system. Curves of the paracetamol and MTBE are also plotted with the loadings as a reference.

A comparison of the variance captured by the 0 mm and 4 mm offsets of the SNV pre-processed SORS spectra is shown in Table 6.6. The percentage related to the solvent content is higher for the PLSR model of the 0 mm spectra compared to the 4 mm spectra from the powder/MTBE system. The smaller difference in percentage seen between the variance captured by the PLSR model of the powder/MTBE systems explains the similarity in the level of error obtained from those offset spectra.

Table 6.6. Percentages of variance captured in PLSR models SORS spectra from 0 and 4 mm of powder/anisole and the powder/MTBE system.

Offset distance/mm	**0**	**4**
LV	Variance in LV/%	
1	68.68	69.14
2	29.16	29.49
3	1.28	0.50
4	-	0.31
Sum of variance related to the solvent	30.44	30.30
Sum of variance	99.12	99.44

In the granular/solvent systems, an improvement in PLSR model performance was seen as a reduced RMSECV and increased R^2 as the collection offset distance increased. In the power/solvent systems, slight improvement could be seen for some of the offset spectra. The differences in the performance of the PLSR models of spectra from the four systems can be attributed to the variation in signal between the paracetamol grades, where higher signal intensity is seen from the granular paracetamol, and the signal obtained from the solvents, where anisole spectra feature a strong intensity peak while the main MTBE peak overlaps with a paracetamol peak. Further analysis is reported in the following section to investigate the observations and enable a general conclusion regarding both of the paracetamol/solvent systems.

6.3.2.3 The effect of wavenumber ranges on PLSR performance

PLSR models were constructed using smaller wavenumber ranges using the granular/anisole and granular/MTBE SORS datasets to evaluate the effect of wavenumber selection on PLSR model performance from the SORS offsets. This would further enable supporting conclusions based on observations from the analysis in sections 6.3.2.1 and 6.3.2.2.

6.3.2.3.1 PLSR using select wavenumber ranges in the granular/anisole spectra

In addition to the full wavenumber range of 250-1750 cm^{-1}, with which the analysis in the previous section was done, four wavenumber ranges were selected. The four wavenumber ranges are 985-1015, 960-1040, 750-850, and 400-500 cm^{-1}. The wavenumber range 985-1015 cm^{-1} includes the strong anisole peak around 1002 cm^{-1} and was selected so as to eliminate sources of variation that might be introduced when using the full spectral range in the PLSR analysis. The wavenumber range 960-1040 cm^{-1} was chosen in order to include a peak of paracetamol in addition to that of the anisole peak, representing an intermediate between the full wavenumber range and 985-1015 cm^{-1}. Wavenumber range 750-850 cm^{-1} includes an anisole peak with strong intensity but overlapping with a paracetamol peak, while the range 400-500 cm^{-1} includes a non-overlapping anisole peak of small intensity. These two wavenumber ranges were selected to gain more insight into whether the solvent-API peak overlap or signal intensity would have more impact on the PLSR performance.

Figure 6.31 shows the RMSECV and RMSEP values for the PLSR models of spectra over the wavenumber ranges described earlier, plotted against each of the offsets. The RMSECV and RMSEP of the PLSR models of the wavenumber range overall follow the same trend as they decrease with offset increases up to 4 mm. The wavenumber ranges 250-1750, 960-1040, 985-1015, and 750-850 cm^{-1} show similar error values. Compared to the other wavenumber ranges, the RMSECV and RMSEP are higher for the

wavenumber range that includes a solvent peak of small intensity, 400-500 cm^{-1}, which highlights the impact of signal intensity on the performance of the PLSR analysis. Among the PLSR of spectra from the offset distances, the error over the wavenumber ranges is more consistent for spectra from a 4 mm offset distance. This suggests a more robust performance of spectra from this offset distance.

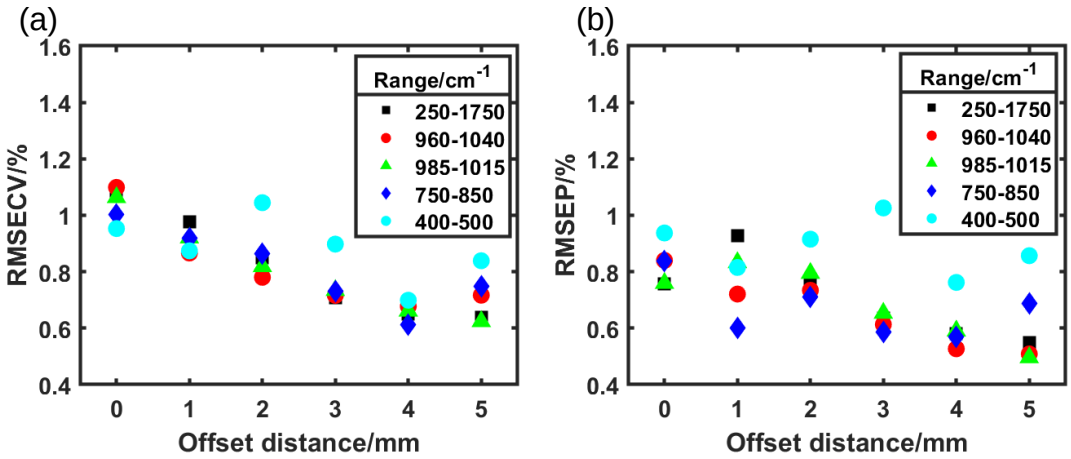

Figure 6.31. (a) RMSECV and (b) RMSEP of PLSR models of SNV pre-processed granular/anisole spectra over five wavenumber ranges.

6.3.2.3.2 PLSR using select wavenumber ranges in the granular/MTBE spectra

In addition to the full wavenumber range of 250-1750 cm^{-1}, PLSR analysis was conducted using the wavenumber range 670-770 cm^{-1}, which contains the main MTBE peak. Figure 6.32 shows a comparison of the RMSECV and RMSEP obtained from SORS spectra at each of the wavenumber ranges. The RMSECV values follow a similar trend for both wavenumber ranges for the PLSR of all offsets, where the RMSECV obtained for the PLSR model of spectra from 1 mm offset is slightly lower. The RMSEP values notably decrease as the offset distance increases for PLSR over the range 670-770 cm^{-1} compared to the full wavenumber range. The decrease in RMSEP of models of the wavenumber range including the main MTBE peak suggests that excluding the other, mainly paracetamol, peaks lead to better prediction.

Despite applying SNV pre-processing to remove scattering effects and emphasise the change in the solvent peak intensity, some residual variation still affects the PLSR model performance as indicated by the lower RMSEP of the model of the smaller wavenumber range.

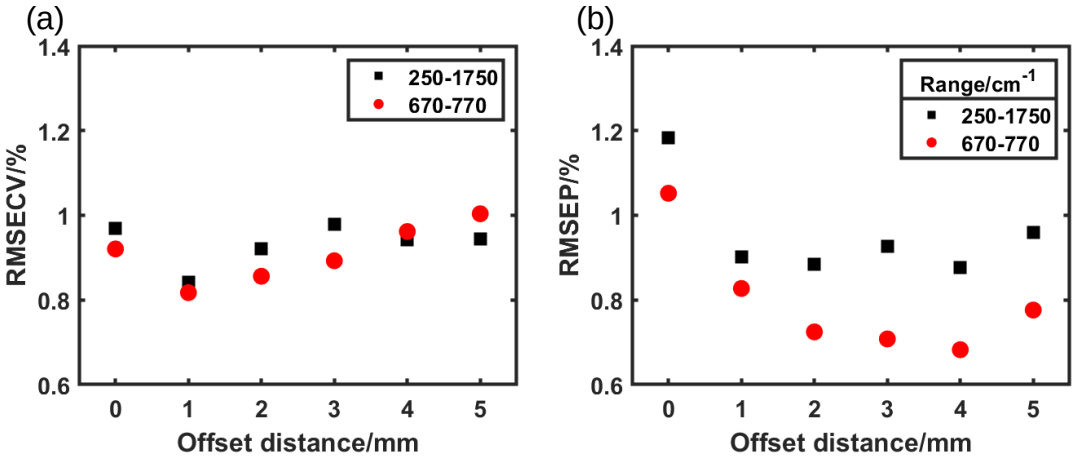

Figure 6.32 (a) RMSECV and (b) RMSEP of PLSR models of SNV pre-processed granular/MTBE spectra over two wavenumber ranges.

6.3.2.4 PLSR analysis combining spectra from multiple configurations

Two methods, augmentation and co-addition, were employed for combining spectra from multiple configurations (collection offset distances). In augmentation, multiple blocks of spectra from multiple configurations are concatenated, and a PLSR model is constructed using the multi-block. In co-addition, spectra from multiple configurations are summed up. SNV pre-processed spectra from two configurations were augmented or co-added in order to enrich PLSR models with data that could lead to more accurate solvent content prediction as it represents multiple layers of the measured sample as opposed to probing a larger volume or depth as the results indicated in sections 6.2 and 6.3.2.1. This was done using SNV pre-processed spectra from the granular paracetamol in anisole system as the RMSECV and RMSEP were seen to decrease as the offset increases for those PLSR models. Granular/anisole spectra from the 4 mm offset distance are combined with spectra from other offset distances to investigate any improvement.

Figure 6.33 shows the RMSECV obtained for the combination of spectra from all offsets with the 4 mm offset spectra compared to the individual spectra and the combination of spectra from all configurations, which is a close representation of the signal obtained from commercial probes. In this figure, the RMSECV and RMSEP obtained from the combinations are values in between those obtained from the individual configurations. In other words, the error is higher than that of the PLSR model of the 4 mm spectra and lower than the other configurations. Combining the spectra through augmentation leads to lower error compared to the PLSR model of the individual offset spectra combined with 4 mm spectra. In contrast, co-addition leads to a similar error to the PLSR model of the individual spectra combined with 4 mm spectra for most offsets except for the 0 mm spectra, which are of stronger intensity. Co-adding spectra from all offsets led to RMSECV and RMSEP values similar to that of the PLSR model of SORS spectra from the configuration with the highest error while combining those spectra through augmentation resulted in slightly lower error compared to co-addition. This suggests that the improvement seen in PLSR performance is the result of including the 4 mm offset spectra.

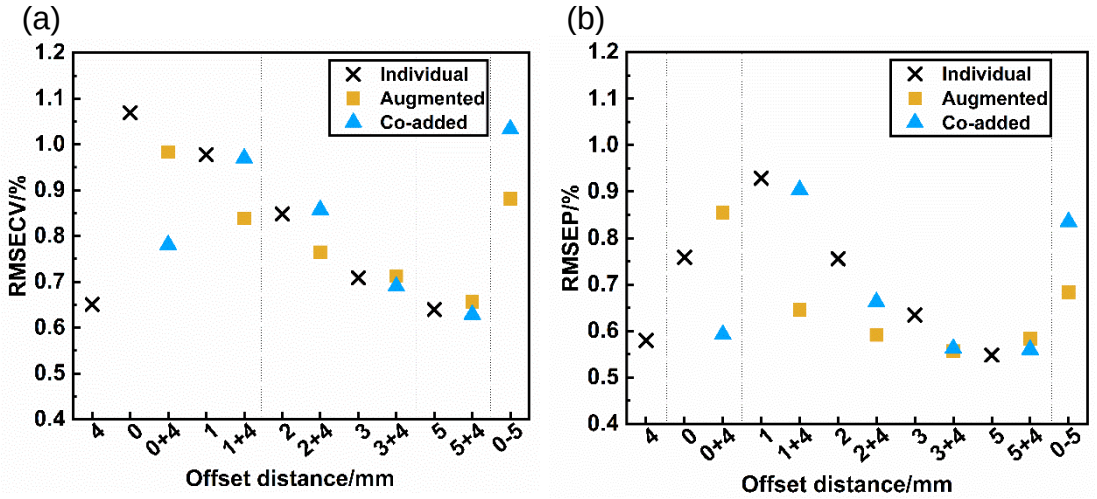

Figure 6.33. (a) RMSECV and (b) RMSEP of SNV pre-processed spectra of granular paracetamol in anisole from 4 mm offset combined with other detectors compared to those of individual detectors. Dotted lines are added as a guide.

6.4 Conclusions

An experiment was conducted to determine the depth through which the signal from a solvent, anisole, may be detected underneath layers of dry API, granular paracetamol. The results showed that the depth through which the solvent signal is detected increases as the offset distance increases, where offset distances of 4-5 mm enable the detection of the solvent signal from depths beyond 6 mm. This provided practical validation for using SORS to monitor pharmaceutical drying.

Then, SORS spectra were collected during the drying of two paracetamol grades, granular and powder, in two solvents, anisole and MTBE. The spectra from the four systems were analysed qualitatively and quantitatively through PLSR analysis. Qualitative analysis from the four systems showed the change in solvent signal intensity can be seen in all offset distance spectra. Furthermore, the characteristic signal intensity decrease seen in SORS as the offset distance increases were countered up to the 4 mm offset distance through the design of the SORS probe, which includes additional collection fibres for the larger offset distances. However, SORS spectra from the 5 mm offset distance suffered from a lower level of intensity compared to the other offset spectra. SNV pre-processing was employed to remove physical scattering effects seen in sample spectra.

PLSR analysis of raw SORS spectra from the granular/solvent systems showed that the RMSECV and RMSEP mostly decrease as the offset distance increases up to 4 mm. Employing SNV pre-processed SORS spectra in PLSR analysis resulted in improved model performance characterised by reduced RMSECV and increase in R^2 compared to the raw spectra. Moreover, RMSECV decreases as the offset distance increases up to 5 mm, showing the particular significance of pre-processing to the signal of lower intensity. Further comparison of the loadings, scores, and percentage of variance captured for the 0 and 4 mm or better performing distance offset spectra showed that PLSR models of the spectra from the larger offset distance capture a higher percentage of solvent-related variance and higher overall total sum of variance

in the PLSR model. The PLSR analysis of SORS spectra from the powder/solvent systems showed some improvement from spectra from the larger offsets. However, the decrease in RMSECV was slight and did not always follow the same trend that was seen in the PLSR of the granular/solvent SORS spectra.

Using wavenumber ranges that contain solvent peaks in PLSR analysis of the granular/anisole system showed that the PLSR model performance of SNV pre-processed spectra over the wavenumber range containing the main solvent peak performed similarly to that of the full spectral range, and that the wavenumber range containing the lower intensity peak had inferior performance compared to that of a strong solvent peak overlapping with a paracetamol peak. For the granular/MTBE system, using a wavenumber range containing the main solvent peak led to reduced RMSECV compared to the full spectral range, in addition to a clearer trend of decrease in RMSECV as the offset distance increases.

SORS spectra of the granular/anisole system from the individual configurations were combined with that of the 4 mm spectra, which previously showed the most improved performance, in PLSR analysis using augmentation and co-addition. Augmentation led to error values lower than the individual offset configuration smaller than 4 mm, but higher than that of the 4 mm offset spectra. This suggested that the improvement seen is a result of including the 4 mm offset spectra. Error values close to the individual spectrum combined with 4 mm spectra were obtained through co-addition for all offsets except for the 0 mm spectra. Augmentation of spectra from all offsets led to an error that is between those of the individual configurations, while co-addition spectra from all offsets led to error values similar to that of the SORS spectra from the configuration with the highest error. Considering the signal collected from the 0 mm offset as a representation of the signal collected from a conventional Raman system, the results presented in this chapter show superior performance by the spatially offset configurations.

The decrease in error of the estimated solvent content seen from PLSR models of the spatially offset spectra suggests that this technique can be used for the monitoring of the decrease in solvent content along with the determination of the end point of the process for suitable API and solvent systems. Overall, the results in these studies show the potential for SORS for application for the monitoring of pharmaceutical drying as indicated by the solvent signal detected from larger depths using larger offset distances, and the improved estimation of solvent content through SORS spectra collected during drying.

7. Combining SR-DRM and SORS for Monitoring Pharmaceutical Drying

7.1 Introduction

Near-infrared and Raman spectroscopy are complementary techniques. While Raman active molecules are those that include symmetric non-polar bonds, near-infrared active molecules possess asymmetric polar bonds. This means that sample spectra of both techniques collected at the same point during drying would reflect the same sample solvent content level.

The results in Chapter 5 and Chapter 6 have demonstrated the capability and suitability of the spatially resolved diffuse reflectance near-infrared and spatially offset Raman spectroscopy for the monitoring of the solvent content during pharmaceutical drying. This Chapter explores the multi-block analysis of spectra of the drying of paracetamol in methyl tert-butyl ether (MTBE) collected using both techniques simultaneously in PLSR analysis for predicting the solvent content.

7.2 SR-DRM and SORS for the monitoring of drying

From the previously monitored paracetamol/solvent systems in Chapters 5 and 6, MTBE spectra displayed NIR and Raman peaks enabling the use of both techniques to monitor the decrease in MTBE content during the drying process. Since it has been demonstrated in the previous two chapters that both SR-DRM and SORS were applicable techniques for monitoring the solvent content, this chapter also includes results of monitoring the drying of granular and powder paracetamol in MTBE collected simultaneously using the combined probe.

Seven drying runs of granular paracetamol and six of powder paracetamol in MTBE were conducted using the same procedure as those monitored with the individual probes described in section 4.3.2. The drying profiles for both grades are shown in Figure 2.1 and are typical of solvents of low boiling points,[26] as previously described in Chapter 2. Similar observations to what was seen in the paracetamol/MTBE runs in Figure 5.3 and Figure 6.4 were seen in this figure, where there is an initial sharp decrease in the solvent content, suggesting that this corresponds to the evaporation of the unbound solvent, followed by a gradual decrease, which may be attributed to the bound solvent. The powder grade requires a longer duration of drying compared to the granular grade. The larger surface area of the smaller powder paracetamol particles allows for larger amounts of the solvent to be retained in addition to the higher likelihood of the coalescence of those particles to form larger agglomerates in which more solvent could be trapped.[19]

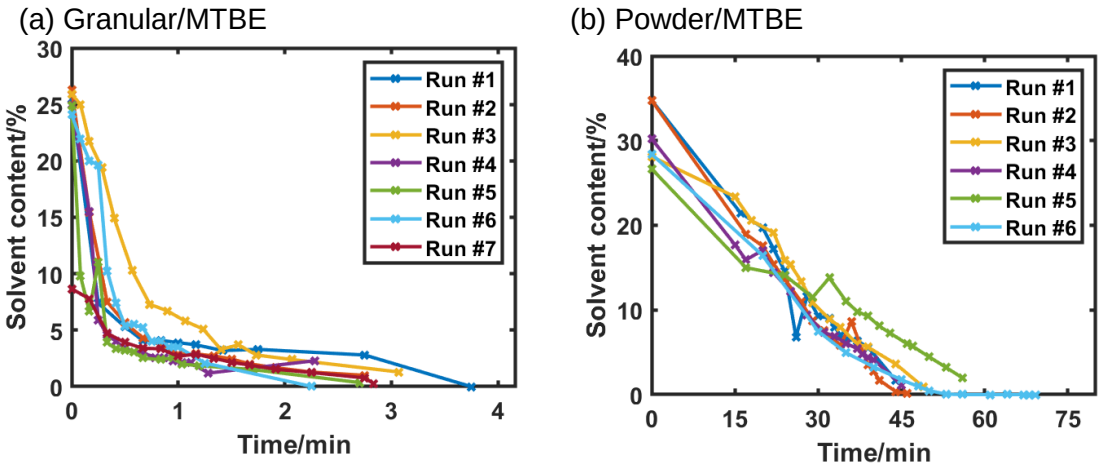

Figure 7.1. The drying profile of (a) granular and (b) powder paracetamol in MTBE monitored using the combined probe. The crosses indicate the measurement points.

Prior to the multi-block analysis of SR-DRM and SORS spectra collected using the combined probe in granular and powder paracetamol in MTBE systems, spectra from each of the techniques were analysed separately in order to assess the dataset's performance compared to the previous datasets collected using the individual probes in chapter 5 and chapter 6.

7.2.1 PLSR analysis results of SR-DRM spectra

Table 7.1 provides a summary of PLSR analysis results of raw and SNV pre-processed SR-DRM spectra of both paracetamol grades in MTBE from the four collection distances, 0.3-1.2 mm. Results of the PLSR analysis of raw granular and powder paracetamol in MTBE spectra show that a similar number of latent variables is required to capture the variance from those spectra suggesting a similar level of complexity in those PLSR models. Larger collection distances of 0.6-0.9 mm of the granular/MTBE system use a slightly larger number of LVs, 6 or 7, but the variance captured through those additional LVs may not be related to the change in solvent content. From Table 7.1, a decrease in RMSECV as the collection distance increases to 0.9 mm is seen, with a slight increase for RMSECV of the PLSR model of the 1.2 mm spectra. The corresponding R^2 values follow the opposite trend of RMSECV, suggesting an improvement in linearity as the collection distance increases. The RMSEP values are comparable to the RMSECV and follow the same trend, suggesting that the calibration set sufficiently represents the system.

For the SNV pre-processed spectra, PLSR analysis results show lower RMSECV values compared to PLSR results of the raw spectra, suggesting that SNV pre-processing resulted in the removal of some of the random variability within the datasets. The decrease in RMSECV is associated with higher R^2 values compared to the raw spectra, indicating the improvement in linearity in those PLSR models following pre-processing. The RMSEP values are also lower in the PLSR models of SNV pre-processed spectra compared to those of the raw spectra. Nevertheless, the PLSR analysis results of both raw and SNV pre-processed spectra show that the decrease in RMSECV between spectra of the collection distances is seen up to 0.9 mm with a slight increase in spectra from the 1.2 mm collection distance. This suggests that those spectra may be a result of more scattering incidents of photons with wet particles, but also express a higher level of noise as a result of the low signal intensity resulting from the diffusion of the light. As previously described in Chapter 5 detailing the results of the analysis of SAR-DRM spectra collected using the SAR-DRM probe, spectra collected from the largest distance are of

lower intensity due to the diffusion of photons within the particles resulting in a lower number of photons returning to the surface. Results in Table 7.1, in addition to those in Chapter 6, suggest that the analysis conducted using the signal collected from the larger distances may be improved by improving the intensity of those signals. This may be done through the use of a stronger incident light.

Table 7.1. Summary of PLSR model performance of SR-DRM spectra of granular and powder paracetamol in MTBE from four collection distances.

Grade	SR-DRM distance/mm	Raw				SNV pre-processed			
		LV	RMSECV/%	RMSEP/%	R^2	LV	RMSECV/%	RMSEP/%	R^2
Granular	**0.3**	6	3.33	3.78	0.25	6	3.03	3.51	0.35
	0.6	7	2.47	2.32	0.56	7	2.21	2.44	0.64
	0.9	4	2.02	2.01	0.70	4	1.91	1.81	0.73
	1.2	4	2.17	2.44	0.66	5	2.07	2.29	0.70
Powder	**0.3**	5	2.02	1.85	0.87	5	1.91	1.74	0.89
	0.6	3	2.05	2.05	0.87	4	1.93	2.01	0.89
	0.9	3	1.78	1.86	0.90	4	1.69	1.82	0.91
	1.2	4	2.02	2.13	0.87	4	1.84	1.99	0.90

7.2.2 PLSR analysis results of SORS spectra

Table 7.2 provides a summary of PLSR analysis results of raw and SNV pre-processed SORS spectra of both paracetamol grades in MTBE from the four offset distances collected with the combined probe. PLSR results of the raw granular paracetamol in MTBE spectra show that the same number of latent variables capture the variance from all offset spectra, suggesting that similar factors contribute to the variance captured in those models. Nevertheless, the RMSECV decreases as the collection offset distance increases from the backscattering spectra to the larger offset distances of 2.5 and 3.5 mm. This is associated with an increase in R^2 as the offset distance increases. The RMSEP of PLSR models of those raw and SNV pre-processed spectra also decrease as the offset distance increases, and are comparable or lower with reference to the RMSECV, suggesting that the calibration model is robust.

As for the SNV pre-processed SORS spectra of the granular/MTBE system, the number of latent variables is similar between spectra of the offsets, between 2-4 LVs, and is also similar to those of the raw spectra. The RMSECV of PLSR models of the SNV pre-processed spectra also decreases as the offset distance increases, along with the increase in R^2. Further decrease is also seen in the RMSEP of the SNV pre-processed spectra compared to the RMSEP of PLSR models of the raw spectra, showing that SNV pre-processing of those spectra led to PLSR models with improved performance.

In the PLSR analysis results of the raw and SNV pre-processed spectra of the powder/MTBE system shown in Table 7.2, the RMSECV also decreases as the offset distance increases and is the lowest for the largest offset distance of 3.5 mm, where R^2 follows an opposite trend and is the highest for the largest offset distances. For both raw and pre-processed spectra, the RMSEP is comparable to the RMSECV, confirming the representativeness of the calibration set spectra and the robustness of the PLSR calibration models.

The similarity in the SORS response in both paracetamol grades suggests that SORS could provide improved predictions for a range of particle sizes. The decrease in model error as the offset distance increase, seen in Table 7.2, conforms to the observations in the datasets collected using the individual SORS probe, reported in Chapter 6, where the observations from the different systems showed the decrease in PLSR model errors as the offset distances increased to 4 mm. Those reproducible observations serve as a confirmation of the performance of SORS to achieve more accurate solvent content predictions.

Table 7.2. Summary of PLSR model performance of SORS spectra of granular and powder paracetamol in MTBE from four offset distances.

Grade	SORS offset/mm	Raw				SNV pre-processed			
		LV	RMSECV/%	RMSEP/%	R^2	LV	RMSECV/%	RMSEP/%	R^2
Granular	**0**	4	2.04	1.62	0.70	4	1.44	1.59	0.85
	1.5	4	1.91	1.40	0.74	2	1.42	1.02	0.85
	2.5	4	1.55	0.91	0.83	5	1.22	0.83	0.89
	3.5	4	1.60	1.39	0.81	4	1.25	0.86	0.89
Powder	**0**	3	1.86	2.56	0.89	3	1.17	1.97	0.96
	1.5	2	1.91	2.24	0.89	3	1.21	1.52	0.95
	2.5	4	1.31	1.76	0.95	4	0.91	1.50	0.97
	3.5	4	1.29	1.62	0.95	4	0.79	1.52	0.98

7.3 Preparation of SR-DRM and SORS spectra for multi-block analysis

Multi-block data analysis in this chapter refers to partial least squares regression (PLSR) analysis conducted using multiple data blocks. Each block of data corresponds to the SR-DRM or SORS measurement from one configuration. Since both of those techniques produce numerical measurements, SR-DRM and SORS spectral datasets are considered homogeneous numerical datasets.[112] Multi-block analysis may be conducted by concatenating the individual dataset blocks before further regression analysis. This could help in the understanding of how the measurements from different techniques are related.[112] Alternatively, other multi-block analysis methods rely on combining the blocks resulting from analyses conducted using the individual blocks. This could result in more precise predictions as the combined blocks are then more correlated.[120] PLSR analysis results in models that are complicated to interpret. Therefore, multi-block data analysis following regression analysis would result in combined models that are more complicated to interpret.

Although SR-DRM and SORS both result in numerical measurements, these two techniques rely on different phenomena and are measured using instruments characterised by different resolutions. Therefore, possible sources of variability that could affect the contribution of each of the blocks and the overall performance of the PLSR analysis of the final block must be identified and addressed prior to the use in the multi-block PLSR analysis. In the previous chapters in sections 5.3.2 and 6.3.2, augmentation and co-addition were both tested for the use of multiple blocks to construct PLSR models. In this chapter, only augmentation, which is the concatenation of data blocks to form a larger final block,[14] is used for combining the blocks of SR-DRM and SORS spectra. This would allow for the investigation of how those two types of measurements relate in addition to exploring any improvement in PLSR performance following the concatenation.

7.3.1 Identifying and addressing sources of variability between SR-DRM and SORS spectra

First, it was necessary to consider two factors, the resolution and the magnitude of each of the SR-DRM and SORS signals. Resolution is instrument-dependent and can be described as the number of columns (variables) containing the signal intensity per wavelength or wavenumber for a sample. A SR-DRM signal from one configuration corresponding to the signal over 900-1700 nm is collected as 512 variables. The number of variables is further reduced to 311 when the 1100-1600 nm wavelength range is selected, and the magnitude of the absorbance signal is low as shown in Figure 7.2 (a) of the granular/MTBE system. As previously described in section 4.2.2, SORS signals are collected as 1024 pixels, corresponding to the signal over 0-1900 cm^{-1}. Following the selection of the relevant wavenumber range, 50-1750 cm^{-1}, the remaining number of variables is 876, while the magnitude of the signal is up to 60 000 arbitrary units as shown in Figure 7.2 (b).

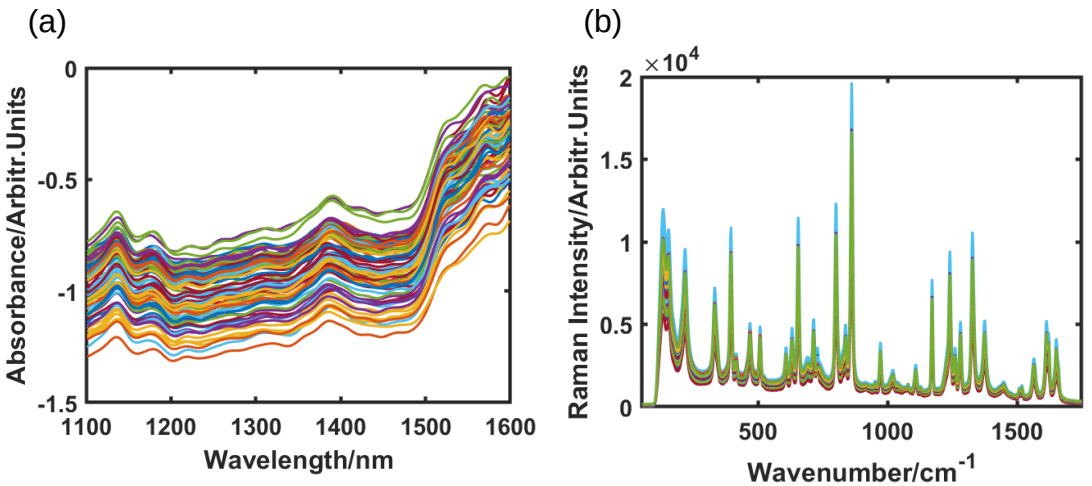

Figure 7.2. Example spectra from the granular/MTBE system. (a) Raw SR-DRM spectra from 1.2 mm distance. (b) raw SORS spectra from 3.5 mm offset.

The concatenation of those two blocks from Figure 7.2 would result in the final block shown in Figure 7.3 (a), which illustrates the contrast in the magnitude of the SR-DRM and SORS measurements combined. Figure 7.3 (a) also shows that including a larger number of variables for one of the blocks, the SORS spectra, could mean that the PLSR analysis of the combined multi-block would be more affected by the SORS data block. Therefore, the adjustment made to obtain a model with even contribution from each type of data was to interpolate the data with lower resolution, the 311 variables of the SR-DRM spectra, to match that of the data with higher resolution, the 876 variables of the SORS spectra.

The contrast in the magnitude of the signals must also be addressed. Therefore, to mitigate the variation in the raw signal intensity shown in Figure 7.3 (a), the raw SR-DRM and SORS spectra were SNV pre-processed. As shown in Figure 7.3 (b), applying this pre-processing within each of the blocks results in a comparable magnitude between the level of the SR-DRM and SORS signals and, most importantly the intensity of the highlighted MTBE peak. SNV pre-processing was selected as this technique allows for the processing of each spectrum individually, avoiding any influence from reference spectra or further processing steps that may be involved in other pre-processing techniques. This allows for the evaluation of the performance of each of the offset spectra separately. The same steps were applied to the powder/MTBE spectral datasets.

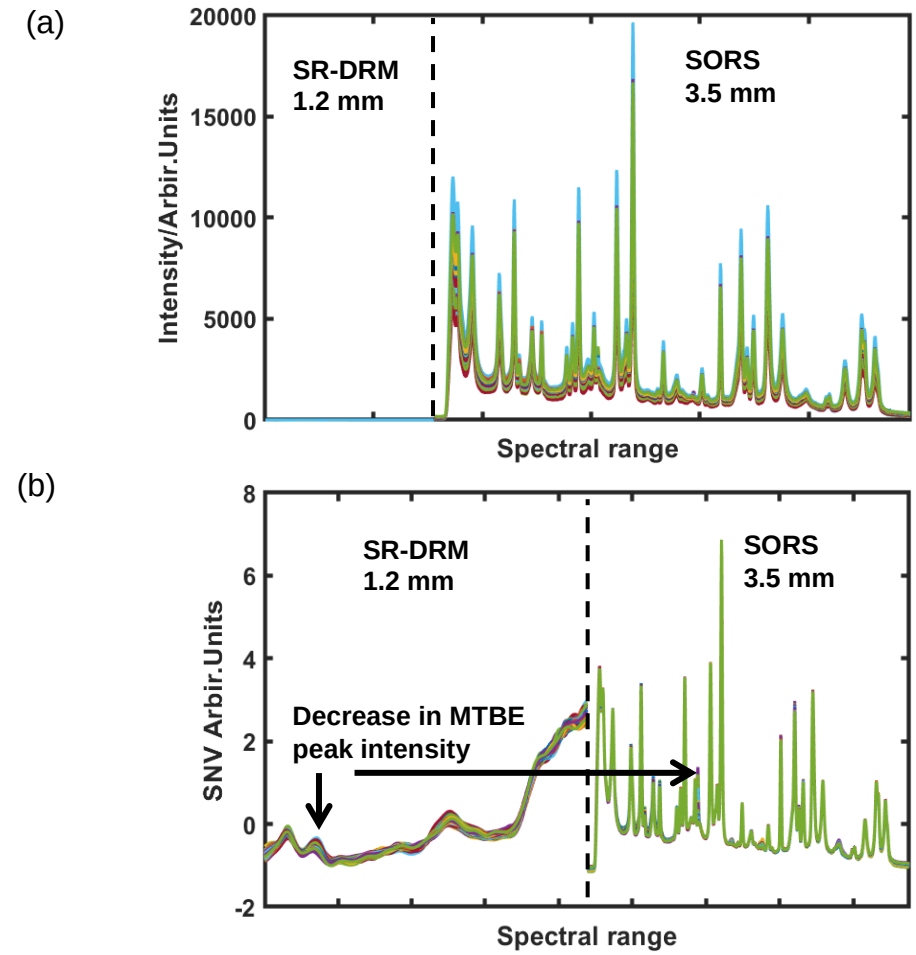

Figure 7.3. Example spectra from the granular/MTBE system. (a) Spectra from Figure 7.2 combined to form one block. (b) Final block composed of interpolated then SNV pre-processed SR-DRM spectra and SNV pre-processed SORS spectra.

7.3.2 Comparison between PLSR results of original and interpolated SR-DRM spectra

In the previous section, section 7.3.1, SR-DRM spectra were interpolated to match the matrix size of the SR-DRM spectra with that of the SORS spectra. The original and interpolated SR-DRM spectra of the granular/MTBE system were compared visually before and after SNV pre-processing. In this section, the PLSR results of the original and interpolated SR-DRM spectra are compared to detect any change, as an improvement or deterioration, in PLSR performance between the original and interpolated spectra.

Table 7.3 includes the PLSR results of original and interpolated SR-DRM spectra of both granular and powder paracetamol in MTBE. Since SNV pre-processing was seen to improve the PLSR performance of both SR-DRM and SORS spectra in section 7.3, the results shown in Table 7.3 are of the pre-processed spectra following interpolation. The variation in PLSR results of the interpolated spectra is seen as a decrease in the error for 0.9-1.2 mm spectra and an increase for 0.3-0.6 mm collection distances. This suggests that the increase in error seen following interpolation and SNV pre-processing may be due to the underlying low signal intensity leading to low quality of the spectra from 0.3-0.6 mm collection distances. The variation in quality, as was seen in SAR-DRM chapter 5, affects the PLSR results. This is because the decrease in MTBE peak intensity as the solvent content decreases is affected by noise in the wavelength range 1100-1300 nm, where the characteristic MTBE peak is observed. Seeing as those closer collection distances had lower quality and overall PLSR performance, it is thought that interpolation adds to the noise in those spectra, leading to a large shift in performance, as seen in the RMSEP of 0.3 mm interpolated spectra; whereas those of farther distances perform robustly.

For the powder/MTBE system, a decrease in the RMSECV associated with a slight increase in R^2 is seen. This is further seen as a decrease in the RMSEP. The observation for 1.2 mm spectra, for example, where there is an increase in RMSECV for 1.2 mm spectra from 1.84% to 1.98% and a decrease in RMSEP from 1.99% to 1.80%, further suggests that the performance is dependent on the quality of the original spectra. The overall decrease in error for the SNV pre-processed interpolated spectra may be attributed to the increase in the resolution following interpolation, where the change in peak intensity is expressed over a larger number of variables compared to the original spectra. The PLSR results in Table 7.3 suggest that the interpolated SR-DRM datasets can be used in the multi-block PLSR analysis.

Table 7.3. Summary of PLSR model performance of SNV pre-processed SR-DRM original and interpolated spectra of granular and powder paracetamol in MTBE.

Grade	SR-DRM distance/mm	Original				Interpolated			
		LV	RMSECV/%	RMSEP/%	R^2	LV	RMSECV/%	RMSEP/%	R^2
Granular	**0.3**	6	3.03	3.51	0.35	5	3.22	3.88	0.29
	0.6	7	2.21	2.44	0.64	6	2.52	2.35	0.54
	0.9	4	1.91	1.81	0.73	3	1.87	1.74	0.75
	1.2	5	2.07	2.29	0.70	3	1.99	1.61	0.71
Powder	**0.3**	5	1.91	1.74	0.89	5	1.79	1.41	0.90
	0.6	4	1.93	2.01	0.89	2	1.53	1.43	0.93
	0.9	4	1.69	1.82	0.91	3	1.58	1.42	0.92
	1.2	4	1.84	1.99	0.90	3	1.98	1.80	0.88

7.4 Multi-block PLSR analysis of SR-DRM and SORS spectra

In this section, the results of the multi-block PLSR analysis of the final SR-DRM/SORS block are reported. First, the selection of the configurations to combine from both techniques must be considered. PLSR analysis of both SR-DRM and SORS spectra individually has shown previously an improvement in performance as the offset distance increases. However, this improvement in SORS spectra as the offset distance increases was clear compared to that of the SR-DRM spectra, where spectra collected from the closest distance for SR-DRM suffer from low quality as the decrease in solvent peak intensity was better seen from spectra of the farther distances.

As a starting point, the four configurations from each technique were combined in incremental order, as shown in Table 7.4, to assess any improvement achieved by including the spectra of the larger offset distances from both techniques compared to those of the shorter collection offsets. Following from those combinations, it is possible to assess other combinations provided that the results suggest improved performance from the combined SR-DRM/SORS spectra.

Table 7.4. Combined spectra from SR-DRM and SORS.

Combination	SR-DRM distance /mm	SORS offset /mm
1	0.3	0
2	0.6	1.5
3	0.9	2.5
4	1.2	3.5

The following section reports the multi-block PLSR analysis results and investigates the impact of pre-processing, which was applied to mitigate the disparity in the magnitude of the SR-DRM and SORS signals. Then, the multi-block PLSR analysis results are compared to the SR-DRM and SORS spectra to explain the multi-block PLSR performance.

7.4.1 Impact of pre-processing on the performance of the multi-block PLSR

The results from the SR-DRM/SORS combinations in PLSR analysis summarised in Table 7.5 show once again the improvement in PLSR performance as the collection distances increase. This is seen as a decrease in the RMSECV and a slight increase in R^2 for the calibration set, where the RMSEP also decreases. Both the PLSR models of the raw and pre-processed spectra show this improvement with the increase in offset distance, where the level of error is also lower in the PLSR model of the pre-processed spectra compared to the PLSR model of the raw spectra. The decrease in RMSECV and a slight increase in R^2 in the combined SNV pre-processed spectra is thought to be the outcome of the scatter correction rather than a result of the collective improvement resulting from the comparability between the magnitude of the SR-DRM and SORS spectra.

Table 7.5. Summary of PLSR model performance of spectra of granular and powder paracetamol in MTBE from combined SR-DRM and SORS configurations.

Grade	SR-DRM distance/mm	SORS offset/mm	Raw				SNV pre-processed			
			LV	RMSE CV/%	RMSE P/%	R^2	LV	RMSE CV/%	RMSE P/%	R^2
Granular	**0.3**	**0**	4	2.04	1.62	0.70	4	1.44	1.65	0.85
	0.6	**1.5**	4	1.91	1.40	0.74	2	1.40	1.01	0.86
	0.9	**2.5**	4	1.55	0.91	0.83	5	1.22	0.85	0.89
	1.2	**3.5**	4	1.60	1.39	0.81	4	1.24	0.85	0.89
Powder	**0.3**	**0**	3	1.86	2.56	0.89	3	1.17	1.97	0.96
	0.6	**1.5**	2	1.91	2.24	0.89	3	1.20	1.52	0.96
	0.9	**2.5**	4	1.31	1.76	0.95	4	0.90	1.49	0.97
	1.2	**3.5**	4	1.29	1.62	0.95	4	0.78	1.52	0.98

To further assess the benefit of pre-processing the combined spectra as a means to mitigate the contrast in signal magnitude, the regression and residuals plots of the PLSR model of the combined spectra from 1.2+3.5 mm configurations from the powder/MTBE system as an example are shown in *Figure 7.4*. The small improvement seen between the estimations from raw spectra in *Figure 7.4* (a-b) and pre-processed spectra in *Figure 7.4* (c-d) suggest that the disparity in the magnitude of those signals did not greatly impact the level of error, but nonetheless has led to an improvement in the prediction of the solvent content. Although Figure 7.4 suggests that SNV pre-processing slightly contributes to the improvement in the performance of the combined spectra PLS, this does not indicate whether the improvement is equally contributed from both SR-DRM and SORS blocks.

Table 6.6 shows a summary of the variance captured by the farthest combinations of raw and SNV pre-processed spectra in order to allow for more understanding of the differences in the PLSR model performance. This table shows that the combined spectra from the farthest distances capture a larger variance, which further improves following SNV pre-processing.

Following the general evaluation of the PLSR models of the combined multi-block spectra, the points to further assess would be the impact of the use of pre-processed spectra and the improvement in PLSR estimation of the solvent content resulting from combining SR-DRM and SORS spectra compared to the individual spectra.

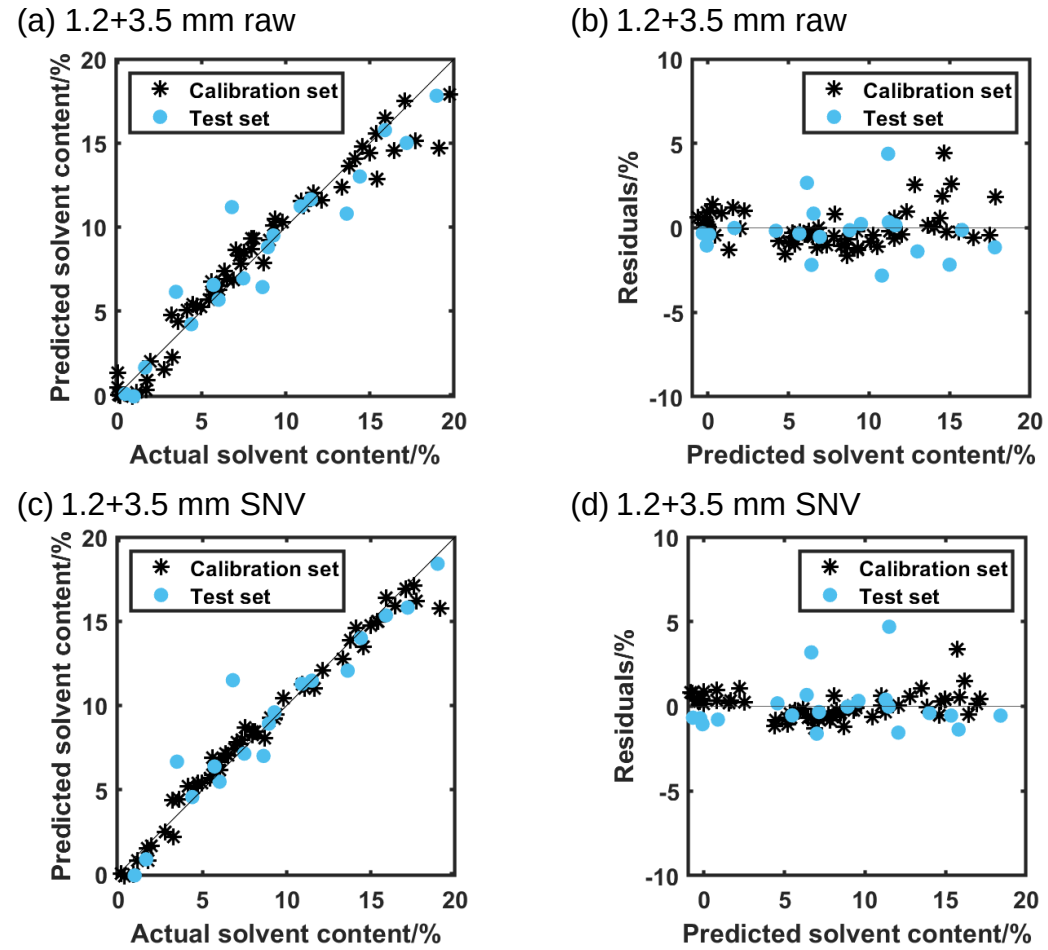

Figure 7.4. (a) Regression and (b) residuals plots of the PLSR model of raw combined 1.2+3.5 mm SR-DRM and SORS spectra. (c) Regression and (d) residuals plots of the PLSR model of SNV pre-processed combined 1.2+3.5 mm SR-DRM and SORS spectra.

Table 7.6. Variance captured in PLSR models from raw and SNV pre-processed combined SR-DRM and SORS spectra from the powder/MTBE system.

Combination	**1.2+3.5 mm**	**1.2+3.5 mm**
LV	**Raw**	**SNV**
1	63.68	65.27
2	31.20	31.43
3	3.48	2.20
4	0.31	0.55
Sum of variance/%	98.68	99.45

7.4.2 Comparing the performance of the multi-block PLSR to the individual spectra

The results from PLSR analysis of the SR-DRM/SORS SNV pre-processed combined spectra, in addition to individual techniques, are shown in Table 7.7. Those show once again the improvement in PLSR performance as the combined collection distances increase. This is seen as a decrease in the RMSECV associated with an increase in R^2 for the calibration dataset. The RMSEP also decreases as the collection distance increases in a similar manner to the RMSECV. The number of latent variables for each of the combined spectra is the same as the number of latent variables of the SORS spectra, suggesting a similar level of variance captured in the PLSR model of the combined spectra compared to the SORS spectra. Moreover, the RMSECV values are similar and are only lower by up to 0.02% compared to the RMSECV of SORS spectra. Those observations were seen in the PLSR results of both granular and powder grades.

To illustrate the difference in the performance of the individual blocks and the combined block of SR-DRM and SORS spectra, the RMSECV and RMSEP obtained from the three PLSR analyses were compared in Figure 7.5 (a) and (b) for granular/MTBE system and in Figure 7.5 (c) and (d) for the powder/MTBE system. The illustration shows the similarity between the error values of the combined block and that of the individual SORS spectra. The best cases in Figure 7.5 show the error of the combined spectra to be almost the same as that of the individual SORS spectra whereas the error of the individual SR-DRM spectra is always higher.

In some cases in the granular/MTBE system, the error of the combined spectra is a value higher than that of the individual SORS spectra. The reason for this is thought to be that the SR-DRM spectra of low quality lead to a deterioration of the performance due to a combination of the lower signal intensity in addition to the overlap between the paracetamol and MTBE peaks as opposed to those peaks in the SORS spectra.

Table 7.7. PLSR results of SNV pre-processed spectra of granular and powder paracetamol in MTBE from individual and combined SR-DRM and SORS.

Grade	Combination	SR-DRM				Combined				SORS			
		LV	RMSECV /%	RMSEP/ %	R^2	LV	RMSECV /%	RMSEP/ %	R^2	LV	RMSECV /%	RMSEP/ %	R^2
Granular	1	6	3.03	3.51	0.35	4	1.44	1.65	0.85	4	1.44	1.59	0.85
	2	7	2.21	2.44	0.64	2	1.40	1.01	0.86	2	1.42	1.02	0.85
	3	4	1.91	1.81	0.73	5	1.22	0.85	0.89	5	1.22	0.83	0.89
	4	5	2.07	2.29	0.70	4	1.24	0.85	0.89	4	1.25	0.86	0.89
Powder	1	5	1.91	1.74	0.89	3	1.17	1.97	0.96	3	1.17	1.97	0.96
	2	4	1.93	2.01	0.89	3	1.20	1.52	0.96	3	1.21	1.52	0.95
	3	4	1.69	1.82	0.91	4	0.90	1.49	0.97	4	0.91	1.50	0.97
	4	4	1.84	1.99	0.90	4	0.78	1.52	0.98	4	0.79	1.52	0.98

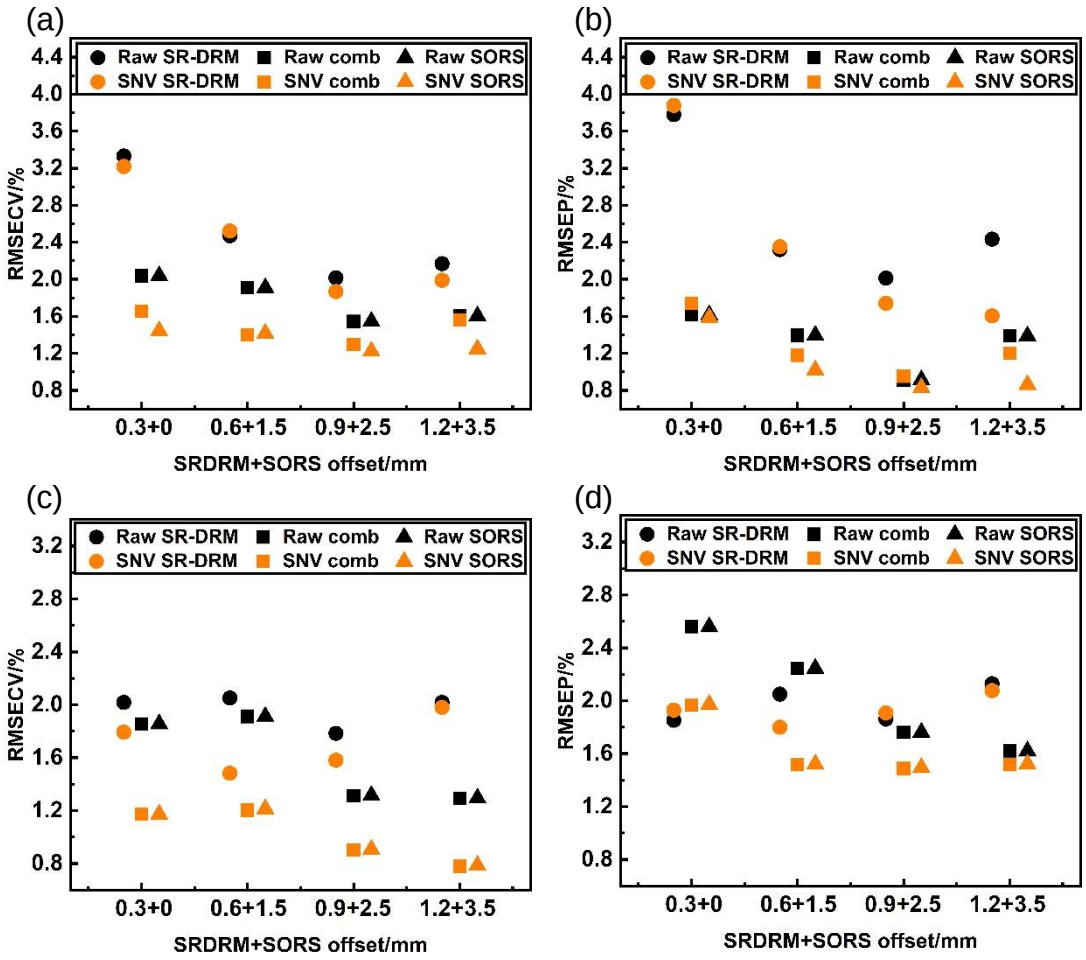

Figure 7.5. PLSR result of raw and pre-processed combined (comb) spectra with individual SR-DRM and SORS spectra. (a) RMSECV and (b) RMSEP of PLSR model of granular/MTBE. (c) RMSECV and (d) RMSEP of PLSR model of powder/MTBE.

Further investigation into the scores and loadings of the combined spectra might show whether the SR-DRM spectra do contribute to the overall performance of the combined block in the cases where the error values are similar to those of the individual SORS spectra, or if those SR-DRM spectra were considered as noise within the PLSR models. Figure 7.6 shows the loadings and scores for each of the four latent variables of the PLSR models of the raw and SNV pre-processed spectra from the powder/MTBE system of the SR-DRM+SORS multi-block from 1.2+3.5 mm, where the loadings for the SR-DRM and SORS blocks are plotted on different scales due to the difference in their loadings despite the pre-processing that has transformed them into comparable measurements.

For example, the loadings curve of LV1 in Figure 7.6 (a) resembles the paracetamol spectra captured through SR-DRM (left side of the figure) and SORS (right side of the figure), both of which correspond to the range -6-1 and 0-100 000, respectively. Nevertheless, the loadings curve of LV1 in Figure 7.6 (a) could also be a sum of the features of paracetamol and MTBE since those peaks overlap. In addition to LV1, loadings of LV2-3 show peaks corresponding to MTBE peaks in both the SR-DRM and SORS blocks. Loadings of LV4 also show a peak corresponding to that of MTBE as highlighted in Figure 7.6 (g). This is seen for both raw and pre-processed spectra in the four latent variables. For the scores shown in Figure 7.6 (b,d,f,h), a trend related to the solvent content may be seen for the scores of LV2-3 of the raw spectra and of LV1-3 of the SNV pre-processed spectra. Observations from the loadings suggest that SORS contributed more to the improvement in PLSR model performance as the MTBE peak may be seen in LV1-4 of raw and pre-processed spectra, whereas those are seen in LV2-3 for SR-DRM and could not be confirmed for LV1 as a result of the peak overlap. The SR-DRM loadings of LV3 of pre-processed spectra suggest that some improvement might have been caused by the pre-processed SR-DRM block as the MTBE peak can be seen, although the scores for this LV show a slight correlation to the solvent content.

Observations from the scores suggest that pre-processing leads to the improvement in PLSR performance as the trend of increase as the solvent content increases may be seen in LV1-3 in the pre-processed spectra as opposed to LV2-3 in the raw spectra. Since the improvement following pre-processing is seen in the SR-DRM spectra, this suggests that this block benefits more from pre-processing compared to the SORS block.

The results of the multi-block PLSR analysis discussed previously show similar performance from the combined SR-DRM+SORS and individual SORS block. Moreover, the decrease in the estimation error seen as the collection distance increases was also observed in those combinations. Therefore, those results do not indicate that the analysis would benefit from multi-block combinations of other configurations. It is thought that the differences between the near-infrared and Raman signals are the cause of the differences in their PLSR performance and the unequal contribution to the combined block. In addition to the disparity in signal intensity (and the signal quality as a result), the Raman spectra of paracetamol and MTBE display less overlap compared to those of the near-infrared spectra. The change in intensity in both SR-DRM and SORS spectra is proportional to the change in solvent content but not to the same extent, which may have also prevented the anticipated improved robustness in PLSR performance from the augmented blocks. Overall, this analysis showed that PLSR analysis of SORS spectra resulted in a more accurate estimation of the solvent content in this system.

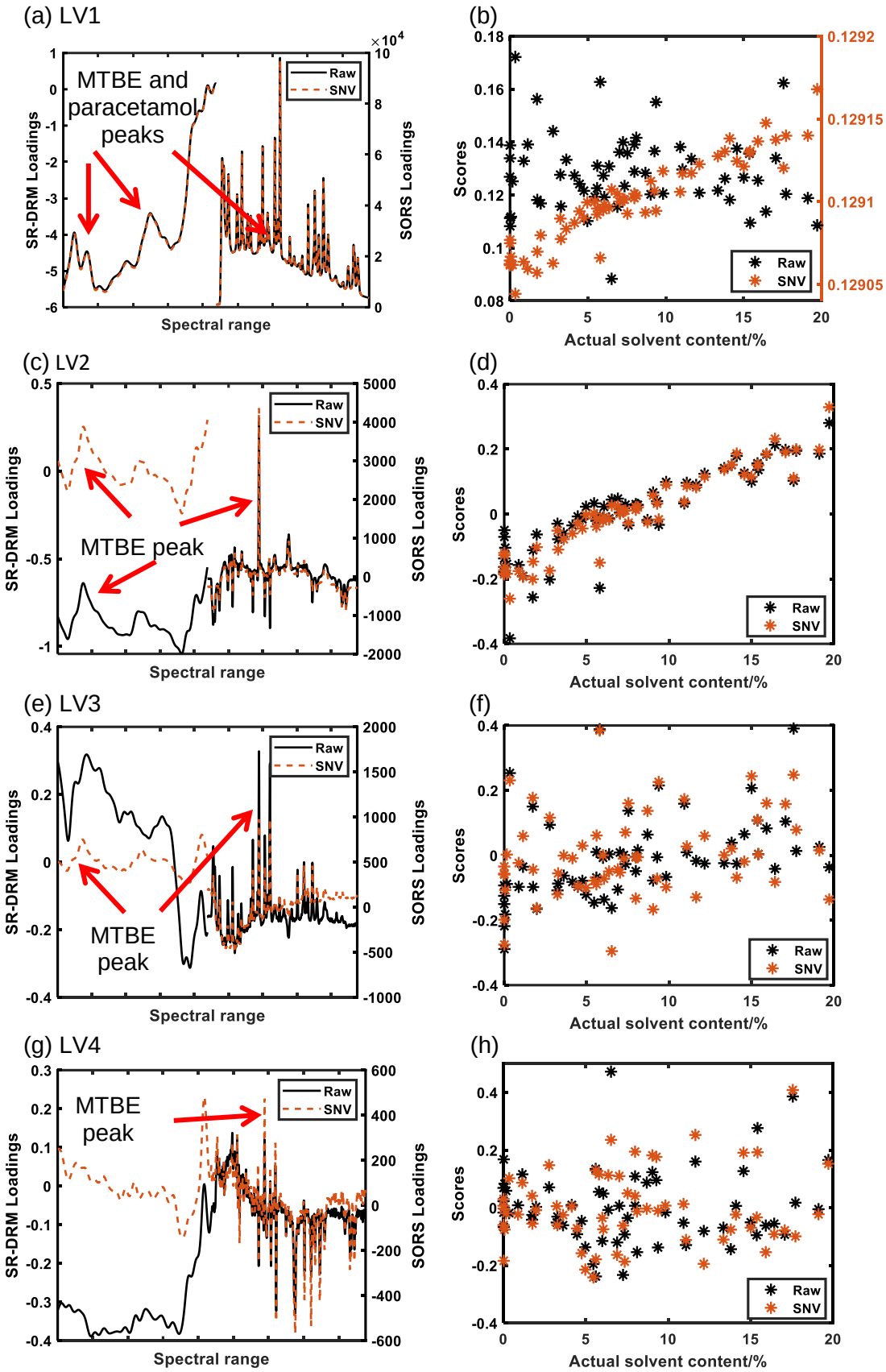

Figure 7.6. Loadings (a,c,e,g) and scores (b,d,f,h) of four LVs of the PLSR model of raw and SNV pre-processed combined 1.2+3.5 mm SR-DRM and SORS spectra.

7.5 Conclusions

Multi-block PLSR analysis was conducted through the augmentation of SR-DRM and SORS spectra. Prior to the concatenation, the number of signal variables and the magnitude of the signal from each of the blocks were assessed. SR-DRM spectra consisted of a lower number of variables because of the lower resolution of the spectrometer and lower signal intensity. Therefore, the SR-DRM spectra were interpolated to match the resolution of the SORS spectra. Comparison of the PLSR analysis results of original and interpolated SR-DRM spectra showed almost identical performance suggesting that the use of either of the spectra in the multi-block PLSR analysis will yield comparable results. Then, SNV pre-processing was applied to SR-DRM and SORS spectra to mitigate the difference in signal magnitude.

Multi-block PLSR analysis of the blocks of SNV pre-processed SORS spectra with the interpolated and SNV pre-processed SR-DRM spectra showed improvement in PLSR performance in predicting the solvent content with the increase in offset distances from the illumination points as seen with the individual SR-DRM and SORS spectra. Moreover, PLSR analysis of combined spectra resulted in PLSR models that perform similar or identical to PLSR models of the individual SORS spectra. This suggested that SR-DRM models had small or no contribution to the performance of the combined blocks. Looking further into PLSR models of the raw and pre-processed combined spectra showed that the percentage of variance captured by the models is larger for the PLSR model of SNV pre-processed spectra compared to those of the raw spectra. To investigate the contribution of SORS and SR-DRM spectra in the PLSR models, the loadings and scores of raw and pre-processed combinations of 1.2+3.5 mm were assessed. Higher loadings related to the solvent peak were seen for the SORS spectra in the latent variables describing the models compared to the lower loadings related to the solvent peak seen for the SR-DRM spectra in the latent variables. This is explained by the stronger signal intensity and sharper peaks of the Raman spectra, in addition to the lower overlap between the paracetamol and MTBE peak compared to the weaker and wider peaks of the near-infrared spectra.

8. Spatially Offset Raman Spectroscopy for Monitoring the Solvent Content During Pharmaceutical Isolation

8.1 Overview

The primary pharmaceutical manufacturing stage for producing solid active pharmaceutical ingredients usually ends with the isolation processes, which can be divided into three steps, filtration, washing, and drying. The isolation processes can affect the quality of the solid active pharmaceutical ingredient obtained at the end of the process.

The results in the previous chapter demonstrate the potential that spatially offset Raman spectroscopy (SORS) offers for monitoring the solvent content during pharmaceutical drying. Building on the previous results, in this chapter SORS is used for estimating the content of two solvents in a filter cake following washing.

This chapter includes an introduction to the pharmaceutical isolation processes and model transfer of multivariate calibration. The introduction is followed by the experimental section detailing the filtration and washing setups and procedures, in addition to SORS data collection and the processing of SORS data collected from the drying experiments. The results section includes an evaluation of the processed SORS dataset collected from drying in addition to reporting the performance of SORS for estimating the solvent content following filtration and washing.

8.2 Introduction

In the primary (upstream) manufacturing stage of pharmaceuticals, isolation unit processes are conducted to obtain a dry active pharmaceutical ingredient (API), where isolation follows the crystallisation of the API. The isolation processes may be divided into filtration, washing, and drying, the purpose of which is the recovery of a pure and dry API.

8.2.1 Pharmaceutical isolation processes

8.2.1.1 Filtration

Once an API is crystallised from a solution, the solution is removed through filtration, which is also termed clarification. The filtration step aims to separate the solid from the solution through a porous filter that allows the fluid to pass and can retain the solid particles larger than the size of the filter pores.[17] In pharmaceutical primary manufacturing, this step separates the API from the crystallisation mother liquor solution and is termed dead-end filtration. The bulk of the solid retained on a filter is termed a filter cake, where the thickness of this cake increases as the solid particles settle from the slurry. This in turn means that the structure and permeability of this filter cake change with time usually leading to the slowing of the rate of filtration due to the blocking of the filter by the settled filter cake. The decrease in the rate of solvent removal is termed cake resistance. To increase the filtration rate, pressure difference may be employed in the form of vacuum pressure that acts as a driver for the filtration as opposed to conventional gravitational filtration. This could lead boiling of the removed liquid as a result of the decreased pressure within the filtrate vessel. Alternatively, the filtration rate may be increased by using a filter of a larger area to increase the filtration area and decrease the thickness of the filter cake. Nevertheless, industrial applications make use of pressure filtration.[19] At the end of the filtration step, the API is still wet with the mother liquor as it is retained on the surface of particles and between the voids in the filter cake.[19,121]

8.2.1.2 Washing

The washing step is conducted to remove the mother liquor along with any impurities remaining within the filter cake. This step is important for the removal of those impurities in addition to preventing the formation of a lumpy product as a result of the drying of the mother liquor within the voids in between the particles. The pharmaceutical washing methods that are currently applied in the industry are displacement and slurry or resuspension washing.[22]

Displacement washing refers to the practice of pouring the wash solvent over the settled filter cake without agitating the cake in order to displace the mother liquor. Setbacks to this method include the redistribution of the mother liquor throughout the filter cake instead of removing it and the formation of channels within the filter cake through which the wash solvent is drained without effectively washing the cake from the mother liquor. Slurry or resuspension washing refers to the resuspension of the filter cake in the wash solvent to create a slurry, where the mother liquor is eventually mixed with the wash solvent, which can then effectively displace the mother liquor.[121,122] Although the properties of the filtered particles affect the removal of the mother liquor, washing a filter cake with three cake volumes is an effective common practice.[22,121]

8.2.1.3 Determination of the residual solvent content following pharmaceutical isolation

The residual solvent content following filtration and washing may be determined through the analysis of the filtrate or the vapours within the headspace over the filter cake. Some of the methods used for filtrate composition analysis include high-pressure liquid chromatography (HPLC), gas chromatography-mass spectrometry (GC-MS), and nuclear magnetic resonance (NMR) spectroscopy. Techniques for the analysis of the overhead vapour composition include selected ion flow tube mass spectrometry (SIFT-MS) and near-infrared (NIR) spectroscopy.[76] Those techniques may be applied on-line, where a stream is directed to the measurement instrument, or off-line,

where a sample is manually extracted for analysis. More traditional methods include recording the mass of the filter cake at each step of the process. Nevertheless, those methods do not directly measure the composition of the filter cake.

8.2.2 Model transfer of multivariate calibration

Multivariate regression analysis, partial least squares regression analysis (PLSR) in this chapter, can be used for the quantitative analysis of spectroscopic data where a dependant characteristic of the samples, e.g. the solvent content, can be related to an independent feature, e.g. Raman spectra. A training or calibration dataset that is representative of the variability within the samples is collected, PLSR models are constructed based on this dataset and are then applied for the prediction of the same characteristic within a test dataset.[107] Those calibration models may be applicable for test datasets of the same components under the same data collection conditions, depending on the modelled characteristic, and the same instrument. Measurements include sample signals in addition to influences from the measurement instrument and condition. When a dataset is collected using a different instrument, differences in the collected data arise. This requires updating the previous calibration model in order to minimise the error in estimating the modelled feature within new test sets. The process of updating the previous calibration model for application to new datasets is termed calibration or model transfer.[123] Nevertheless, model transfer is concerned with the processing of calibration models after those models have been developed. In this chapter, a similar concept is applied. However, the differences in the spectra collected using an equipment setup are addressed prior to constructing the calibration models so as to reduce the error in estimating a test set collected using another equipment setup.

8.3 Experimental

This section is further divided into sections reporting the materials, experimental setup, and data processing.

8.3.1 Materials

Granular paracetamol (Mallinckrodt Inc., Raleigh, N.C.), was the active pharmaceutical ingredient used in this study. Granular paracetamol had a mean particle size (D50) of 265 µm, measured with laser diffraction (Mastersizer 3000 with a dry dispersion unit, Malvern Instruments Ltd, UK). Two wash solvents, in which paracetamol is considered insoluble were used; those were Anisole (99%, Alfa Aesar, Lancashire, UK) and methyl tertiary-butyl ether (MTBE) (99%, Alfa Aesar, Lancashire, UK). This was done to emulate the washing step following the filtration of the mother liquor. Nevertheless, the two wash solvents were used in this experiment in order to avoid the change in particle size through using solvents in which paracetamol shows minimal solubility. Those two solvents were selected as their Raman spectra contain at least one peak with minimal overlap with the other two components as shown in Figure 8.1. The Raman spectra of MTBE include a peak of strong intensity around 730 cm^{-1} that does not overlap with anisole peaks and overlaps with a paracetamol peak of lower intensity. Raman spectra of anisole include a peak of strong intensity around 1002 cm^{-1}, which does not overlap with peaks in the paracetamol and MTBE Raman spectra.

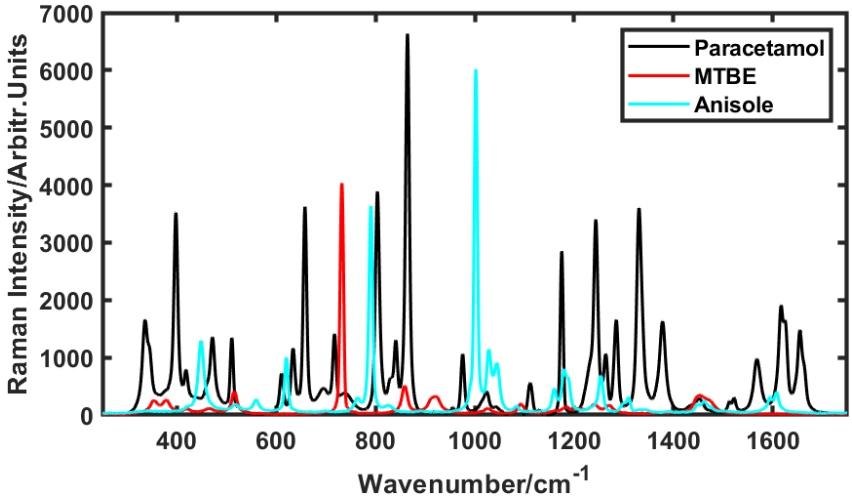

Figure 8.1. Raman spectra of Paracetamol, anisole, and MTBE.

8.3.2 Experimental setup and procedure

Small-scale experiments for the filtration and washing of paracetamol were conducted. The details of the setup and experimental procedure followed are reported in this section.

8.3.2.1 Filtration and washing setup

The filtration and washing setup shown in Figure 8.2 is composed of a 70 mL filter tube (10 µm frit, Isolute® polyethylene single fritted filtration columns, Biotage, Sweden), a filtrate bottle with a two-nozzle screw cap, and a vacuum pump. The filter tube is fixed on one nozzle of the filtrate bottle cap while a tube connected to the vacuum pump is fixed on the other nozzle.

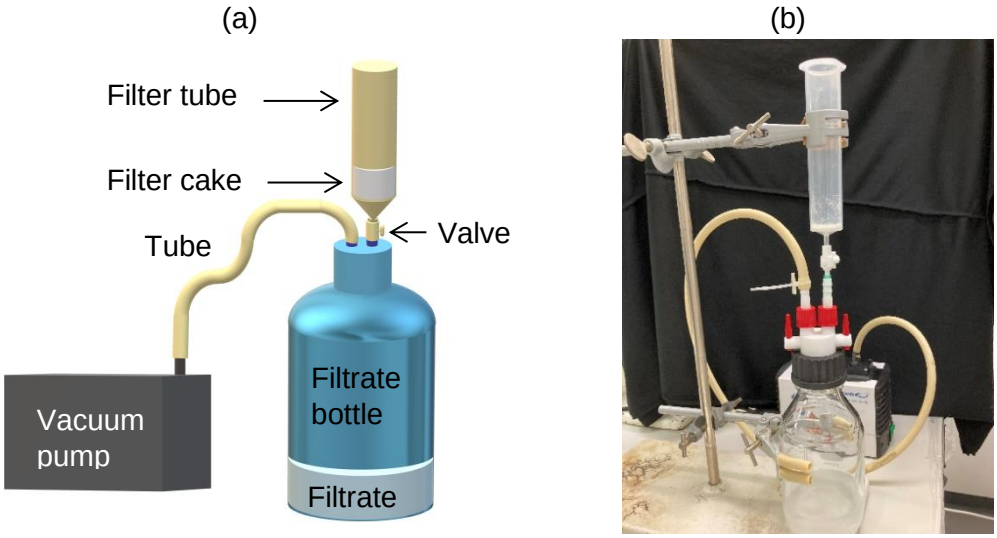

Figure 8.2. (a) Illustration and (b) actual filtration and washing setup.

8.3.2.2 Preparation of the validation set samples

Four spectral datasets are used in the analysis of this experimental work. Two of those datasets are the calibration datasets collected using the SORS and combined probes during the drying of pure anisole and pure MTBE from paracetamol, respectively, as was described in Chapter 4. Two new spectral datasets were collected in this experiment. The first new dataset is a validation

dataset containing a mixture of known percentages of each of the two solvents, anisole and MTBE to enable the suitability of the experimental procedure and API/solvent system for obtaining reference solvent content values and representative spectral measurements. The second new dataset is a test dataset where paracetamol is washed with one cake volume of anisole and then 0.5-3 cake volumes of MTBE consecutively, and the amount of each solvent remaining in the filter cake is determined based on the mass of the filtrate as well as using GC-MS.

Preparation of the solvent mixtures

Mixtures of anisole and MTBE adding up to 40 g of the percentages shown in Table 8.1 were prepared by weighing each of the solvents in a beaker on a balance. A total of 19 mixtures were prepared in addition to the two pure solvents.

Table 8.1 Percentage of each of the solvents used to make up the solvent mixtures

#	Anisole/%	MTBE/%
1	0	100
2	5	95
3	10	90
4	15	85
5	20	80
6	25	75
7	30	70
8	35	65
9	40	60
10	45	55
11	50	50
12	55	45
13	60	40
14	65	35
15	70	30
16	75	25
17	80	20
18	85	15
19	90	10
20	95	5
21	100	0

Wetting of paracetamol

For each of the 21 samples, 15 grams of paracetamol were weighed and loaded into a 70 mL filter. Then, the solvent mixture was poured into the filter tube and the slurry was homogenised by mixing with a spatula to ensure the wetting of the paracetamol granules. Next, to filter the slurry, the filter valve was released and the vacuum pump was started. When the excess liquid was no longer visible around the circumference inside the tube, the vacuum pump was stopped and the filter valve was turned to close after the dripping of the solvent into the filtrate bottle stopped. This was done to ensure that less than 20% of the solvent mixture is retained in the filter cake, which is the solvent percentage expected in a filter cake following de-liquoring and would be within the solvent content range of the SORS calibration sets previously collected.

SORS signal collection and Loss on drying reference measurements for the validation set

Following filtration, a sample of the wet paracetamol from the filter tube was then placed in a beaker and introduced to the combined probe for SORS spectra collection. An average of 5.4 g of wet sample was obtained from each of the samples. The content of the beaker was then emptied in a sample bottle, weighed, and dried in a vacuum oven before being weighed again when dry to obtain the solvent content through loss on drying (LOD) measurements. LOD measurements provide the total solvent content in the wet cake and the mass of each of the solvents is calculated from the theoretical percentages shown in Table 8.1 since the solvents were added as a mixture.

8.3.2.3 Preparation of the test set samples

Following the preparation of the validation set of solvent mixtures, another set of samples was prepared where one wash solvent, anisole, was washed by a second wash solvent, MTBE. However, in the test set, one cake volume of anisole is washed with increasing amounts, 0.5-3 in 0.25 increments cake

volumes, of MTBE, considering 3 cake volumes as the recommended volume for washing a filter cake.[22]

In order to use increasing cake volumes of the wash solvent MTBE and collect measurements that could reflect the filter cake, 8 g of granular paracetamol was weighed and poured into the filter tube. Then, the height of the dry granules was measured using a ruler and was equal to 2 cm. The diameter of the filter tube was also measured and is equal to 2.6 cm. The volume of the cake was calculated from the diameter of the filter tube in addition to the cake height. Those dimensions resulted in a cake volume of 10.6 cm^3. According to the density of each of the solvents, 0.995 g/cm^3 for anisole and 0.740 g/cm^3 for MTBE, one cake volume would be equal to 10.6 g of anisole and 7.9 g with an average of 9.2 g. To facilitate the measurement and addition of fixed amounts of the solvents, 10 g was considered as one cake volume for both solvents. The mass of paracetamol, the mass of solvents, the number of cake volumes of MTBE added to wash anisole and the theoretical percentage of each solvent expected in the solvent mixture in the wet cake is shown in Table 8.2.

Table 8.2. Mass of solvents and number of cake volumes of MTBE used for the washing along with the theoretical percentage of each solvent in the wet cake.

Test sample number	Anisole/g	MTBE/g	Number of cake volumes	Anisole/%	MTBE/%
1	10	5	0.5	66.7	33.3
2	10	10	1	50.0	50.0
3	10	12.5	1.25	44.4	55.6
4	10	15	1.5	40.0	60.0
5	10	17.5	1.75	36.4	63.6
6	10	20	2	33.3	66.7
7	10	22.5	2.25	30.8	69.2
8	10	25	2.5	28.6	71.4
9	10	27.5	2.75	26.7	73.3
10	10	30	3	25.0	75.0

Washing and filtration of paracetamol

For each of the ten test samples described in Table 8.2, the filter tube was weighed prior to adding the dry paracetamol and then weighed again after 8 g of paracetamol was added. Then, 10 g of anisole was added into the filter tube and the components were homogenised through mixing with a spatula. Next, anisole was filtered through the filter tube by opening the filtration valve and turning the vacuum pump on. The filtration was stopped after solvent dripping was no longer observed in the filtrate bottle. For washing with the second solvent, MTBE was added and filtered following the same steps used with anisole. The filtrate bottle was weighed empty and following the filtration of each of the solvents to enable the calculation of the percentage of each of the solvents remaining in the wet cake.

SORS signal collection and reference measurements for the test set

Following the filtration of MTBE, the wet paracetamol in the filter tube was emptied into a glass beaker, where the combined probe was used for the collection of SORS measurements with 20 seconds as the acquisition time. The beaker contents for each of the filter tubes were then placed in a sample bottle, weighed, and moved to a vacuum oven to dry the wet paracetamol before being weighed again when dry to obtain total solvent content measurements from the LOD measurements. The total solvent content obtained through the LOD measurements can then be used to determine the mass of each solvent remaining in the wet cake as the reference solvent content is vital for the use in the quantitative analysis of Raman spectroscopy, where the error in estimating the solvent content may arise from the spectroscopic measurement, but is also due dependant on the reference measurement considered to be the actual value of the solvent content.

The mass of each of the two solvents, needed as reference measurements for the quantitative analysis, may be determined through multiplying the total solvent content by the percentage of each solvent. The complication arises from the fact that the desired output is the quantification of the mass of each

of the solvents in the wet cake, with the LOD giving the total solvent content in the wet cake. Applicable methods for quantifying the percentage of each of the solvents in the wet cake rely on either the composition of the filtrate that has been filtered out of the cake or the composition of the vapour in the headspace of the filter tube. This highlights the importance of the development of real-time in-line methods like quantitative Raman spectroscopy. Moreover, the solvents used in this experiment are in contrast to physical properties, where MTBE is a volatile solvent with a boiling point of 55.2°C and anisole has a boiling point of 154°C. Therefore, when filtering MTBE, it may be expected that some of the filtered solvents may evaporate, and the recorded mass of the filtrate would not reflect the accurate mass of the solvent filtered. Therefore, multiple methods were considered for the quantification of each of the solvents remaining in the wet cake, where each of the methods could still suffer from inaccuracy inherent in the preparation of the samples, the methods themselves, and the properties of the solvents.

In this experimental setup, three methods were possible for determining the percentage of each of the solvents remaining in the wet cake:

1. the theoretical percentages of each of the solvents added as shown in Table 8.2.
2. the mass of the solvents obtained through weighing the filtrate.
3. GC-MS analysis of the filtrate collected in the filtrate bottle after filtering MTBE.

The GC-MS (7890B GC, 5977A MSD, Agilent Technologies, UK) analysis was conducted using a sample of the filtrate, where 10 µL aliquots were extracted from the filtrate bottle using a Gilson pipette and placed in a 1 mL glass vial containing 990 µL of methanol and placed in the GC-MS. The percentage of each of the solvents was then calculated based on the peak area of each of the solvents in the MS chromatogram.

To assess the suitability of the method before using the GC-MS analysis, with reference to the boiling points of the two solvents, a test was done to assess whether the more volatile solvent would either evaporate following the

preparation of the samples or would be overestimated in the resulting chromatogram due to its high volatility. Three conditions of the following anisole:MTBE solvent compositions 10:90, 50:50, and 90:10 were prepared for GC-MS analysis and the resulting percentages are shown in Table 8.3. The percentages of the MS chromatogram peak areas are in close agreement with the percentages of the solvent prepared. The largest error of 5% is seen for the measurement of the 50:50 composition, whereas the other measurement shows a 1-2% error. Those errors may be attributed to the preparation of the sample as small aliquots are extracted from the mixture, making it more likely to contribute to the error. To demonstrate the possibility of the evaporation of MTBE within the prepared samples, GC-MS analysis of the same samples was conducted two days later and the chromatogram showed only peaks of anisole with no peaks of MTBE in any of the three samples.

Table 8.3. The percentage of anisole and MTBE solvent in three conditions used to assess the feasibility of using GC-MS analysis.

Measurement #	1		2		3	
Solvent	Anisole/ %	**MTBE/ %**	Anisole/ %	**MTBE/ %**	Anisole/ %	**MTBE/ %**
Theoretical percentage/%	10	**90**	50	**50**	90	**10**
MS chromatogram area/%	10.8	**89.2**	55	**45.0**	88.2	**11.8**

8.3.3 SORS dataset processing

In this experiment, four datasets are used. Those are the two calibration datasets collected during the drying of each of the solvents, anisole and MTBE, in paracetamol, in addition to the two datasets collected as validation and test sets of scenarios where the solvents are mixed. However, in Chapter 6, SORS spectra were collected using the SORS probe during the drying of paracetamol from anisole, while in chapter 7, SORS spectra were collected using the combined probe during the drying of paracetamol from MTBE. In this chapter, the SORS spectra were also collected using the combined probe. The SORS

probe enables collecting SORS spectra 0-5 mm in 1 mm increments, while the combined probe enables the collection of SORS spectra at 0, 1.5, 2.5, and 3.5 mm offset distances. Therefore, to use the anisole calibration dataset, the anisole dataset spectra must be re-processed to produce spectra corresponding to the offsets of the combined probe. This section describes the processing of the anisole dataset as well as the new datasets to enable their use in PLSR analysis.

8.3.3.1 Preparation of calibration sets for PLSR analysis

SORS spectra were previously collected from the drying of granular paracetamol in anisole and MTBE using the SORS and combined probes respectively. In order to use both existing datasets, it is essential to address differences in the SORS signal collected from each of the probes, those differences and the methods used to address them are shown in Table 8.4.

Table 8.4. Sources of variability in the signal collected from the combined and SORS probes.

Source of variability	Method to address variability	Dataset to apply to (anisole, MTBE, filtration, all)
Spatial offset distances	Interpolate the signal from the SORS probe for the calibration set samples for each of the wavenumber values	Anisole
Number of collection fibres per offset	Extract the signal from one fibre per offset (1FPO) for the signal	All
Probe performance (i.e. signal throughput)	Pre-process spectra (SNV)	All

The approach followed in processing the SORS signals for use in the estimation of the two solvent contents is shown in Figure 8.3.

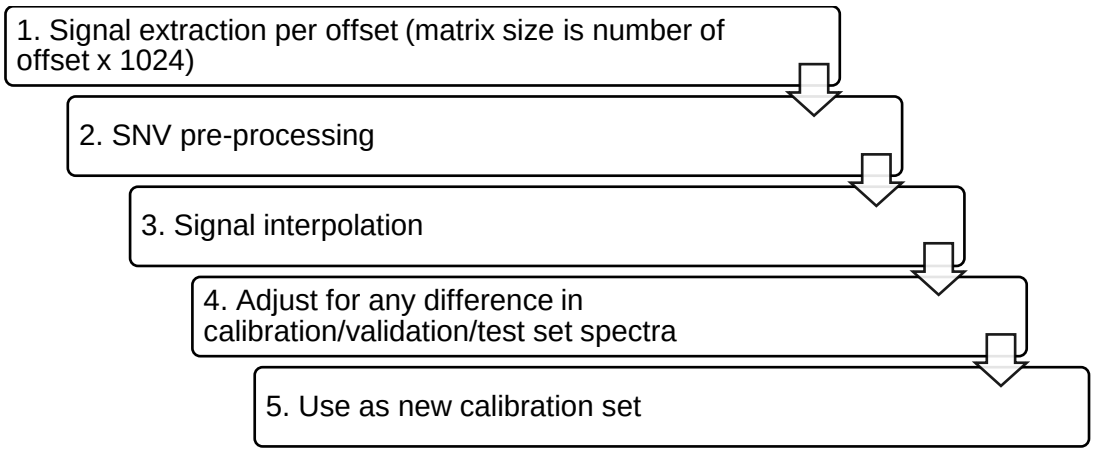

Figure 8.3. Step-wise approach for preparing the calibration and test sets.

Step 1 is applied to both calibration and test set SORS spectra, in order to obtain a comparable signal as opposed to the variation that might be encountered in case of using spectra of the signals summed from multiple fibres for the different offset. Figure 8.4 shows an example of the spectral image collected from the Argon spectral calibration lamp (3060AR, 10 mA, Newport, USA) for an acquisition time of 20 milliseconds, where the image is divided to extract the SORS signal from one fibre per offset from the SORS measurement.

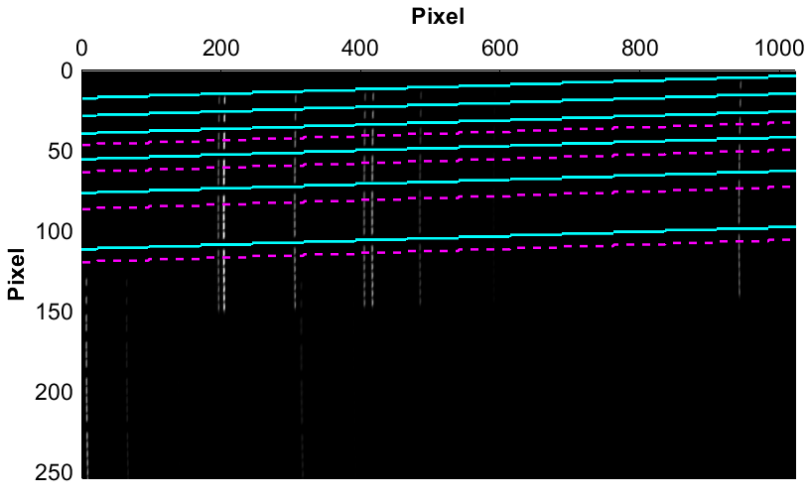

Figure 8.4. Spectral image of an argon lamp, cyan lines highlight the beginning of the pixel range summed to obtain spectra, the magenta lines mark the end of the horizontal pixel range where spectra from only one fibre were summed for the offset with multiple collection fibres (2, 3, 4, and 5 mm offset distances).

To assess the decrease in signal intensity as the offset distance increases, SORS spectra of granular paracetamol collected using 100 mW laser power for 20 seconds were extracted as one fibre per offset and the maximum peak intensity for each of the offset was plotted in Figure 8.5, this figure shows the decrease in signal intensity as the offset distance increases as well as highlighting the polynomial trend of decrease in the curve.

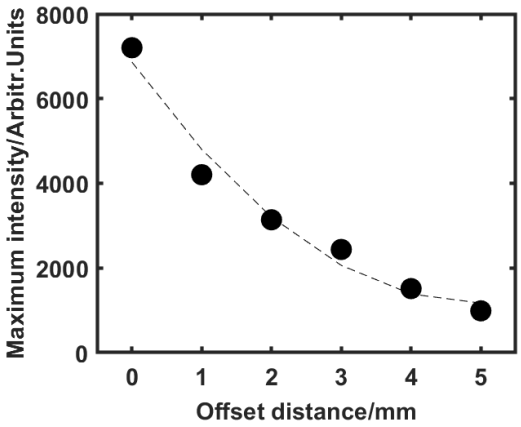

Figure 8.5. The maximum intensity of paracetamol peaks extracted as one fibre per offset.

In step 2, SORS spectra from all datasets are pre-processed using SNV, which would remove baseline variation between samples and aims to decrease the variation between the SORS spectra collected using the SORS probe and the combined probe.

For step 3, the SORS signals from the anisole dataset were interpolated in order to obtain the spectra from the offsets corresponding to the combined probe. The interpolation was done using the built-in MATLAB function interp1, specifying the method as cubic. The results from this step are spectra corresponding to offsets between the original SORS probe offsets; those are 0.5-4.5 mm with 1 mm increments. Spectra of 0, 1.5, 2.5, and 3.5 mm offset distances are then used to form the final anisole calibration dataset used in this study.

Step 4 follows from the visual examination of the spectra produced in the previous step and includes adjusting the spectra for any other variation that

was not addressed in the previous steps. Following the assessment of the SNV pre-processed spectra collected using the SORS probe and the combined probe, a visible horizontal offset was seen between those two, where the baseline of the pre-processed spectra from the SORS probe was larger by around 0.2 arbitrary units compared to those collected using the combined probe. Therefore, the offset was subtracted from all spectra collected using the SORS probe.

8.3.4 Description of dataset

The datasets used as the calibration sets for the estimation of both anisole and MTBE content in the test set are shown in Table 8.5. For each sample, four SORS spectra corresponding to 0, 1.5, 2.5, and 3.5 mm offset distances are used.

Table 8.5. Description of the anisole and MTBE datasets collected during the drying of each of the solvents in granular paracetamol.

Dataset	**MTBE calibration**	**Anisole calibration**
Number of samples	83	69
Solvent content range in samples/%	0-20	0-20

The datasets collected from the washing experiments and used as the validation and test sets for the estimation of both anisole and MTBE content in the wet filter cake are described in Table 8.6.

Table 8.6. Description of the samples collected from granular paracetamol wet filter cakes using the combined probe following washing anisole with MTBE.

Dataset	**MTBE/Anisole validation set**	**MTBE/Anisole test set**
Number of samples	21	10
Total solvent content range in samples/%	4.35 - 14.45	2.3 – 16.4
Anisole content range in samples/%	0 - 14.5	0.1 – 11.6
MTBE content range in samples/%	0 - 5.7	0.5 – 7.2

8.3.5 Multivariate regression analysis

To construct partial least squares regression (PLSR) analysis models, a script developed in MATLAB (Mathworks, USA) and employed in earlier studies,[14,58] was used. The spectral range and pre-processing methods of the spectra in the calibration and test datasets are specified. Cross-validation is then performed on the calibration set to test the predictive performance of the PLSR model based on the calibration set spectra. The suitable PLSR model is applied to predict the solvent content in the test set.

The parameters used for PLSR for each of the SORS spectra as well as the combined spectra from each of the datasets are summarised in Table 8.7. The PLSR analysis of those datasets is done to compare the results of the originally processed spectra, where the signal from multiple fibres was summed up for the larger distances, to the signal from 1FPO.

Table 8.7. Description of the datasets used in the PLSR analysis for assessing the performance of re-processed 1FPO MTBE dataset and re-processed and interpolated 1FPO anisole dataset.

Dataset	**MTBE calibration**	**Anisole calibration**
Calibration set	63	52
Test set	20	17
Cross-validation	6-fold	6-fold
Original/Interpolated offset spectra	Original	Interpolated

Then, the calibration sets from Table 8.7 are used along with the validation and test sets described in Table 8.8.

Table 8.8. Description of the datasets used in the PLSR analysis for estimating the content of two solvents, anisole and MTBE, following washing.

Dataset	**MTBE/Anisole validation set**	**MTBE/Anisole test set**
Calibration set	21	10
Spectral ranges/cm^{-1}	Anisole: 960-1040 MTBE: 670-770	

8.4 Results

The results are divided into two sections. The first section reports the analysis of the reprocessed and interpolated calibration datasets, while the second section reports the PLSR analysis performance in the estimation of the solvent content of anisole and MTBE in the paracetamol filter cakes following washing.

8.4.1 Assessing the performance of the re-processed SORS spectra

This section details the analysis results of the interpolation of the anisole calibration dataset as well as the comparison between the 1FPO and original datasets.

8.4.1.1 Interpolation of anisole SORS spectra to obtain the anisole calibration set

SORS spectra collected from the drying of granular paracetamol in anisole were collected using the SORS probe, which includes offsets collected from 0-5 mm from the incidence laser. The interpolated spectra were those from 0.5-4.5 mm in 1 mm increments. An example of the spectra of samples of variable solvent content from the interpolated offset distance of 1.5 mm is shown in Figure 8.6 (a). This figure illustrates that the decrease in anisole peak intensity as the solvent content decreases can be seen in the interpolated spectra. To assess the response from the original and interpolated offsets following SNV pre-processing, Figure 8.6 (b) shows a zoom on the anisole peak in the spectra of a sample containing 18.6% anisole from all offset distances. The comparable intensity following pre-processing as well as a slight peak shift can be seen, which was also present in the original SORS spectra from the offsets due to the alignment to the detector.

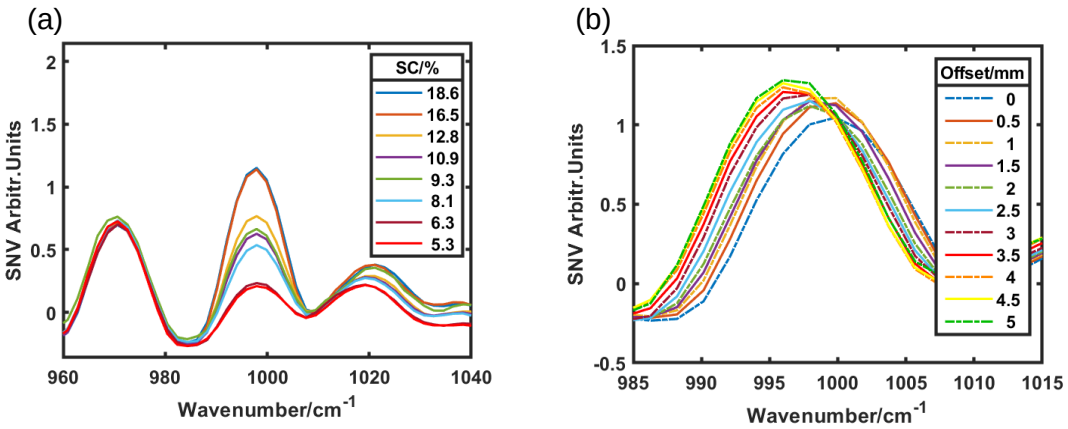

Figure 8.6. (a) Example of interpolated spectra at 1.5 mm offset distance. (b) Example of a sample containing 18.6% from original and interpolated spectra. Original offset spectra are in solid lines and interpolated spectra are in dashed lines.

Following the assessment of the spectra from the interpolated offsets with reference to the original offset distances, SORS spectra of variable solvent content of anisole in granular paracetamol collected with the SORS probe were compared to the SORS spectra collected using the combined probe; this is shown in Figure 8.7 (a) of the anisole peak, where a difference in peak width and an offset in the baseline of pre-processed spectra from both probes can be seen. While the difference in peak width is a result of the different alignment of each of the probes and cannot be adjusted in the calibration set, the baseline difference was adjusted by subtracting the offset from the granular paracetamol in anisole spectra as shown in Figure 8.7 (b) as was described in section 8.3.3.

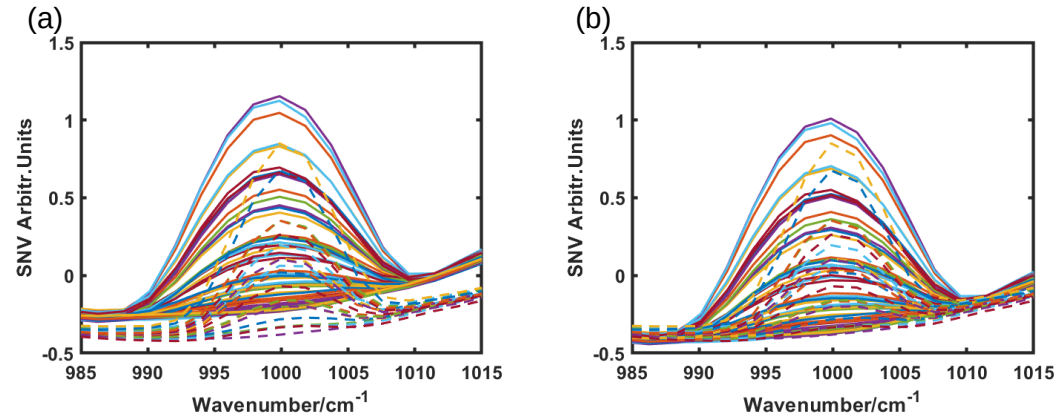

Figure 8.7. SNV pre-processed backscattering spectra from granular paracetamol in anisole calibration (solid lines) and the filtration (dashed line) datasets (a) before and (b) after addressing the baseline offset seen in (a).

8.4.1.2 Comparison of 1FPO and interpolated spectra PLSR analysis result with the original anisole calibration set

The PLSR results of the original granular paracetamol in anisole were compared with the dataset where spectra were extracted as one fibre per offset (1FPO), as well as with the interpolated offset spectra. The comparison is done in order to assess the differences in results using 1FPO spectra to construct the PLSR model in comparison to the signal obtained from all fibres for the same offset and evaluate the improvement in PLSR prediction as the collection offset distance increases.

Figure 8.8 shows the comparison between RMSECV and RMSEP from the PLSR analysis of the original and interpolated SNV pre-processed spectra of granular paracetamol in anisole over two spectral ranges, where the full spectral range of 250-1750 cm^{-1} is shown in black markers, and the anisole peak spectral range of 960-1040 cm^{-1} is shown in red markers. The RMSECV and RMSEP of the PLSR models of the original dataset over the two spectral ranges, shown as hollow circular markers, are seen to decrease as the offset distance increases. Comparing the RMSCV and RMSEP of the PLSR models of the original dataset to the PLSR models of the 1FPO dataset over the two spectral ranges, indicated by the square marker, shows a similar level of error up to the 3 mm offset distance and increase for the 4 mm and 5 mm offset distances. This increase in PLSR error indicates that the quality of the SORS spectra from the larger offset distances is reduced as a result of the lower signal intensity obtained as the offset distance increases as light diffuses in the sample before the signal is collected, as is shown in Figure 8.5. This is particularly seen in Figure 8.8 starting from the PLSR model of the 4 mm offset to the 5 mm offset spectra.

To further investigate the reproducibility of these observations, RMSECV and RMSEP of the PLSR models of spectra over the wavenumber range 960-1040 cm^{-1}, which includes the anisole peak of strongest intensity is overall similar to or lower than the full spectral range and follows the decrease in RMSECV as the collection offset distance increases. The smaller wavenumber range is

thought to show lower RMSECV as a result of including less variation that is not related to the solvent content since the wavenumber range includes the anisole peak with the strongest intensity. This would explain the almost identical RMSECV of the backscattering spectra compared to the offsets. However, as the offset distance increases to over 3 mm, the RMSECV and RMSEP of the PLSR models of spectra from those larger offset distances increase suggesting that the reduced variation that benefitted the PLSR models of the smaller offsets is hindered by a decrease in signal-to-noise ratio for the PLSR models of the 1FPO of larger offset distances.

Following from comparing the RMSECV and RMSEP of the PLSR models of the original and 1FPO, the RMSECV and RMSEP of the PLSR models of the 1FPO interpolated spectra at 1.5, 2.5, and 3.5 mm corresponding to the collection offset distances of the combined probe are compared. Those are indicated by the diamond-shaped markers in Figure 8.8. The RMSECV of the PLSR models of the interpolated spectra over the two spectral ranges show RMSECV values similar to or in between the spectra obtained from the original offsets. Although the RMSECV increases at the larger offset distances, the maximum offset distance used for analysis in the following section is 3.5 mm, and the RMSECV of the PLSR model of spectra interpolated from this offset distance is similar to that of the PLSR model of 1FPO spectra collected at 3 mm. The RMSEP shows a similar trend and is at a level slightly lower than that of the RMSECV, suggesting that the calibration sets represent the granular paracetamol in the anisole system sufficiently to obtain good estimations based on spectra obtained from the test set.

(a) (b)

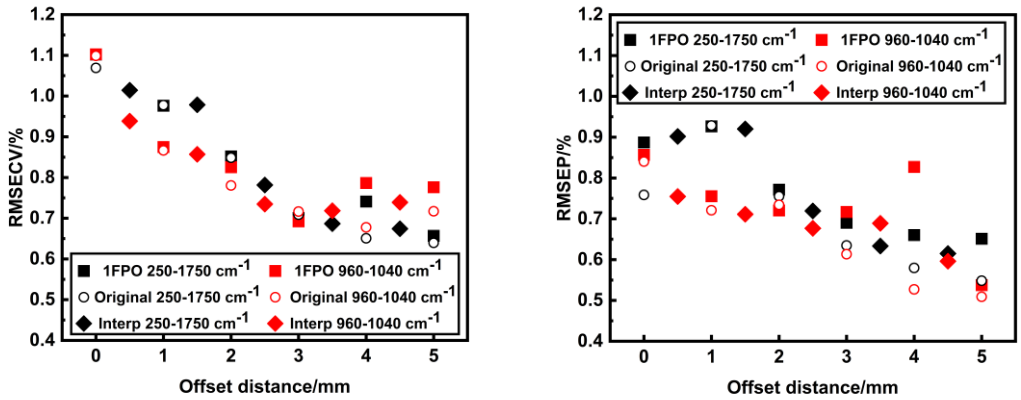

Figure 8.8. Comparison of (a) RMSECV and (b) RMSEP of PLSR models of the original, 1FPO spectra, and 1FPO interpolated granular paracetamol in anisole datasets over two spectral ranges.

8.4.1.3 Comparison of 1FPO spectra PLSR analysis result with the original MTBE calibration set

PLSR analysis results of the dataset collected from the drying of granular paracetamol in MTBE using the combined probe, where the signal was extracted from all of the multiple fibres per offset, were compared to the dataset in which spectra were extracted as 1FPO. Figure 8.9 shows the comparison of RMSECV and RMSEP of the PLSR models over the full wavenumber range, 50-1750 cm^{-1}, compared to the wavenumber range containing the solvent peak of strongest intensity, 670-770 cm^{-1}. Comparable RMSECV levels can be seen for the original and 1FPO spectra; this was evident in both of the spectral ranges. A similar observation can be seen from the RMSEP.

Looking at the 1FPO PLSR results represented by the RMSECV and RMSEP of the PLSR models of spectra granular paracetamol in anisole and MTBE in Figure 8.8 and Figure 8.9, respectively, the offset distances 0-3.5 mm show more consistency for spectra collected using the two probes, while the RMSECV and RMSEP are slightly higher for the larger offset distances of 4-5 mm for the anisole dataset. This indicates that the number of fibres used for collecting the signal from larger offset distances has more impact on collected spectra and consequently PLSR performance in estimating the solvent content.

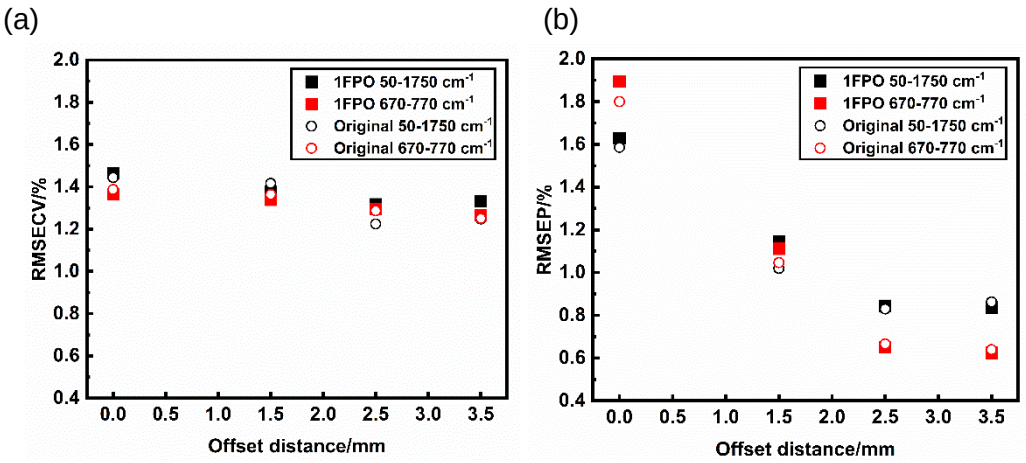

Figure 8.9. Comparison of (a) RMSECV and (b) RMSEP from the original and the 1FPO spectral dataset of granular paracetamol in MTBE datasets over two spectral ranges.

The comparisons between the original and 1FPO spectral datasets between 0-4 mm offset distances show a similar performance. Therefore, those datasets may be used as calibration sets for the estimation of the anisole and MTBE content in a granular paracetamol filter cake.

8.4.2 SORS for the estimation of the solvent content during cake washing

To assess the feasibility of using spatially offset Raman spectroscopy for monitoring two solvents during pharmaceutical cake washing, two experiments were conducted. In the first experiment, granular paracetamol was washed with a mixture of known percentages of two wash solvents, anisole and MTBE, and SORS spectra were collected. Through this dataset, SORS spectra would be assessed to detect the peaks of the two solvents in the samples containing different percentages of the solvents. In the second experiment, granular paracetamol is washed with anisole then MTBE consecutively and SORS spectra of the filter cake are collected. The calibration sets in the previous section are used here to estimate the solvent content in the samples of the second experiment as a test set, while spectra collected from the first set are used as a validation set to assess the suitability of the experimental setup and collected data.

8.4.2.1 Validation set

SORS spectra were collected following the wetting and filtration of granular paracetamol with a mixture of MTBE and anisole, reference solvent content values were obtained using LOD measurements. The percentage of each of the solvents in the total solvent content obtained from the LOD measurements was assumed to be equal to the percentages within the prepared solvent mixtures that were used to wash the paracetamol filter cake.

Loss on drying reference measurements

The total solvent content obtained from the LOD reference measurements is shown in Figure 8.10 in addition to the percentage of each of the solvents in the wet sample. A wider distribution of anisole compared to MTBE may be seen, which highlights the difference in the percentage of solvent removed with

reference to the percentage of each of the solvents in the mixture. In other words, samples washed with a mixture containing a larger percentage of anisole retained more of the solvent mixture following filtration. Moreover, lower amounts, as indicated by the narrower percentage, of MTBE remained in the sample overall. These observations regarding the two solvents imply that the determination of the actual percentage of each of the solvents may not be the most accurate if determined based on the theoretical percentage of each of the solvents.

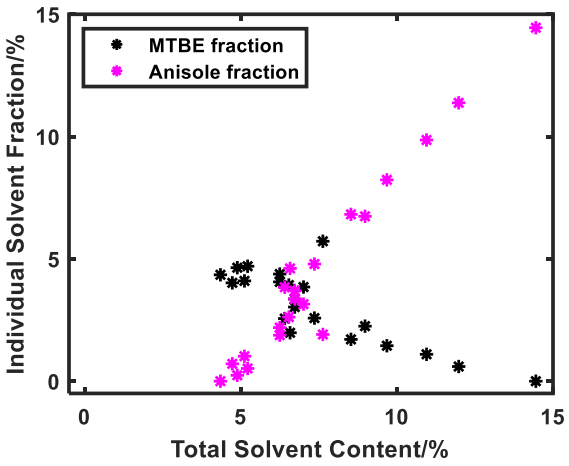

Figure 8.10. Total solvent content in the wet samples collected following the wetting and filtration of paracetamol and the individual percentage of each of the solvents.

SORS spectra of the validation set samples

SORS spectra of 21 samples of granular paracetamol wet with a solvent mixture of varying percentages of anisole and MTBE were collected using the combined probe. An example of those spectra from the 2.5 mm offset distance over the full spectral range following SNV pre-processing is shown in Figure 8.11 (a), where paracetamol peaks are seen along with characteristic MTBE and anisole peaks that vary as the percentage of each of the solvents in the total solvent content within those samples changes. To illustrate the change in the spectra with reference to the change in the percentage of the solvents, the spectra are divided into four groups based on the percentage of each solvent

in the total solvent content. A zoom-in view of the spectra in Figure 8.11 (a) is shown in Figure 8.11 (b) and (c) over the wavenumber range 670-770 cm^{-1} and 960-1060 cm^{-1} including the strongest intensity MTBE and anisole peak, respectively. Figure 8.11 (b) shows stronger MTBE peak intensity in the samples containing the largest percentage of MTBE in the mixture, where the change in MTBE peak intensity follows the change in the percentage of MTBE. Similarly, Figure 8.11 (c) shows that the change in anisole peak intensity follows the change in the percentage of anisole in the solvent mixture. Comparing spectra within the same group in Figure 8.11 (b) and Figure 8.11 (c) shows a complementary trend of a decrease in MTBE peak intensity as the MTBE percentage decreases along with the increase in anisole peak intensity. This indicates that the anticipated change in spectra as the percentage of each solvent changes can be seen and suggests that those spectra may be further used in PLSR analysis.

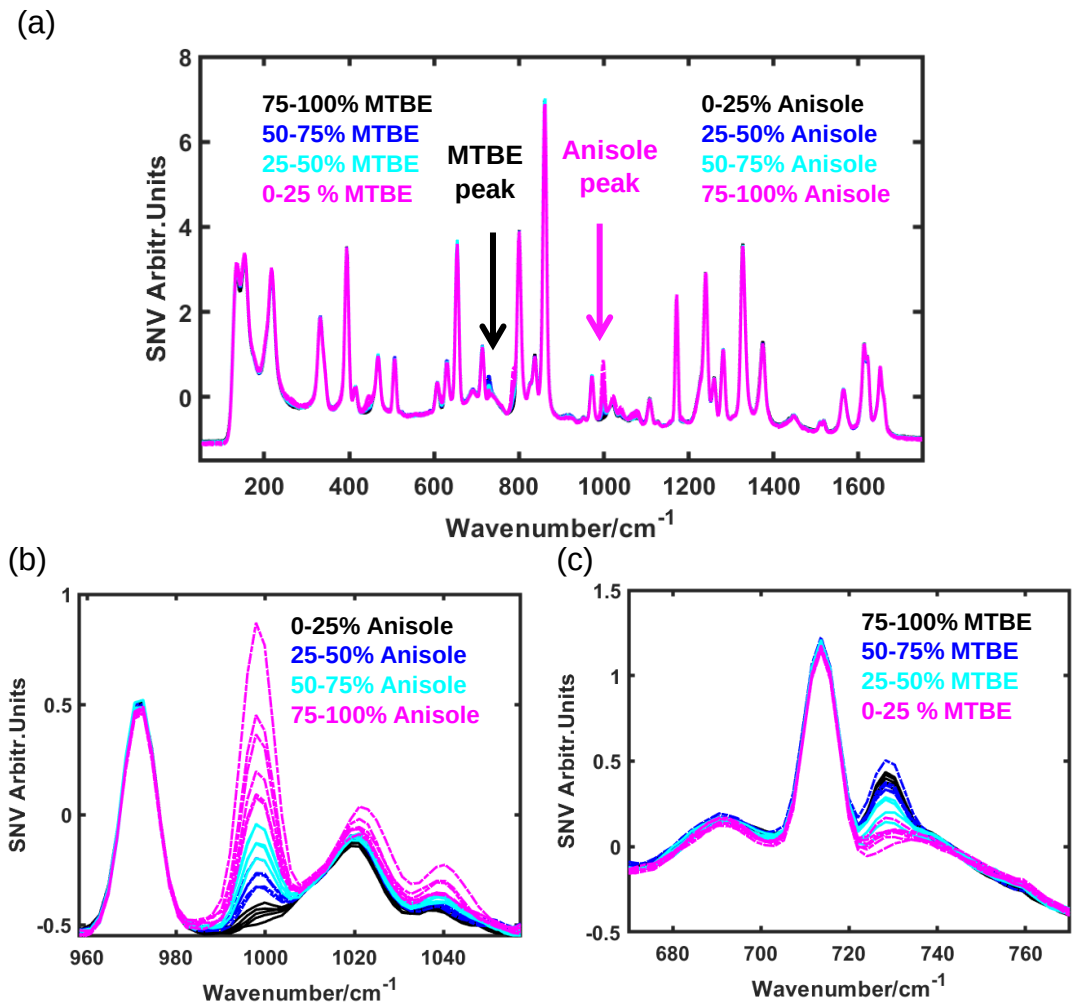

Figure 8.11. (a) SORS spectra from the 2.5 mm offset collected of the paracetamol samples washed with a mixture of variable percentages of anisole and MTBE with a zoom-in on the spectral range, (b) 960-1060 cm^{-1} shows the change in anisole peak intensity. The legend divides the samples into four groups according to the theoretical fraction of solvent content, and (c) 670-770 cm^{-1} shows the change in MTBE peak intensity.

Comparison of peak intensity in calibration and validation sets

Spectra of samples of similar solvent content for both solvents were compared to assess the suitability of those datasets for use in solvent content estimation. Figure 8.12 (a) shows the MTBE peak of samples from the calibration set along with that of the validation set. A slight systematic shift of the peaks in the spectra of the calibration set to the higher wavenumber range is seen. To investigate whether this is due to the alignment of the probe to the spectrometer, spectra from the argon calibration lamp acquired using both

probes were assessed, and the comparison showed no change in alignment. Therefore, this is attributed to the use of a different laser for the collection of the spectra for the test set from solvent mixture experiments. Figure 8.12 (b) shows the strongest anisole peak in addition to the neighbouring paracetamol peaks. A similar shift to the right is seen in those peaks, in addition to the difference in peak width within the spectra from the two datasets due to the alignment of each of the probes as was noted in Section 8.4.1.1. Most importantly, the peak intensity of spectra of similar solvent content (solid and dashed lines) is comparable. Therefore, it can be concluded that the validation set spectra, and the reference LOD measurements, do represent the solvent content of anisole and MTBE and can be used for further analysis.

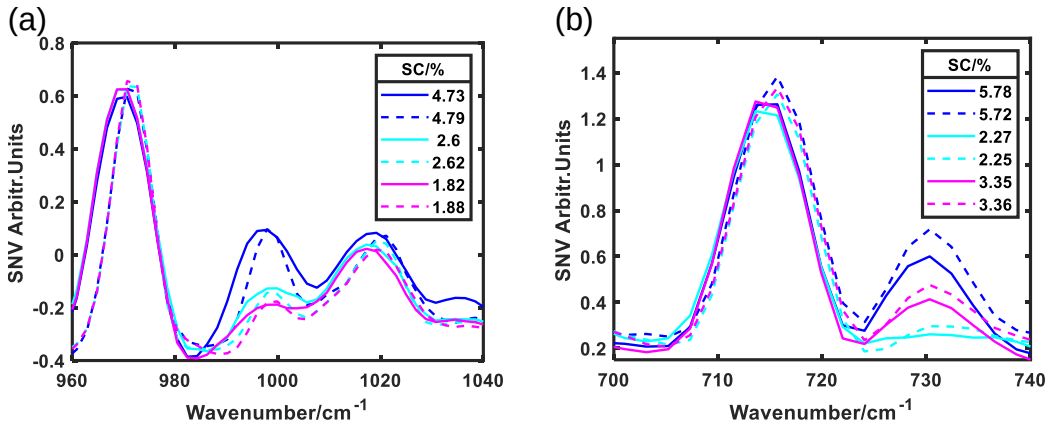

Figure 8.12. Comparison of calibration set spectra (solid line) with validation set (dashed line) of (a) anisole peak and (b) MTBE peak from 3.5 mm offset.

8.4.2.2 Test set

First, the granular paracetamol in the MTBE dataset collected using the combined probe was extracted as spectra of one fibre per offset and the granular paracetamol in the anisole dataset collected using the SORS probe was extracted as one fibre per offset. Then, the spectral intensities over the full spectral range were interpolated to obtain spectra corresponding to the offsets in the combined probe. Those MTBE and anisole datasets were used as the calibration sets for the estimation of the solvent content of each of the solvents in the spectra of samples washed with two solvents. Spectra of

paracetamol washed with a mixture of the two solvents were collected and used as a validation set. In this section, the spectra collected following the washing of a paracetamol filter cake with anisole and MTBE consecutively and the dataset is used as a test, where the content of each of the solvents is estimated based on the individual calibration sets.

Comparing the reference measurements collected for the test set

Three methods were used for determining the percentage of each of the solvents in the wet cake using the theoretical percentage of the two solvents, the mass of the filtrate following the filtration of each of the solvents, and the percentage of the peak area of each of the solvents in the MS chromatogram.

The percentages of each of the solvents obtained from the filtrate mass are expected to be in good agreement with the mass of the filtrate from each of the solvents, provided that the two solvents adsorb onto paracetamol to a similar extent and that no significant evaporation from the filtrate bottle occurred. Similarly, the GC-MS analysis percentages are expected to be in good agreement with the filtrate mass per the previous presumption in addition to the assumption that no major error was introduced during the GC-MS sample preparation.

The theoretical percentages of each of the solvents in addition to the resulting percentages from the filtrate mass and GC-MS are shown in Table 8.9. Since none of the methods describes directly the percentage of the solvents in the wet cake, a comparison between the two experimental methods, filtrate mass and GC-MS, to the theoretical percentage is done to select a reliable reference percentage. Overall, the three methods show that the percentage of MTBE in the solvents wetting paracetamol is increasing as the wash volume is increased and this increase is associated with the decrease in anisole percentage. The percentages from samples 1-2 are similar for the three methods. A discrepancy is seen between the three methods for sample 3, where the increase in MTBE seen in the percentage from the filtrate mass

suggests that more anisole was retained in the filter cake compared to MTBE, whilst the lower GC-MS percentage could be attributed to the evaporation of MTBE. Sample 4 shows a lower percentage of MTBE and a higher percentage of anisole in the filtrate mass compared to the theoretical percentage suggesting that anisole was washed off the filter cake when MTBE was filtered, but MTBE then evaporated from the filtrate; however, the GC-MS percentage is almost identical to the theoretical percentage suggesting an error in the filtrate mass measurement. Samples 5-10 show higher percentages of MTBE and lower anisole in the filtrate mass and GC-MS, to different extents in 5-7 and 8-10, compared to the theoretical percentage, suggesting that anisole was retained on the filter cake while MTBE was filtered out. It was noted that the results of one particular GC-MS sample, sample 9, were affected by the GC-MS instrument sampling method, where 2-propanol is used to wash the sampling needle between samples. In the sample, the 2-propanol peak was co-eluted with that of MTBE resulting in a slightly larger peak area and, therefore, a larger calculated percentage of MTBE. Since the percentages according to the filtrate mass are a value in between the theoretical and GC-MS percentages for half of the samples and considering that no sample preparation was included compared to the GC-MS analysis, those percentages were used for multiplication by the total solvent content obtained from LOD and were then used as the reference in the PLSR analysis.

Table 8.9. The percentage of anisole and MTBE solvent in the filter cake determined through theoretical percentage, filtrate mass, and GC-MS analysis. The shading colours relate to the colours of objects in Figure 8.2 (a).

Method	Theoretical percentage		Filtrate mass		GC-MS	
#	Anisole/%	**MTBE/%**	Anisole/%	**MTBE/%**	Anisole/%	**MTBE/%**
1	66.7	**33.3**	70.7	**29.3**	69.1	**30.9**
2	50.0	**50.0**	49.4	**50.6**	47.0	**53.0**
3	44.4	**55.6**	25.8	**74.2**	32.2	**67.8**
4	40.0	**60.0**	47.6	**52.4**	39.9	**60.1**
5	36.4	**63.6**	26.2	**73.8**	28.0	**72.0**
6	33.3	**66.7**	26.7	**73.3**	25.5	**74.5**
7	30.8	**69.2**	22.2	**77.8**	23.6	**76.4**
8	28.6	**71.4**	26.9	**73.1**	22.8	**77.2**
9	26.7	**73.3**	23.7	**76.3**	18.0	**82.0**
10	25.0	**75.0**	24.3	**75.7**	20.5	**79.5**

The total solvent content obtained from the LOD reference measurements is shown in Table 8.10. The percentages of each of the solvents in the total solvent content obtained from the LOD measurements are also shown in the same table. Those indicate that the anisole content decreases as the volume of MTBE used for washing is increased between samples 1-10.

Table 8.10. Total solvent content in wet paracetamol filter cakes and the content of each anisole and MTBE according to the percentage obtained from the filtrate mass.

#	Total solvent content/%	Anisole/%	MTBE/%
1	16.40	11.60	4.80
2	11.00	5.43	5.57
3	9.64	2.49	7.15
4	11.17	5.32	5.85
5	3.65	0.96	2.70
6	1.83	0.49	1.34
7	1.97	0.44	1.53
8	2.06	0.55	1.51
9	0.60	0.14	0.46
10	2.27	0.55	1.72

8.4.2.3 SORS for the estimation of the solvent content following cake washing

SORS spectra of the ten samples were collected using the combined probe. Figure 8.13 shows the change in anisole and MTBE peaks according to the change in the content of each of the solvents, where the spectra were sorted according to the solvent content value to assess this change more clearly. Figure 8.13 (a) shows the decrease in anisole peak intensity as the anisole content decreases. Two samples of similar anisole content of 0.6%, for example, have similar peak intensity and follow the anisole content as measured through the percentage of anisole in the filtrate. Similarly, Figure 8.13 (b) shows that the peak intensities correspond to the MTBE content, which may be seen in the consistency of the peak intensity in samples containing 1.5% of MTBE for example. Observations from Figure 8.13 (a-b)

confirm that the total solvent content and percentages estimated through the filtrate mass do represent the solvent content within the samples. However, some level of error would still be expected due to the differences mentioned earlier between datasets and reference methods. In order to show the change in anisole content as the MTBE wash volume increases, the anisole peak intensity in Figure 8.13 (a) was plotted against the MTBE wash volume and is shown in Figure 8.13 (c). This figure shows the decrease in anisole peak intensity, except sample 3 of the 1.25 volume wash, as the MTBE wash volume increases to 2.5 and plateaus over 2.75-3 cake volumes. This is true apart from the spectra of the 1.25 wash volume which could be attributed to evaporation during sample handling during the experiment. Figure 8.13 (c) in turn confirms the effectiveness of the increase in cake volume in displacing anisole from the filter cake.

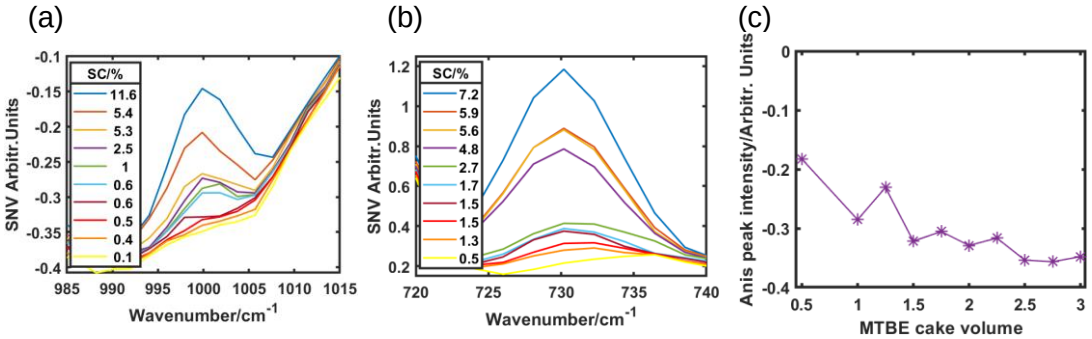

Figure 8.13. SORS spectra of the 10 test samples collected from 3.5 mm offset distance showing an example of (a) the anisole and (b) MTBE peak intensity decrease as the percentage of the solvent decreases. The legend shows the solvent content (SC%) of each solvent from the fractions obtained through the filtrate mass. (c) Anisole peak intensity of unsorted spectra from (a) versus MTBE cake volume.

PLSR analysis was conducted using the anisole and MTBE calibration sets and the spectra dataset shown in Figure 8.13 as the test set. To exclude the unintended interference in the PLSR model due to the difference between the calibration and test sets, spectral ranges containing the main solvent peaks were used in the PLSR analysis. Those were 670-770 cm^{-1} for MTBE and 960-1040 cm^{-1} for anisole as previously detailed in section 8.3.5.

A summary of the PLSR analysis results for the MTBE content is shown in Table 8.12. The number of LVs is selected based on the RMSECV curve for the calibration set. The number of latent variables capturing the variation in the dataset is 4 LVs for the backscattering spectra and 2 LVs for 1.5-3.5 mm spectra. The RMSECV for spectra from the three offset distances is lower by 0.1% for 1.5-3.5 mm compared to the backscattering spectra. The coefficient of determination, R^2, is also consistent and suggests a similar and strong correlation to the solvent content within the MTBE calibration set. The slight increase in the percentage of variance in the PLSR models as the offset distance increases is consistent with observations in Chapter 6 and Chapter 7, and suggests that spectra from the larger offsets better represent the system. The RMSEP for the PLSR models of the washing dataset shows a similar level of error for the offset spectra and is three times higher than the RMSECV. The R^2 of the test set prediction is around 0.73, suggesting a good fit between those datasets. The higher level of the RMSEP may be attributed to the differences between the calibration and test datasets, the collection setup of those datasets, as well as the reference methods. The test set spectra represent a three-component system, where the variation within each of the three components affects the results, even though the wavenumber range used in the PLSR analysis does not include anisole peaks. Moreover, the differences in spectra arising due to the difference in the SORS systems used for collecting the spectra, which led to the slight shift seen in Figure 8.12 (b). The reference method used for measuring the solving content within the calibration set was directly through the wet sample using LOD since only one solvent was to be quantified. However, the quantification of the MTBE content within the test was indirectly using the filtrate mass. Those three sources of variation are thought to contribute, to different extents, to the high RMSEP level. The variance, also reported in Table 8.11, increases as the offset distance increases.

Table 8.11. Summary of PLSR analysis results for the estimation of the MTBE content using SORS spectra over the wavenumber range 670-770 cm^{-1}.

Offset/mm	LVs	RMSECV/%	CV - R^2	RMSEP/%	P - R^2	Variance/%
0	4	1.36	0.86	3.55	0.76	94.7
1.5	2	1.34	0.87	4.02	0.73	94.6
2.5	2	1.30	0.88	4.01	0.73	95.0
3.5	2	1.26	0.88	3.96	0.73	95.4

To further look into the performance of the offset spectra, the regression and residuals plots of the PLSR models built using the 3.5 mm spectra are shown in Figure 8.14 (a) and (b), respectively. While the MTBE content within the calibration set is predicted accurately over the solvent content range of 0-10%, the MTBE content within the test set is predicted with low error over the low MTBE content range of 0-5% compared to 5-10%, where the MTBE content is over-estimated.

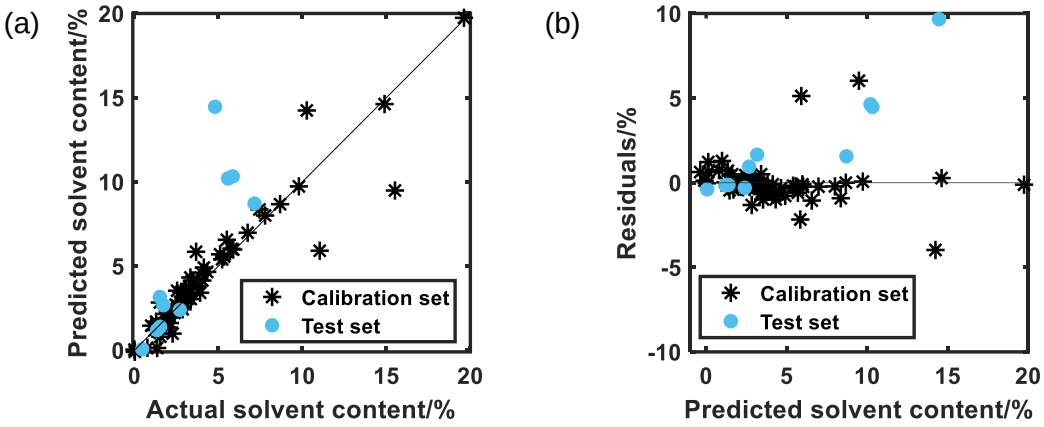

Figure 8.14. (a) Regression and (b) residuals plots from PLSR of the 3.5 mm SORS spectra predicting the MTBE solvent content.

A summary of the PLSR analysis results for the anisole content is shown in Table 8.12. The number of latent variables is 2 LVs for 0-1.5 mm offset spectra and 3 for 2.5-3.5 mm offset spectra. This may be attributed to the components of the system within the calibration set, paracetamol and anisole, in addition to another source of variation within the larger offset spectra, which may arise due to the larger distance through which light travels through the sample before

being collected at the detector. The RMSECV in Table 8.12 is the highest for the backscattering spectra and decreases as the offset distance increases, where the lower RMSECV indicates more accurate estimations based on the spectra from a larger offset. The R^2 shows an opposing trend as the values are high overall, but are larger for the offsets, indicating a stronger correlation to the actual anisole content. This is also indicated by the larger percentage of variance captured within the models of the larger offset distance spectra compared to the backscattering spectra. RMSEP of the anisole content within the washing dataset is approximately 4 times higher than the RMSECV, where the RMSEP similarly decreases as the offset distance increases. The prediction R^2 shows an opposite trend to that of the RMSEP indicating a stronger correlation found from the larger offset spectra. However, the prediction R^2 is lower than that of the cross-validation R^2 indicating variation affecting the linearity between the calibration and test set leading to lower accuracy in predicting the solvent content within the test set. The three factors leading to the high RMSEP mentioned for the MTBE dataset, which was the variation between the datasets, the collection setup of those datasets, and the reference methods, also apply here. However, another factor affecting the performance of for predicting the anisole content in the washing dataset is that the calibration anisole dataset is an interpolated dataset. Therefore, the test set spectra would also include variation, attributed to the experimental setup, not represented within the calibration set leading to the lower prediction R^2 seen. The variance, also reported in Table 8.12, increases as the offset distance increases, which conforms to what was seen in the PLSR of the spectra range including the MTBE peak.

Table 8.12. Summary of PLSR analysis results for the estimation of the anisole content using SORS spectra over the wavenumber range 960-1040 cm^{-1}.

Offset/mm	LVs	RMSECV/%	CV - R^2	RMSEP/%	P - R^2	Variance/%
0	2	1.10	0.94	4.28	0.38	97.6
1.5	2	0.89	0.96	4.07	0.61	98.5
2.5	3	0.73	0.98	3.13	0.69	99.0
3.5	3	0.70	0.98	3.44	0.53	99.1

Figure 8.15 (a) and (b), show the regression and residuals plots, respectively, of the PLSR models constructed with the 3.5 mm offset spectra. Those figures show that, similar to the prediction of MTBE, the anisole content estimated from spectra corresponding to the lower anisole content spectra, 0-5%, are predicted more accurately compared to those of higher solvent content. The higher anisole content, where the RMSEP is higher, is under-estimated. This is the opposite of the observation of the prediction of the MTBE content where the error was due to the over-estimation of the MTBE content.

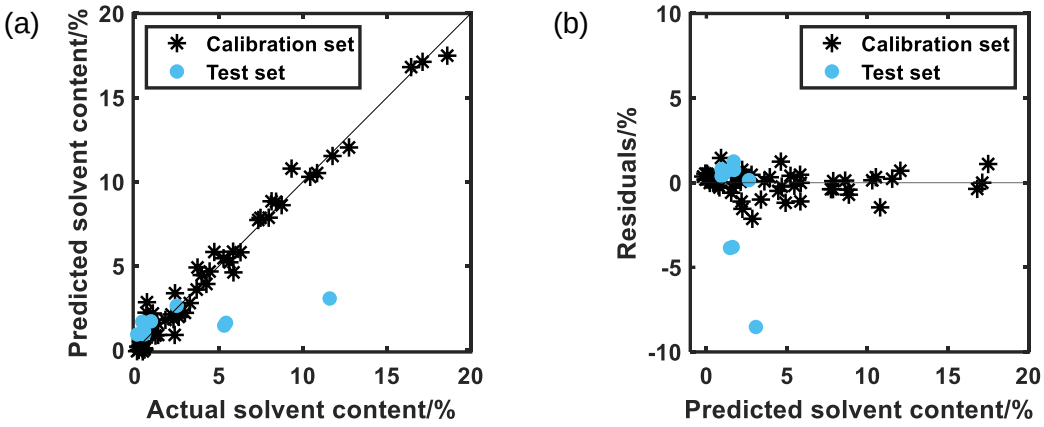

Figure 8.15. (a) Regression and (b) residuals plots from PLSR of the 3.5 mm SORS spectra predicting the anisole solvent content.

8.5 Conclusions

The application of spatially offset Raman spectroscopy coupled with partial least squares regression for the estimation of the solvent content of two wash solvents, anisole and MTBE, within a paracetamol filter cake, was explored. Two individual datasets of SORS spectra of paracetamol in anisole and paracetamol in MTBE were used in PLSR for the estimation of the content of each solvent in a SORS test set collected from a filter cake wet with variable percentages of both solvents. Prior to the use of the two calibration sets, the differences between the SORS spectra in each of the solvent datasets were addressed as the paracetamol in anisole spectral dataset was collected using a SORS probe with 0-5 mm equidistant offsets while the paracetamol in MTBE dataset was collected using a probe with 0, 1.5, 2.5, ad 3.5 mm offset distances, which was also used to collect the dataset of paracetamol washed with both solvent. The differences between the datasets were addressed through the use of signals obtained through one collection fibre as opposed to multiple fibres in previous experiments, applying SNV pre-processing, and interpolating the signal from the 0-5 offset distances from the SORS probe to obtain spectra corresponding to 1.5, 2.5, and 3.5 mm collection offsets. The new datasets were then used to construct PLSR models and their performance was assessed in comparison the original datasets. Once deemed reliable, the new calibration PLSR models of anisole and MTBE were used to estimate the content of each of the solvents in the washing dataset spectra. The PLSR results show that the maximum root mean square error prediction is five-fold of the root mean square error of calibration. The sources of inaccuracy contributing to the higher RMSEP include the differences in the calibration sets collected from each of the solvents in addition to the reference method for quantifying the actual solvent content within the cake, where three methods were used before selecting one. The PLSR results indicate that SORS spectra show potential for use in estimating the solvent content in drying and washing, in addition to the relevant process with similar system components.

9. Conclusions and Future Work

This thesis reported the investigation of the application of spatially and angularly resolved diffuse reflectance NIR measurements and spatially offset Raman spectroscopy collected using bespoke probes for monitoring the solvent content in laboratory-scale pharmaceutical drying. The analysis conducted in the previous chapters has led to some observations and conclusions regarding the application of spatially resolved spectroscopy for the monitoring of pharmaceutical drying and washing. Moreover, areas where additional work would have been beneficial, but may have been outwith the capacity of this project were also identified. Those conclusions and suggestions for future work are detailed in this chapter.

9.1 Conclusions

In this thesis, spatially offset Raman spectroscopy and spatially and angularly resolved diffuse reflectance near infrared spectroscopy, individually and combined were applied in an industrial process for the first time up to our knowledge. During pharmaceutical drying processes SORS and SAR-DRM signals were collected from model systems for each of the techniques. The spectra were then evaluated qualitatively and quantitatively.

Quantitative PLSR analysis of SAR-DRM spectra individually showed slight improvement represented by decrease in RMSECV and increase in R^2 as the collection distance increased from 0.3 mm to 0.9 mm; this was most evident where 0° illumination angle was used. When analysed in combinations, a trend was seen where PLSR model performance is superior for those models including configurations from the larger collection distances and for those from the 0° illumination angle. Quantitative PLSR analysis of SORS spectra also showed improvement in PLSR model performance as the collection offset distance increased. This provides practical validation for using spatially resolved spectroscopy to monitor pharmaceutical drying.

Combined together, PLSR models including SORS and SR-DRM configurations were found to perform similarly to the PLSR models of the SORS configurations; this was attributed to the superior Raman signal resolution and intensity compared to the NIR signals. The monitored systems, paracetamol in either heptane, anisole or MTBE, indicated that for both SORS and SAR-DRM techniques, the PLSR model performance is improved for the systems with higher signal intensity and lower overlap between the component peaks, which may be a limitation for both conventional and spatially resolved spectroscopy.

Following from using SORS the monitoring of the content of a wash solvent during drying, the calibration sets used for each of the solvents anisole and MTBE, collected with two different probes, were used to estimate the content

of the two solvents in a filter cake wet with both solvents. This demonstrates the transferability of those calibration sets collected using different equipment and under different conditions and corroborates the applicability of spatially resolved spectroscopy to an additional part in the isolation unit processes, thus showing further potential for application in other pharmaceutical unit processes. Hence, further potential of those spatially resolved spectroscopic techniques for applications monitored through conventional spectroscopy, such as API content, blending uniformity, polymorphic forms, and hydrate or solvate formation, is demonstrated.

9.2 Future work

Following the investigation of spatially resolved spectroscopy for monitoring the solvent content in pharmaceutical isolation unit processes, future work is recommended as an optimisation or an extension for each of the studies.

9.2.1 SAR-DRM for monitoring pharmaceutical drying

Among the two paracetamol/solvent systems monitored using SAR-DRM, it was noted that superior performance was seen in PLSR models of paracetamol/n-heptane as opposed to the paracetamol/MTBE systems. This was explained by the differences in the spectra of the solvents, where the n-heptane spectrum includes a characteristic peak with minimal overlap with the paracetamol peak while the peaks in the MTBE spectrum overlap with those of paracetamol. Further investigation of the quantitative analysis of such systems, where the signals from the system components display significant overlap, could offer insight into possible solutions. Moreover, the analysis in this thesis focusses on the wavelength range of 1100-1600 nm as this is the range enabled by the spectrometer. Paracetamol and the wash solvents also display peaks at longer wavelengths within the NIR range 1600-2200 nm, which could benefit the analysis if included. This is in addition to enabling a better understanding of the difference in solvent content estimation in each of the paracetamol particle size grades at the longer wavelength ranges.

The issue of signal intensity poses a limitation to the investigation and application of SAR-DRM, as the collected spectra suffer from low signal-to-noise ratio, particularly for the signals obtained from wider illumination angles and larger collection distances. This limits the application and utilisation of data but may be addressed through the use of an illumination source of stronger intensity or the use of longer acquisition duration for spectra collected from configurations that require so. Since the quick collection of spectra is vital for process monitoring, the use of a stronger light source is the preferred option.

The use of a stronger light source could also lead to achieving a better evaluation of the depth through which the solvent signal may be predicted.

9.2.2 SORS for monitoring pharmaceutical drying

Investigation of the solvent content estimation of anisole in a wet paracetamol filter cake showed a decrease in error as the collection offset distance increased. However, the investigation of the solvent content estimation of paracetamol wet with MTBE did not initially show a clear trend similar to the one seen in the paracetamol/anisole system. The differences between the spectra from those two systems are in the fact that the anisole spectrum includes a strong intensity peak that can be seen decreasing in intensity as the anisole is dried, as opposed to the MTBE peak, which overlaps with a paracetamol peak and is less clear as a result. This difference in intensity was also seen in the loadings within PLSR models constructed from both systems. Further investigation of the signals from the system that display components with spectra that significantly overlap could offer insight into better utilisation of such datasets for estimating the solvent content.

9.2.3 Combined SR-DRM and SORS for monitoring pharmaceutical drying

In this thesis, SR-DRM and SORS signals were combined, where each of the SR-DRM and SORS data blocks consisted of different numbers of variables and were characterised by variable intensities. Although signal interpolation and pre-processing were applied, the resulting PLSR model performance was almost identical to that of the SORS signal, which was higher in resolution and intensity compared to the SR-DRM signal. Evaluating the impact of the matrix size and the magnitude of the signal from each of the combined signals could offer insight into the possible ways for optimising the multi-block analysis for improved results.

Here, the data blocks were augmented (concatenated) to form multi-blocks. This method is termed a low-level multi-block fusion. Alternatively, mid and high-level fusion methods could be explored. Mid-level fusion is applied through the use of a regression model for feature extraction from the individual blocks, followed by multi-block analysis. In high-level fusion, a prediction is made based on the individual block, and the results are then combined. Mid-level fusion is recommended for the multi-block PLSR analysis since although the RMSECV and R^2 of the calibration models were closer to those of the PLSR model of the individual SORS spectra, examining the loadings curved of the larger LVs showed curves similar to the NIR signal of the solvent. This suggested that, although weak, the contribution from the SR-DRM signal in the multi-block analysis could lead to improved results.

Provided that the use of stronger incidence light as recommended in section 9.2.1 leads to an estimation of the depth through which a solvent signal may be detected using SR-DRM, it may be possible to establish the connection between the depth of signal detection from Raman and NIR signals from variable collection distances. This in turn could help in the optimisation of the selection of configurations combined in multi-block data analysis.

9.2.4 SORS for monitoring pharmaceutical isolation processes

SORS signals were interpolated to obtain spectra corresponding to certain offset distances. The interpolation of the signal obtained from the offset spectra has led to obtaining spectra that do represent the spatially offset spectra from further offsets. This suggests that, if variation in datasets and spectral offset signals are accounted for, spatially offset spectra can be simulated using algorithms and used for further data analysis and property prediction.

In this thesis, the SORS calibration datasets were used in the estimation of the two solvent contents following filtration and washing. Provided that two miscible solvents with NIR signals that do not significantly overlap with paracetamol are found, e.g. n-heptane and MTBE or acetone, SR-DRM may be used to monitor the solvent content following filtration and washing.

References

1 USFDA. PAT-A Framework for Innovative Pharmaceutical Development, Manufacturing, and Quality Assurance.(Guidance for Industry). (2004).

2 Hinz, D. C. Process analytical technologies in the pharmaceutical industry: The FDA's PAT initiative. *Anal. Bioanal. Chem.* **384**, 1036-1042, doi:10.1007/s00216-005-3394-y (2006).

3 Conder, E. W. *et al.* The Pharmaceutical Drying Unit Operation: An Industry Perspective on Advancing the Science and Development Approach for Scale-Up and Technology Transfer. *Organic Process Research and Development* **21**, 420-429, doi:10.1021/acs.oprd.6b00406 (2017).

4 Wang, I. C. *et al.* Polymorph transformation in paracetamol monitored by in-line NIR spectroscopy during a cooling crystallization process. *AAPS PharmSciTech* **12**, 764-770, doi:10.1208/s12249-011-9642-x (2011).

5 Ortega-Zúñiga, C. *et al.* Development of near infrared spectroscopic calibration models for in-line determination of low drug concentration, bulk density, and relative specific void volume within a feed frame. *J. Pharm. Biomed. Anal.* **164**, 211-222, doi:https://doi.org/10.1016/j.jpba.2018.10.046 (2019).

6 Harms, Z. D., Shi, Z., Kulkarni, R. A. & Myers, D. P. Characterization of Near-Infrared and Raman Spectroscopy for In-Line Monitoring of a Low-Drug Load Formulation in a Continuous Manufacturing Process. *Anal. Chem.* **91**, 8045-8053, doi:10.1021/acs.analchem.8b05002 (2019).

7 Blanco, M., Cueva-Mestanza, R. & Peguero, A. Controlling individual steps in the production process of paracetamol tablets by use of NIR spectroscopy. *J. Pharm. Biomed. Anal.* **51**, 797-804, doi:https://doi.org/10.1016/j.jpba.2009.09.038 (2010).

8 Román-Ospino, A. D. *et al.* Near infrared spectroscopic calibration models for real time monitoring of powder density. *Int. J. Pharm.* **512**, 61-74, doi:https://doi.org/10.1016/j.ijpharm.2016.08.029 (2016).

9 Matousek, P. & Parker, A. W. Bulk Raman Analysis of Pharmaceutical Tablets. *Applied Spectroscopy* **60**, 1353-1357, doi:10.1366/000370206779321463 (2006).

10 Hu, Y., Wikström, H., Byrn, S. R. & Taylor, L. S. Analysis of the Effect of Particle Size on Polymorphic Quantitation by Raman Spectroscopy. *Applied Spectroscopy* **60**, 977-984, doi:10.1366/000370206778397272 (2006).

11 De Beer, T. R. M. *et al.* Implementation of a Process Analytical Technology System in a Freeze-Drying Process Using Raman Spectroscopy for In-Line Process Monitoring. *Anal. Chem.* **79**, 7992-8003, doi:10.1021/ac070549h (2007).

12 Rantanen, J. Process analytical applications of Raman spectroscopy. *J. Pharm. Pharmacol.* **59**, 171-177, doi:10.1211/jpp.59.2.0004 (2007).

13 Igne, B., Talwar, S., Feng, H., Drennen, J. K. & Anderson, C. A. Near-Infrared Spatially Resolved Spectroscopy for Tablet Quality Determination. *J. Pharm. Sci.* **104**, 4074-4081, doi:https://doi.org/10.1002/jps.24618 (2015).

14 Chen, Y.-C., Foo, D., Dehanov, N. & Thennadil, S. N. Spatially and angularly resolved spectroscopy for in-situ estimation of concentration and particle size in colloidal suspensions. *Anal. Bioanal. Chem.* **409**, 6975-6988, doi:10.1007/s00216-017-0672-4 (2017).

15 Stone, N., Baker, R., Rogers, K., Parker, A. W. & Matousek, P. Subsurface probing of calcifications with spatially offset Raman spectroscopy (SORS):

future possibilities for the diagnosis of breast cancer. *Analyst* **132**, 899-905, doi:10.1039/B705029A (2007).
16 Mosca, S., Conti, C., Stone, N. & Matousek, P. Spatially offset Raman spectroscopy. *Nature Reviews Methods Primers* **1**, 21, doi:10.1038/s43586-021-00019-0 (2021).
17 Aulton, M. E., Taylor, K.M.G. *Aulton's Pharmaceutics, The Design and Manufacture of Medicines*. 5th edn, (Elsevier Health Sciences, 2018).
18 Brown, C. J. *et al.* Enabling precision manufacturing of active pharmaceutical ingredients: workflow for seeded cooling continuous crystallisations. *Molecular Systems Design & Engineering* **3**, 518-549, doi:10.1039/C7ME00096K (2018).
19 Ottoboni, S. *et al.* Understanding effect of filtration and washing on dried product: Paracetamol case study. *Powder Technology* **366**, 305-323, doi:https://doi.org/10.1016/j.powtec.2020.02.064 (2020).
20 Florence, A. T. & Attwood, D. *Physicochemical Principles of Pharmacy: In Manufacture, Formulation and Clinical Use*. (Pharmaceutical Press, 2015).
21 Mujumdar, A. S. *Handbook of Industrial Drying, Fourth Edition*. (Taylor & Francis, 2014).
22 Murugesan, S., Sharma, Praveen K., Tabora, Jose E. in *Chemical Engineering in the Pharmaceutical Industry* (ed David J. am Ende) 315-345 (2010).
23 EMA. ICH guideline Q3C (R8) - impurities guidelines for residual solvents. *EMA/CHMP/ICH/82260/2006* (2020).
24 Mortier, S. T. F. C., Gernaey, K. V., De Beer, T. & Nopens, I. Development of a Population Balance Model of a pharmaceutical drying process and testing of solution methods. *Comput. Chem. Eng.* **50**, 39-53, doi:https://doi.org/10.1016/j.compchemeng.2012.11.005 (2013).
25 Murru, M., Giorgio, G., Montomoli, S., Ricard, F. & Stepanek, F. Model-based scale-up of vacuum contact drying of pharmaceutical compounds. *Chem. Eng. Sci.* **66**, 5045-5054, doi:https://doi.org/10.1016/j.ces.2011.06.059 (2011).
26 Hsieh, D. S. *et al.* From Drying Kinetics, Solvate Structure, Particle Morphology, and Modeling to Optimal Drying Protocol. *Org. Process Res. Dev.* **21**, 1509-1520, doi:10.1021/acs.oprd.7b00162 (2017).
27 Sahni, E. K. & Chaudhuri, B. Contact drying: A review of experimental and mechanistic modeling approaches. *Int. J. Pharm.* **434**, 334-348, doi:https://doi.org/10.1016/j.ijpharm.2012.06.010 (2012).
28 Lekhal, A. *et al.* Impact of agitated drying on crystal morphology: KCl–water system. *Powder Technology* **132**, 119-130, doi:https://doi.org/10.1016/S0032-5910(03)00056-1 (2003).
29 Liang, H., Shinohara, K., Minoshima, H. & Matsushima, K. Analysis of constant rate period of spray drying of slurry. *Chem. Eng. Sci.* **56**, 2205-2213, doi:https://doi.org/10.1016/S0009-2509(00)00505-4 (2001).
30 Obregón, L., Quiñones, L. & Velázquez, C. Model predictive control of a fluidized bed dryer with an inline NIR as moisture sensor. *Control Engineering Practice* **21**, 509-517, doi:https://doi.org/10.1016/j.conengprac.2012.11.002 (2013).
31 Aulton, M. E., Somavarapu, S. in *Aulton's Pharmaceutics, The Design and Manufacture of Medicines* (ed M.E. Aulton, Taylor, K.M.G.) (Elsevier Health Sciences, 2018).
32 Rantanen, J., Lehtola, S., Rämet, P., Mannermaa, J.-P. & Yliruusi, J. On-line monitoring of moisture content in an instrumented fluidized bed granulator with a multi-channel NIR moisture sensor. *Powder Technology* **99**, 163-170, doi:https://doi.org/10.1016/S0032-5910(98)00100-4 (1998).

33 Burgbacher, J. & Wiss, J. Industrial Applications of Online Monitoring of Drying Processes of Drug Substances Using NIR. *Org. Process Res. Dev.* **12**, 235-242, doi:10.1021/op700293p (2008).
34 Lekhal, A. *et al.* The effect of agitated drying on the morphology of l-threonine (needle-like) crystals. *Int. J. Pharm.* **270**, 263-277, doi:https://doi.org/10.1016/j.ijpharm.2003.10.022 (2004).
35 Murugesan, K., Suresh, H. N., Seetharamu, K. N., Aswatha Narayana, P. A. & Sundararajan, T. A theoretical model of brick drying as a conjugate problem. *International Journal of Heat and Mass Transfer* **44**, 4075-4086, doi:https://doi.org/10.1016/S0017-9310(01)00065-5 (2001).
36 Adamson, J. *et al.* Development of Suitable Plant-Scale Drying Conditions That Prevent API Agglomeration and Dehydration. *Org. Process Res. Dev.* **20**, 51-58, doi:10.1021/acs.oprd.5b00327 (2015).
37 Cypes, S. H. *et al.* Drying an Organic Monohydrate: Crystal Form Instabilities and a Factory-Scale Drying Scheme to Ensure Monohydrate Preservation. *Org. Process Res. Dev.* **8**, 576-582, doi:10.1021/op049956a (2004).
38 EMA. ICH Q8 (R2) harmonised tripartite guideline, pharmaceutical development (2009).
39 Peinado, A., Hammond, J. & Scott, A. Development, validation and transfer of a Near Infrared method to determine in-line the end point of a fluidised drying process for commercial production batches of an approved oral solid dose pharmaceutical product. *J. Pharm. Biomed. Anal.* **54**, 13-20, doi:https://doi.org/10.1016/j.jpba.2010.07.036 (2011).
40 Green, R. L. *et al.* In-Line Monitoring of Moisture Content in Fluid Bed Dryers Using Near-IR Spectroscopy with Consideration of Sampling Effects on Method Accuracy. *Anal. Chem.* **77**, 4515-4522, doi:10.1021/ac050272q (2005).
41 Räsänen, E., Rantanen, J., Mannermaa, J.-P., Yliruusi, J. & Vuorela, H. Dehydration studies using a novel multichamber microscale fluid bed dryer with in-line near-infrared measurement. *J. Pharm. Sci.* **92**, 2074-2081, doi:10.1002/jps.10456 (2003).
42 Aaltonen, J., Kogermann, K., Strachan, C. J. & Rantanen, J. In-line monitoring of solid-state transitions during fluidisation. *Chem. Eng. Sci.* **62**, 408-415, doi:https://doi.org/10.1016/j.ces.2006.08.061 (2007).
43 Kogermann, K. *et al.* Establishing quantitative in-line analysis of multiple solid-state transformations during dehydration. *J. Pharm. Sci.* **97**, 4983-4999, doi:10.1002/jps.21357 (2008).
44 Römer, M. *et al.* Phase transformation of erythromycin A dihydrate during fluid bed drying. *J. Pharm. Sci.* **97**, 4020-4029, doi:10.1002/jps.21272 (2008).
45 Hamilton, P. *et al.* Studies of particle drying using non-invasive Raman spectrometry and particle size analysis. *Analyst* **136**, 2168-2174, doi:10.1039/C0AN00893A (2011).
46 Nieuwmeyer, F. J. S. *et al.* Granule Characterization During Fluid Bed Drying by Development of a Near Infrared Method to Determine Water Content and Median Granule Size. *Pharm. Res.* **24**, 1854-1861, doi:10.1007/s11095-007-9305-5 (2007).
47 Chua, K. J., Mujumdar, A. S. & Chou, S. K. Intermittent drying of bioproducts––an overview. *Bioresource Technology* **90**, 285-295, doi:https://doi.org/10.1016/S0960-8524(03)00133-0 (2003).
48 EMA. *Quality by Design*, <https://www.ema.europa.eu/en/human-regulatory/research-development/quality-design> (2011).

49 De Beer, T. *et al.* Near infrared and Raman spectroscopy for the in-process monitoring of pharmaceutical production processes. *Int. J. Pharm.* **417**, 32-47, doi:https://doi.org/10.1016/j.ijpharm.2010.12.012 (2011).

50 Bordawekar, S. *et al.* Industry Perspectives on Process Analytical Technology: Tools and Applications in API Manufacturing. *Org. Process Res. Dev.* **19**, 1174-1185, doi:10.1021/acs.oprd.5b00088 (2015).

51 Larkin, P. J. in *Infrared and Raman Spectroscopy: Principles and Spectral Interpretation* (Elsevier Science, 2011).

52 Sinsheimer, J. E. & Poswalk, N. M. Pharmaceutical applications of the near infrared determination of water. *J. Pharm. Sci.* **57**, 2007-2010, doi:10.1002/jps.2600571144 (1968).

53 Ward, H. W. & Sistare, F. E. On-line determination and control of the water content in a continuous conversion reactor using NIR spectroscopy. *Anal. Chim. Acta* **595**, 319-322, doi:https://doi.org/10.1016/j.aca.2007.03.020 (2007).

54 Martelli, F., Del Bianco, S. & Zaccanti, G. Effect of the refractive index mismatch on light propagation through diffusive layered media. *Physical Review E* **70**, 011907, doi:10.1103/PhysRevE.70.011907 (2004).

55 Martelli, F., Tiziano, B., Del Bianco, S., André, L. & Alwin, K. (SPIE).

56 Müllertz, A. *Analytical Techniques in the Pharmaceutical Sciences*. (New York, NY: Springer New York, 2016).

57 Ozaki, Y., Huck, C., Tsuchikawa, S. & Engelsen, S. B. *Near-Infrared Spectroscopy: Theory, Spectral Analysis, Instrumentation, and Applications*. (Springer Singapore, 2020).

58 Steponavičius, R. & Thennadil, S. N. Extraction of Chemical Information of Suspensions Using Radiative Transfer Theory to Remove Multiple Scattering Effects: Application to a Model Two-Component System. *Anal. Chem.* **81**, 7713-7723, doi:10.1021/ac9011667 (2009).

59 Li, X. *et al.* Review of NIR spectroscopy methods for nondestructive quality analysis of oilseeds and edible oils. *Trends in Food Science & Technology* **101**, 172-181, doi:https://doi.org/10.1016/j.tifs.2020.05.002 (2020).

60 Pandiselvam, R. *et al.* Recent advancements in NIR spectroscopy for assessing the quality and safety of horticultural products: A comprehensive review. *Frontiers in Nutrition* **9**, doi:10.3389/fnut.2022.973457 (2022).

61 Sakudo, A. Near-infrared spectroscopy for medical applications: Current status and future perspectives. *Clin. Chim. Acta* **455**, 181-188, doi:https://doi.org/10.1016/j.cca.2016.02.009 (2016).

62 Beć, K. B., Grabska, J. & Huck, C. W. Near-Infrared Spectroscopy in Bio-Applications. *Molecules* **25**, 2948, doi:https://doi.org/10.3390/molecules25122948 (2020).

63 Candolfi, A., De Maesschalck, R., Massart, D. L., Hailey, P. A. & Harrington, A. C. E. Identification of pharmaceutical excipients using NIR spectroscopy and SIMCA. *J. Pharm. Biomed. Anal.* **19**, 923-935, doi:https://doi.org/10.1016/S0731-7085(98)00234-9 (1999).

64 Guo, J.-H., Skinner, G. W., Harcum, W. W., Malone, J. P. & Weyer, L. G. Application of Near-Infrared Spectroscopy in the Pharmaceutical Solid Dosage Form. *Drug Dev. Ind. Pharm.* **25**, 1267-1270, doi:10.1081/DDC-100102297 (1999).

65 Iyer, M., Morris, H. R. & Drennen, J. K. Solid Dosage Form Analysis by near Infrared Spectroscopy: Comparison of Reflectance and Transmittance Measurements Including the Determination of Effective Sample Mass. *Journal of Near Infrared Spectroscopy* **10**, 233-245, doi:10.1255/jnirs.340 (2002).

66 Räsänen, E. & Sandler, N. Near infrared spectroscopy in the development of solid dosage forms. *J. Pharm. Pharmacol.* **59**, 147-159, doi:10.1211/jpp.59.2.0002 (2007).
67 Said, M. M., Gibbons, S., Moffat, A. C. & Zloh, M. Near-infrared spectroscopy (NIRS) and chemometric analysis of Malaysian and UK paracetamol tablets: a spectral database study. *Int. J. Pharm.* **415**, 102-109, doi:10.1016/j.ijpharm.2011.05.057 (2011).
68 Boiret, M. & Chauchard, F. Use of near-infrared spectroscopy and multipoint measurements for quality control of pharmaceutical drug products. *Anal. Bioanal. Chem.* **409**, 683+ (2017).
69 Brouckaert, D. *et al.* Towards real-time release of pharmaceutical tablets: 100% in-line control via near-infrared spatially resolved spectroscopy and 3D microwave resonance technology. *J. Pharm. Biomed. Anal.* **209**, 114491, doi:10.1016/j.jpba.2021.114491 (2022).
70 Román-Ospino, A. D. *et al.* Sampling optimization for blend monitoring of a low dose formulation in a tablet press feed frame using spatially resolved near-infrared spectroscopy. *Int. J. Pharm.* **602**, 120594, doi:https://doi.org/10.1016/j.ijpharm.2021.120594 (2021).
71 Scheibelhofer, O., Wahl, P. R., Larchevêque, B., Chauchard, F. & Khinast, J. G. Spatially Resolved Spectral Powder Analysis: Experiments and Modeling. *Applied Spectroscopy* **72**, 521-534, doi:10.1177/0003702817749839 (2018).
72 Rey-Bayle, M., Bendoula, R., Caillol, N. & Roger, J.-M. Multiangle near infrared spectroscopy associated with common components and specific weights analysis for in line monitoring. *Journal of Near Infrared Spectroscopy* **27**, 134-146, doi:10.1177/0967033519830062 (2019).
73 Ali, E. M. A., Edwards, H. G. M. & Scowen, I. J. Raman spectroscopy and security applications: the detection of explosives and precursors on clothing. *J. Raman Spectrosc.* **40**, 2009-2014, doi:https://doi.org/10.1002/jrs.2360 (2009).
74 Kuhar, N., Sil, S., Verma, T. & Umapathy, S. Challenges in application of Raman spectroscopy to biology and materials. *RSC Advances* **8**, 25888-25908, doi:10.1039/C8RA04491K (2018).
75 Lyng, F. M. *et al.* Discrimination of breast cancer from benign tumours using Raman spectroscopy. *PLoS One* **14**, e0212376 (2019).
76 Chanda, A. *et al.* Industry Perspectives on Process Analytical Technology: Tools and Applications in API Development. *Org. Process Res. Dev.* **19**, 63-83, doi:10.1021/op400358b (2015).
77 Matousek, P. *et al.* Subsurface Probing in Diffusely Scattering Media Using Spatially Offset Raman Spectroscopy. *Applied Spectroscopy* **59**, 393-400, doi:10.1366/0003702053641450 (2005).
78 Matousek, P. *et al.* Numerical Simulations of Subsurface Probing in Diffusely Scattering Media Using Spatially Offset Raman Spectroscopy. *Applied Spectroscopy* **59**, 1485-1492 (2005).
79 Eliasson, C., Macleod, N. A. & Matousek, P. Noninvasive Detection of Concealed Liquid Explosives Using Raman Spectroscopy. *Anal. Chem.* **79**, 8185-8189, doi:10.1021/ac071383n (2007).
80 Nicolson, F., Kircher, M. F., Stone, N. & Matousek, P. Spatially offset Raman spectroscopy for biomedical applications. *Chem. Soc. Rev.* **50**, 556-568, doi:10.1039/D0CS00855A (2021).
81 Gulia, S., Gulati, K., Gambhir, V. & Sharma, R. Detection of explosive materials and their precursors through translucent commercial bottles using spatially offset Raman spectroscopy using excitation wavelength in visible range. *Optical Engineering* **58**, 127102 (2019).

82 Nicolson, F. *et al.* Through barrier detection of ethanol using handheld Raman spectroscopy—Conventional Raman versus spatially offset Raman spectroscopy (SORS). *J. Raman Spectrosc.* **48**, 1828-1838, doi:https://doi.org/10.1002/jrs.5258 (2017).
83 Ghita, A., Matousek, P. & Stone, N. High sensitivity non-invasive detection of calcifications deep inside biological tissue using Transmission Raman Spectroscopy. *Journal of Biophotonics* **11**, e201600260, doi:https://doi.org/10.1002/jbio.201600260 (2018).
84 Dooley, M., McLaren, J., Rose, F. R. A. J. & Notingher, I. Investigating the feasibility of spatially offset Raman spectroscopy for in-vivo monitoring of bone healing in rat calvarial defect models. *Journal of Biophotonics* **13**, e202000190, doi:https://doi.org/10.1002/jbio.202000190 (2020).
85 Eliasson, C. & Matousek, P. Noninvasive Authentication of Pharmaceutical Products through Packaging Using Spatially Offset Raman Spectroscopy. *Anal. Chem.* **79**, 1696-1701, doi:10.1021/ac062223z (2007).
86 Matousek, P. & Parker, A. W. Non-invasive probing of pharmaceutical capsules using transmission Raman spectroscopy. *J. Raman Spectrosc.* **38**, 563-567, doi:https://doi.org/10.1002/jrs.1688 (2007).
87 Chao, K. *et al.* A Spatially Offset Raman Spectroscopy Method for Non-Destructive Detection of Gelatin-Encapsulated Powders. *Sensors* **17**, 618, doi:https://doi.org/10.3390/s17030618 (2017).
88 Johansson, J., Sparén, A., Svensson, O., Folestad, S. & Claybourn, M. Quantitative Transmission Raman Spectroscopy of Pharmaceutical Tablets and Capsules. *Applied Spectroscopy* **61**, 1211-1218, doi:10.1366/000370207782597085 (2007).
89 Keller, M. D. *et al.* Development of a spatially offset Raman spectroscopy probe for breast tumor surgical margin evaluation. *Journal of biomedical optics* **16 7**, 077006 (2011).
90 Matousek, P. Inverse Spatially Offset Raman Spectroscopy for Deep Noninvasive Probing of Turbid Media. *Applied Spectroscopy* **60**, 1341-1347, doi:10.1366/000370206778999102 (2006).
91 Schulmerich, M. V., Dooley, K. A., Vanasse, T. M., Goldstein, S. A. & Morris, M. D. Subsurface and Transcutaneous Raman Spectroscopy and Mapping Using Concentric Illumination Rings and Collection with a Circular Fiber-Optic Array. *Applied Spectroscopy* **61**, 671-678, doi:10.1366/000370207781393307 (2007).
92 Rinnan, Å., Berg, F. v. d. & Engelsen, S. B. Review of the most common pre-processing techniques for near-infrared spectra. *TrAC Trends in Analytical Chemistry* **28**, 1201-1222, doi:https://doi.org/10.1016/j.trac.2009.07.007 (2009).
93 Bi, Y. *et al.* A local pre-processing method for near-infrared spectra, combined with spectral segmentation and standard normal variate transformation. *Anal. Chim. Acta* **909**, 30-40, doi:https://doi.org/10.1016/j.aca.2016.01.010 (2016).
94 Savitzky, A. & Golay, M. J. E. Smoothing and Differentiation of Data by Simplified Least Squares Procedures. *Anal. Chem.* **36**, 1627-1639, doi:10.1021/ac60214a047 (1964).
95 Rinnan, Å. Pre-processing in vibrational spectroscopy – when, why and how. *Analytical Methods* **6**, 7124-7129, doi:10.1039/C3AY42270D (2014).
96 Huang, J., Romero-Torres, S. & Moshgbar, M. Practical considerations in data pre-treatment for NIR and Raman spectroscopy. *American Pharmaceutical Review* **13**, 116-127 (2010).
97 Zeaiter, M., Roger, J. M. & Bellon-Maurel, V. Robustness of models developed by multivariate calibration. Part II: The influence of pre-processing methods.

TrAC Trends in Analytical Chemistry **24**, 437-445, doi:https://doi.org/10.1016/j.trac.2004.11.023 (2005).
98 Barnes, R. J., Dhanoa, M. S. & Lister, S. J. Standard Normal Variate Transformation and De-Trending of Near-Infrared Diffuse Reflectance Spectra. *Applied Spectroscopy* **43**, 772-777, doi:10.1366/0003702894202201 (1989).
99 Geladi, P., Macdougall, D. & Martens, H. Linearization and Scatter-Correction for Near-Infrared Reflectance Spectra of Meat. *Applied Spectroscopy* **39**, 491 - 500 (1985).
100 Maleki, M. R., Mouazen, A. M., Ramon, H. & De Baerdemaeker, J. Multiplicative Scatter Correction during On-line Measurement with Near Infrared Spectroscopy. *Biosystems Engineering* **96**, 427-433, doi:https://doi.org/10.1016/j.biosystemseng.2006.11.014 (2007).
101 Roggo, Y. *et al.* A review of near infrared spectroscopy and chemometrics in pharmaceutical technologies. *J. Pharm. Biomed. Anal.* **44**, 683-700, doi:https://doi.org/10.1016/j.jpba.2007.03.023 (2007).
102 Brereton, R. G. *Chemometrics : data analysis for the laboratory and chemical plant*. (New York : J. Wiley, 2002).
103 Miller, J. *Statistics and Chemometrics for Analytical Chemistry*. 6th ed.. edn, (Harlow: Pearson Education UK, 2010).
104 Massart, D. L., Vandeginste, B. G. M., Deming, S. N., Michotte, Y. & Kaufman, L. *Chemometrics : a textbook*. 2 edn, (Elsevier Science Pub. Co., 1988).
105 Li, B., Martin, E. & Morris, J. Latent variable selection in partial least squares modelling. *IFAC Proceedings Volumes* **34**, 463-468, doi:https://doi.org/10.1016/S1474-6670(17)33867-3 (2001).
106 EMA. ICH Q14 Guideline on Analytical Procedure Development. (2022).
107 Næs, T., Isaksson, T., Fearn, T. & Davies, T. *A user-friendly guide to multivariate calibration and classification*. (NIR Publications, 2002).
108 Hanssen, L. M. & Snail, K. A. in *Handbook of Vibrational Spectroscopy* (eds J M Chalmers & P R Griffiths) (2006).
109 Stoliarskaia, D. *Investigation of the effects of colloidal suspension properties on spatially resolved diffuse reflectance*, Thesis [PhD] --University of Strathclyde, 2020, (2020).
110 Olinger, J. M. & Griffiths, P. R. Quantitative effects of an absorbing matrix on near-infrared diffuse reflectance spectra. *Anal. Chem.* **60**, 2427-2435, doi:10.1021/ac00172a022 (1988).
111 Qin, J. *et al.* A line-scan hyperspectral Raman system for spatially offset Raman spectroscopy. *J. Raman Spectrosc.* **47**, 437-443, doi:https://doi.org/10.1002/jrs.4825 (2016).
112 Smilde, A. K., Næs, T. & Liland, K. H. *Multiblock Data Fusion in Statistics and Machine Learning: Applications in the Natural and Life Sciences*. (Wiley, 2022).
113 Devaux, M.-F., Nathier-Dufour, N., Robert, P. & Bertrand, D. Effects of Particle Size on the Near-Infrared Reflectance Spectra of Wheat and Rape Seed Meal Mixtures. *Applied Spectroscopy* **49**, 84-91, doi:10.1366/0003702953963256 (1995).
114 Mishra, P., Rutledge, D. N., Roger, J.-M., Wali, K. & Khan, H. A. Chemometric pre-processing can negatively affect the performance of near-infrared spectroscopy models for fruit quality prediction. *Talanta* **229**, 122303, doi:https://doi.org/10.1016/j.talanta.2021.122303 (2021).
115 Szostak, R. & Mazurek, S. A quantitative analysis of liquid hydrocarbon mixtures on the basis of FT-Raman spectra registered under unstable

conditions. *Journal of Molecular Structure* **704**, 235-245, doi:https://doi.org/10.1016/j.molstruc.2004.01.058 (2004).
116 Chen, Z.-P. *et al.* Quantitative Analysis of Powder Mixtures by Raman Spectrometry: the influence of particle size and its correction. *Anal. Chem.* **84**, 4088-4094, doi:10.1021/ac300189p (2012).
117 Pellow-Jarman, M. V., Hendra, P. J. & Lehnert, R. J. The dependence of Raman signal intensity on particle size for crystal powders. *Vibrational Spectroscopy* **12**, 257-261, doi:https://doi.org/10.1016/0924-2031(96)00023-9 (1996).
118 Wang, H., Mann, C. K. & Vickers, T. J. Effect of Powder Properties on the Intensity of Raman Scattering by Crystalline Solids. *Applied Spectroscopy* **56**, 1538-1544, doi:10.1366/000370202321115779 (2002).
119 Reis, M. M., Araújo, P. H. H., Sayer, C. & Giudici, R. Evidences of correlation between polymer particle size and Raman scattering. *Polymer* **44**, 6123-6128, doi:https://doi.org/10.1016/S0032-3861(03)00669-4 (2003).
120 Borràs, E. *et al.* Data fusion methodologies for food and beverage authentication and quality assessment – A review. *Anal. Chim. Acta* **891**, 1-14, doi:https://doi.org/10.1016/j.aca.2015.04.042 (2015).
121 Price, C. J., Barton, A. & Coleman, S. J. in *The Handbook of Continuous Crystallization* (eds Nima Yazdanpanah & Zoltan K. Nagy) Ch. 13, 469-507 (The Royal Society of Chemistry, 2020).
122 Perry, R. H., Cecil, Hamilton Chilton, Perry, John Howard. *Chemical Engineers' Handbook*. 5 edn, (McGraw-Hill, 1973).
123 Shi, Y.-Y., Li, J.-Y. & Chu, X.-L. Progress and Applications of Multivariate Calibration Model Transfer Methods. *Chinese Journal of Analytical Chemistry* **47**, 479-487, doi:https://doi.org/10.1016/S1872-2040(19)61152-7 (2019).